

Roman G. Pavelko

SnO<sub>2</sub> BASED OXIDE SYSTEMS: SYNTHESIS,  
MATERIAL SCIENCE AND SENSING  
PROPERTIES AS A FUNCTION OF SURFACE  
HYDROXYLS

DOCTORAL THESIS

Supervised by Dr. A. A. Vasiliev

Department of Electronic, Electrical & Automatic Control Engineering



UNIVERSITAT ROVIRA I VIRGILI

Tarragona  
2010

UNIVERSITAT ROVIRA I VIRGILI

SNO<sub>2</sub> BASED OXIDE SYSTEMS: SYNTHESIS, MATERIAL SCIENCE AND SENSING PROPERTIES AS A FUNCTION OF SURFACE HYDROXYLS

ISBN:978-84-693-3388-4/DL:T.1000-2010

*The danger of the past was that men became slaves.  
The danger of the future is that men may become robots...*

*Erich Fromm*

UNIVERSITAT ROVIRA I VIRGILI

SNO<sub>2</sub> BASED OXIDE SYSTEMS: SYNTHESIS, MATERIAL SCIENCE AND SENSING PROPERTIES AS A FUNCTION OF SURFACE HYDROXYLS

ISBN:978-84-693-3388-4/DL:T.1000-2010





Departament d'Enginyeria Electrónica, Eléctrica i Automática  
Av. Paisos Catalans 26  
43007 Tarragona

I, Alexey Vasiliev, Ramon and Cajal Research Professor at the Department of Electronic, Electrical & Automatic Control Engineering of the University Rovira i Virgili

CERTIFY:

That the present study, entitled “ SnO<sub>2</sub> based oxide systems: synthesis, material science and sensing properties as a function of surface hydroxyls”, presented by Roman G. Pavelko for the award of the degree of Doctor, has been carried out under my supervision at Department of Electronic, Electrical & Automatic Control Engineering of the University Rovira i Virgili, and that it fulfils all the requirements to be eligible for the European Doctorate Label.

Tarragona, 29 Janury 2010

UNIVERSITAT ROVIRA I VIRGILI

SNO<sub>2</sub> BASED OXIDE SYSTEMS: SYNTHESIS, MATERIAL SCIENCE AND SENSING PROPERTIES AS A FUNCTION OF SURFACE HYDROXYLS

ISBN:978-84-693-3388-4/DL:T.1000-2010

# Abstract

The thesis is dedicated to the synthesis, comprehensive material science and some sensing properties of SnO<sub>2</sub>-MetO<sub>x</sub> oxide systems (where MetO<sub>x</sub> are IVB and IIIB metal oxides). The study was performed in comparison with blank SnO<sub>2</sub>, and SnO<sub>2</sub> doped with noble metals (Pd, Pt, Rh and their binary mixtures). Results of 8 *ex-situ* (TEM, HRTEM, XRD, FTIR, UV-Vis, BET, XPS and element analysis), 5 *in-situ* (TGA, MS-analysis, DRIFT, TXRD, TPR) techniques and sensing properties characterization (DC measurements as a function of temperature and gas composition) are discussed regarding surface chemistry of SnO<sub>2</sub> sensing phenomenon. The special attention is paid to the role of surface hydroxyls in the processes related with conductivity change of semiconductor adsorbents upon hydrogen chemisorption and oxidation in dry and humid air.

# Resumen

Los principales objetivos de la presente investigación fueron la síntesis de los sistemas oxídicos SnO<sub>2</sub>-MetO<sub>x</sub> (donde MetO<sub>x</sub> corresponde a los óxidos de grupos IVB y IIIB), el estudio extensivo de sus propiedades fisicoquímicas y sus propiedades como sensores de gases. La investigación se ha basado en la comparación de estos materiales con el SnO<sub>2</sub> puro y el SnO<sub>2</sub> dopado con metales nobles (Pd, Pt, Rh y sus combinaciones binarias). Resultados de 8 estudios *ex-situ* (TEM, HRTEM, XRD, FTIR, UV-Vis, BET, XPS y MS-análisis de elementos), 5 estudios *in-situ* (TGA, MS-analysis, DRIFT, TXRD, TPR) y la caracterización de los sensores de gases (conductividad de los materiales semiconductores en función de la temperatura y los componentes de los gases compuestos) se analizan considerando las reacciones químicas superficiales del SnO<sub>2</sub>. Se ha prestado una especial atención en la participación de los grupos hidroxilo superficiales en el mecanismo de cambio de conductividad del adsorbente semiconductor durante la quimisorción u oxidación del hidrógeno en el aire seco o húmedo.

# Acknowledgments

This thesis would not have been possible without the scholarship from the University Rovira i Virgili as well as collaboration and help of a number of people. Here, I would like to express my gratitude to all of them.

My sincere gratitude goes to my scientific advisor Dr. A. A. Vasiliev, for offering me the opportunity to carry out this work, for his guidance, suggestions and support either with research or everyday life. The group leaders – Prof. X. Correig, Prof. E. Llobet and As. Prof. X. Vilanova – were extremely benevolent helping in the every question related with my first and followed research steps abroad, I am deeply grateful to them. I am sincerely acknowledged to Prof. V. G. Sevastyanov, Ac., Prof. N. Kuzetsov and Dr. E. P. Simonenko for their invaluable help and endless backing from Russia during my implementation of the thesis. I thank the members of Minos and Nephos groups for their personal, scientific or technical assistance during our work together: R. Calavia, Dr. S. Vallejos, Dr. L. Vojkúvka, D. Shaposhnik, T. Stoycheva, R. Leghrib, C. Burian, R. Ingles and A. Santos.

I am much obliged to Prof. N. Barsan whose thoughtful suggestions to a large extent influenced both my personality and the ideas presented here. His readiness to help and advise won't be forgotten as well. I would like to express my gratitude to Dr. A. Oprea for sharing with me his valuable knowledge and helping me better understand physics of gas sensors. In the course of my 3-month research stage in Tuebingen we became friends with a number of people who helped me a lot and created friendly working and social atmosphere: M. Hübner, A. Haensch, Dr. M. Kwoka and T. Heine. I thank them all and hope to continue our collaboration.

One of the most important parts of the results was possible to gain through very fruitful collaboration with the group of Prof. C. Hardacre in the frameworks of EU Transnational Access Program. His brilliant suggestions and ideas helped me a lot in the planning and understanding of the experiment. I am thankful to H. Daly whose energy and skills were probably the most effective “catalysts” to realize the planned experiment. The experience that I have gained during my 2-month stage in Belfast will be of invaluable importance.

It's difficult to overestimate the help of Dr. N. Barrabés and her supervisor Prof. F. Medina from the group of heterogeneous catalysis (URV) as well as Dr. C. Álvarez and Dr. J. L. Garcia Fierro from Consejo Superior de Investigaciones Científicas (Madrid). Without their assistance and support some important experiments would not be possible at all.

Finally, I am deeply grateful to my parents, sister and of course my wife Anya for their love, faith and endless patience...

# Index

<b>Index .....</b>	<b>9</b>
<b>1. Introduction .....</b>	<b>12</b>
<i>1.1. Motivation.....</i>	<i>12</i>
<i>1.2. Scope of the work.....</i>	<i>15</i>
<b>2. Basics and survey.....</b>	<b>17</b>
<i>2.1. Colloid chemical methods for SnO<sub>2</sub> synthesis .....</i>	<i>18</i>
2.1.1. Precursors .....	20
2.1.1.1. Metalorganic precursors.....	21
2.1.1.2. Inorganic precursors.....	23
2.1.2. Sol formation and precipitation.....	24
2.1.3. Gelation .....	27
2.1.4. Properties comparison of synthesized SnO <sub>2</sub> .....	29
<i>2.2. Bulk properties of tin dioxide .....</i>	<i>32</i>
2.2.1. Physical properties .....	33
2.2.2. Chemical properties.....	36
<i>2.3. Surface Properties of tin dioxide .....</i>	<i>37</i>
2.3.1. Electronic structure .....	38
2.3.2. Surface chemistry .....	41
2.3.2.1. Interaction with oxygen and water .....	41
2.3.2.2. Hydroxylated SnO <sub>2</sub> surface.....	43
<i>2.4. Some properties of SnO<sub>2</sub>-MetO<sub>x</sub> systems .....</i>	<i>45</i>
2.4.1. SnO <sub>2</sub> -MetO <sub>2</sub> , where Met = Ti, Zr, Hf (IVB group).....	46
2.4.2. SnO <sub>2</sub> -Met <sub>2</sub> O <sub>3</sub> , where Met = Sc, Y, La (IIIB group).....	47
<i>2.5. Physical models of gas sensing.....</i>	<i>49</i>
2.5.1. Interaction with acceptor molecules and some general remarks.....	51
2.5.2. Interaction with donor molecules.....	55
2.5.3. Interaction with water.....	57

<b>3. Experimental</b> .....	<b>59</b>
3.1. <i>Synthesis</i> .....	60
3.1.1. Blank SnO <sub>2</sub> .....	61
3.1.1.1. Precursor synthesis.....	61
3.1.1.2. Colloid systems SnO <sub>x</sub> H <sub>y</sub> .....	62
3.1.2. SnO <sub>2</sub> -MetO <sub>x</sub> and SnO <sub>2</sub> bulk doped with impurities.....	64
3.1.3. Post-synthesis procedures.....	65
3.1.4. Deposition of noble metals.....	66
3.1.5. List of the synthesized materials.....	67
3.2. <i>Material characterization</i> .....	68
3.2.1. <i>Ex-situ</i> techniques.....	69
3.2.1.1. Transmission electron microscopy.....	69
3.2.1.2. XRD and crystallite size calculations.....	69
3.2.1.3. FTIR spectroscopy.....	70
3.2.1.4. UV-VIS spectroscopy.....	70
3.2.1.5. Other methods.....	71
3.2.2. <i>In-situ</i> techniques.....	72
3.2.2.1. TGA/DSC analysis.....	73
3.2.2.2. MS-study of the catalytic activity: H <sub>2</sub> oxidation in air.....	73
3.2.2.3. TPR.....	74
3.2.2.4. DRIFT spectroscopy.....	74
3.2.2.5. TXRD.....	75
3.3. <i>Characterization of sensing properties</i> .....	77
3.3.1. Deposition of the sensing material.....	78
3.3.2. Heater calibration.....	79
3.3.3. Experimental set-up.....	80
3.3.4. Methodology of the experiment.....	81
<b>4. Results and discussion</b> .....	<b>85</b>
4.1. <i>Tin dioxide synthesis</i> .....	86
4.1.1. Tin (II) or tin (IV) acetate complexes?.....	87
4.1.1.1. Physical properties.....	87
4.1.1.2. FTIR and XRD study.....	87
4.1.2. Comparison of synthesized materials.....	92
4.1.3. Summary.....	97
4.2. <i>Material science: ex situ characterization</i> .....	98
4.2.1. Oxide system SnO <sub>2</sub> -MetO <sub>x</sub> .....	100
4.2.1.1. SnO <sub>2</sub> -MetO <sub>2</sub> , Met=Ti, Zr, Hf.....	100
4.2.1.2. SnO <sub>2</sub> -Met <sub>2</sub> O <sub>3</sub> , Met=Sc, Y, La.....	106
4.2.2. SnO <sub>2</sub> with deposited noble metals: Pd, Pt, Rh.....	112
4.2.3. Summary.....	119
4.3. <i>Material science: in situ characterization</i> .....	121
4.3.1. TGA analysis.....	122



4.3.1.1.	Blank materials.....	122
4.3.1.2.	SnO <sub>2</sub> -MetO <sub>2</sub> , Met=Ti, Zr, Hf .....	123
4.3.1.3.	SnO <sub>2</sub> -Met <sub>2</sub> O <sub>3</sub> , Met=Sc, Y, La .....	124
4.3.1.4.	SnO <sub>2</sub> with deposited catalysts: Pd, Pt, Rh.....	125
4.3.1.5.	Summary .....	126
4.3.2.	MS-study of the catalytic activity: H <sub>2</sub> oxidation in air.....	127
4.3.3.	TPR.....	131
4.3.3.1.	5% H <sub>2</sub> in argon .....	131
4.3.3.2.	0.1% H <sub>2</sub> in air .....	132
4.3.3.3.	Summary .....	133
4.3.4.	DRIFT spectroscopy .....	134
4.3.4.1.	Dry air .....	134
4.3.4.2.	0.01% H <sub>2</sub> in dry air.....	135
4.3.4.3.	2.1% H <sub>2</sub> O in air .....	136
4.3.4.4.	Summary .....	137
4.3.5.	TXRD study of crystallite growth kinetics .....	139
4.3.5.1.	Comparison of kinetics models by example of SnO <sub>2</sub> Ac .....	139
4.3.5.2.	Impurity effect.....	142
4.3.5.3.	Comparison of synthesized compounds SnO <sub>2</sub> -MetO <sub>x</sub> .....	144
4.3.5.4.	Effect of noble metal .....	145
4.3.5.5.	Summary .....	148
<b>4.4.</b>	<b>Sensing properties.....</b>	<b>149</b>
4.4.1.	Blank materials.....	150
4.4.2.	SnO <sub>2</sub> -MetO <sub>2</sub> , Met=Ti, Zr, Hf .....	156
4.4.3.	SnO <sub>2</sub> -Met <sub>2</sub> O <sub>3</sub> , Met=Y, La .....	159
4.4.4.	SnO <sub>2</sub> with deposited noble metals: Pd, Pt, Rh .....	161
4.4.5.	Summary .....	167
<b>4.5.</b>	<b>Conclusion .....</b>	<b>168</b>
4.5.1.	Synthesis.....	168
4.5.2.	Material science.....	169
4.5.2.1.	<i>Ex-situ</i> methods .....	169
4.5.2.2.	<i>In-situ</i> methods.....	169
4.5.3.	Sensing properties .....	170
<b>5.</b>	<b>Bibliography.....</b>	<b>172</b>
<b>6.</b>	<b>List of Tables.....</b>	<b>183</b>
<b>7.</b>	<b>List of Figures .....</b>	<b>185</b>
<b>8.</b>	<b>List of Publications.....</b>	<b>189</b>
8.1.	<i>Chapters in books</i> .....	189
8.2.	<i>Full papers</i> .....	189
8.3.	<i>Conference proceedings</i> .....	190
<b>9.</b>	<b>Curriculum vitae .....</b>	<b>193</b>

# 1. Introduction

## 1.1. Motivation

Absolute necessity to create sensors in general and chemoresistive gas sensors in particular is determined by rapid technological growth in gaining, processing and analysis of information about our environment. Fast and unambiguous analysis of human surroundings will be in the near future inseparable part of public health, security and life quality control.

Up to now there have been developed a number of techniques to measure gas concentrations in surrounding atmosphere, *e.g.* optical, electrochemical, calorimetric, capacitive, chemoresistive, mass-sensitive technique *etc.* In the field of combustible gas monitoring, CO and NO<sub>x</sub> sensing, chemoresistive gas sensors are the most popular according to the market analysis in Japan [1]. However, the most crucial disadvantages of this type of sensors are still actual nowadays: poor selectivity and insufficient long-term stability (for nanomaterials-based technologies), which limits widespread sensor employment in cars, indoor and outdoor detection system.

Selectivity problem rose almost simultaneously with discovery of sensor effect on metal oxide semiconductors. F. F. Volkenshtein, I. A. Myasnikov, T. Seiyama and many others after them found that change in electrophysical parameters of sensing materials occurs in the presence of large number of gases [2-10]. Poor selectivity is a result of similar effects on electronic structure of a semiconductor caused either by donor/acceptor chemisorption or by surface oxidation of various reducing gases.

To some extent this problem could be resolved by technical methods (variation or modulation of detection temperature [11-13], using different filters to separate the target gas from the interfering ones [14, 15] *etc.*). However, the common trend to improve selectivity and in the same time decrease working temperature of chemoresistive sensors is related with semiconductor oxide modification through surface doping with noble metals [16-18]. However, most of the metals, deposited for example on dispersed SnO<sub>2</sub>, during long-term heating form

ternary compounds diffusing into the bulk. This causes recrystallization processes, change in the background conductivity, and finally drift of the sensor electric parameters [19, 20]. Moreover, noble metals, suffer from poisoning by halogens, sulfur and volatile silicone compounds, which also makes them very vulnerable from chemical point of view [21].

In addition, one should not discard poor thermal stability of the highly dispersed oxides themselves even without deposited second phase. Especially this should be taken into account in the case of nanoparticles with diameter of less than 10 nm. Indeed, particles with the size of several nanometers consist of 30-75% coordinatively unsaturated atoms (*e.g.*  $Sn_{4c}^{4+}$ ,  $Sn_{5c}^{4+}$ ,  $O_{2c}^{2-}$  *etc.*), which make them non-equilibrium structures with high crystallite boundary energy [22], depressed surface stress [23] and finally – low melting point [24].

The problem of recrystallization and thermal stability of sensing materials has been partially resolved in commercial sensors by using materials sintered at high temperatures (*ca.* 1000 °C). However, this approach eliminates all the advantageous properties of highly dispersed oxides, so intensively reported during past decade [25]. Thus, selectivity enhancement, comprising employment of highly dispersed solids with deposited catalysts, seems to be always accompanied by the problem of material thermal stability.

From this standpoint doping with oxides to modify catalytic/sensing properties of semiconductor materials is much more attractive than that with noble metal clusters, since oxide thermal stability in general is higher in respect with metal clusters. In addition, oxide systems without noble metals are known to catalyze a wide spectrum of chemical reactions, which can be effectively used in the field of gas sensors [26-28].

Accordingly this work aims to synthesize and to comprehensively study physicochemical and sensing properties of two-component oxide systems on the basis of tin dioxide and IVB and IIIB elements introduced into the bulk by co-precipitation procedure. The IVB and IIIB oxides were chosen as a second components for SnO<sub>2</sub> based oxide system for a number of reasons, among them one can mark out several the most important ones:

- IVB and IIIB groups were chosen due to the fact that some oxides from these groups are known as very active catalysts in heterogeneous catalysis, *e.g.* TiO<sub>2</sub>, ZrO<sub>2</sub>, Y<sub>2</sub>O<sub>3</sub> and La<sub>2</sub>O<sub>3</sub> [26-28];
- the rest of the elements in the group were chosen to trace systematically the differences in the physicochemical properties within the one group of the dopants;
- IVB and IIIB oxides represent the opposite cases of solubility in SnO<sub>2</sub> phase, which can play a crucial role in the properties of the two-component materials.

In addition to the mentioned oxide systems, herein we synthesize and study physicochemical and sensing properties of tin dioxide doped with noble metals (Pd, Pt, Rh), since the majority of the R&D activity in the field of chemoresistive gas sensors, as well as the lion share of commercial sensors themselves are focused and based on materials doped with precious metals. This approach allows us to study the surface chemistry of tin dioxide sensing phenomenon in a comparative way, which is known to be one of the most efficient trick to gain the information in the most complex system ever known – Nature.

## 1.2. **Scope of the work**

This thesis represents a part of the author's work in the last three years regarding synthesis, material science and characterization of sensing properties of tin dioxide based oxide systems. In the each specified field (*i.e.* synthesis, material science *etc.*) a set of fundamental problems arose along the experimental study. Later on, the problems in the field of synthesis, related for example with different isoelectric point of SnO<sub>2</sub> colloids synthesized from different metalorganic precursors, seemed to be partially resolved through determination of the complex structure and tailoring the solvent, but in the same time transformed into another bigger problem related with crystallite size and hydroxylation degree of the synthesized materials. Finally it was found that surface hydroxyls play a crucial role in the sensing mechanism and their properties and quantity can be modified by precursor. The circle closed up, exhibiting a brilliant example of closely interconnected questions from one area of research and answers from another... Many other similar examples suggested that sensing properties of the materials should be investigated in the closest relation with their precursor nature, synthesis conditions and material science of the resulting compounds. To realize such a complex approach the aim of the study was divided on several categories:

- Elaboration of technologically flexible method, starting from cheap and available precursors, which leads to the synthesis of pure and highly dispersed SnO<sub>2</sub>; method development for synthesis of various oxide systems on the basis of SnO<sub>2</sub>; study of the precursor nature and its influence on oxide properties.
- Comprehensive characterization of the synthesized materials by means of *ex-situ* and *in-situ* techniques to investigate the effect of surface and bulk doping on physicochemical properties of SnO<sub>2</sub> based systems.
- Study of electrophysical properties of the synthesized materials as a function of temperature and gas composition; analysis of the gas sensing selectivity of the synthesized compounds by example of hydrogen detection in the presence of water.
- Ascertainment of the interconnection between the material synthesis, material physicochemical properties and its sensing performance; understanding the surface chemistry of the sensing phenomenon.

To put it more easily, the research strategy can be formulated as a sequence of Synthesis, Material science, Sensing phenomenon and finally Interconnection between each field of research. Accordingly, the thesis is built up with the same idea in mind. Each part – Basics and survey, Experimental, and Results and Discussion – is organized closely adhering the same

sequence: we start with synthesis and precursors, go through material science, afterwards we pass to the sensing properties, finishing with analysis of the main results and summaries. This way of acquiring of information seems to be the most natural and efficient since allows one to decrease “alienation” of the researcher in the field of gas sensors, which is usually abstracted from the origin of the matter under investigation. The idea of “alienation” was developed by German psychoanalyst E. Fromm, which quotation begins the thesis.

The thesis contains 154 pictures, schemes, graphs and diagrams, 26 tables and *ca.* 48 000 words, written on 155 pages. The material presented here is partially published in 5 journal articles and 4 proceedings of international conferences.

## 2. Basics and survey

According with the strategy specified in the previous chapter, this part starts with an overview of colloid chemical methods used to synthesize dispersed oxide systems on the basis of SnO<sub>2</sub> (mainly starting from metalorganic precursors). SnO<sub>2</sub> main physical and chemical properties (bulk and surface ones) follow the synthetic part. Then a short overview on SnO<sub>2</sub>-MetO<sub>x</sub> systems (their physical, chemical and sensing properties) is given in the next chapters. The final part is dedicated to the physical models of gas sensing.

## 2.1. Colloid chemical methods for SnO<sub>2</sub> synthesis

Before considering SnO<sub>2</sub> synthesis methods one should establish the most crucial requirements for the synthesized material in respect with the useful properties for gas sensor applications.

It is well known that physical and chemical properties of dispersed materials strongly depend on size and morphology of constituent particles. The most crucial change in material properties is observed for nanoclusters of 1-4 nm, where percentage of surface atoms as it was already mentioned, varies from 30 up to 75 % of total atom number in cluster [29]. High catalytic activity and enhanced selectivity [29], high sensitivity to gas ambient [30], tunable electrooptical properties [31, 32] and many others promising features of highly dispersed semiconductor solids have been reported. Thus, the most desirable and crucial requirement for the synthesized material is high surface area. In addition, we should meet the following conditions for a “good” sensor material: purity, phase homogeneity of the synthesized compound, fairly narrow particle size distribution, and stability of all these features during sensor operation at 200-450 °C [33].

Different wet and dry methods are used to achieve one or several advanced properties of the final product. Dry methods, being employed basically for coating deposition, have good control of compound stoichiometry and morphology. Together with high purity and reproducibility they are, may be the best candidates for large-scale production. However, there is a lack of technical flexibility, in terms of composition or morphology modification, due to very sophisticated and expensive experimental set up [34].

From the other hand, wet colloid chemical methods, suffering from poorer morphology control, undesirable impurities and sometimes unsatisfactory reproducibility, provide us with low-cost unlimited ways to modify composition (and to some extent morphology) of the final product. It is colloid chemistry, that is still used extensively in R&D activity to find out a cherished bunch of unique properties of new synthesized materials for various advanced applications, including chemical gas sensors [35].

The overview presented here is dedicated to the colloid chemical methods for the synthesis of dispersed tin dioxide materials at low temperatures.

Let us start with a definition. *Colloid* is a system of uniform in size and shape particles in the dispersing medium, stable to the sedimentation, and having at least one dimension in the size between 1 and 1000 nm [36, 37]. Since the suspended particles are uniform, highly dispersed and their chemical composition can be limited only by difficulties to prepare molecular solution, the



colloidal route is the most convenient way to synthesize metal oxide systems for R&D in the field of gas sensors.

However, it is not so easy to transfer all these remarkable properties of the suspended material to a final solid system: the dispersed charged particles, stabilized in the liquid medium, tend to readily agglomerate during separation procedure. There are number of methods dedicated to overcome this problem the most effective ones are separation of colloidal suspension *via* particle sedimentation and *via* gelation [37]. The basic steps of wet chemistry processing used to synthesize dispersed metal oxide systems schematically are shown in **Figure 1**.

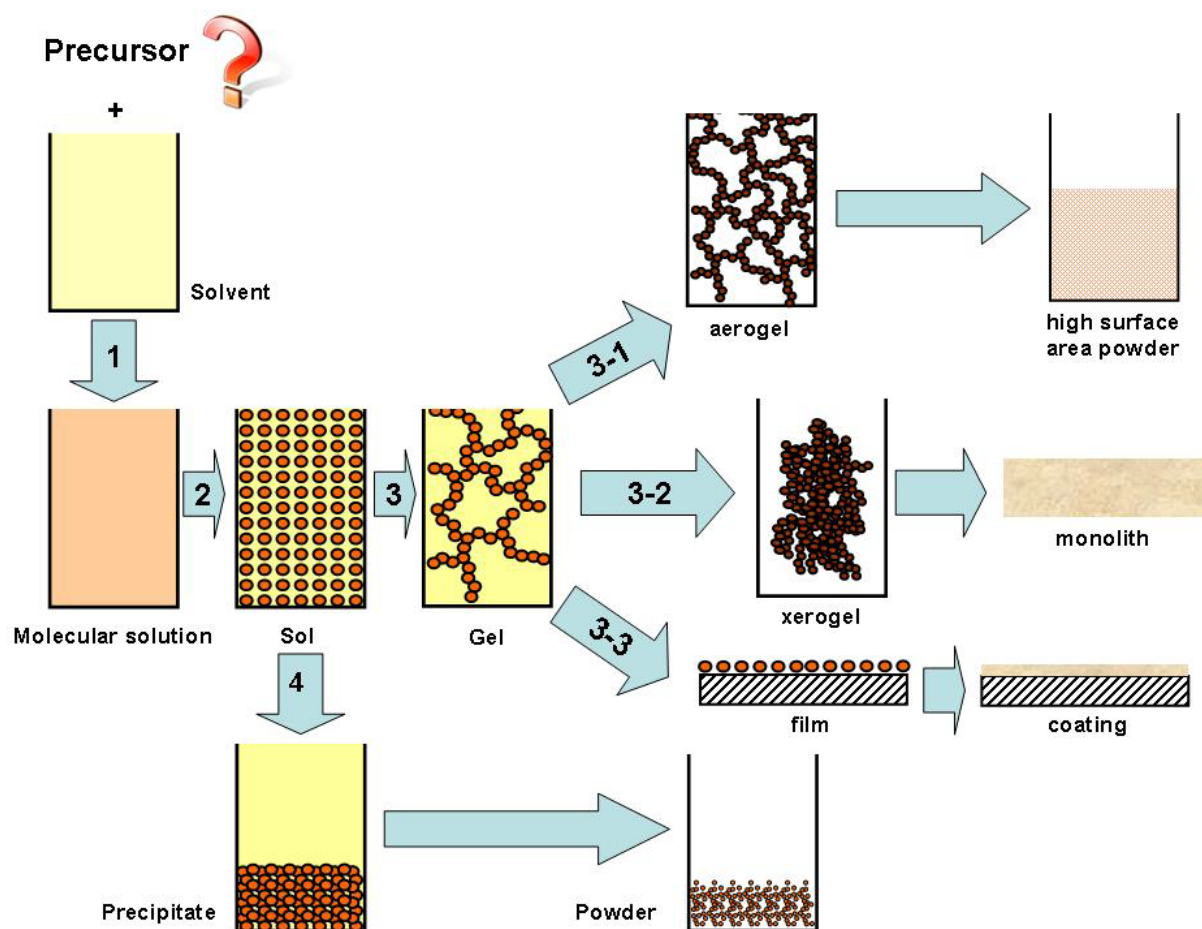


**Figure 1.** The evolution of wet chemical process: 1 – precursor dissolution, 2 – precursor hydrolysis and condensation, 3 – gelation as a result of colloid condensation and polymerization, 3-1 – solvent extraction under supercritical drying, 3-2 – conventional solvent evaporation, 3-3 – solvent evaporation from the thin layer, 4 – sedimentation.

This overview is built up using the same structure as shown in the **Figure 1**. The following sections are dedicated to one or several process steps. First section is dedicated to precursors: the selection strategy and short overview of their physical and chemical properties. Sections 2.1.2

and 2.1.3 consider theoretical and practical aspects of sol and gel formation. In the final part properties of SnO<sub>2</sub> synthesized using different wet chemical techniques are compared.

### 2.1.1. Precursors

The first step in the wet chemistry processing is to choose the starting compound – the precursor. The precursor selection is very important since it plays a key role in each stage of the synthesis: hydrolysis, condensation, polymerization, coagulation, sedimentation and solvent extraction. Thus, the precursor nature determines to a great extent the structure, surface composition and surface area of the future dispersed oxide. Let us consider first the case of the most popular inorganic precursor – SnCl<sub>4</sub>, intensively used in SnO<sub>2</sub> synthesis.

In general, hydrolysis of all inorganic salts (including tin sulfate) requires many weeks of oxide washing in deionized water to remove the remaining impurities [38]. In addition to the laborious chemical routes it is possible to scavenge the impurities by means of physical methods, like long-term aging at *ca.* 600 °C, which brings about formation of volatile chlorine or sulfur products [39]. But in this case quite intensive particle agglomeration at high temperature leads to a drop of surface area of the oxide [40]. But why we should remove the impurities at all?

Impurities form a multi-component system with unpredictable physical and chemical properties. For example, the halogen impurities act as electron acceptors and alter conductivity even of metallic tin [41]. So, what can expect one from the semiconductor oxide “doped” with 0.5 w.% of Cl!? In addition, chlorine and sulfur are very well known as catalyst poisons [21]. The latter together with high diffusion coefficients of the halogen ions [42, 43], which contributes to the recrystallization process in the dispersed solids, makes one seriously think before using inorganic precursors. However, for all that, the lion share of the SnO<sub>2</sub> synthesis for different applications (including gas sensors) is still based on the halogen contained precursors [16, 44-46].

The oxide affinity to bond with halogens can be demonstrated by the examples of synthesis of metalorganic complexes starting from SnCl<sub>4</sub>. Interaction of the salt with a polar organic compound, such as ethanol, propanol *etc.*, leads to formation of partially substituted compositions schematically represented with the formula SnCl<sub>x</sub>(OR)<sub>4-x</sub>·ROH [47, 48]. Complete chlorine substitution does not occur and that is why its chemical removal from the final product is extremely difficult procedure [38, 40, 48]. The same situation is for fluorinated stannic compounds, which are used intentionally to synthesize fluorine-doped tin dioxide by conventional sol-gel processing [41]. It seems that halogens tend to form strong bond with the tin

atom, and that is why tin dioxide synthesis, starting from metalorganic precursors contained halogens, results in high Cl<sup>-</sup> or F<sup>-</sup> contamination.

Taking into account the above stated facts, it becomes evident that only halogen (and sulfur) free metalorganic compounds are the most suitable for the synthesis of pure tin dioxide based oxide systems. The following sections give a short overview on metalorganic and inorganic precursors used to synthesize tin dioxide.

### 2.1.1.1. Metalorganic precursors

The distinctive feature of metalorganic compounds (or metal alkoxides) is that they have an organic ligand attached through oxygen to the metal atom. There are a number of metalorganic compounds with tin in both oxidation states (*i.e.* II and IV). However, after literature analysis (using database of ISI Web of Knowledge [49]) it was found, that all sol-gel derived SnO<sub>2</sub> materials were synthesized from tin(IV) alkoxides. The most often used alkoxides for tin dioxide synthesis are tin(IV) *iso*-propoxide and tin(IV) *tert*-butoxide [50-56]. No article was found reporting sol-gel synthesis from tin(II) alkoxides. And this is quite understandable – the colorless or yellowish tin(II) complexes can be easily oxidized and decomposed by traces of water vapors to form oxide hydrates. This makes difficult to handle with tin(II) complexes in ambient air and, what is more important, it is much more difficult to control the hydrolysis and condensation processes during sol or gel formation [57]. **Table 1** gives physical properties of some tin(II) and (IV) homoleptic (with all ligands identical) alkoxides.

The common feature of tin alkoxides is that they are quite susceptible towards humidity, especially tin(II) complexes. The general rule for all metalorganic complexes could be applicable also in this case: the more central atom (either tin(II) or tin(IV)) is screened with the surrounding ligands the higher chemical stability of the complex is observed. In general, the screening degree of the central atom determines a major part of physical and chemical properties of the alkoxide, and therefore could be used to predict its stability both in air and in solution. For example, strong polydentate ligands like  $\beta$ -diketones, crown ethers, formate, acetate or oxalate form complexes which are quite stable to oxidation even in water solutions. While, monodentate ligands (*e.g.* ethoxy group) are easy hydrolysable and tend to decompose in air or in light [58].

The complex stability determines the degree of hydrolysis, rates of condensation and polymerization during formation of sol. In other words ligand strength and screening degree of the central atom determine particle size and shape of the future oxide material [59]. That is why the selection of the precursor is very important and is considered as an effective tool to design the whole bunch of material properties.

**Table 1.** Physical properties of homoleptic tin (IV) complexes.

Sn(II)/ Sn(IV)	Compound <sup>1</sup>	Physical & Chemical Properties <sup>2</sup>	Solubility	Ref.
Sn(II)	Sn(CO <sub>2</sub> ) <sub>2</sub>	White powder, polymer, Z=4, decomp. ca 242° C,	Dilute HCl and presumably in polar solvents	[60-63]
	Sn(OMe) <sub>2</sub>	White, amorphous solid, polymeric, highly reactive towards O <sub>2</sub> and H <sub>2</sub> O, decomposes at above 100 °C w/melting (with SnO form.)	Methanol, diethyl ether, THF, hydrocarbons, Cl-hydrocarbons	[57]
	Sn(HCO <sub>2</sub> ) <sub>2</sub>	White lamina-shaped crystals, decomp. w/melting ~ 200° C, slow oxidizes by air (around month)	H <sub>2</sub> O (slow hydrolysis at RT), H <sub>3</sub> CO <sub>2</sub> , ethanol, acetone	[60]
	Sn(Ac) <sub>2</sub>	Colorless, needle-shaped crystals, polymer, chain structure, Z=8, mp 180-182° C, decomp. ca > 240° C (with SnO form.), slow oxidizes by air (several months)	Acetic acid, ethanol, acetone, low soluble in non-polar solvents	[60, 64]
	Sn(acac) <sub>2</sub>	Pale yellow liquid, monomer, highly reactive towards H <sub>2</sub> O, Z=4, bp. ca. 101 °C (0.15 mm)	Formic acid, benzene, Ethanol, n-Hexane, THF	[65]
Sn(IV)	Sn (HCO <sub>2</sub> ) <sub>4</sub>	White crystals, polymer, planar structure, Z=4, started to darken (decomp.) at 156° C, black at 200° C	Presumably in polar solvents	[66]
	Sn(OMe) <sub>4</sub>	“Highly associated” solid with tetrameric structure, bp. 230 °C (5mm).	Benzene, methanol and ethanol (under heat.)	[57, 67]
	Sn(OEt) <sub>4</sub>	Solid with tetrameric structure, decomposes ca. < 100° C	Benzene, ethanol, hydrocarbons, xylol	[57, 67]
	Sn(O- <i>i</i> -Pr) <sub>4</sub> · <i>i</i> -PrOH	Waxy solid, dimeric in <i>i</i> -propanol sol., decomp. 125° C	Benzene, <i>i</i> -propanol	[51, 68]
	Sn(O- <i>t</i> -Bu) <sub>4</sub>	White crystals, monomeric, Z=4, mp. 40-42 °C	benzene, highly soluble in hydrocarbons	[67, 69]
	Sn(OPh) <sub>4</sub>	Solid, Z=6, mp. ~ 50 °C	Presumably in benzene	[67]
	Sn(acac) <sub>4</sub>	Was never observed because of steric hindrance	-	[55]
	Sn(Ac) <sub>4</sub>	White, lath-shaped crystals, Z=8, mp 253° C	Acetic acid, benzene, ethanol, acetone, carbon tetrachloride	[38, 70, 71]

<sup>1</sup> Me – CH<sub>3</sub>, Et – C<sub>2</sub>H<sub>5</sub>, Ac – C<sub>2</sub>H<sub>3</sub>O<sub>2</sub><sup>-</sup>, Pr – C<sub>3</sub>H<sub>7</sub>, Bu – C<sub>4</sub>H<sub>9</sub>, Ph – C<sub>6</sub>H<sub>5</sub>, acac – C<sub>5</sub>H<sub>7</sub>O<sub>2</sub><sup>-</sup> (2, 4 pentandion)

<sup>2</sup> mp. – melting point, bp. – boiling point, Z – coordination number

### 2.1.1.2. Inorganic precursors

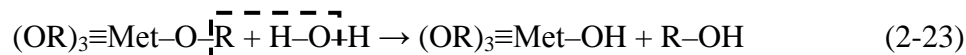
The most popular inorganic precursors are hydrated tin (II) and (IV) chlorides, which are cheap, easy to handle compounds with well known properties. However, as it was already mentioned, a number of disadvantages arise with residual impurities in the final product. The same problem is observed for other inorganic precursors, like  $K/Na_2SnO_3 \cdot 3H_2O$ , which are used in spontaneous gelation of stannic acid by ion exchange mechanism [72].

The only possible candidates for inorganic precursors, which lead to formation volatile byproducts at relatively low temperatures – are tin nitrates. However,  $Sn(NO_3)_2 \cdot 20H_2O$  and  $Sn(NO_3)_4$  are very unstable and decomposes at temperatures:  $< 100$  °C and  $50$  °C resp. Nevertheless, there is a well known “classic” technique to synthesize dispersed tin dioxide by oxidation of metallic tin with hot concentrated nitric acid [38]. Without any doubts the oxidation occurs *via* tin nitrates formation, which decompose on tin dioxide and nitrogen dioxide at relatively low temperatures.

## 2.1.2. Sol formation and precipitation

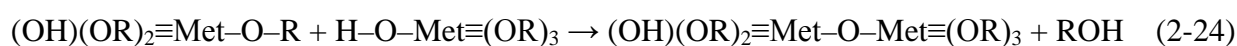
Once the precursor is chosen it is dissolved in an organic polar solvent usually absolute ethanol, *iso*-propanol, acetonitrile or toluene. Several studies have revealed that polar coordinating solvents favor formation of high specific surface area materials [73]. Also sometimes a modifier is added to stabilize the dissolved complex and to prevent the premature hydrolysis. The most frequently used ones are  $\beta$ -diketons, especially acetylacetone. However, one should take into account that the stabilization occurs due to partial ligand substitution and mixture of several new complexes is formed [55, 56, 74].

The dissolved metalorganic precursor is hydrolyzed through water addition (usually water-alcohol solution) while carefully controlling the pH and reaction temperature. There are two different mechanisms of condensation/hydrolysis reactions which depend on the coordination of central metal atom. When the preferred coordination is satisfied, hydrolysis occurs by nucleophilic substitution ( $S_n$ ) with hydronium ion as a catalyst. When the preferred coordination cannot be satisfied, hydrolysis occurs by nucleophilic addition ( $A_n$ ) with OH ion as a catalyst [75]. In general, the reaction can be represented as follow:



Briefly, the hydrolysis reaction under acidic conditions involves protonation of the alkoxide group followed by nucleophilic attack of water to form penta-coordinated intermediate. Under basic conditions, the mechanism involves nucleophilic attack on the metal atom by the hydroxide anion to form negatively charged penta-coordinated intermediate. It was observed that basic conditions favor hydrolysis of  $Si(OR)_4$ . In contrary, in the case of  $Ti(OBu)_4$  the hydrolysis rate was higher under acidic or neutral conditions. For transition metals acid-catalyzed condensation favors formation of extended less branched polymers [76]. For  $SnO_2$  the information has not been found.

Two partially hydrolyzed molecules can link together in different types of condensation such as *alkoxolation*:



*oxolation*:



*olation*:



Condensation, starting with nucleophyl attack and followed by either nucleophilic substitution ( $S_N$ ) or by nucleophilic addition ( $A_N$ ), liberates a small molecule like water or

alcohol depending of the type of leaving group. This reaction continues to build metal contained clusters by the process of polymerization. Note, that only olation leads to formation of bridging hydroxyls. The rate of this process is known to be higher when the central atom has low charge and large radius [76].

When the clusters are big enough (within 1-5 nm) and their position is stabilized in solution by various short-range forces such as van der Waals attraction and surface charges, the colloidal suspension – *sol*, is formed (**Figure 1**, stage 2).

A *sol* –is a dispersion of colloidal particles (separate or agglomerated clusters of 1-100 nm) or micelles (charged aggregates of ~10 nm) in a liquid, which are stable to the sedimentation [76]. The degree of condensation/polymerization determines the size and the shape of suspended metal oxide cluster. As it was said above, one of the factor which strongly affects the polycondensation and hydrolysis kinetics is the ligand nature [59]. Among the others factors one should consider: water-to-precursor ratio, pH, catalyst amount (often coincide with pH) and temperature. The mentioned conditions should be carefully chosen to ensure formation of monodisperse colloid.

At the early stages of sol formation it is possible to increase either polycondensation or hydrolysis rate adjusting the specified conditions. The former results in formation of an interconnected network of the polymer on the basis of partially hydrolyzed metal alkoxides. The transformation of this type is called *sol-gel* and will be considered in more detail in the next section. When hydrolysis rate is higher than that of polymerization, formation of the colloid oxide particles occurs in the liquid medium.

It is generally accepted that colloid system consists of agglomerated primary particles, usually uniform in shape and size. Depending on the interparticle forces, the suspension can be prepared in the dispersed, weakly flocculated and strongly flocculated states. Long-range forces resulting from van der Waals interactions are always attractive between like particles and must be mitigated during colloidal processing to achieve the desired degree of suspension stability. To overcome the van der Waals attraction one should rely on some type of interparticle repulsion, such as *electrostatic*, *steric* or other stabilizing forces [37].

*Electrostatic forces*, which are generated by like-charges on the surface of suspended particles in the form of double-charged layer, have a repulsive nature and therefore determine the aggregation kinetics. The electrostatic forces can be tuned either by adjusting ionic strength or pH. A certain pH value, at which charged particles suspended in solution have no electrical charge, is *isoelectric point* (IEP). Increasing ionic strength or changing pH towards the isoelectric point one reduces the surface charge of the particles and render precipitation [37].

Many factors affect the IEP value, among them: hydration state of the suspended particle, purity and ionic strength of the solutions. The IEP values for SnO<sub>2</sub> vary from 3.9 to 8.5, more detailed information on the matter can be found elsewhere [77, 78].

*Steric* stabilization also provides an effective route to overcome particle attraction. In this case adsorbed organic molecules (usually polymeric) strongly anchored to the particle surface. Adjusting the polymer molecular structure, polymer surface concentration and the thickness of the adsorbed layers one can achieve precise control of pore and particle size [37].

Using one or several approaches to stabilize suspended particles there have been developed various colloidal methods to accurately control size and/or polydispersity of the particles which have been used for SnO<sub>2</sub> synthesis: water-in-oil microemulsion [79-81], reverse and normal micelles [82, 83], two-phase liquid-liquid systems [82] *etc.*

The stabilized colloids undergo either slow drying procedure at relatively mild temperatures or centrifugation to remove the solvent.



### 2.1.3. Gelation

Sol-gel method has been recognized by numerous scientists in the 1950s and 1960s as a best technique to achieve very high levels of chemical homogeneity in ceramic oxide compositions and was used to synthesize a large number of novel multicomponent compounds [84]. The potential advantages of sol-gel processing include also following features: purity and large surface area of synthesized oxides at low temperature, control over surface hydroxylation, ease of dopation with the most elements of periodic table that are capable of solid oxide formation and finally ability to make monoliths, films, fibers and monodispersed powders (see **Figure 1**) [75]. All the bunch of the attractive factors from the scientific points of view together with low cost procedure has led to the fast progress in the development of sol-gel technique during the past two decades.

A *gel* – is a two-component system of a semisolid nature, which consists of continuous interconnected, rigid network of solid in fluid phase. This continuous net of hydrated metal oxide polymer forms as a result of further growing and condensation processes between suspended oxide clusters. Two types of kinetics growth are generally recognized: monomer-cluster growth and cluster-cluster growth. Both of them realize under reaction-limited or diffusion limited conditions. Monomer-cluster growth occurs only by the addition of monomers to a growing polymer or cluster, whereas cluster-cluster growth occurs by the addition of monomers or clusters to other monomers or clusters [67]. Finally, randomly branched polymers in the form of fractals bound together to form a rigid network in a liquid phase.

pH of condensation plays crucial role in particle size and morphology. It was found that at pH 8-11 silica particles, which are initially formed with diameter of approximately 1 nm, increase in size up 100 nm during the synthesis. When the reaction is performed under neutral conditions, the particles in sol vary between 2.5-20 nm. Under acid conditions the particles are very uniform with narrow size distribution: 0.5-3.0 nm. Thus, it is generally accepted that for silica the surface area decreases with pH increase. However, for alumina or magnesia, the pH effect is not so pronounced [75]. For tin dioxide the information has not been found.

Another crucial parameter, which reflects chemistry of precursor-water interaction, is the degree of hydrolysis – *h*. This value defines a ratio of water (or other hydrolyzing compound, *e.g.* ethanol, which sometimes used without water addition) added per tin atom. It is obvious that *h* depends on many factors like ligand nature, solvent nature, availability of hydrolysis catalysts, temperature *etc.* The fundamental *h* value is usually given in a certain range where the clear sol could be obtained and no precipitation occurs. In general, the less *h* is, the more time one needs

to obtain an interconnected metal oxide net. Apart from this the water-to-metal ratio determines the crystallite size of the product. In the presence of large excess of water (more than 300 times) clusters of SnO<sub>2</sub> tend to be higher crystallized than at low water content, when the amorphous metal oxides are formed [67]. Different *h* values for SnO<sub>2</sub> reported in literature are listed in **Table 2**.

**Table 2.** Degree of hydrolysis (*h*) for different precursors and experimental conditions.

<i>h</i> , [H <sub>2</sub> O]/[Sn]	Precursors and experimental conditions	Ref.
0.5-10	SnF(OR <sup>1</sup> )(R <sup>2</sup> COCHCOR <sup>2</sup> ) <sub>2</sub> in acetonitrile, RT	[41]
2-10	Sn(O- <i>t</i> -Am) <sub>2</sub> (acac) <sub>2</sub> in acetonitrile, RT	[73]
3-8	Sn(OEt) <sub>2</sub> (η <sup>2</sup> -acac) <sub>2</sub> and Sn <sub>4</sub> (μ <sup>3</sup> -O) <sub>2</sub> (μ <sup>2</sup> -OEt) <sub>4</sub> (OEt) <sub>6</sub> (η <sup>2</sup> -acac) <sub>2</sub> in ethanol	[56]
2.05	Sn(O- <i>n</i> -Bu) <sub>4</sub> in <i>n</i> -butanol and Hacac, RT	[53]
~ 9	Sn(O- <i>i</i> -Pr) <sub>4</sub> <i>i</i> -PrOH in boiling alcohol	[67]
10	Sn(O- <i>i</i> -Pr) <sub>2</sub> (acac) <sub>2</sub> in ethanol, pH 0-0.6, 60 °C	[55]
81.7	Sn(O-Bu) <sub>4</sub> in propanol, RT	[54]
171	Sn(O- <i>t</i> -Bu) <sub>4</sub> in ethanol, RT	[52]
289.4	(C <sub>4</sub> H <sub>9</sub> ) <sub>2</sub> Sn(acac) <sub>2</sub> in ethanol, 30 °C, catalysts: HCl (pH 2.5) and NH <sub>4</sub> OH (pH 8)	[85]
366 (EtOH)	Sn(O- <i>i</i> -Pr) <sub>4</sub> <i>i</i> -PrOH in ethanol, catalyst: HNO <sub>3</sub>	[51]

Depending on the drying conditions of the gel, one can obtain *xerogel* or *aerogel* (**Figure 1**, stage 3-1 and 3-2). The first one is a product of conventional liquid phase evaporation from the gel, the second is formed during supercritical extraction of solvent. Typically, surface area of aerogels is more than that of xerogels. However, it worth to note, that although drying removes liquid phase from the polymeric network, causing significant compaction, both xerogels and aerogels retain on the surface great amount of terminal hydroxyl and alkoxide groups uniformly distributed throughout the gel [76]. Another evident disadvantage is related with high density of the conventional xerogel, which usually represents a dense monolith, suggesting that conventional drying is more suitable for layer deposition rather than for preparation of dispersed powders.

#### 2.1.4. Properties comparison of synthesized SnO<sub>2</sub>

As it was mentioned in the previous section the surface of SnO<sub>2</sub> synthesized from metalorganic precursors contains organic moieties and chemisorbed water. Apparently this will play a remarkable role in the surface chemistry of the sensing material. To consider this particularity in more detail let us start with the interesting study, performed by Monredon *et al.* [55], demonstrating general trends in surface and material properties of SnO<sub>2</sub> synthesized from metalorganic precursors.

Using FTIR, TGA and solid state NMR authors revealed that surface of SnO<sub>2</sub> xerosols (with mean crystallite size of 1-2 nm), synthesized *via* hydrolysis of tin isopropoxide in the presence of acetylacetonate, is covered with carbonyl, CH and CH<sub>3</sub> groups even after calcination at 250 °C. These groups as well as other organic residues completely disappear only at 450 °C. On the other hand, thermal treatment at 450 °C for 2 h results in abrupt growth of crystallite size up to 11 nm (no remarkable growth occurs at 300 °C). The size remains the same after 2 h at 750 °C and rises to 22 nm after annealing at 1000 °C for the same time. The most remarkable feature of this study is that the crystallite growth, observed starting from 450 °C, coincides with disappearance of organic residues from the surface. This suggests that surface chemisorbed species prevent the crystallites from the thermal growth and their complete desorption at relatively high temperatures most probably causes surface unsaturation, leading to crystallite coalescence.

An extensive overview on synthesis and properties comparison of high surface area tin dioxide was published in 2007 by Hagemeyer *et al.* [72]. They compared 17 different materials synthesized *via* 9 well known techniques including hydrolytic precipitation, sol-gel, Pechini process (thermal decomposition of the polymer resin in which tin cations are uniformly dispersed [72, 86]), oxidation of metallic Sn by HNO<sub>3</sub>, and thermal decomposition of organic precursors. Results of this study are summarized in **Table 3**.

The highest surface area (250 m<sup>2</sup>/g, ~3 nm) and the best thermal stability (175 m<sup>2</sup>/g, ~ 5 nm after 600 °C for 2 h) was found for material synthesized by ***precipitation method*** from SnCl<sub>4</sub> with hydrazine used as a precipitating agent. However, the authors admit that the most crucial disadvantage of the material is chloride contamination, which difficult to remove. Sergent *et al.* report the same method for SnO<sub>2</sub> synthesis in [87], where as synthesized particle size was equal to 3.4 nm, which is also roughly 250 m<sup>2</sup>/g. Successive heating at 100, 200, 300, 400, 500 and 600 °C with 2 h dwell for each temperature resulted in 130 m<sup>2</sup>/g (~7 nm) surface area at the final

stage. Thermal stability of these two materials difficult to compare since calcination procedure in the latter was different from the former.

**Table 3** BET surface area of SnO<sub>2</sub> synthesized *via* different methods as reported in [72]

Synthetic method	Precursor	Precipitation/gelation agent/oxidation agent	Calcination, °C / time, h	BET, m <sup>2</sup> /g
Precipitation	SnCl <sub>4</sub>	Urea	300/4	168
		Hydrazine	300/2	250
			600/2	175
	Sn <sup>IV</sup> (Ac) <sub>4</sub> /acac	Ketoglutaric acid (aq.)	350/5	195
	Sn <sup>II</sup> (Ac) <sub>2</sub> /acac	Ketoglutaric acid (aq.)	350/5	118
	Sn <sup>IV</sup> (Ac) <sub>4</sub> /acetic	Ketoglutaric acid (aq.)	350/5	201
	Sn <sup>IV</sup> (Ac) <sub>4</sub> /formic	Ketoglutaric acid (aq.)	350/5	149
Sol-gel	Sn(O- <i>i</i> -Pr) <sub>4</sub>	Hydrochloric acid	400/2	88
Modified Pechini method	Sn <sup>IV</sup> (Ac) <sub>4</sub>	Glyoxylic acid	290/4	201
	Sn <sup>IV</sup> (Ac) <sub>4</sub>	Oxalacetic acid	310/4	207
	Sn <sup>IV</sup> (Ac) <sub>4</sub>	Tartaric acid	310/4	231
Oxidation	Sn(met) powder	Nitric acid	300/2	75
T. decomposition	Sn(Ac) <sub>4</sub>	Malonic acid	300/4	133

From **Table 3** all precipitation methods based on hydrolysis of metalorganic complexes together with modified Pechini methods also result in high surface area (*ca.* 200 m<sup>2</sup>/g). However, unlike the hydrolysis technique, Pichini one suffers from even higher carbon contamination and therefore requires quite high annealing temperatures to remove it. In the case of hydrolytic precipitation from acetic complexes it is worthwhile to highlight the solvent effect on SnO<sub>2</sub> surface area. Using acetylacetone or acetic acid, the highest specific surface was reached, while formic acid leads to decrease in surface area.

To the same conclusion arrived Ristic *et al.* studying different methods for SnO<sub>2</sub> synthesis. Authors found that Sn(O-*i*-Pr)<sub>4</sub>, is better precursor than SnCl<sub>4</sub> (slowly hydrolyzed for 10 years), to synthesize very fine powder with crystallite size 2 nm and even less [88]. The same precursor was used in [55] to achieve 1-2 nm crystallite size. The size rose to 11 nm after 2 h either at 450 or 750 °C.

**Sol-gel method**, in general, can be used to achieve very fine powder. For example in [73] authors report synthesized material with surface area of 330 m<sup>2</sup>/g. In [53] authors achieved even

better results – SnO<sub>2</sub> aerogels with BET surface area of 357 m<sup>2</sup>/g. The complex procedure to carefully remove solvent from the gel network comprises two solvent exchange steps. First, residual solution is replaced by butanol and then butanol is replaced by liquid CO<sub>2</sub> in an autoclave at 5 MPa and 2 °C.

However, such dispersed materials seem to be very sensitive to sintering. Upon heating at 400 °C for 30 min the area drops to 130 m<sup>2</sup>/g, while at 550 °C – 65 m<sup>2</sup>/g [73]. The similar phenomenon was observed by Hagemeyer *et al.* (**Table 3**).

According to Hagemeyer *oxidation of metallic tin* by boiling nitric acid does not seem to be appropriate for the synthesis of high surface area material. On the other hand, Sergent *et al.* report more fine particles can be obtained through this method. They found mean particle size equal to 4.5 nm (192 m<sup>2</sup>/g) for SnO<sub>2</sub> synthesized likewise and dried at 120 °C [87]. However, this material demonstrates low thermal stability in comparison with SnO<sub>2</sub> synthesized through precipitation method (upon hydrazine addition). After the annealing procedure (successive heating at 100, 200, 300, 400, 500 and 600 °C with 2 h dwell for each temperature) the surface drops to 25 m<sup>2</sup>/g.

**Thermal decomposition** of solid tin (II and IV) acetate complexes yields materials with low surface area (less than 55 m<sup>2</sup>/g). The same result was reported for tin (II) oxalate [62]. The surface increases if one dissolves the complex in an organic solvent. The best results were obtained for malonic acid (see **Table 3**).

Thus, it seems that precipitation methods are the most effective ones to synthesize highly dispersed SnO<sub>2</sub>. Using metalorganic precursors and/or organic precipitation agents and solvents results in formation of surface carbonaceous fragments. These organic moieties play an outstanding role in thermal stability of the nanodispersed solid. Most probably the species are also responsible for oxygen vacancies formation upon desorption at elevated temperatures.

## **2.2. *Bulk properties of tin dioxide***

This chapter deals with physical and chemical properties of nearly stoichiometric tin dioxide. Crystallographic data, electronic structure, properties of the charge carriers and some thermodynamic values are given in the first part. Chemical properties are briefly given in the following part and mainly related with stannic acids.

### 2.2.1. Physical properties

Tin dioxide has the cassiterite structure with tetragonal crystal symmetry  $P4_2/mnm$ . This crystalline structure is composed of metal and oxygen atoms in octahedral (sixfold) and planar (threefold) coordination resp. Unit cell parameters are:  $a = b = 4.737 \text{ \AA}$ ,  $c = 3.186 \text{ \AA}$ , cell volume is  $71.51 \text{ \AA}^3$ , and Sn–O bond length amounts to  $2.05 \text{ \AA}$  (**Figure 2**). The ionic radius for  $\text{Sn}^{4+}$  at sixfold coordination was found  $0.69 \text{ \AA}$ . The oxide density at RT is in the range  $7.00 - 6.88 \text{ g/cm}^3$ , depending on the method (XRD calculation or experimental) [89-91].

In spite of the high enthalpy of Sn–O bond formation ( $\Delta H_f^{\circ} = -286 \text{ kJ/mol}$  [91]) the bond is not completely ionized. The oxidation state  $\text{Sn}^{4+}$  (with ideal electron configuration  $4d^{10} 5s^0 5p^0$ ) can be reached only for highly electronegative elements, *e.g.*  $\text{SnF}_4$  or  $\text{K}_2\text{SnF}_6$ , while in the case of  $\text{SnO}_2$  some of 5s electrons participate in  $sp^3$  hybridization [91]. Calculations show the tin atoms to have a charge of 2.52 and the oxygen atoms to have a charge of -1.26. This means that the bond has a covalent character to a high degree [90].

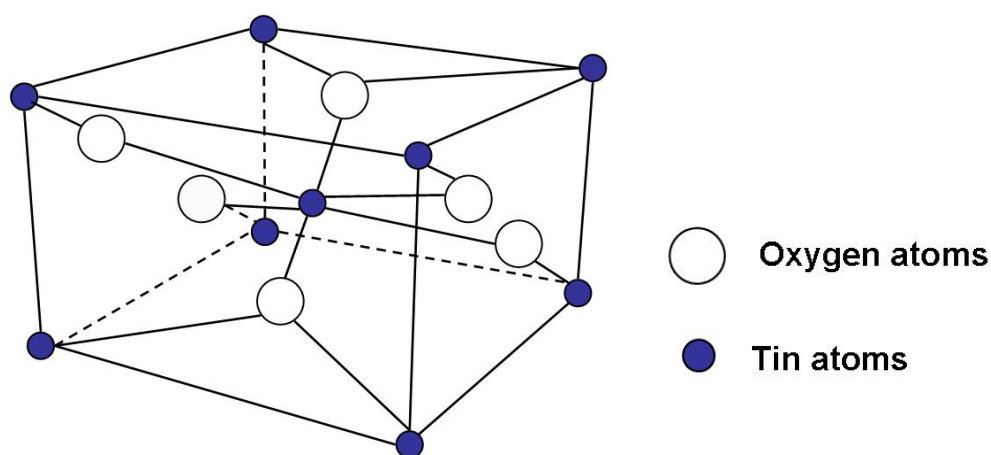


**Figure 2.** SnO<sub>2</sub> unit cell with tin atoms in octahedral coordination

Because of such bond “partial” ionization and intrinsic defects in crystallite structure (mostly bulk and surface oxygen vacancies), SnO<sub>2</sub> exhibits properties of an *n*-type semiconductor. From atomic orbital configuration of Sn and O atoms ( $5s^2 5p^2$  and  $2s^2 2p^4$ ) one can derive a simplified band model which consists of conduction band, made up of Sn 5s states, band gap and valence band made up of O 2p states (**Figure 3**). It is believed that *s*-character of the conduction band is one of the reasons why SnO<sub>2</sub> is a good transparent conductor [92].

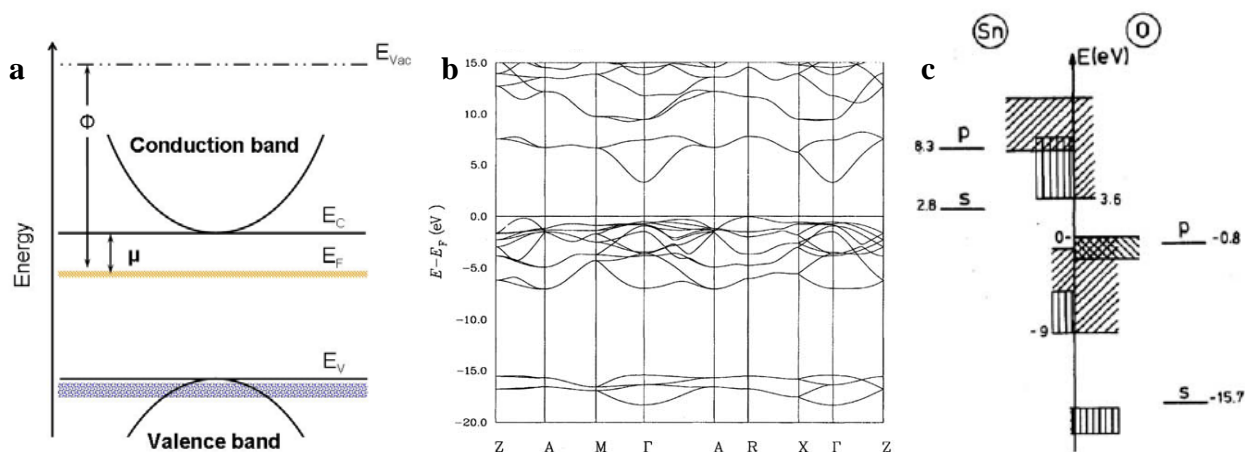


**Figure 3.** Band model (a), calculated band structure (b, from [92]) and illustration of the contribution of the hybridization of Sn and O molecular orbitals for the valence and conduction bands (c, from [92]).  $\Phi$  denotes the work function,  $\mu$  is the electrochemical potential,  $E_{vac}$ ,  $E_C$ ,  $E_V$ ,  $E_F$  are the vacuum energy level, bottom of the conduction band, top of the valence band and Fermi level energies, respectively.

From experimental study the band gap value amounts to 3.6 eV, and known to be direct [90, 91]. Polycrystalline nonstoichiometric material displays a significant density of surface electronic states in the band gap, which results in very different band structure and more shallow band gap [92, 93].

Due to the wide band gap, the stoichiometric compound exhibits optical transparency: the band gap is higher than the highest frequency of visible light, *i.e.* 3.1 eV [90]. Under normal conditions, electron concentration and mobility, estimated from Hall effect measurements for SnO<sub>2</sub> monocrystals, equal to *ca.*  $10^{16}$  cm<sup>-3</sup> and 200-400 cm<sup>2</sup>V<sup>-1</sup>s<sup>-1</sup>, resp. [91]. For polycrystalline material (pc-SnO<sub>2</sub>) with grain size *ca.* 50 nm these parameters at 400K are as follows:  $10^{19}$  cm<sup>-3</sup> and 18 cm<sup>2</sup>V<sup>-1</sup>s<sup>-1</sup> resp. [94].

Carrier concentration at higher temperatures rises up, *e.g.* at 300° C was found to be *ca.*  $10^{17}$  cm<sup>-3</sup> for SnO<sub>2</sub> monocrystal (mc-SnO<sub>2</sub>) and  $6 \cdot 10^{19}$  cm<sup>-3</sup> for pc-SnO<sub>2</sub>. Mobility in its turn drops with increase of temperature and carrier concentration (**Figure 4a**). Temperature dependency for mc-SnO<sub>2</sub> can be described by equation:  $\mu = \mu_0 \cdot T^{-n}$ , where  $n$  was found between 1.1 and 1.5 [91, 94].

Conductivity is thought to be due to intrinsic defect formation, which results in oxygen deficient structure. The later maybe caused either by oxygen vacancies or by partially reduced Sn atoms [90]. Conductivity is not only a function of temperature, but also depends on doping level, sample pre-treatment history and oxygen partial pressure during annealing (**Figure 4b**).



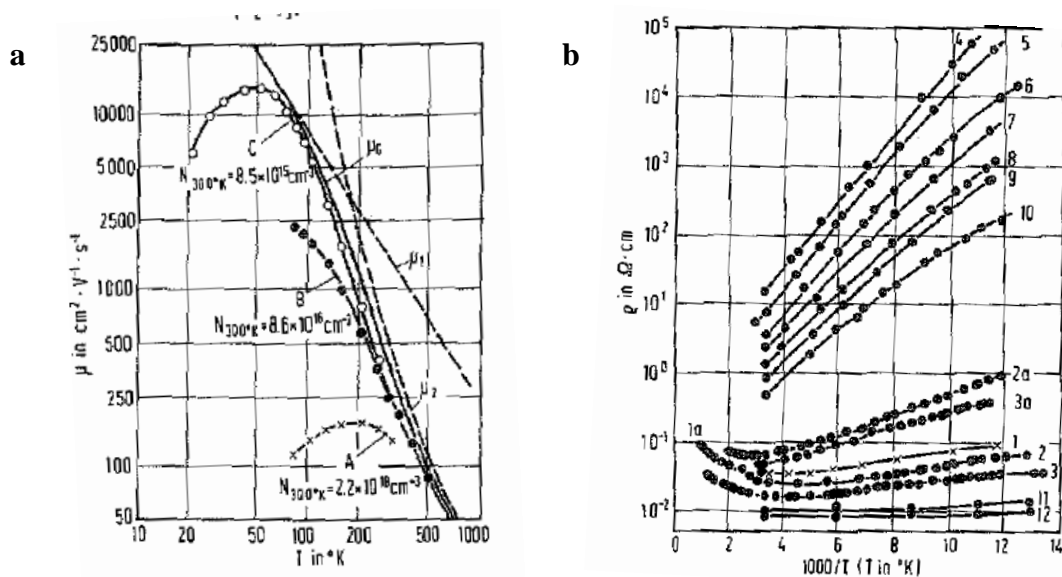


**Figure 4.** Electron mobility (a) and resistance (b) as a function of temperature in mc-SnO<sub>2</sub>. Curves in figure b are: 1 – initial sample, 2 and 3 – pre-annealed in air, 2a and 3a – pre-annealed in dry Ar, 4 – pre-annealed at 0.06 atm of O<sub>2</sub> and stabilized for 282 h, 5-10 pre-annealed at 1 atm of oxygen for various periods of time (from 71 to 161 h), 11-12 – SnO<sub>2</sub> doped with Sb [91].

Melting occurs at temperatures above 1900 °C with decomposition on SnO and O<sub>2</sub> starting already at 1500 °C [92]. Sn vapour pressure at 500 °C was found *ca.*  $6 \cdot 10^{-12}$  atm (against 0.01 atm for Zn in ZnO at the same temperature). The overall vapour pressure is about  $2.6 \cdot 10^{-4}$  atm at 1400 °C. From these facts one can derive that oxygen partial pressure should be much higher for this compound than that of metal. The sublimation enthalpy amounts to 596 kJ/mol. Sn self-diffusion in SnO<sub>2</sub> material, synthesized *via* pressure assisted sintering at 1400 °C equals to 106 cm<sup>2</sup>/s with an activation energy of 496 kJ/mol (for the range 1000-1260 °C) [91, 92].

### 2.2.2. Chemical properties

Tin dioxide is chemically inert compound as many other oxides. The chemical properties can be brought down to the few main features. The compound dissolves only in hot concentrated H<sub>2</sub>SO<sub>4</sub> or in fused alkali hydroxides. Stoichiometric SnO<sub>2</sub> can be reduced to metallic tin in hydrogen atmosphere or in contact with carbon at 500-600 and 800-900 °C, resp [95, 96].

On the other hand, hydrated forms of SnO<sub>2</sub> (*i.e.*  $\alpha$ - and  $\beta$ -stannic acids) are more reactive and their chemical properties are very important regarding SnO<sub>2</sub> synthesis through wet chemistry. In general, freshly prepared colloid of stannic acid in water media is called  $\alpha$ -stannic acid, whereas aged precipitate –  $\beta$ -stannic acid. While  $\alpha$ -form spontaneously evolves with time into the  $\beta$ -one, the latter can't be easily transformed back to the  $\alpha$ -acid.  $\beta$ -stannic acid also forms during tin interaction with hot nitric acid [95].

$\alpha$ -form is soluble in sulfuric, hydrochloric and nitric acids as well as in sodium hydroxide solution forming the corresponding Sn(IV) salts. Conversely,  $\beta$ -stannic acid demonstrates properties of the bulk oxide and can't be dissolved in the same reactants, which act as peptisation agents for the precipitate. Aging of colloidal particles, and consequently formation of  $\beta$ -form, is believed to occur through polymerization of the oxide molecules  $x\text{SnO}_2 \cdot y\text{H}_2\text{O}$  with water detachment [95, 97].

### **2.3. *Surface Properties of tin dioxide***

Surface properties of SnO<sub>2</sub> are given in the two following parts, dedicated to surface electronic structure and chemistry of tin dioxide surface. The former deals with electronic band model of non-stoichiometric SnO<sub>2-x</sub> surface, introducing the main surface states on reduced clean (110) surface. The next chapter accounts for the surface reactivity towards oxygen and water, dedicating special attention to hydroxylated SnO<sub>2</sub> surfaces.

### 2.3.1. Electronic structure

Since very early works of F. F. Volkenshtein, I. A. Myasnikov and T. Seiyama it was known that surface chemistry and physics of some metal oxide semiconductors highly depend on gas environment. As it generally accepted for highly dispersed materials, the electrical resistance is of the Schottky barrier type, which magnitude is modulated by the coverage and charge of surface chemisorbed species [98]. This phenomenon has underlain the concept of gas detection through measuring metal oxide resistance as a function of volatile compound concentration, which has been applied in chemoresistive gas sensors. This is why surface chemistry and physics are extremely important to understand the basics of the gas detection.

Extensive experimental and theoretical research has been performed on SnO<sub>2</sub> surfaces, among the others (110) orientation is the most frequently studied [92]. The reason for this is that the face is the most stable and dominant in polycrystalline materials [99]. Let us consider first ideal, stoichiometric SnO<sub>2</sub> surface (110) and temperature effect on surface composition (**Figure 5**). Under normal conditions the stoichiometric surface is nonpolar (!) and consists of following species [93]:

- two-coordinated chemisorbed oxygen O<sup>2-</sup> or “bridging oxygen” (red balls);
- each bridging oxygen is bonded to two fully coordinated (sixfold) Sn<sup>4+</sup> atoms (blue balls, shielded by bridging oxygen);
- “in-plane” O<sup>2-</sup> (white balls) differs from the bridging oxygen by its threefold coordination;
- second layer of Sn<sup>4+</sup> atoms (blue balls) is five-coordinated which is the last atomic layer with unsaturated coordination sphere;
- following oxygen layers (yellow, orange and brawn balls) are fully coordinated.

The ideal oxidized surface manifests very high electronic density of states in the valence band and very small of them in the band-gap. The features observed in the valence band correspond to the O 2p lone pair which density correlates with surface (bridging) oxygen concentration [93].

The “bridging oxygen” is believed to be easily removed upon heating in vacuum (as low as 500K [93]), which exposes tin atoms with two coordination vacancies (**Figure 5b**). Heating in vacuum at temperatures up to 1000K completely removes in-plane oxygen and the surface in this case contains five, four and free coordinated tin atoms, however no metallic tin is formed as it was found by XPS [93].

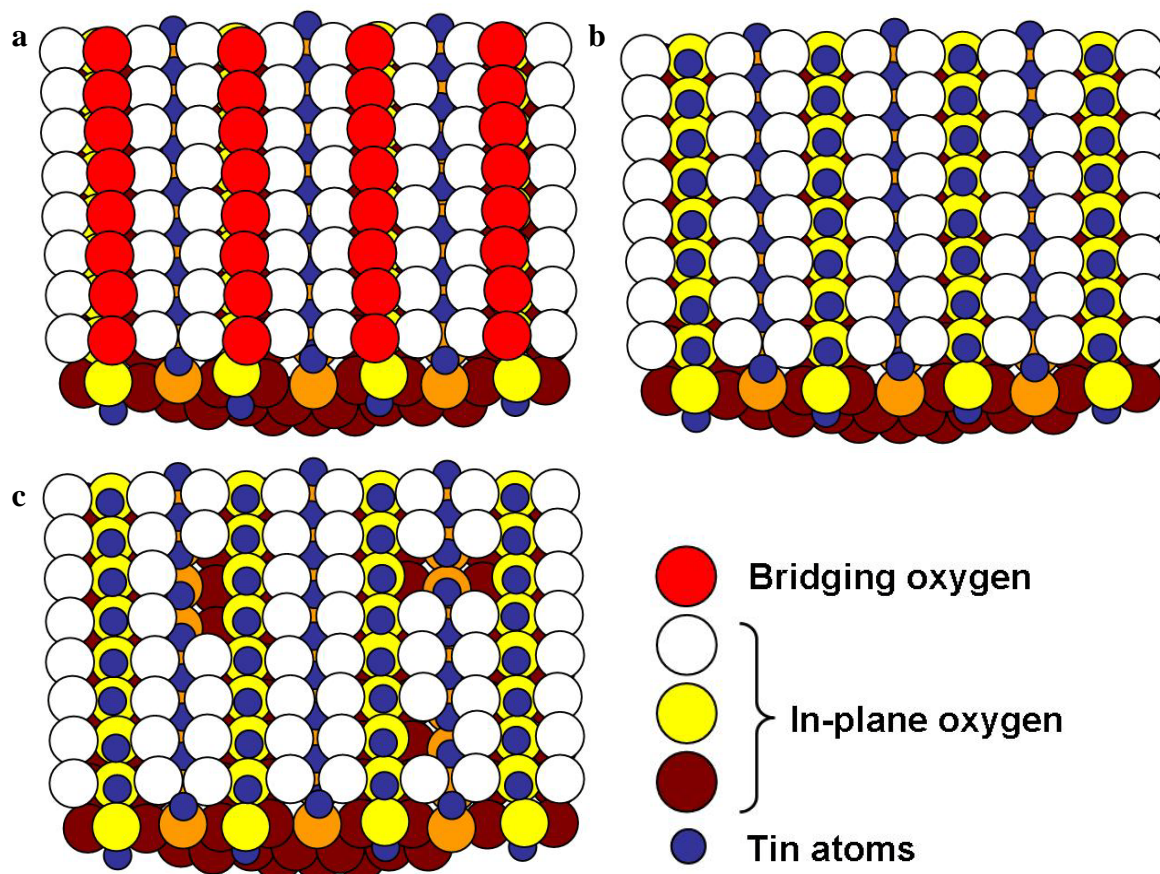


**Figure 5.** Ball model representation of stoichiometric (a), reduced (b) and defective (c) (110) SnO<sub>2</sub> surface, based on ionic radii of Sn<sup>4+</sup> and O<sup>2-</sup> (adapted from [93]).

Formation of surface oxygen vacancies is essential for gas sensor application since they are known to act as n-type donors and increase conductivity by more than two orders of magnitude [92]. In general, formation of surface donor states causes downward band bending and decrease of work function and electron affinity. Cox *et al.* found that generation of bridging and in-plane oxygen vacancies has very different impact on all these parameters. For example, removal of bridging oxygen atoms associated with formation of occupied states in the gap close to the valence band minimum (VBM) due to the drop of coordination number of half the surface tin atoms from six to four. The later is believed to correspond to the reduced Sn(II) atoms with Sn 5s-5p lone pair hybrids.

On the other hand in-plane oxygen detachment creates electronic density between VBM and the Fermi level and this is accompanied by a large increase in conductivity. The opposite effect – upwards band bending – is observed upon oxygen chemisorption, which acts as electron acceptor and depletes the gap states, causing decrease of conductivity [93]. Both cases are schematically shown in **Figure 6**.

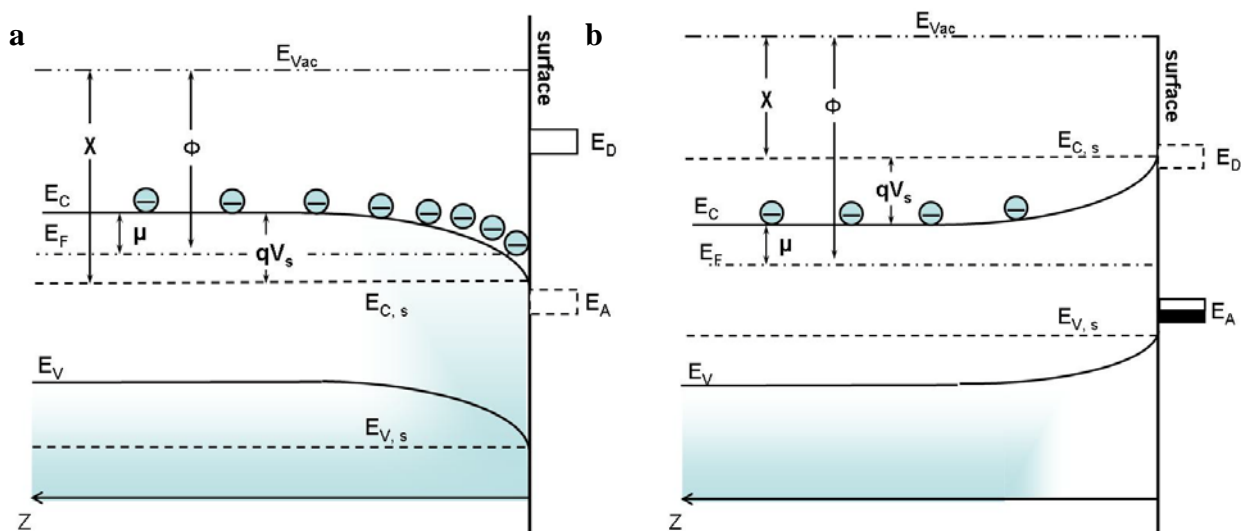


**Figure 6.** Band model of an semiconductor: the case of reduced and defective surface (a) and fully oxidized surface (b) (adapted from [100]).  $E_{Vac}$ ,  $E_C$ ,  $E_F$ ,  $E_V$ , – vacuum, conduction band, Fermi, and valence band energy levels;  $E_{C,s}$ ,  $E_{V,s}$  – conduction and valence band energy levels on the surface;  $E_A$ ,  $E_D$  – acceptor and donor energy levels;  $X$ ,  $\mu$ ,  $qV_s$  – electron affinity, electrochemical potential and band bending value, resp.

As it can be seen, surface electronic properties are determined entirely by the nature and density of the surface defects. Therefore, reproducible preparation of defective surface is probably the most important issue for scientists to study the fundamental basics of the gas sensing material. However, even well known and reproducible physical techniques to produce surface defects (*e.g.* vacuum annealing, plasma treatment or ion sputtering) applied for mono crystals lead to very different results [92].

### 2.3.2. Surface chemistry

Surface defects are known to be active in gas adsorption, since they have coordination vacancies. However, chemical reactivity of low-coordinated surface species is very different. Their comparison can be done in the framework of surface acid-base approach. First let us consider the concepts of Brønsted and Lewis acids or bases. The difference between *Brønsted* and *Lewis acids* is that the first one corresponds to a chemical compound which can donate a proton ( $H^+$ ), while the second one accept a pair of electrons. Consequently, *Brønsted* and *Lewis bases* the ones which can accept a proton and donate a pair of electrons.

As we have seen, defective and reduced SnO<sub>2</sub> surface in vacuum is composed of low-coordinated tin and oxygen atoms. Sn<sup>4+</sup> atom has its outer electronic shell almost empty and tends to refill it with electrons; therefore it acts as hard Lewis acids. In the case of four-coordinated Sn<sup>2+</sup> atoms, their 5s lone pair is believed to be inactive, however, according to Pearson's classification, it represents borderline (neither hard nor soft) Lewis acid. Low-coordinated oxygen atoms have a lone pair, which can be provided to make a bond (including with a proton), therefore they are described as Brønsted or Lewis bases [92]. Thus, keeping in mind that Sn/O ratio can be easily tuned by either physical or chemical methods, one gains a possibility to change surface character from basic (oxidized form) to acid (reduced form) to enhance surface reactivity towards acid or basic volatile compounds, resp.

#### 2.3.2.1. Interaction with oxygen and water

Molecular oxygen is a Lewis base, since each atom possesses a lone pair of electrons that can be donated to Lewis acidic sites. It is known from the literature that oxygen hardly interacts with ideal stoichiometric surface (filled with bridging oxygen and five-fold coordinated Sn<sup>4+</sup>), while with defective surface it is very reactive, which results in chemisorption with desorption peak at around 500 °C [101]. First, oxygen molecule gets coordinated with tin atom (more probably with low coordinated Sn<sup>4+</sup> in oxygen vacancy: Sn<sub>4c</sub><sup>4+</sup>), which results in formation of an intermediate O<sub>2</sub><sup>-</sup> ion with superoxide structure. The later is unstable and exists only at temperatures below 150 °C [101]. Formation of peroxide structure suggests that oxygen acts in this case as Lewis acid, accepting electrons from Sn<sub>4c</sub><sup>4+</sup>.

The following interaction mechanism is even more tentative since only theoretical calculations are available up to date. The peroxide structure dissociates upon interaction with neighbouring bridging oxygen vacancy Sn<sub>4c</sub><sup>4+</sup> or adjacent five-coordinated tin atom Sn<sub>5c</sub><sup>4+</sup> [102]. On the basis of pseudo-potential calculations it was found that oxygen homolytic dissociation on two adjacent oxygen vacancies is more exothermic than that on oxygen vacancy and low

coordinated tin atom (-5.68 against -0.59 eV) [102]. The resulting stable two bridging oxygen atoms (or one bridging and one terminal) are strong electron acceptors and bend the conduction and valence band upwards as it shown in **Figure 6b**. The band bending amounts to *ca.* 0.2 eV according to XPS study [92].

Bridging and terminal chemisorbed oxygen can be identified by IR vibration spectroscopy: several strong bands below 800 cm<sup>-1</sup> correspond to O—Sn—O, Sn—O—Sn and Sn—O stretching vibration modes [98, 103]. Raman active modes for lattice oxygen can be observed between 500 and 800 cm<sup>-1</sup> [92, 104].

Water molecule is also Lewis base, however, with two lone pairs located on oxygen atom. And therefore water also tends to interact with the same low coordinated Sn<sup>4+</sup> ions. However, unlike oxygen, water dissociates at RT even on ideal oxide surfaces, which suggests that the molecule is stronger Lewis base than oxygen. For stoichiometric SnO<sub>2</sub> surface TDS desorption peak was found centred at 390K with *ca.* 15% of total amount of water desorbed at this temperature, while the defective surface shows high temperature peak (with a broad and complex structure) around 450K with *ca.* 35% of desorbed water [105]. However, on defective surface desorption does not occur completely and OH groups are still present after SnO<sub>2</sub> heat treatment in vacuum at 773K [106].

So, defective surface is, therefore, more reactive towards water dissociation because low coordinated ions demonstrate higher affinity to the lone pair (*i.e.* manifest higher acidity). The interaction with the surface, first, comprises coordination on Sn<sup>4+</sup> site with following formation of hydrogen bond between the molecule and the neighbouring bridging oxygen providing the distance (H<sub>2</sub>O)—O<sup>2-</sup> is about 2.7Å. The strong hydrogen bonding is believed to be a precursor to water dissociation. The latter is realized through proton transfer from water to the surface. Thus, water dissociation results in formation of terminal and bridging hydroxyls, depending on molecule surrounding on surface (**Figure 7a**) [107].



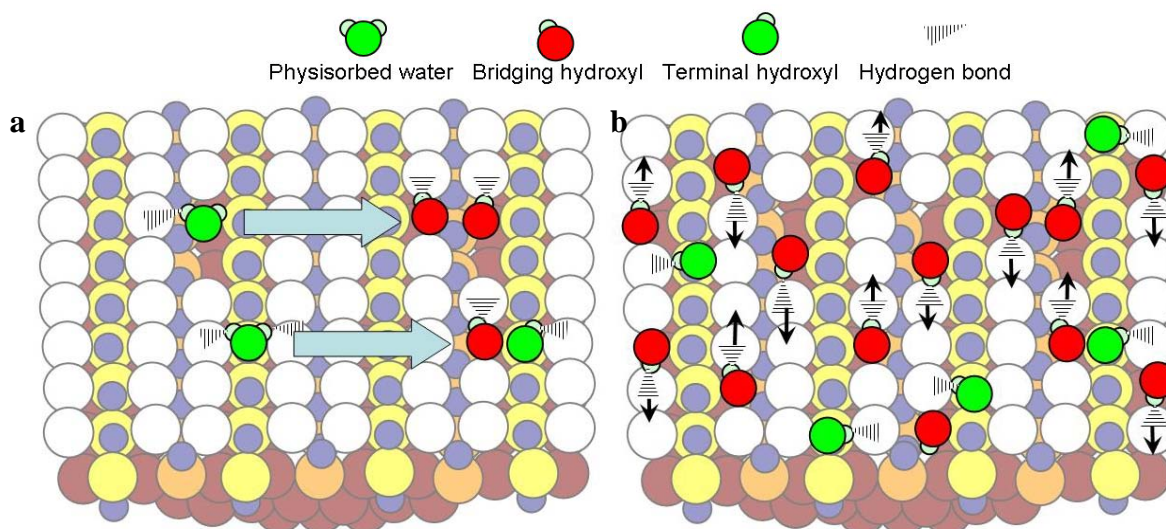


**Figure 7.** The ball model representation of water chemisorption on defective SnO<sub>2</sub> surface (a) and the model of hydroxylated defective SnO<sub>2</sub> surface (b), adapted from [108].

It is very important to note that at elevated temperatures (*ca.* 500K) protons generated due to water dissociation are mobile along the rows of bridging oxygen sites and bridging hydroxyls statistically share the proton with neighbouring bridging oxygen [107]. Such a recombination is a result of strong hydrogen bonding between bridging hydroxyl and surrounding bridging oxygen, which leads to “movement” of bridging hydroxyl within the oxygen rows (**Figure 7b**). To the same conclusion one can arrive, studying FTIR spectra of the hydroxylated surface, which is given in the next paragraph.

### 2.3.2.2. Hydroxylated SnO<sub>2</sub> surface

As we have already mentioned, the chemisorbed water is stable up to 500 °C and even higher. And since water is an omnipresent compound in the ambient atmosphere it is essential to study hydroxylated SnO<sub>2</sub> surface in more detail. In addition, surface hydroxyls are not inert species and readily participate in the surface processes.

The catalytic activity of surface hydroxyls in heterogeneous reactions (*e.g.* water gas shift reaction and methanol production from synthesis gas [109, 110]) has been recognised relatively recently, while in the field of semiconductor gas sensors these species have been considered as reactive intermediates even more rarely. Barsan *et al.* have studied the role of surface hydroxyls in sensing mechanisms, reporting their participation in CO oxidation [111-113]. Thus, we should paid particular attention to the role of chemisorbed water in surface chemistry of SnO<sub>2</sub>.

To understand the difference between oxygen and hydroxyl surface chemistry it will be useful to compare oxidation reactivity of these species found in gas phase elementary reactions.

Kanofsky *et al.* provided strong evidence for the high selectivity of hydroxyl radicals in comparison with oxygen atoms in alkyne oxidation reactions [114]. The interaction with atomic oxygen results in numerous reaction channels and this number increases with the complexity of the alkyne. In contrast, hydroxyl radicals interact similarly with various alkynes forming only one main product. For example, for the reactions  $\text{OH} + \text{C}_2\text{H}_2$  and  $\text{OH} + \text{CH}_3\text{CCH}$  the only product is the ketene  $\text{C}_2\text{H}_2\text{O}$ . Dissociation of the triple bond occurs before the rupture of the OH bond due to its high stability which is believed to be the reason for the selective oxidation ability of OH radicals.

There are basically two types of OH groups on tin dioxide hydroxylated surface: bridging and terminal hydroxyls (**Figure 7**). Since oxygen coordination is different for these two species, they exhibit different chemical properties. The bridging hydroxyls are known to be Brønsted acids. Acidic character means that proton is loosely bonded to the oxygen atom. In addition, the proton tends to form hydrogen bonds with neighbouring oxygen atoms, together with former fact this makes it multi-coordinated and mobile along the rows of bridging oxygen. Complex nature of hydrogen interaction with neighbouring oxygen atoms in the bridging OH group explains broad nature of IR fundamental stretching vibrations, which occur in the region  $2900\text{-}3400\text{ cm}^{-1}$ . Hydrogen additional bonding with neighbouring oxygen ions shifts the band towards lower frequencies [103, 109]. Depending on synthesis route bridging hydroxyls can be partially occluded in the bulk or near-surface region, and therefore can not participate in the surface reactions [106].

Terminal hydroxyls on  $\text{SnO}_2$  surface are less acidic than bridging OHs and, depending on surroundings, can demonstrate moderate Brønsted acidity or non-acidic character. These species are believed to be more reactive in oxidation processes compared with bridging hydroxyls. Their interaction with adsorbed molecules occurs apparently through hydrogen bonding, which was found for CO (weak basicity) adsorbed on blank dispersed  $\text{SnO}_2$  at 120K [106]. The IR bands corresponded to stretching vibrations of terminal OH groups occur in the region  $3600\text{-}3750\text{ cm}^{-1}$ , while that of deformation modes –  $950\text{-}1250\text{ cm}^{-1}$  [103, 106]. It is worthwhile to note that OH acidic properties seem to increase with frequency, *i.e.* species at  $3640\text{ cm}^{-1}$  are more acid than that at  $3740\text{ cm}^{-1}$  [106].

## **2.4. *Some properties of SnO<sub>2</sub>-MetO<sub>x</sub> systems***

This chapter gives a short overview of physical and chemical properties for two-component systems on the basis of tin dioxide and IVB and IIIB metal oxides. Sensing and catalytic properties of the compounds in question are also discussed.

### 2.4.1. SnO<sub>2</sub>-MetO<sub>2</sub>, where Met = Ti, Zr, Hf (IVB group)

One of the main reason to chose IVB metal oxides for SnO<sub>2</sub> doping is the fact that they have good solubility in tin dioxide in a wide range of concentrations (due to iso-structural lattice of some crystal modifications) [115]. The solubility of the oxides comprises metal substitution in the crystalline lattice of the host (SnO<sub>2</sub>). This inevitably results in the change of cell parameters. The more ionic radius differs from that of tin ion and the higher guest concentration in the system, the higher change is observed. The ionic radii of the elements from IVB and IIIB groups and their ionization energies (for the highest oxidation state) are shown in the **Table 4** [116]. From the table one can conclude that amid elements of IVB group the most pronounced change in cell parameters should be observed for Sn<sub>x</sub>Ti<sub>1-x</sub>O<sub>2</sub>. However, for this system with  $x \geq 0.8$ , the cell parameters, *e.g.* cell volume decreases only by a factor of 0.03, in comparison with pure SnO<sub>2</sub>, which is less than 15% of the total possible change in this crystalline structure [117]. For zirconium and hafnium the change is still lower [118]. Comparison of ionization potentials reveals that substitution of tin atoms by Ti will result in slight electron donation into the SnO<sub>2</sub> conduction band. On the other hand, Zr and Hf will demonstrate more pronounced effect, due to the fact that much less energy is needed to detach electron from the zirconium or hafnium atoms.

**Table 4.** Ionic radii, ionization energies and electronegativities of the selected elements

Element	Ionic radius (highest oxidation state), pm	Ionization energy (highest oxidation state), eV	Electronegativity (Pualing scale)
Sn	69	46.4	1.96
Ti	60.5	43.24	1.54
Zr	72	33.97	1.33
Hf	71	31	1.3

Another reason to choose elements from IVB group is related with the physicochemical properties of the respective oxide systems. For example, two phase system SnO<sub>2</sub>/TiO<sub>2</sub> is widely known as prospective material in photocatalysis [28]. The enhancement of the photocatalytic activity is explained by the effective charge separation between SnO<sub>2</sub> and TiO<sub>2</sub> nanoparticles: the electrons are driven away from titania into the conduction band of tin dioxide creating catalytically active holes on TiO<sub>2</sub> surface. By the same manner the guest atoms on the surface will create charge disturbances and therefore enhance catalytic properties of the system in general. Note, that amid the selected elements we have gradual decrease of the ionization energy

and electronegativity in a series Ti, Zr, Hf, which suggests that electron transfer will increase likewise (Table 4).

In the case of two-phase material, the phase of ZrO<sub>2</sub> and HfO<sub>2</sub> can probably increase thermal stability of the nanocomposites, since the oxides are known as refractory with melting temperature 2680 and 2780 °C resp. against 1127 °C of SnO<sub>2</sub> [119].

Sensing properties of titania and zirconia doped tin dioxide have been reported in literature. Combination of SnO<sub>2</sub> and TiO<sub>2</sub> as well as SnO<sub>2</sub> and ZrO<sub>2</sub> layers, synthesized by sol-gel route, has been used in humidity sensors which demonstrated low hysteresis and increased chemical stability [120, 121]. Zakrzewska showed that sensing materials on the basis of SnO<sub>2</sub>-TiO<sub>2</sub> solid solution are good candidates for sensor applications [115, 122]. It was proposed that Ti introduction into the SnO<sub>2</sub> lattice increase the density of the surface states active for the chemisorption. By example of hydrogen detection it was shown that small addition of titanium improves sensing properties of blank SnO<sub>2</sub> material to a large extent. In respect with SnO<sub>2</sub>-HfO<sub>2</sub> system, the present knowledge of its sensing properties seems to be quite limited.

#### 2.4.2. SnO<sub>2</sub>-Met<sub>2</sub>O<sub>3</sub>, where Met = Sc, Y, La (IIIB group)

According to the empirical rule of Hume-Rothery, formation of the substitutional solid solutions can not be achieved in the system where ionic radii of the solute and solvent elements differ more than 15% [123]. As it can be seen from **Table 5** ionic radii of Sc, Y and La are larger than that of tin more than by 15%. In addition the oxides do not have matching crystal structures with solvent phase, which definitely discard possibility of the formation of solid solutions in the system.

**Table 5.** Ionic radii, ionization energies and electronegativity of the selected elements

Element	Ionic radius (highest oxidation state), pm	Ionization energy (highest oxidation state), eV	Electronegativity (Pualing scale)
Sn	69	46.4	1.96
Sc	88.5	24.7	1.36
Y	104	20.5	1.22
La	117	19.7	1.1

So, in comparison with IVB group rare earth elements do not form solid solutions with SnO<sub>2</sub>. Instead, they tend to form a compound with general chemical formula A<sub>2</sub>Sn<sub>2</sub>O<sub>7</sub>, which corresponds to the pyrochlore structure [117]. Stannates of rare earth metals exhibit a lot of

intriguing properties like ionic conductivity (especially when A has large ionic radius), *p* and *n* type of conductivity, remarkable catalytic properties and many others [124]. Pure oxides in their turn (Sc<sub>2</sub>O<sub>3</sub>, Y<sub>2</sub>O<sub>3</sub> and La<sub>2</sub>O<sub>3</sub>) were found to be rather selective in catalytic reduction of NO<sub>x</sub> in the presence of methane. Their advantage in comparison with other oxides includes the fact that water vapours and SO<sub>2</sub> do not significantly inhibit the activity of these materials [125].

Sensing properties of the oxide systems in question are scarce in the literature. The only sensing material studied up to date is tin dioxide loaded with La<sub>2</sub>O<sub>3</sub>. It was found that this oxide system can be employed for CO<sub>2</sub> detection. Authors noted that yttrium introduction into the system resulted in sensing material's durability [126]. High La content (more than 7 w.%) in the system results in the signal change from *n*-type to *p*-type in the presence of the reducing gases [127]. Authors admit that much more work should be done in order to understand this phenomenon.

In general, SnO<sub>2</sub> doping with rare earth elements represents a completely different case of oxide system compared to the doping with the elements from IVB group. Their promising catalytic properties and the fact that some of the oxide systems (SnO<sub>2</sub>-Sc<sub>2</sub>O<sub>3</sub> and SnO<sub>2</sub>-Y<sub>2</sub>O<sub>3</sub>) never have been reported in literature as sensing materials, enable us to choose them as a reference system for titanium, zirconium and hafnium doped tin dioxide.

## 2.5. *Physical models of gas sensing*

Since early works in the field of semiconductor material science, there have been demonstrated that ambient gas atmosphere changes electro-physical properties of numerous semiconductors. A number of theories were developed to explain the nature of interaction between semiconductor surface and adsorbed species, among them: “theory of surface traps”, developed by Brattain and Bardeen; “boundary layer theory of chemisorption”, by Engell, Hauffe and Schottky; “electron theory of chemisorption and catalysis on semiconductors” by Wolkenstein [128]. However, the theoretical foundations, did not lead authors to the idea to employ the described effect for gas detection. The later, by example of ZnO, was proposed by several groups in middle 1950s: Mollwo and Heiland (Germany, 1956), Myasnikov (USSR, 1957) and Seiyama (1962) [128-130]. Finally, Taguchi in 1970 brought semiconductor sensors based on different metal oxides (SnO<sub>2</sub>, ZnO, Fe<sub>2</sub>O<sub>3</sub>, NiO and Cr<sub>2</sub>O<sub>3</sub>) to industrial production [131]. At present there is a growing market of semiconductor gas sensors for various industrial, automotive and domestic applications.

Since first reports on semiconductor gas sensing properties there has been intensive scientific research to optimise sensitivity, response rate, selectivity and economic efficiency of the semiconductor gas sensors. Large number of scientific publications is dedicated to describe physics and chemistry of gas sensing mechanisms, which still are not well understood [128].

In general, sensing material is believed to consist of two interconnected systems: the receptor, which chemically interacts with foreign compound, and the transducer, which converts the energy of this chemical interaction into electrical signal. In the particular case of semiconductor metal oxide sensors, the receptor functions are assigned to the surface: adsorption centers, coordinatively unsaturated species (cus) *etc.* While transducer functions are inherent to the electronic state of the bulk material, which is determined by work function, electron concentration, electron mobility, and the height of Schottky intergrain barrier (if it is considered by the model) [1].

As it was already mentioned in Chapter 2.3, tin dioxide surface, consists of a number of coordinatively unsaturated species which are represented at elevated temperatures by oxygen vacancies (*i.e.* undercoordinated tin cations *e.g.* Sn<sub>4c</sub><sup>4+</sup>) or even reduced tin cations. The fact that surface contains excess of metal cations means that it is highly doped with electron donors which are chemically active species and tend to covalently bond adsorbed molecules changing their electronic state. Surface oxygen also plays important role in surface process especially in oxidation reactions and therefore should be considered as constituent part of receptor family.

Bearing this in mind let us consider the existing mechanisms of acceptor and reducing molecules interaction with defective SnO<sub>2</sub> surface.



### 2.5.1. Interaction with acceptor molecules and some general remarks

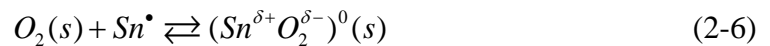
Tin dioxide interaction with oxygen will be considered as a model case for other acceptor molecules. Again, as we have already seen in Chapter 2.3, oxygen readily interacts with defective surface, bringing about decrease of conductivity in the bulk. This change in conductance was experimentally found to be the power function of oxygen pressure:

$$\sigma \approx P_{O_2}^{-m} \quad (2-1)$$

where,  $m$  is the numeric factor varying from 0.5 to 0 [130]. For SnO<sub>2</sub>, TiO<sub>2</sub> and ZnO films the value of  $m$  was found close to 0.5, which suggests that roughly 2 electrons per oxygen molecule are involved in charge transfer due oxygen chemisorption. Thus, the adsorption induced change in the conductivity can be represented as follows:



The experimental evidence of surface superoxide in Eq. 2-3 has been proved by *operando* FTIR studies and some UHV techniques, while process 2-4 is doubtful since it has not been demonstrated experimentally yet [128]. However, the most serious inconsistency of the proposed model was given by Kupriyanov in [130]. Among the other facts provided by the author, the rise of superoxide concentration, occurring at different moment than the change of conductance, seems to be the most crucial. Myasnikov *et al.* proposed that conduction change induced by oxygen adsorption does not occur due to the change of *oxygen oxidation state* (either through 2-3 or 2-4), but is a result of the change in *donor concentration* of the surface-adjacent layer. In the case of SnO<sub>2</sub> the electron donors are superstoichiometric metal cations (*e.g.* Sn<sub>4c</sub><sup>4+</sup>, Sn<sub>4c</sub><sup>2+</sup>) at oxygen vacancies and surface defects. In this case, the overall mechanism can be represented as follows:



where O<sub>2</sub>(s) is the physisorbed oxygen, Sn<sup>•</sup> is the superstoichiometric tin atom and (Sn<sup>δ+</sup>O<sup>δ-</sup>) is the neutral surface specie, which formation leads to the decrease of the dopant concentration. Assuming linear character of adsorption (*i.e.* when  $[O_2(s)] \approx P_{O_2}$ ) and that  $\sigma \sim [Met^\bullet]$ , the conductivity change upon oxygen adsorption can be given as:

$$\sigma \approx \frac{\langle \sigma_0 \rangle}{\sqrt{1 + \frac{\Gamma k(T) P_{O_2}}{\langle h \rangle}}} \quad (2-7)$$

where  $\langle \sigma_0 \rangle$  is the average initial conductance (or average initial concentration of superstoichiometric metal species),  $P_{O_2}$  is the oxygen partial pressure,  $\Gamma$  is the Henry's constant,  $k(T)$  is the equilibrium constant of the process 2-6, and  $\langle h \rangle$  is the constant defining the nature of particle-particle interaction, namely the average thickness of the bridges connecting to particles. It should be noted that the found relation 2-7 can be applicable to other acceptor molecule, *e.g.* NH<sub>3</sub>, Cl<sub>2</sub>, F<sub>2</sub> *etc.*

The drop of the donor concentration in the surface and adjacent layers results in the upwards bending of the bottom of the conduction band (**Figure 6**) and leads to the formation of the electron depleted region in the particle (**Figure 8**).

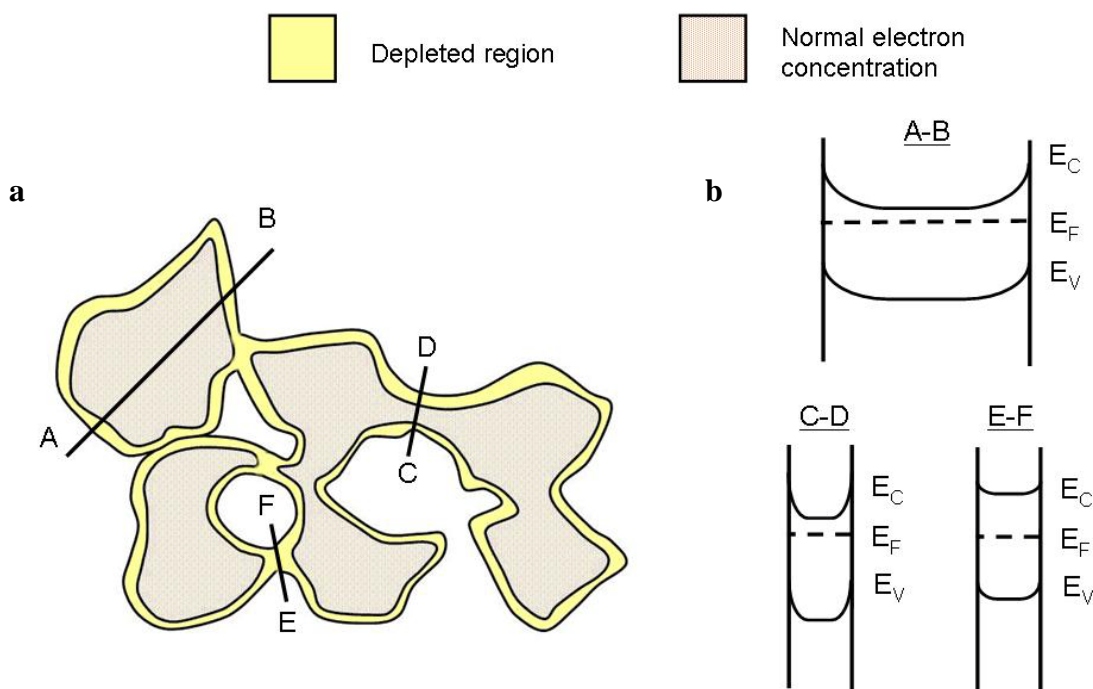


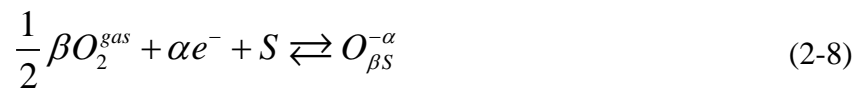
**Figure 8.** Representation of the electron depleted regions in a polycrystalline material (a) and representation of the band bending as a function of the particle cross section (b), adapted from [130].

The thickness of the depleted region was experimentally found to be between 0.7 and 2.1 nm [132], which means that bridges or necks between particles as well as very fine particles with diameter  $\leq 5$  nm are completely depleted. Such depleted regions are usually represented as

Shottky barriers with the height equal to  $eV_s$ , where  $V_s$  is the surface potential. In microcrystalline material only thin necks seem to be the most sensitive to the electron depletion induced by adsorption of an acceptor molecules. That is why the parameter of neck geometry  $\langle h \rangle$  appears in the 2-7. For nanocrystalline material the particles themselves together with necks can be exhausted of free charge carriers and therefore the conductance drop will be more pronounced. In this case the  $\langle h \rangle$  will represent the particle size, or generally speaking: the ratio of particle volume to its surface [130].

Note that apart from the change in the concentration of free carriers (due to the change of the donor concentration upon contact with acceptor molecules) another parameter can influence the overall conduction of semiconductor material – carrier mobility. Kupriyanov reported that the contribution of this parameter was experimentally observed only for high concentration of the chemisorbed acceptor molecules on microcrystalline SnO<sub>2</sub>. The latter results in formation of high energy barriers and “apparent scattering” of the carriers [130]. To the same conclusion arrived A. Oprea *et al.* in [133]. They showed that when mean free electron path is much less than grain diameter ( $l \ll d$ ) “the surface and its chemistry will act on the conductance only through the carrier concentration”. However, for very fine grains when  $l \sim d$ , the contribution of the electron mobility should be taken into account.

Unlike Myasnikov’s assumption that the conduction change induced by oxygen adsorption is a result of the change in *donor concentration* in the surface-adjacent layer and not that of the change in *oxygen oxidation state*, A. Oprea, N. Barsan *et al.* developed theory assuming the latter phenomenon [133]. Accordingly the oxygen chemisorption can be written as:



where  $O_{\beta S}^{-\alpha}$  is the adsorbed oxygen,  $\alpha$  is the ionization degree and  $\beta$  indicates atomic or molecular adsorbed specie (equals to 1 or 2 resp.). Consequently the conductance dependency on oxygen partial pressure was given as:

$$\sigma \propto p_{O_2}^{-\beta\gamma/2(\alpha+\delta)}, \text{ when } l \ll d \quad (2-9)$$

$$\sigma \propto (p_{O_2}^{-\beta/2(\alpha+1)} + cp_{O_2}^{-\beta/(\alpha+1)}) \text{ , when } l \sim d \quad (2-10)$$

where  $\gamma$  and  $\delta$  are fitting parameters (less than 1) and  $c$  is the weighting coefficient. Authors admit that for the first case the fitting parameters are not in the expected range. However, when  $l \sim d$  for temperatures above 250 °C the conductivity can be described fairly well with the

proposed model. The model suggests that under these conditions chemisorbed oxygen mainly exists in the form of double ionized atomic oxygen  $O^{2-}$ .

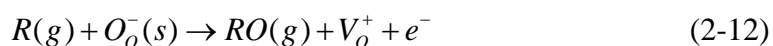
### 2.5.2. Interaction with donor molecules

Now let us consider the interaction of donor molecules with SnO<sub>2</sub> surface. Let us suppose that the equilibrium between surface and oxygen had already been reached when the donor molecule comes into contact with the surface. This means that defective SnO<sub>2</sub> surface consists of oxygen vacancies, chemisorbed oxygen and in-plane oxygen. There are basically three possible processes of the interaction [130]:

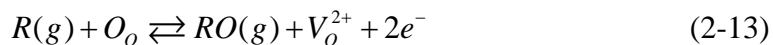
1) the molecule adsorbs without formation of oxidized volatile species and donates electron to the conduction band:



2) the molecule interacts with chemisorbed oxygen (terminal one) through oxidation reaction. The electron is formed as a result of surface donor formation:



3) the molecule interacts with in-plane oxygen through oxidation reaction and due to formation of ionized oxygen vacancy the conductivity rises:



The first case can be observed upon donor adsorption in the low temperature region (*e.g.* between 70 and -190 °C). However, as it was shown by Myasnikov *et al.*, even such a simple case as hydrogen adsorption (7-8 torr) on reduced ZnO surface has pretty complex nature and the rise of conductivity does not occur due to the molecule ionization. It was found that in this case at low temperatures surface H<sub>2</sub> is totally ionized with very low activation energy ~ 2 kcal (~ 8 kJ) [130]. However, the activation energy of the change of electrical conductivity was found ~ 30 kcal (~ 125 kJ). Therefore, the change in the electron concentration due to ionization of the surface states (surface charging) through 2-11 was ruled out. Oxide reduction and volume dissolution of H<sub>2</sub> in oxide were also rejected due to the strong experimental proofs. It turned out that apart from the processes 2-12 there is a recombination reactions between ionized and neutral

atoms of hydrogen which leads to formation of the complex:  $\begin{array}{c} \text{H}^- \text{---} \text{H}^+ \\ | \quad \quad | \\ \text{Met} - \text{O} \end{array}$ . According to the authors, the main process contributing to the conductivity increase in the low temperature region is desorption of the metal bonded H atom.

At higher temperatures processes 2-12 and 2-13 are dominant. However, the surface chemistry is very complex and involves very big number of reaction paths. The dependency of

conductance on partial pressure of reducing gas was experimentally found to be a power law as well as in the case of oxygen:  $\sigma \approx P_R^{-m}$ , where  $0 < m < 1$ .

By example of CO interaction with SnO<sub>2</sub>, N. Barsan *et al.* proposed a more specified relationship between conductance and partial pressure of the reducing gas [133]:

$$\sigma \propto P_{CO}^{\beta\gamma/2(\alpha+\delta)}, \text{ when } l \ll d \quad (2-14)$$

$$\sigma \propto (P_{CO}^{\beta/(\alpha+1)} + \tau P_{CO}^{2\beta/(\alpha+1)}), \text{ when } l \sim d \quad (2-15)$$

where,  $\alpha$  and  $\beta$  are the ionization and chemical states of oxygen as mentioned above. Note that this representation of the model for the sake of simplicity does not contain oxygen partial pressure and other constants (rate constants of adsorption/desorption, concentration of free carriers, permittivity *etc.*), which are included into the proportionality constant. As it can be seen the model takes into account the nature of chemisorbed oxygen, however in the real conditions several type of surface oxygen can participate in the reaction simultaneously, which probably will complicate the model even more.

Another interesting and rather simple model was developed by R. Ionescu *et al.* [134]. Assuming that “surface behaves like an n-type semiconductor isolated from the bulk” by highly resistive region formed upon tin and oxygen thermal diffusion towards and from the surface resp. authors proposed an alternative to the approach of surface Schottky barriers:

$$\sigma = \sqrt{N_D^0 \frac{k_D + k'_R P_R}{k'_A P_{O_2}^m}} \quad (2-16)$$

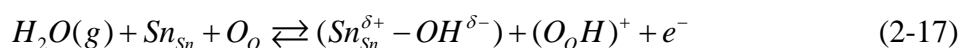
where  $N_D^0$  is the surface density of vacancies occupied by chemisorbed oxygen,  $k_D$ ,  $k_R$  and  $k_A$  are the rate constants,  $p_R$  and  $p_{O_2}$  partial pressures of reducing gas and oxygen resp. However, this model also accounts only for the simplest case of the surface interaction, namely through single chemisorbed oxygen species.

### 2.5.3. Interaction with water

The above case of reducing gas interaction with metal oxide semiconductor surface demonstrates very complex relationship between SnO<sub>2</sub> conductance and the partial pressure of the reducing gas in the presence of oxygen. However, the majority of the chemoresistive sensor applications are intended for ambient atmospheres. This means that at least one more component in the gas phase will interact with semiconductor surface – water. As we have seen earlier water – polar molecule with two lone pairs on oxygen – readily interacts with defective tin dioxide surface. The resulting chemisorbed species are very stable (up to 500 °C) and demonstrate a bunch of chemical properties depending on oxygen coordination. This makes water the most important and tough participant in the gas sensing phenomenon.

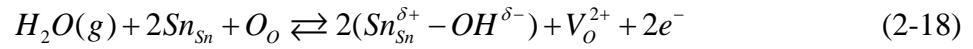
Depending on various factors (*e.g.* season, temperature, location *etc.*) the atmospheric water content can vary from *ca.* 0.1 up to 4 vol%, which notably changes electrical properties of the sensors and dramatically influences their sensitivity. A number of studies have been performed to understand this phenomenon in order to reduce the effect of humidity on sensor performance [94, 112, 135-138].

Experimental dependence of material conductance on partial pressure of water vapours was found to be a power law function as well as for other gases (Eq. 2-1), with *m* close to 0.5. Three models are commonly used to describe the interaction of water with semiconductor surfaces resulting in an increase in surface conductivity [111, 139]. The first one is based on formation of bridging hydroxyl which causes the change in the conductivity:

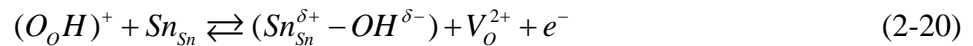
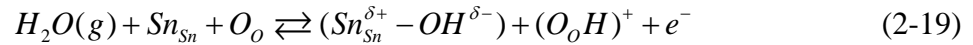


where,  $Sn_{Sn}$  is lattice tin atom,  $O_o$  is the bridging (in-plane) oxygen,  $(Sn_{Sn}^{\delta+} - OH^{\delta-})$  is the terminal OH group,  $(O_oH)^+$  is the bridging hydroxyl. The model assumes that bridging oxygen becomes ionized when bonding with hydrogen and therefore donate electron to the conduction band. However, as we have already shown in Chapter 2.3, bonds between twofold in-plane oxygen and tin atoms are known to be strongly polarized [32]. Even if we substitute one of these three tin atoms with hydrogen one (the case of bridging hydroxyl), which has higher ionization potential in comparison with tin atom, the bond H–O will be still highly polarized. Therefore,  $(O_oH)^+$  should rather be shown as  $(O_o^-H^+)$  with very little contribution to the overall conduction.

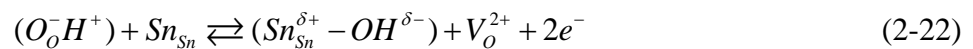
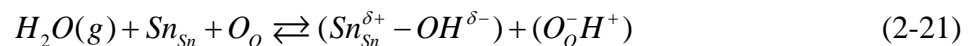
The second model implies the same mechanism as the previous one with following interaction between bridging hydroxyl and neighboring tin atom with formation of terminal hydroxyl and oxygen vacancy:



where,  $V_o^{2+}$  is the surface oxygen vacancy. If we take into account that the first step of this interaction is exactly the same as 2-17 the mechanism should be written as follows:



This mechanism seems to be more appropriate to explain conductivity change upon water contact. Taking into account the above mentioned considerations it is unlikely that process 2-19 results in electron injection. On the other hand, 2.20 is in line with the assumption of conductivity rise due to increase of surface donors, stated by Myasnikov. Thus, in our opinion the charge transfer occurs mainly due to formation of the oxygen vacancy. And the mechanism can be rewritten as follows:



The third mechanism is based on indirect interaction of either hydroxyl group or hydrogen atom with surface states changing their electron affinity and increasing conductivity of the material.

The case of conductivity change upon water chemisorption strongly supports Myasnikov's theory of conductivity change due to the change of donor concentration on the surface. Indeed, no Red/Ox reactions occur upon water contact with semiconductor, the only parameter that changes is the ratio between donor and acceptor states on the surface. Therefore, even for the case of reducing gases we should take into account a considerable contribution of surface processes non-related to the Red/Ox reactions to the overall change of conductivity.



## 3. Experimental

This section describes in detail protocols, methods and techniques applied for synthesis, material characterization and characterization of sensing properties of the synthesized compounds. The first chapter deals with synthesis, since as it was shown earlier physicochemical properties of dispersed materials are entirely determined by synthesis route and particularities of the method used. This chapter also includes auxiliary experiments which are not directly sometimes related with the oxide synthesis; however, they were essential to better understand the processes occurring in the chemical vessel, transparent for naked eye but impermeable and obscure sometimes for comprehension.

The second chapter is dedicated to *ca.* 13 *ex situ* and *in situ* techniques used for characterization of the synthesized materials. The third part describes deposition of sensing materials, calibration procedures and methodology used for characterization of sensing properties.

### **3.1. Synthesis**

As it was shown in Chapter 2.1 the best candidates for research activity amid various chemical, physical, dry and wet synthetic routes are colloid chemical methods due to fairly optimized ratio between: technique flexibility (extremely high), reproducibility (“could be better”) and product cost (could be very cheap as well as rather expensive). In the same chapter we have specified the weak points of this approach. The most substantial for nanodispersed sensing materials is impurity level, since we can remove the impurities neither by thorough washing, nor by heating at elevated temperatures.

Accordingly, we decided to focus our efforts on elaboration of the method which would be based only on precursors free of halogen and sulphur to synthesise blank SnO<sub>2</sub>, as well as two-component oxide systems SnO<sub>2</sub>-MetO<sub>x</sub>, where “Met” are metals from group IVB and IIIB. The best candidates for precursors, matching this requirement, are metalorganic complexes. The same approach was applied to the selection of the precursor for noble metals.

This chapter is built up from several parts dealing with synthesis of blank SnO<sub>2</sub>, mixed oxides, post synthesis procedures and catalyst deposition. The first one is probably the most important since it describes procedure for SnO<sub>2</sub> colloid synthesis, applied universally for all other oxide systems reported herein. The second part gives details on synthesis protocol of two-component oxide systems. The following part accounts for the post-synthesis procedures: phase separation, purification, drying and calcination after the synthesis. The catalyst deposition procedure is given afterwards. The synthesized materials, intended for the following material characterization and characterization of sensing properties, are listed at the end of this chapter.

### 3.1.1. Blank SnO<sub>2</sub>

Following reagents were used throughout all the synthesis protocols:

Deionised water, Fluka Trace SELECT®, p/n 95305;

Deionised water, Fluka Trace SELECT™ Ultra, p/n 14211;

Ethanol absolute, Sigma-Aldrich, p/n 24194;

Acetic acid, Fluka, puriss, p/n 45731.

In the synthesis only glass vessels were used. First the vessels were washed with concentrated nitric acid, then were rinsed out several times with Trace SELECT® water and left filled with Trace SELECT™ Ultra water for several hours. Acetic acid was used to remove traces of water just before the synthesis.

#### 3.1.1.1. Precursor synthesis

Reagents: tin powder, 325 mesh, purity 99.8%, Sigma Aldrich.

As precursor we have chosen tin acetate complexes from various points of view. Firstly, the acetic acid is a strong organic ligand demonstrating high acidic properties which makes possible to synthesize tin acetate complexes *via* direct interaction of the acid with metallic tin. Secondly, in comparison to another strong organic ligand with acidic properties – formic acid – acetic acid is not so toxic and harmful compound: maximum permissible concentration of formic acid in Russian Federation is five times lower than that of acetic acid (1 against 5 mg/m<sup>3</sup>) [140]. Finally the starting products are cheap and one-step synthesis of the precursor makes the method very economically efficient.

The simplest way to synthesize tin acetate complexes is direct interaction of metallic Sn with hot acetic acid. As a model to our protocol we used following procedure described in [141]: fine powder of metallic tin is put in the glacial acetic acid and undergo boiling under inert atmosphere with reflux condense for 80-90 hours; this results in formation of tin(II) acetate solution in acetic acid.

This procedure was slightly modified to minimise experimental costs and time, and maximise yield of the product. Namely, the interaction was performed in ambient air and tin powder with particle size of 45 µm was dispersed in the acid with the help of ultrasonic bath. Thus, the modified method was as follows. 3 g of tin powder is added stepwise to the 350 ml of acetic acid, the mixture is dispersed in ultrasonic bath for 10 min and then heated up to 90 °C with reflux condense at magnetic stirring. The heating lasts for 20 hours when the solution becomes almost transparent of intense yellow colour and no metallic tin is present in the vessel. The cooled solution is filtered with Whatman cellulose filter (pores <2 µm). The filtered solution

is absolutely transparent, chemically stable (can be stored at RT for several days or even longer) and was used for SnO<sub>2</sub> synthesis.

We should note that formation of tin(II) acetate is already questionable in the presence of the moisture. Most probably a mixture of tin(II) and tin(IV) is formed under these conditions and the excess of acetic acid ensures stability of the dissolved tin complexes in the presence of water traces. It is worthwhile to note that cooling down concentrated solutions to *ca.* 5 °C does not lead to freezing as it is normally observed for pure acetic acid (mp ≈ 16 °C)

To study precursor composition the filtered solution was carefully evaporated at RT in air during 30 hours. As a result yellow transparent crystals were obtained. The crystals were washed with pentane using ultrasound bath to remove synthesis by-products. The obtained crystals of yellow colour underwent thermal treatment for 20 h at 50, 100 or 300 °C.

### 3.1.1.2. Colloid systems SnO<sub>x</sub>H<sub>y</sub>

Synthesis of the colloidal suspension was performed using modified method elaborated on the basis of the techniques reported in [119] for Sn(SO<sub>4</sub>)<sub>2</sub> and SnCl<sub>4</sub> hydrolysis. 120 ml of tin acetate complex in acetic acid was cooled and its temperature was maintained at *ca.* 5 °C by external cooling. Upon magnetic stirring 10 ml of hydrogen peroxide was added dropwise to the cooled solution. The colour of the mixture turned pale. Then, 320 ml of 12.5% NH<sub>3</sub>H<sub>2</sub>O was added dropwise to the mixture and the cooling of the resulting transparent mixture was switched off and the mixture was heated. The opalescence was observed between 30 and 40 °C at slightly acidic media, which pH was found always to be 6.3±0.1 (additional experiments were performed to establish the pH of the colloid formation at RT). The colloid formation occurs spontaneously in the solution volume upon heating the mixture between 50 and 60 °C under continuous stirring.

The pH value found is very close to the IEP of stannous oxide (*i.e.* SnO) in the hydrated form, as reported in [142]. According to the paper, the compound was synthesized from SnCl<sub>2</sub> solution upon addition of NaOH and its IEP was found 6.6, which allow us to suppose that in our synthesis the colloid is probably close to the stannous acid than to the stannic one (IEP between 3.5 and 5.5). However, in our case the colloid mixture contains very small amounts of free water which probably affects the ionic strength of the solution and therefore the obtained pH values should be compared very carefully with the results reported in [142].

The specified above method was adapted for the synthesis starting from tin(IV) acetate (supplied by Aldrich, p/n 345172). 1 g of Sn(Ac)<sub>4</sub> was dissolved in 100 ml of acetic acid and 8 ml of H<sub>2</sub>O<sub>2</sub> was added dropwise to the cooled solution. Under magnetic stirring 240 ml of NH<sub>3</sub>H<sub>2</sub>O was added dropwise to 90 ml of the cooled precursor solution. The precipitation was

observed at pH *ca.* 7, which indicates that the colloid formed starting from tin(IV) acetate has quite similar composition to that synthesized presumably from tin(II) acetate.

### 3.1.2. SnO<sub>2</sub>-MetO<sub>x</sub> and SnO<sub>2</sub> bulk doped with impurities

The following metalorganic compounds were used to introduce IVB and IIIB metals into tin oxide lattice:

Titanium(IV) isopropoxide, purum, Aldrich, p/n 87560;

Zirconium(IV) acetate solution in dilute acetic acid, Aldrich, p/n 413801;

Hafnium(IV) acetylacetonate, synthesized at IGIC RAS;

Scandium(III) nitrate hydrate, Aldrich, p/n 325902;

Yttrium(III) acetate hydrate, Aldrich, p/n 326046;

Lanthanum(III) acetate hydrate, Aldrich, p/n 306339.

All precursors except Ti (O-*i*-Pr)<sub>4</sub> were dissolved in glacial acetic acid and then were added to the Sn(Ac)<sub>2</sub> solution. The corresponding quantities of H<sub>2</sub>O<sub>2</sub> and NH<sub>3</sub>H<sub>2</sub>O were mixed under magnetic stirring and external cooling to produce transparent mixtures, which were heated up to form colloid suspension. Due to low solubility in acetic acid, Ti (O-*i*-Pr)<sub>4</sub> was first dissolved in ethyl ether and then added to the Sn(Ac)<sub>2</sub> solution. The colloid formation was performed without H<sub>2</sub>O<sub>2</sub> addition, since the titanium isopropoxide is extremely sensitive to hydrolytically active compounds. The precursor quantities were calculated assuming the MetO<sub>x</sub> content is 10 w.% in the SnO<sub>2</sub>-MetO<sub>x</sub> system.

Since the technique is based on halogen-, sulphur- and sodium-free precursors it will be of particular interest to study the influence of impurities on physicochemical properties of *nc*-SnO<sub>2</sub>. With this aim we synthesized SnO<sub>2</sub> doped with chlorine, sulphur, sodium and palladium. The following reagents were used:

Hydrochloric acid, 37 %, Sigma-Aldrich, p/n 258148,

Sulphuric acid, 95-98%, Sigma-Aldrich, p/n 320501,

Tetraamminepalladium(II) nitrate, 10% water solution, Aldrich, p/n 377384,

The specified reagents were dissolved in acetic acid and added to tin acetate solution prior to the addition of H<sub>2</sub>O<sub>2</sub> and ammonia. The quantity of the added reagents was set to 0.03 w.% of the admixture content in the dry oxide material.

### **3.1.3. Post-synthesis procedures**

The milky white colloid, heated up to 70 °C, was left to for sedimentation at RT during 3-4 hours. Then the liquid medium is decanted and the residual mixture is separated by means of centrifugation at rotation speed 6000 rpm for 5 min. The separated solid was washed with Trace SELECT™ Ultra water at 80 °C and then again was centrifuged at 6000 rpm for 30 min. Note that in water medium complete sedimentation of the colloid did not occur even after 30 min at 6000 rpm, while in the mother solution the colloid tends to coagulation and spontaneous sedimentation.

The washing procedure was repeated three times. The washed colloid was dried at 90 and at 200 °C for 8 hours at each temperature. The resulting powder is grinded carefully in the agate mortar with a pestle for 15 minutes and then the powder was calcinated at 300 °C for 24 hours.

In the case of impurity containing tin dioxide the procedure of washing was omitted and the samples underwent drying directly after the separation of the solid from mother solution.

### 3.1.4. Deposition of noble metals

The following complexes were used to deposit palladium, platinum and rhodium catalysts:

Tetraamminepalladium(II) nitrate, 10% water solution, Aldrich, p/n 377384,

Tetraammineplatinum(II) nitrate, powder, assay 99.995%, Aldrich, p/n 482293,

Rhodium(III) nitrate hydrate, puriss, Aldrich, p/n 83750.

The deposition was carried out as follows. If the complex was solid (*e.g.* Pt(NH<sub>3</sub>)<sub>4</sub>(NO<sub>3</sub>)<sub>2</sub> or Rh(H<sub>2</sub>O)(OH)<sub>3-y</sub>(NO<sub>3</sub>)<sub>y</sub>) it was first dissolved in Trace SELECT™ Ultra water. In the same time the blank oxides were impregnated with Trace SELECT™ Ultra water in the agate mortar. A calculated volume of the water complex solution was added to the mixture of water and oxide powder. The resulting mixture was grinded with a pestle for 30-40 minutes until the water evaporated completely. Then the powder was placed into the oven and dried stepwise at 90 °C for 8 hours, 200 °C for 8 hours and at 300 °C for 12 hours. The calculated catalyst to SnO<sub>2</sub> ratio was 1 w. % for all materials.

To deposit two catalysts simultaneously, their corresponding water solutions were mixed in the weight ratio 1:1. The resulting solution was added to the mixture of water and blank oxide. As to the rest, the procedure was the same as the one specified above. The overall content of two catalysts is close to 2 w. % respective to SnO<sub>2</sub>.



### 3.1.5. List of the synthesized materials

The synthesized materials which characterization will be covered in the following chapters are listed in **Table 6**. The sample names given in the table will be used also throughout the text hereinafter.

**Table 6.** List of the synthesized materials.

Sample name	Remarks
SnO <sub>2</sub> Ac	Tin dioxide synthesized from metallic tin. Calcinated at 300 °C.
[Sn(OH) <sub>n</sub> (OAc) <sub>m</sub> ] RT	Tin acetate complex obtained by evaporation of the precursor solution at RT and underwent heat treatment at 50, 100 and 300 °C.
[Sn(OH) <sub>n</sub> (OAc) <sub>m</sub> ] 50C	
[Sn(OH) <sub>n</sub> (OAc) <sub>m</sub> ] 100C	
[Sn(OH) <sub>n</sub> (OAc) <sub>m</sub> ] 300C	
SnO <sub>2</sub> Ac(IV)	Tin dioxide synthesized from tin (IV) acetate complex (Sigma Aldrich). Calcinated at 300 °C.
SnO <sub>2</sub> Aldr	Tin (IV) oxide nanopowder (≤ 100 nm), Aldrich, p/n 549657.
SnO <sub>2</sub> Aldr-Pd	Pd-doped tin (IV) oxide nanopowder, Aldrich, p/n 549657.
SnO <sub>2</sub> -Pd	Catalyst doped SnO <sub>2</sub> , synthesized from metallic tin. The catalyst to SnO <sub>2</sub> ratio is 1 w. % for all materials with one noble metal deposited. For those containing two noble metals the calculated ratio is as follows: SnO <sub>2</sub> /Met <sub>1</sub> /Met <sub>2</sub> =98/1/1. All materials were calcinated at 300 °C.
SnO <sub>2</sub> -Pt	
SnO <sub>2</sub> -Rh	
SnO <sub>2</sub> -Pd/Pt	
SnO <sub>2</sub> -Pd/Rh	
SnO <sub>2</sub> -Pt/Rh	
SnO <sub>2</sub> -Sc <sub>2</sub> O <sub>3</sub>	Presumably two-phase oxide systems consisted of either pure oxides, or SnO <sub>2</sub> and A <sub>2</sub> Sn <sub>2</sub> O <sub>7</sub> . The guest phase content is 2 w. %. The precursor – tin acetate complex, synthesized from metallic tin. Calcinated at 300 °C.
SnO <sub>2</sub> -Y <sub>2</sub> O <sub>3</sub>	
SnO <sub>2</sub> -La <sub>2</sub> O <sub>3</sub>	
SnO <sub>2</sub> -TiO <sub>2</sub>	Presumably solid solutions of titania, zirconia and hafnia in tin dioxide. The content of the dissolved oxides is <i>ca.</i> 2 w. %. The precursor – tin acetate complex, synthesized from metallic tin. Calcinated at 300 °C.
SnO <sub>2</sub> -ZrO <sub>2</sub>	
SnO <sub>2</sub> -HfO <sub>2</sub>	
SnO <sub>2</sub> -PdO	Tin dioxide synthesized from metallic tin and doped with various impurities in the quantity of 0.03 w. %. Calcinated at 300 °C.
SnO <sub>2</sub> -Cl	
SnO <sub>2</sub> -S	
SnO <sub>2</sub> -NaCl	

### **3.2. Material characterization**

This chapter is divided into two parts describing separately conventional or *ex situ* analytical methods and *in situ* ones. Description of some techniques, performed outside the Scientific Resources Service at URV, contain information about the institutions where the analysis was carried out. Where the place is not specified the analysis was realized at URV in Scientific Resources Service.

The description of *in-situ* techniques is opened by short overview and definitions of the technique in comparison with operando methods.

### 3.2.1. *Ex-situ* techniques

All synthesized materials were analyzed by means of following *ex-situ* techniques: TEM, XRD, FTIR and UV-Vis. These techniques are given separately from the other ones, performed for the selected materials only. If method was used to estimate a certain parameter requiring data processing (*e.g.* crystallite size or optic band gap) the calculation procedure is also given in this case.

#### 3.2.1.1. Transmission electron microscopy

Jeol JEM 1011 microscope operating at 100 kV (tungsten cathode) was used to estimate the particle morphology. The sample preparation was as follows. A specimen of the solid was dispersed in absolute ethanol (Sigma-Aldrich, p/n 24194) using ultrasound bath. Then, a drop of the suspension was deposited on copper grid for TEM analysis and left for 20-30 min in air at RT to evaporate the solvent. Afterwards, the support is placed into the holder and inserted into the TEM chamber.

#### 3.2.1.2. XRD and crystallite size calculations

X-ray diffraction patterns were recorded using Siemens D5000 diffractometer. The experimental parameters were as follows: Bragg-Brentano parafocusing geometry, vertical  $\theta$ - $\theta$  goniometer, Ni-filtered Cu<sub>k $\alpha$</sub>  radiation (30 mA, 40 kV), the angular  $2\theta$  diffraction range was between 20 and 96°, constant step size of aprox. 0.02° and 0.4 s per step (*i.e.* ~25 min per pattern).

The majority of the diffractograms were recorded using aluminium sample holder filled with as received powders. Some of the measurements were performed using Pt ribbon as a sample holder. In this case the powder to be analyzed was mixed with ethanol and the mixture was deposited evenly on the Pt ribbon.

To calculate mean crystallite size of the polycrystalline phase X-ray diffractograms were analyzed using TOPAS 3.1 program [143]. A pseudo-Voigth function was used to fit the diffraction pattern. The instrumental contribution to the peak width was obtained from a sample of LaB<sub>6</sub>, supplied by NIST (SRM 676b). The LaB<sub>6</sub> pattern was analyzed with the same software by fitting a pseudo-Voigth function. The calculated parameters for LaB<sub>6</sub> were maintained constant for SnO<sub>2</sub> samples. It was assumed for all samples that only crystallite size affects the XRD peak broadening and no effects of microstrains were observed in the XRD line width. For each pattern we fitted following parameters: the zero-shift, a 2-degree Chebyshev polynomial as

a background and cell parameters for SnO<sub>2</sub> (Cassiterite, P4<sub>2</sub>/mm, a=b= 4.73820 Å, c= 3.18710 Å).

Crystallite size was calculated from the integral breadth,  $\beta_i$ , according to the Scherrer's equation [144]:

$$\beta_i = \lambda / D \cos \theta \quad (3-1)$$

where  $\lambda$  is the wavelength,  $D$  is the crystallite size and  $\theta$  is the Bragg angle. In our case, all reflections of SnO<sub>2</sub> contributed to the crystallite size calculation in such a way that the obtained crystallite size represents the mean for the whole sample, assuming that crystallites are ideal spheres. The software TOPAS 3.1 was used in the so-called "launch mode", which permits the fitting of a number of diffractograms in a sequential way.

### 3.2.1.3. FTIR spectroscopy

FTIR spectra were recorded using JASCO 680 Plus spectrometer. The sample in a quantity of 0.0060(5) g was mixed with 0.300 (5) g of KBr powder (Sigma, IR grade) and then grinded in the agate mortar with a pestle for 2 min. The resulting powder was pressed into self-supporting disks (at pressure *ca.* 10 tons) and then used for the measurements. To record the background spectrum the self-supporting disk of blank KBr is used. The spectra acquisition was performed in the absorption mode with 32 scan times and resolution 2 cm<sup>-1</sup>. All measurements were carried out at RT and in air.

### 3.2.1.4. UV-VIS spectroscopy

This technique is widely used to study energy absorption by the solid semiconductor due to the direct electron transition from valence to conduction band. As it is commonly accepted the energy of the adsorption edge is represents the band gap width of the fine particle or cluster and therefore can be found from the UV-VIS spectra [145]. The band gap width was calculated using the method described in [146].

UV-VIS spectra were recorded using a Perkin Elmer Lambda 650S spectrometer which was fitted with a Praying Mantis diffuse reflectance (DR) accessory (Harrick). All spectra were recorded over 200-800 nm wavelength range using MgO as reference material.

The obtained DR spectra were processed by Kubelka-Munk conversion (**Figure 9 a**) and then were plotted as  $[F(R) \cdot hv]^2$  vs  $hv$ , where  $F(R)$  is the Kubelka-Munk function and  $hv$  is the energy of the incident photon (**Figure 9 b**).

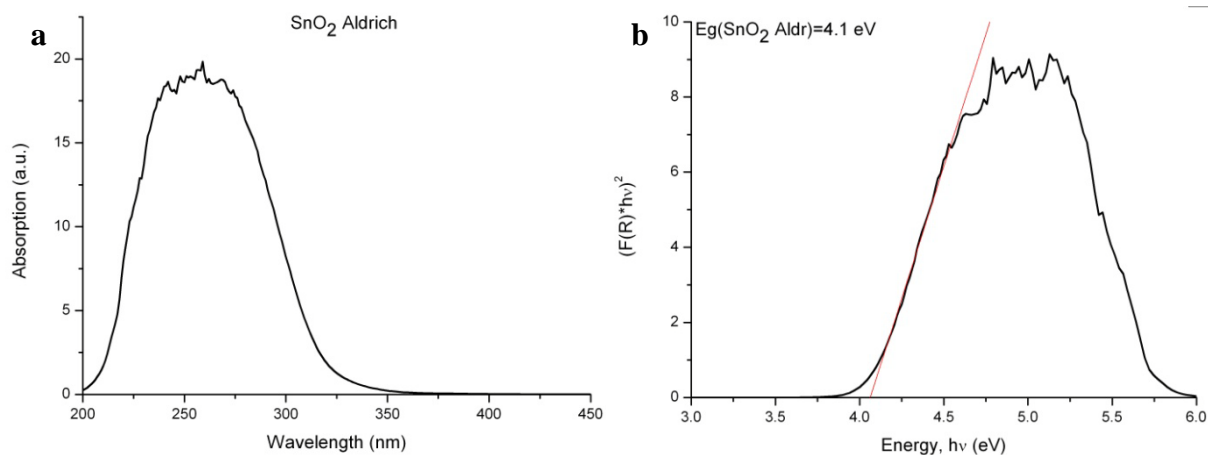


**Figure 9.** UV-Vis absorbance spectra of commercial SnO<sub>2</sub> (Aldrich) after Kubelka-Munk conversion (a) and least squares fit of a line through the low energy edge of the transformed spectrum (b).

These measurements were realized through EU Transnational Access Program at CenTACat Research Centre of the Queen's University (Belfast, UK) under the direction of Prof. C. Hardacre.

### 3.2.1.5. Other methods

High-Resolution Transmission Electron Microscopy (HRTEM) was carried out at 200 kV with a JEOL JEM 2100 instrument equipped with a LaB<sub>6</sub> source. The point-to-point resolution of the microscope was 0.20 nm. Samples were deposited on holey-carbon-coated Cu grids from alcohol suspensions. The analysis was realized at Institute of Energy Technology (Universitat Politècnica de Catalunya, Barcelona, Spain) by Prof. J. Llorca.

X-ray photoelectron spectroscopy (XPS) measurements were performed on a VG ESCALAB 200R spectrometer. The instrument was equipped with a hemispherical electron analyzer and an Mg K $\alpha$  X-ray source (1253.6 eV, 1 eV = 1.6022  $\times 10^{-19}$  J). The samples were mounted on a sample rod placed in the pretreatment chamber and evacuated at room temperature prior to being moved to the analysis chamber. The pressure in the ion-pumped analysis chamber was below 3  $\times 10^{-9}$  mbar during data acquisition. The energy regions of the photoelectrons of interest were scanned at 20 eV spectrometer pass energy. The Sn3d<sub>5/2</sub>, O 1s and Pd3d<sub>5/2</sub> core level spectra were recorded. The intensities were estimated by calculating the integral of each peak after subtraction of the "S-shaped" background and fitting the experimental curve to a combination of Lorentzian and Gaussian lines of variable proportions. All binding energies (BE) were referenced to the C 1s signal at 284.6 eV from carbon contamination of the samples to correct the charging effects. Quantification of the atomic fractions on the sample surface was

obtained by integration of the peaks with appropriate corrections for sensitivity factors [147]. The analyses were carried out at Instituto de Catálisis y Petroleoquímica, Consejo Superior de Investigaciones Científicas (Madrid, Spain) by Dr. J. L. Garcia Fierro with the help of Dr. C. Álvarez.

BET surface area was calculated from N<sub>2</sub> adsorption-desorption isotherms. The physisorption was performed on Micromeritics ASAP 2000 surface analyzer at 77 K. Before analysis, all the samples were degassed in vacuum at 393 K for 6 h. The analysis was realized at Chemical Engineering Department of the URV by N. Barrabés.

The impurity as well as catalyst content was measured by laser-spark mass-spectrometry using EMAL-2 instrument at N.S. Kurnakov Institute of General and Inorganic Chemistry of Russian Academy of Science (Moscow), under the direction of Prof. V.G. Sevastyanov.

### 3.2.2. *In-situ* techniques

The “*in situ*” techniques emerged relatively recently in heterogeneous catalysis aiming to enlighten and resolve contradictions between conflicting models deduced from *ex situ* analysis of the catalysts. The main idea of the *in situ* experiment is to study the catalyst controlling either gas composition, pressure or temperature.

Another powerful technique, widely applied in catalysis to study material under conditions close to the real industrial ones, is *operando* technique. The key difference between *in situ* and *operando* techniques is that *in situ* analysis is not time-resolved method regarding formation of reaction products during catalytic reaction [148, 149]. Accordingly, the two keystones of *operando* analysis are time and reaction. Taking this into account, electric characterization of sensing materials also should be considered as the simplest case of *operando* analysis since monitoring of electric properties usually occurs in real time and together with catalytic reaction. Combining the electrical measurements with spectroscopic characterization of the sensing material or/and analysis of the exhaust gases is known to be powerful *operando* approach to study sensing mechanisms [128]. Barsan *et al.* were the first who employed DRIFT spectroscopy simultaneously with electrical measurements under *operando* conditions to investigate interaction between sensing materials and target gases (e.g. CO, CH<sub>4</sub> etc.) [112, 150-152]. Applying this approach authors not only proposed mechanisms for target gas detection but also were able to investigate in detail water vapour effect on detection mechanism.

In this work all applied methods can be defined as *in situ* ones. In spite of the fact that some of them were used to monitor catalytic reactions, they were not performed in the time-resolved mode. In contrary to the *operando* approach, we studied catalytic reaction trying to

reach equilibrium conditions as close as possible. Observing physicochemical properties under equilibrium conditions we were able to get more pronounced difference caused either by temperature, material or gas composition. Regarding the latter parameter the following idea also should be considered. In real life drastic change of the gas phase composition hardly occurs, whilst gradual, very slow, concentration rise is more natural. Accordingly, sensing characterization performed under equilibrium between gas phase and the solid can provide more reliable information about sensing mechanisms occurring in the real life.

Thus, bearing this in mind let us describe the *in situ* techniques applied for characterization of SnO<sub>2</sub> materials.

### 3.2.2.1. TGA/DSC analysis

To estimate the water desorption kinetics in a temperature range of 25-600 °C, the thermogravimetric analysis coupled with differential scanning calorimetry (TGA/DSC) was performed using SDT Q600 analyzer at IGIC RAS (Moscow, Russia). About 0.05 g of the sample was placed in a ceramic crucible where the specimen underwent weight stabilization at RT in a flow of dry argon. Weight loss of the samples was measured while heating at a constant rate of 10 °C min<sup>-1</sup>. The gravimetric and thermal sensitivity of the instrument were 10<sup>-7</sup> g and 0.001 °C, respectively.

This analysis was performed at N.S. Kurnakov Institute of General and Inorganic Chemistry of Russian Academy of Science (Moscow), under the direction of Prof. V.G. Sevastyanov.

### 3.2.2.2. MS-study of the catalytic activity: H<sub>2</sub> oxidation in air

The analysis of the catalytic activity was performed on experimental set-up equipped with gas mixing system, flow quartz reactor placed in to the oven and connected to the quadruple mass-spectrometer Pfeiffer Omnistar GSD 301. 25 mg of the sample is placed in the quartz reactor, comprised of quartz tube with sample holder made of quartz wool. The thermocouple is placed into the tube close to the catalyst bed and the tube is connected to the gas mixing system. Mass spectrometer is connected to the outlet of the reactor.

The experiments were aimed to study catalytic activity of the materials in hydrogen oxidation reaction as a function of temperature. We used 3100 ppm of hydrogen in synthetic air at flow rate 200 cm<sup>3</sup>min<sup>-1</sup> throughout all experiments. First, the sample underwent pre-treatment under specified conditions (gas and flow) at 450 °C for 5 h and then left at RT for 5 h. The MS was set to monitor hydrogen (mass 2) and water (mass 18 and 17) in the exhaust gases. Once the MS-signal had reached at RT the stabilization, the gas composition was measured successively at

100, 150, 200, 250, 300, 350, 400 and 450 °C. Each temperature was held for 90 min at continuous recording of MS-signal together with the actual temperature measured close to the catalyst bed.

The quartz reactor itself has some impact on the hydrogen oxidation reaction. Accordingly we performed blank experiment to exclude the effect of the reactor. Thermocouple and the same amount of the quartz wool were placed into the quartz tube and the reactor was connected to the gas mixing system with mass spectrometer. The blank experiments were performed under the same conditions as the conventional ones.

Catalytic activity study was realized through EU Transnational Access Program at CenTACat Research Centre of the Queen's University (Belfast, UK) under the direction of Prof. C. Hardacre.

### 3.2.2.3. TPR

Temperature programmed reduction (TPR) study was performed using a ThermoFinnigan TPD/R/O 1100 instrument equipped with a thermal conductivity detector. Before the TPR experiments, 0.10(±2) g of the sample was dried for 24 h in helium flow (20 ml/min) at 120 °C. After that, the reduction process in the reducing gas mixture flow (5% H<sub>2</sub> in argon, flow rate was equal to 20 ml/min) was started at room temperature and finished at 800° C at a heating rate of 10 °C/min. Hydrogen consumption was measured using thermal conductivity detector.

Similar experiment was carried out in the oxygen contained gas mixture: 0.1% H<sub>2</sub> in air.

These experiments were realized at Chemical Engineering Department of URV, under the direction of Prof. F. Medina and with the help of N. Barrabés.

### 3.2.2.4. DRIFT spectroscopy

Diffuse Reflectance Infrared Fourier Transform spectroscopy is a powerful technique to study reaction mechanisms in heterogeneous system. In this work DRIFTS experiments were performed separately from electrical measurements but under identical conditions (material, temperature, gas composition). *In situ* spectroscopic measurements were realized on Bruker Equinox 55 spectrometer, operating at a resolution of 2 cm<sup>-1</sup>. The samples (*ca.* 0.050 g) were placed into the DRIFTS cell reactor with an environmental high temperature chamber (suppl. by Thermo Fisher Scientific, Inc). The chamber was fitted with ZnSe windows and connected to a cylinder with synthetic air *via* stainless steel lines. Details describing the cell and DRIFTS chamber can be found elsewhere [153]. Spectra were collected in a single channel mode at room temperature (22 °C), 50, 100, 150, 200, 250, 300, 350 and 400 °C with 512 scans per spectrum. The temperature was measured by a thermocouple located in the catalyst bed.



Before the measurements, the samples were heated in a constant flow of the target gas at 400 °C for 10 h followed by 10 h at room temperature (RT). The spectra acquisition was performed 1 h after the system had reached the preset temperature. The following gas mixtures were used in the experiment: dry synthetic air, 2.1 vol. % of H<sub>2</sub>O in dry synthetic air, and 100 ppm of H<sub>2</sub> in dry synthetic air. Dry synthetic air, used for gas mixture preparation, contained less than 3 ppm of residual water vapor. High purity water in a saturator was used to prepare 2.1 vol.% H<sub>2</sub>O in synthetic air (*ca.* 80% RH at 22 °C). Flow rate for all gas mixtures was 200 cm<sup>3</sup> min<sup>-1</sup>. The outlet of the DRIFTS cell was connected to the quadruple mass spectrometer (Hiden HPR 20), in order to monitor the gas composition during experiments.

DRIFTS experiments were realized through EU Transnational Access Program at CenTACat Research Centre of the Queen's University (Belfast, UK) under the direction of Prof. C. Hardacre.

### 3.2.2.5. TXRD

Thermo X-ray diffraction is widely used method to study kinetics of the crystallite growth, aging and recrystallization as a function of time and temperature of the annealing. On the basis of the diffraction line broadening analysis, which comprises reflection fitting in the whole range of the diffraction pattern, one calculates mean crystallite size using the procedure given in section 3.2.1.2. The plots of mean crystallite size against temperature or time of the annealing are used to study the growth kinetics and estimate apparent activation energy of the growth processes [154].

In our experiments the technique was applied to study evolution of the crystallite size during isothermal annealing at 600, 700 and 800 °C. This study is of great interest for gas sensor application, since as it was shown earlier the most promising sensing properties were observed for very fine particles of 1-5 nm. The later are known to be unstable and tend to reduce the surface already at low temperatures. Thus, the analysis is aimed to provide us with information about thermal stability of the sensing systems in question.

XRD patterns were collected using Siemens D5000 diffractometer equipped with Anton-Paar HTK10 heating stage (Bragg-Brentano parafocusing geometry and vertical  $\theta$ - $\theta$  goniometer, Ni-filtered Cu<sub>K $\alpha$</sub>  radiation and Braun position sensitive detector). The angular  $2\theta$  diffraction range was between 20 and 96°, constant step size of aprox. 0.02° and 0.4 s/step.

Samples were mixed with a few drops of absolute ethanol and then deposited as a thin flat and even layer onto platinum ribbon used as a heater. Static air was used throughout all the measurements.

The measurements were performed under isothermal conditions: at 600, 700 or 800 °C. The first pattern was recorded at room temperature (30 °C) and was not used in the kinetic calculations, the second one – immediately after the preset temperature was reached with a heating rate of 10° per minute. The third and followings patterns were obtained at constant temperature with 30 minutes delay between each other. Overall 31 patterns were collected during 32 hours of isothermal heat treatment.

All the synthesized materials were studied at 700 °C, for the selected materials TXRD experiment was performed at 600 and 800 °C as well. The list of the materials with specified experiment temperature is shown in **Table 7**.

**Table 7.** Details of TXRD experiment.

Sample name	Experiment temperature, °C	Studied phenomena
SnO <sub>2</sub> Ac	600, 700, 800	Crystallite growth kinetics as a function of synthesis route
SnO <sub>2</sub> Ac-Pd	600, 700, 800	Crystallite growth kinetics as a function of catalyst and doping type
SnO <sub>2</sub> Ac-PdO	600, 700, 800	
SnO <sub>2</sub> Ac-Pt	700	
SnO <sub>2</sub> -Sc <sub>2</sub> O <sub>3</sub>	700	Crystallite growth kinetics as a function of bulk doping or second phase
SnO <sub>2</sub> -Y <sub>2</sub> O <sub>3</sub>	700	
SnO <sub>2</sub> -La <sub>2</sub> O <sub>3</sub>	700	
SnO <sub>2</sub> -TiO <sub>2</sub>	700	
SnO <sub>2</sub> -ZrO <sub>2</sub>	700	
SnO <sub>2</sub> -HfO <sub>2</sub>	700	
SnO <sub>2</sub> Ac-Cl	700	Crystallite growth kinetics as a function of impurity type
SnO <sub>2</sub> Ac-S	700	
SnO <sub>2</sub> Ac-NaCl	700	

### **3.3. Characterization of sensing properties**

This chapter starts with the section “Deposition of the sensing material”. Details about the substrate type and heat treatment procedure for deposited material can be found here. Calibration of the heater and description of the experimental set-up are given in the following sections. The final part of the chapter deals with methodology of the experiment performed to study sensing properties of synthesized materials. Information regarding experimental conditions (*e.g.* gas composition, heater temperature *etc*) can be found here.

### 3.3.1. Deposition of the sensing material

The characterization of the sensing properties of synthesized materials was performed on an Al<sub>2</sub>O<sub>3</sub> microsubstrate (2.0×0.4×0.2 mm) with gap platinum electrodes (the gap is ~300 μm, the area to be covered is *ca.* 0.4 mm<sup>2</sup>) and a platinum heater described in [155]. The microsubstrate assembled in TO-8 package (**Figure 10**).

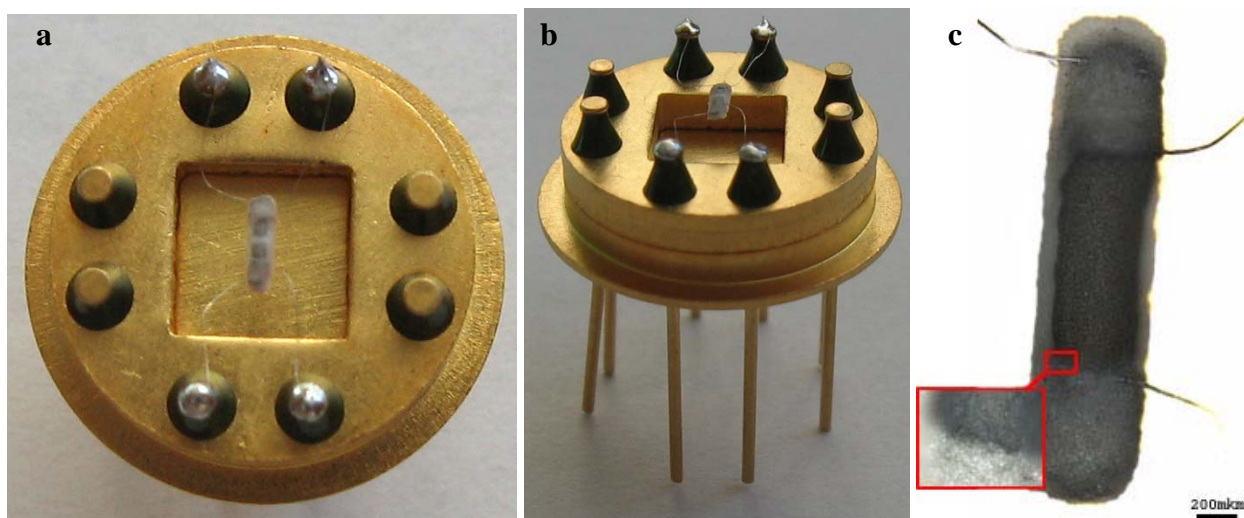


**Figure 10.** Top (a) and lateral (b) view of the microsubstrate mounted on TO-8 package; the microsubstrate with deposited sensing material (c).

The powders were prepared for deposition as follows. The material is mixed with 1,2-propanediol (Aldrich, p/n 540242) in a weight ratio 2.5:1 (resp.) and is grinded for 15 min to form printable ink. The latter was deposited on microsubstrates by drop deposition. The deposited ink was dried at 70 °C for 30 min, calcinated at 300 °C for 10 min, and annealed at 700 °C for 10 min. The freshly prepared sensors were stabilized in ambient air at 350 °C for 120 h.

### 3.3.2. Heater calibration

The heater calibration for microsubstrates was performed as follows. The chip together with thermocouple was placed in the oven and heater resistance was measured as a function of temperature. The plot of the temperature change ( $\Delta T$ ) against  $R_t/R_0$  (where  $R_t$  is a resistance at a certain temperature and  $R_0$  is the one at RT) is shown in **Figure 11**.

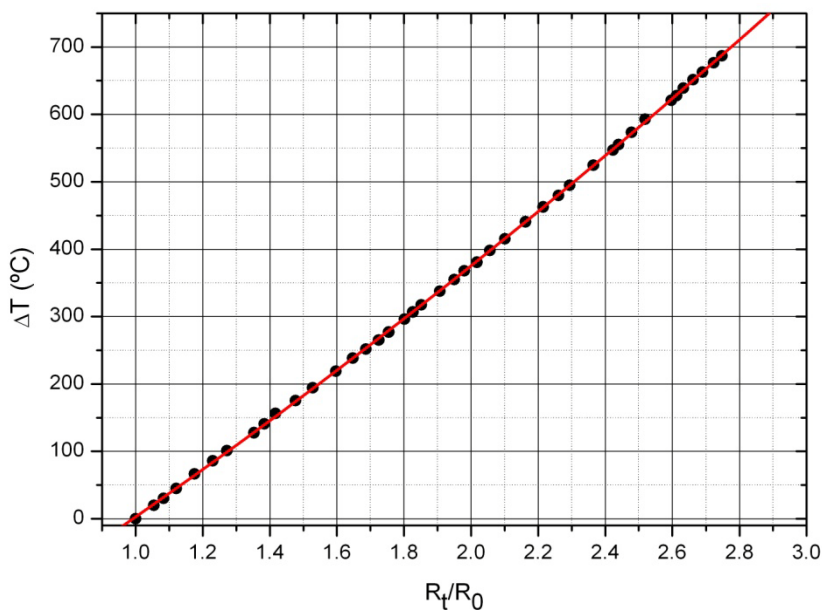


**Figure 11.** An example of calibration plots obtained for a microsubstrate.

### 3.3.3. Experimental set-up

All the experiments presented here and aimed to characterize the electrical properties of synthesized materials under controlled gas atmosphere were carried out at URV using experimental set-up schematically shown in **Figure 12**. The substrates with deposited materials were covered with a porous cap and fixed in the stainless steel chamber. The pins of the TO-8 package were connected by soldering to digital multimeter Agilent 34401A, and to Agilent 5751A instrument, used as a DC power supply for the platinum heater. Gas mixtures, including humidified gases, were prepared using Environics Series 4000 Computerized Gas Mixing System and Environics Series 4000 software, acting as user interface to the instrument. The humidity in the gas mixtures together with gas temperature was monitored by thermo hygrometer supplied by Practic NC (capacitive humidity sensor:  $\pm 2\%$  RH, the range – 0-99% RH). Stainless steel tubes (1/8 inch) were used to connect the gas mixing system and the sensor chamber.

Two initial gas mixtures were used in this study: dry synthetic air, with residual water and hydrocarbon impurity levels less than 3 ppm, and 20 ppm of hydrogen in synthetic air of the same impurity levels. Distilled water was used in the Environics saturator to prepare humidified mixtures at a constant temperature:  $25 \pm 1$  °C.

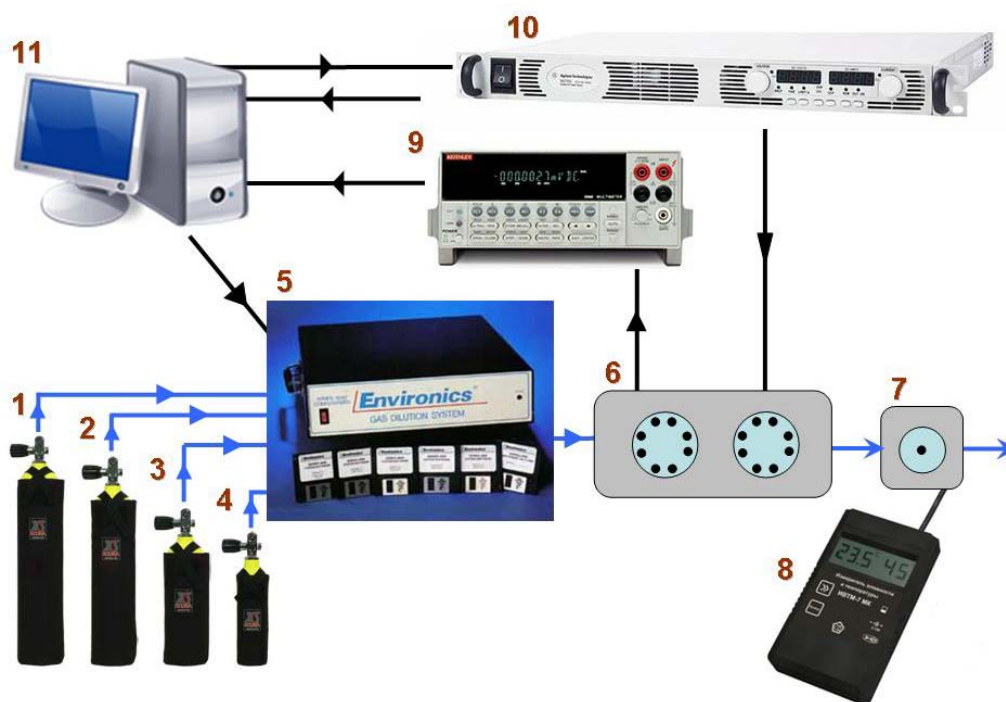


**Figure 12.** Experimental set-up for sensing properties characterization. 1-4 – gas cylinders, 5 – gas mixing system (Environics), 6 – stainless steel chamber with sensors, 7 – Teflon™ chamber with humidity and temperature sensor (Practic NC), 8 – portable unite for humidity and temperature measurements (Practic NC), 9 – digital multimeter (Agilent), 10 – power supply (Agilent), 11 – computer.

### 3.3.4. Methodology of the experiment

All the measurements presented herein were gained using the experimental set-up shown in **Figure 12** and microsubstrates shown in **Figure 10**. Let us start with the methodology of these measurements. The experiments were aimed to study sensing properties of synthesized materials as a function of temperature and analyte(s) concentration. Hydrogen, water and their mixture were used as principal analytes. The experiment in this case has 3 independent parameters influencing sensing properties of one material: temperature, hydrogen and water concentration. Accordingly, the measurements were performed in such a way to maintain gas composition constant and measure sensor signal as a function of temperature.

The experiment was performed as follows. After stabilization procedure in ambient air (350 °C for 120 h) sensors were placed in the chamber and underwent stabilization in the target atmosphere. This procedure comprised of 10 h at 350 °C and 3 h at RT (25 °C). The flow rate of the gas mixtures used throughout all experiments was 200 cm<sup>3</sup> min<sup>-1</sup>. The material resistance was recorded during increase of heater temperature from 25 up to 600 °C with a rate 10 °C min<sup>-1</sup>. After the temperature had reached 600 °C the heater voltage was switched off, data acquisition was stopped and the sensor was left at RT. Each measurement was performed three times with 2 h delay at RT between the measurements. Only second or third measurement was taken into account and was used for further calculations of the signal. Note once again that resistance measurements were carried out separately for each gas mixture. Accordingly, the results represent the resistance of the sensing layer as a function of heater temperature in a certain gas mixture (**Figure 13**).

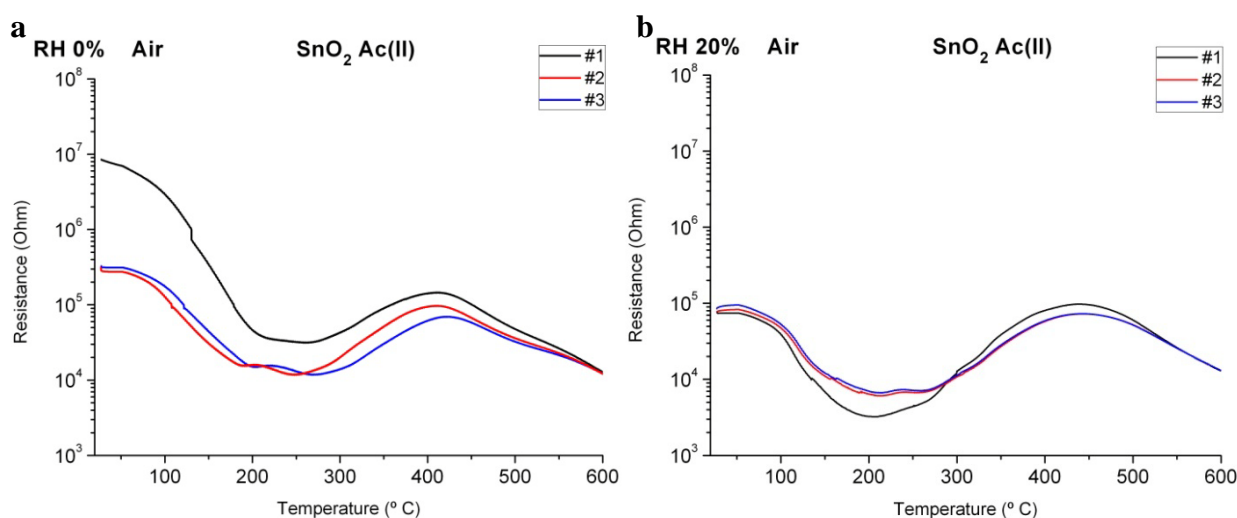


**Figure 13.** Plots of resistance vs heater temperature for blank SnO<sub>2</sub> in dry air (a) and in humid air (b). The legends denote the number of the successive measurements.

The digital multimeter Agilent 34401A used in the experiment was limited to measure resistance up to 100 MΩ, which was an obstacle to perform measurements for SnO<sub>2</sub>-Sc<sub>2</sub>O<sub>3</sub> in the whole temperature range in air and in the range of 50-450 °C in 20 ppm H<sub>2</sub>, irrespective of RH. It was experimentally proved that high electric resistance is due to the material and not due to the other factors related with deposition procedure, contacts *etc.* For this reason sensing properties of SnO<sub>2</sub>-Sc<sub>2</sub>O<sub>3</sub> will not be discussed in this study. This limitation also prevented us to measure sensing layer resistance in the low temperature region for some other materials (mainly catalyst doped). However, in this case the resistance values higher than 100 MΩ were observed only up to 150 °C in dry air.

Once the resistance had been measured in a certain gas mixture, the same procedure was repeated for another gas mixture, starting from stabilization in the target atmosphere (10 h at 350 °C and 3 h at RT). The list of the gas mixtures used to measure resistance as a function of temperature is shown in **Table 8**.

The obtained results were used to calculate sensor signal which was defined as resistance ratio:  $S = R_0(T) / R_g(T)$ , where  $R_0(T)$  is the resistance of the sensing layer in dry synthetic air or dry 20 ppm H<sub>2</sub> as a function of temperature and  $R_g(T)$  is the one obtained in humid air or in 20 ppm H<sub>2</sub> (either dry or humid). For example the sensor signal to 20% RH for SnO<sub>2</sub> Ac material was found by division data presented in **Figure 13a** by the ones shown in **Figure 13b**.

The method used here (*i.e.* resistance as a function of increasing at a certain rate temperature) differs of course from the one when the resistance is measured under isothermal conditions. To estimate the influence of the heating rate on resistance profile and evaluate the difference between isothermal conditions and dynamic ones we performed additional experiment.

**Table 8.** The gas mixtures used in the experiment.

№	Gas carrier	RH (%)	Gas composition
1.	Air	0	Dry synthetic air, with residual water and hydrocarbon impurity levels less than 3 ppm (gas carrier)
2.		20	6500 ppm H <sub>2</sub> O in air, which corresponds to 20 % RH <sup>3</sup> at 25 °C
3.		50	16100 ppm H <sub>2</sub> O in air
4.		80	25800 ppm in air

<sup>3</sup> For the sake of brevity the water concentration in the humidified mixtures will be expressed in percents of RH.



5.	20 ppm H <sub>2</sub> in air	0	20 ppm of hydrogen in air, with residual water and hydrocarbon impurity levels less than 3 ppm (gas carrier)
6.		20	6500 ppm H <sub>2</sub> O and 20 ppm H <sub>2</sub> in air
7.		50	16100 ppm H <sub>2</sub> O and 20 ppm H <sub>2</sub> in air
8.		80	25800 ppm H <sub>2</sub> O and 20 ppm H <sub>2</sub> in air

This experiment was performed for SnO<sub>2</sub> Ac in dry air and in dry 20 ppm H<sub>2</sub> in air. After the sensor stabilization in the target atmosphere the resistance was recorded at the following heating rates: 1, 5, 10 and 20 °C min<sup>-1</sup> (in the range 25-600 °C). Finally, the resistance was measured under isothermal conditions: at 300, 325, 350, 375 and 400 °C for 3 hours at each temperature. It was found that sensor signals obtained under isothermal conditions are *higher* and occur at *lower* temperature than that observed for ramp heating mode. In the case of heating rate 10 °C min<sup>-1</sup> the difference between signals amounted to 15% (in its highest value) and the one between the temperatures of the signal to 60(3) °C. The latter was taken into account when plotting sensor signal against temperature. Signal value was decided to remain unchanged.

Since sensor signal is known to be thermally activated process, the obtained results were used to estimate apparent activation energy of the change in the electric conductivity. This parameter was calculated from the Arrhenius plots of signal logarithm vs.  $1/kT$ , where  $k$  is the Boltzmann constant and  $T$  is temperature in Kelvin. An example of the plot is shown in **Figure 14**.

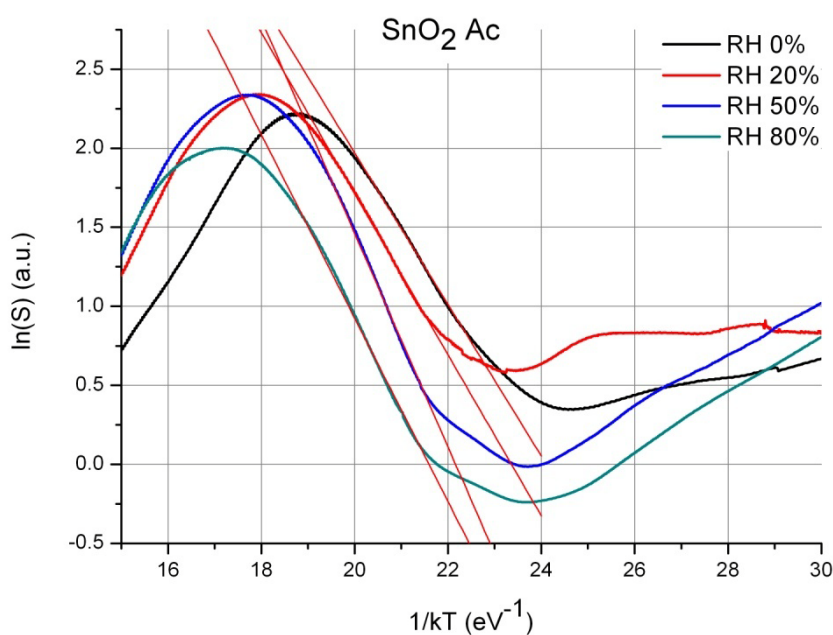


**Figure 14.** Arrhenius plot: sensor signal against  $1/kT$ .

The slope of the fitted lines corresponds to the apparent activation energy according to the well established relationship between sample resistance ( $R$ ), temperature ( $T$ ) and partial pressure of the gas to be absorbed ( $p$ ) [130, 156]. Taking into account that signal ( $S$ ) was defined as resistance ratio, the expression for the activation energy found will be as follows:

$$S = \frac{R_0}{R_{H_2}} = \frac{r_0^{O_2}}{r_0^{H_2}} \exp\left(\frac{E_{act}^{H_2} - E_{act}^{O_2}}{kT}\right) \frac{\sqrt[N]{p^{O_2}}}{M \sqrt[p]{p^{H_2}}} = A \exp\left(\frac{E_{act}}{kT}\right) B \quad (3-2)$$

where  $r_0$ ,  $N$ ,  $M$ , and partial pressures of the gases are constants within experiment (as well as resulting  $A$  and  $B$  parameters),  $E_{act}^{O_2}$  and  $E_{act}^{H_2}$  are the activation energies of the resistance change in air and in 20 ppm H<sub>2</sub> in air due to thermal activation of the charge carriers and adsorption/desorption processes (both oxygen and hydrogen),  $E_{act}$  is the activation energy related only with H<sub>2</sub> adsorption/desorption processes.

## 4. Results and discussion

This section is built up from five main chapters giving results and discussion for: SnO<sub>2</sub> synthesis from tin acetate complexes, *ex situ* and *in situ* characterization of the synthesized materials, sensing properties of the synthesized materials, and conclusion. Each of the mentioned chapter contains corresponding parts and summary. The most prominent results and conclusive remarks are given in the conclusion.

#### **4.1. Tin dioxide synthesis**

To our knowledge the synthesis of SnO<sub>2</sub> based colloids starting from metallic tin and acetic acid, followed by tin acetate hydrolysis in acetic acid, is proposed for the first time. Moreover, scarce information is available in the literature regarding synthesis of tin dioxide through hydrolysis of tin acetate solutions. But even if the authors report hydrolysis of tin acetate complex they usually use commercial tin(IV) acetate for the synthesis (see *e.g.* [89]), which is rather expensive compound (*ca.* 260 EUR per 10 g according to Sigma Aldrich price-list in 2008). High price of the precursor is mostly due to the fact that the acetate complexes are usually readily hydrolysed and laborious procedure is needed to separate the complex from the mother solution avoiding contact with moisture [157].

The advantage of the proposed method is that the stage of tin acetate separation is omitted and thus, moisture is not the obstacle in the synthesis since the precursor solution is stable in its presence. On the other hand water presence in the precursor solution (from ambient air) can notably change the precursor structure and we could not be aware whether tin(II) acetate is the product of the synthesis as it was suggested in [60] and [156], or rather hydrolyzed forms of tin(II) and/or tin(IV) acetates are present in the solution.

Accordingly, we performed comparative study of the synthesized precursor and commercial tin(IV) acetate complex (Aldrich p/n 345172) by means of FTIR spectroscopy. In addition, using commercial tin(IV) acetate we realized SnO<sub>2</sub> synthesis to compare the oxide properties with the one synthesized *via* original method. The results are given in the following parts.

#### 4.1.1. Tin (II) or tin (IV) acetate complexes?

##### 4.1.1.1. Physical properties

Colour and melting temperature are probably the most important properties which can help us in primary determination of the tin oxidation state in the complex. The mother solution as well as synthesized compound possess yellow colour. Donaldson *et al.* studying tin(II)-acetates indicated that colourless complexes turned yellowish after several months of the storage due to oxidation of tin(II) to tin(IV) [158]. However, in our experiments solutions of commercial tin(IV) acetate in acetic acid were colourless. This suggests that yellow colour does not indicate only the tin oxidation state but more probably the presence of water or OH groups in the composition. The formation of the latter seems to be accompanied by tin oxidation.

The authors found as well that when the interaction time between metallic tin and hot acetic acid is less than 80 hours (*e.g.* 50), the product is tin(II) acetate-2-acetic acid, otherwise tin(II) acetate is formed. In our case the interaction lasted 20 hours.

The melting temperature of tin(II) and tin(IV) acetates is known to be *ca.* 180 and 253 °C (see **Table 1**). However, the synthesized compound decomposes without melting at *ca.* 300 °C to give tin(IV) oxide (XRD data will be given later). This feature is similar to the properties of Sn(CH<sub>3</sub>COO)<sub>2</sub>·2CH<sub>3</sub>COOH: decomposition in oxygen free atmosphere without melting at 295 °C, giving SnO<sub>2</sub> [158].

Thus, the preliminary analysis shows that the synthesized complex is neither tin(II) nor tin(IV) acetate. The physical properties of the synthesized material very resemble the ones of Sn(CH<sub>3</sub>COO)<sub>2</sub>·2CH<sub>3</sub>COOH. Most probably the compound is formed through tin(II) acetate-2-acetic acid, however, contains metal atom in the highest oxidation state. Water traces in the system apparently provoke tin oxidation and bring about incorporation of OH groups into the coordination sphere of the complex.

##### 4.1.1.2. FTIR and XRD study

Both tin(II) and tin(IV) acetates have bidentate chelating type of coordination. The coordination numbers for the solids are 6 and 8 resp., which corresponds to the trigonal bipyramid with lone electron pair in the case of tin(II) acetate and dodecahedral geometry of the molecule in the case of tin(IV) acetate. However, the geometrical structures of the molecules are known to be distorted due to the sterical activity of the lone pair in the Sn(CH<sub>3</sub>COO)<sub>2</sub> and coordination overcrowding in the Sn(CH<sub>3</sub>COO)<sub>4</sub> [58, 64, 159].

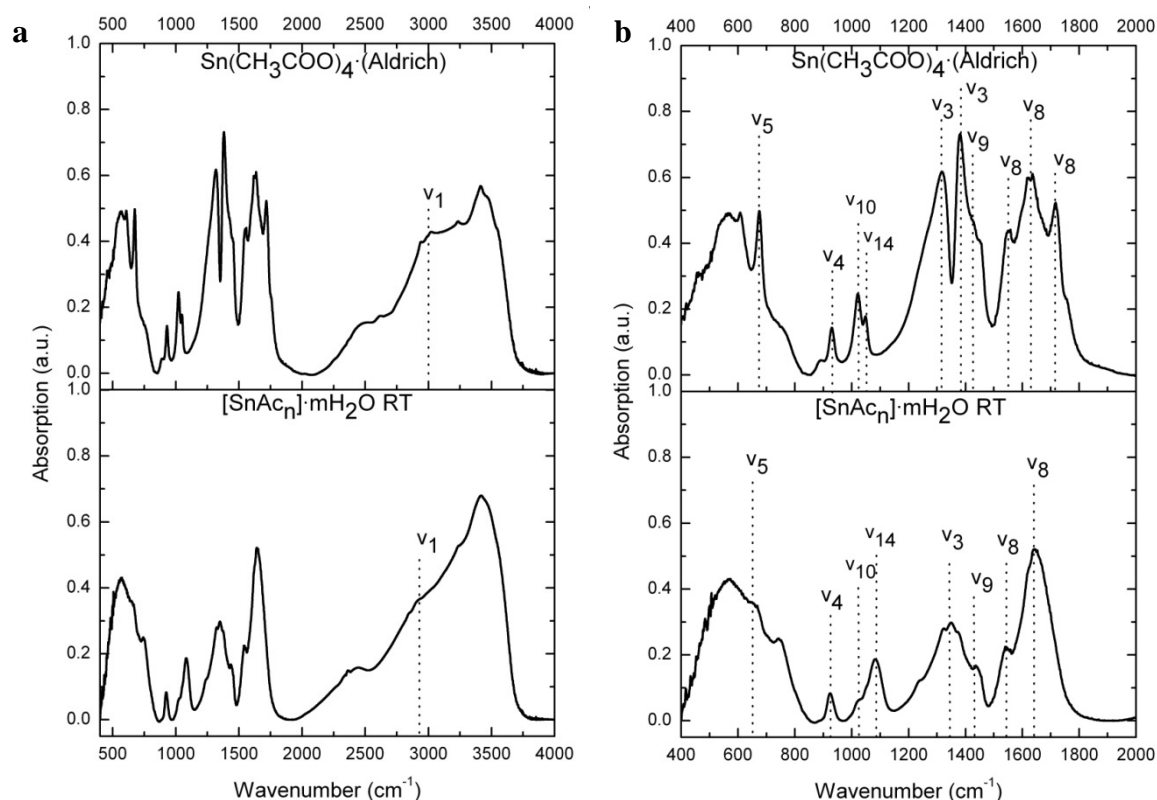


**Figure 15.** FTIR spectra of the synthesized tin acetate complex and commercial tin tetraacetate in the range of 400-4000  $\text{cm}^{-1}$  (a) and 400-2000  $\text{cm}^{-1}$  (b).

The coordination type of the complexes can be estimated to some extent from IR spectroscopy. As it was shown in [160], the coordination of the acetate ion can be derived from the position of C-O frequencies, which are available in the literature for both complexes [64, 160].

**Figure 15a** shows FTIR spectra of tin acetate complexes obtained by acetic acid evaporation at RT from the mother solution ( $[\text{Sn}(\text{Ac})_n] \cdot m\text{H}_2\text{O}$  RT) and the one of commercial tin tetraacetate ( $[\text{SnAc}_4]$  RT). The found peak positions and their comparison with the literature data for tin(II) and tin(IV) acetates are summarized in **Table 9**.

Position of the peaks corresponding to  $\nu_3$  and  $\nu_8$  can be used to distinguish unidentate and bidentate acetates in the complex [160]. Unidentate ligands demonstrate  $\nu_3$  and  $\nu_8$  at lower and higher wavenumbers (resp.) in comparison with bidentate ligands. Therefore, in the case of commercial tin tetraacetate complex the nature of the  $\nu_8$  vibration with the prominent peaks at 1717, 1636 and 1553  $\text{cm}^{-1}$  can be explained either by the presence of two types of the ligands or by asymmetric chelating acetate, where two Sn-O distances are very different. The latter seems more probable and occurs in the case of overcrowded coordination sphere where there is not enough space for 4 acetate ligands [160].

**Table 9.** Comparison of peak positions (in cm<sup>-1</sup>) in the IR spectra of Sn(Ac)<sub>2</sub>, Sn(Ac)<sub>4</sub> reported in the literature, and Sn(Ac)<sub>4</sub>, [SnAc<sub>n</sub>]<sub>m</sub>H<sub>2</sub>O RT found in this work.

Group	Notation	Assignment	Sn(Ac) <sub>2</sub> , Ref. [64]	Sn(Ac) <sub>4</sub> , Ref. [160]	Sn(Ac) <sub>4</sub> , this work	[Sn(Ac) <sub>n</sub> ] <sub>m</sub> H <sub>2</sub> O RT, this work
CH <sub>3</sub>	v <sub>1</sub> and v <sub>7</sub>	sym. and asym str.		3000, 2955	3023, 2942	2950-2925
	v <sub>9</sub>	def.		1430-1440	1430	1436
	v <sub>10</sub>	rock	1015	1009 <sup>4</sup>	1022	1026
	v <sub>14</sub>	rock		1045	1048	1082
C-O	v <sub>3</sub>	sym. str.	1395	1400, 1315	1381, 1317	1373, 1324
	v <sub>8</sub>	asym. str.	1530	1635, 1575	1636	1640
C-C	v <sub>4</sub>	str.	930	970, 922	930	924
CO <sub>2</sub>	v <sub>5</sub>	sym. def.	661	652, 630	675	640-670

The case of the synthesized complex is very different. The intensity of v<sub>3</sub> is remarkably lower than that of v<sub>8</sub> which indicates that asymmetrical chelating in the complex is higher than in tetraacetate. This means that acetate ligand is bonded to the tin atom through very different Sn-O-C bonds: one with oxygen close to the tin atom, and another one with oxygen close to the carbon atom.

**Figure 16** shows FTIR spectra of the synthesized complex after heat treatment at various temperatures. Heating in ambient air for 20 h at 50 and 100 °C brings about intensity decrease of the vibrations corresponded to the organic ligands, which means complex decomposition. At 300 °C the complex is decomposed. The band between 1600 and 1670 cm<sup>-1</sup> can be assigned either to the presence of the organic fragments or molecular water in the material, the deformation mode of the latter is known to occur between 1500-1650 cm<sup>-1</sup> [107]. Complex in its nature, the band consists of at least four well pronounced peaks at 1616, 1635, 1646, 1653 cm<sup>-1</sup> (not shown). These can be acetate fragments coordinated as unidentate and bidentate ligands (v<sub>8</sub> vibration). On the other hand coordination of molecular water should not be discarded, since molecular water is known to be rather strong ligand.

<sup>4</sup> Estimated from the spectra of CH<sub>3</sub>COONa

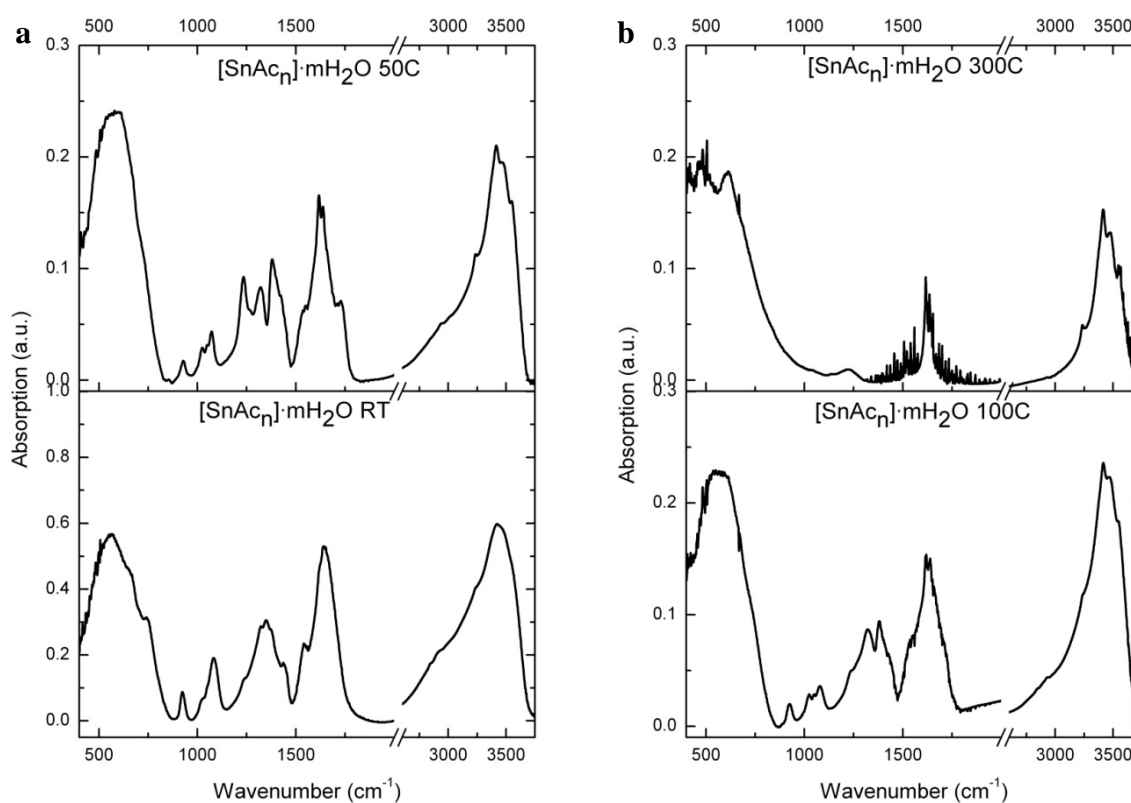


**Figure 16.** FTIR spectra of the synthesized complex after heat treatment at 50, 100 and 300 °C for 20 h at each temperature.

XRD analysis revealed that already at 100 °C the complex decomposes to give tin dioxide with cassiterite structure. The diffraction bands are very broad with remarkable amorphous halo. The mean crystallite size of the oxide amounts to 0.89(4) nm.

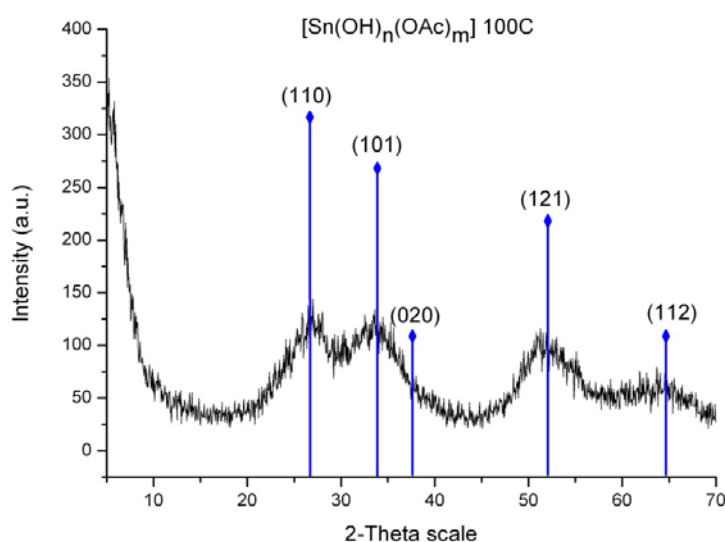


**Figure 17.** XRD diffractograms of the complex after heat treatment at 100 °C for 20 h.



The above considerations suggest that synthesized complex is tin(IV) acetate with partially substituted acetate ligands by bridging hydroxyls ones. Indeed, hydroxides are good bridging ligands and this explains low temperature formation of the tin(IV) oxide [58]. Probably the complex has second coordination sphere with molecular water, which enables facile substitution of acetate ligands with hydroxyl groups at elevated temperatures. One of the possible molecular structures of tin(IV) hydroxide acetate is shown in **Figure 18b**.

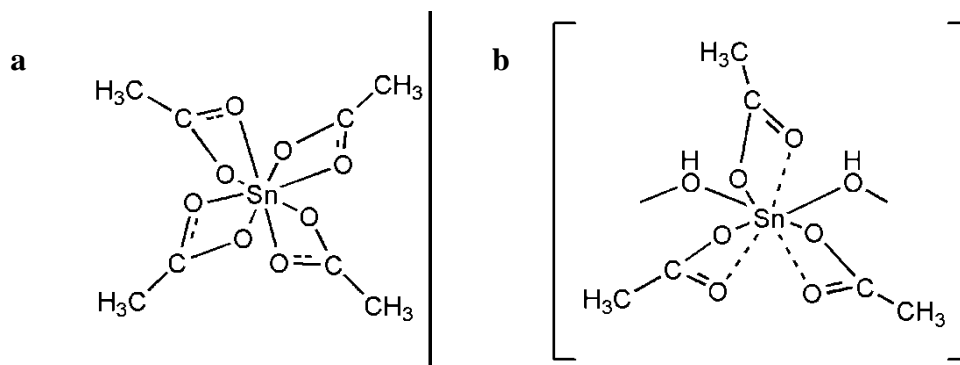


**Figure 18.** Molecular structure of tin tetraacetate (a) and supposed structure of the synthesized complex (b).

#### 4.1.2. Comparison of synthesized materials

SnO<sub>2</sub> Ac and SnO<sub>2</sub> Ac (IV), synthesized from the complexes [Sn(OH)<sub>n</sub>Ac<sub>m</sub>] and Sn(Ac)<sub>4</sub>, resp., represent slightly yellowish white powders. TEM analysis revealed that mean particle size of SnO<sub>2</sub> Ac is in the range of 2-5 nm, whilst that of SnO<sub>2</sub> Ac (IV) is 4-10 nm (**Figure 19**). Both materials are quite agglomerated, however SnO<sub>2</sub> Ac seems more porous in comparison with SnO<sub>2</sub> Ac (IV).

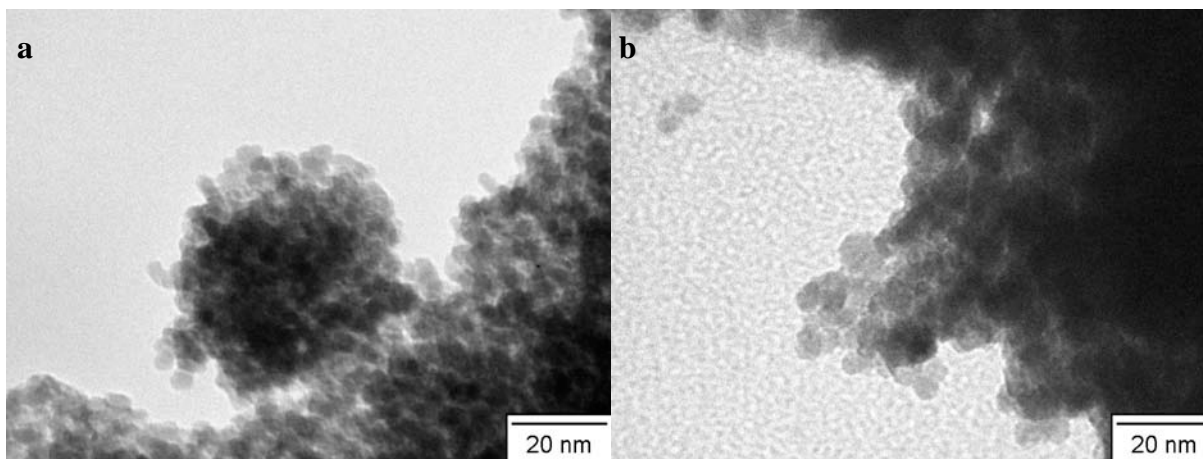


**Figure 19.** TEM images of SnO<sub>2</sub> Ac (a) and SnO<sub>2</sub> Ac (IV) (b).

Precipitation from both precursors results in formation of tin dioxide phase crystallized in cassiterite structure (**Figure 20a**). Again, the difference between two materials is mainly related with the mean crystallite size: 1.69(11) and 2.21(5) for SnO<sub>2</sub> Ac and SnO<sub>2</sub> Ac (IV), resp.

Using XPS technique it was found out that surface tin atoms of both oxides are in the highest oxidation state with a binding energy for Sn3d<sub>5/2</sub> core level of 486.7 eV (**Figure 20b**). Surface atomic ratio *O/Sn* was found 2.52 for SnO<sub>2</sub> Ac and 2.12 for SnO<sub>2</sub> Ac (IV). Since the obtained ratio for both materials is higher than the stoichiometric one (*O/Sn* = 2), we can conclude that tin dioxide synthesized from tin hydroxide acetate comprises more oxygen contained species on the surface in comparison with SnO<sub>2</sub> Ac (IV).

The fact that *O/Sn* ratio is higher for SnO<sub>2</sub> Ac also supports the assumption of higher hydroxylation degree of this material if we take into account that O1s XPS spectra (**Figure 21**), used for calculation *O/Sn* ratio, evidence the presence of two different oxygen species with a binding energy *ca.* 530 and 532.3 eV. The values correspond to the lattice oxygen and oxygen from hydroxyl groups, resp. Therefore the *O/Sn* ratio should be written as (*O<sub>OH</sub>* + *O<sub>lat</sub>*)/*Sn*, where *O<sub>OH</sub>* is the surface hydroxyl concentration, *O<sub>lat</sub>* is the one of lattice oxygen, *Sn* is the

concentration of surface tin atoms. The intensity ratio of the corresponding bands reveals that SnO<sub>2</sub> Ac contains more OH groups than SnO<sub>2</sub> Ac (IV) by a factor of 1.2 (0.33 against 0.27).

**Table 10.** Comparison of XPS results

Material	$(O_{OH}+O_{lat})/Sn$	$O_{OH}/O_{lat}$
SnO <sub>2</sub> Ac	2.52	0.33
SnO <sub>2</sub> Ac (IV)	2.12	0.27

The found overall oxygen-to-tin and hydroxyl-to-lattice oxygen ratios are given in **Table 10**. Using the obtained results we can compare the formation of oxygen vacancies in the case of two materials. Let us write down the overall oxygen-to-tin ratio for both materials in the following way:

$$\left( \frac{O_{OH} + O_{lat}}{Sn} \right)_{SnO_2Ac} = 2.52 \quad (4-1)$$

$$\left( \frac{O_{OH} + O_{lat}}{Sn} \right)_{SnO_2Ac(IV)} = 2.12 \quad (4-2)$$

If we divide the both parts of equations by concentration of lattice oxygen  $O_{lat}$ , and substitute the resulting ratio ( $O_{OH}/O_{lat}$ ) by the corresponding values from **Table 20**, we obtain the following ratios:

$$\left( \frac{Sn}{O_{lat}} \right)_{SnO_2Ac} = 0.53 \quad (4-3)$$

$$\left( \frac{Sn}{O_{lat}} \right)_{SnO_2Ac(IV)} = 0.60 \quad (4-4)$$

The results indicate that either the content of lattice oxygen is slightly higher or that of surface tin atoms is slightly lower (by a factor of 1.13) in the case of SnO<sub>2</sub> Ac compared with SnO<sub>2</sub> Ac (IV). This means that hydrolysis of tin tetraacetate complex gives oxide material with slightly higher concentration of surface oxygen vacancies and lower concentration of surface hydroxyls.

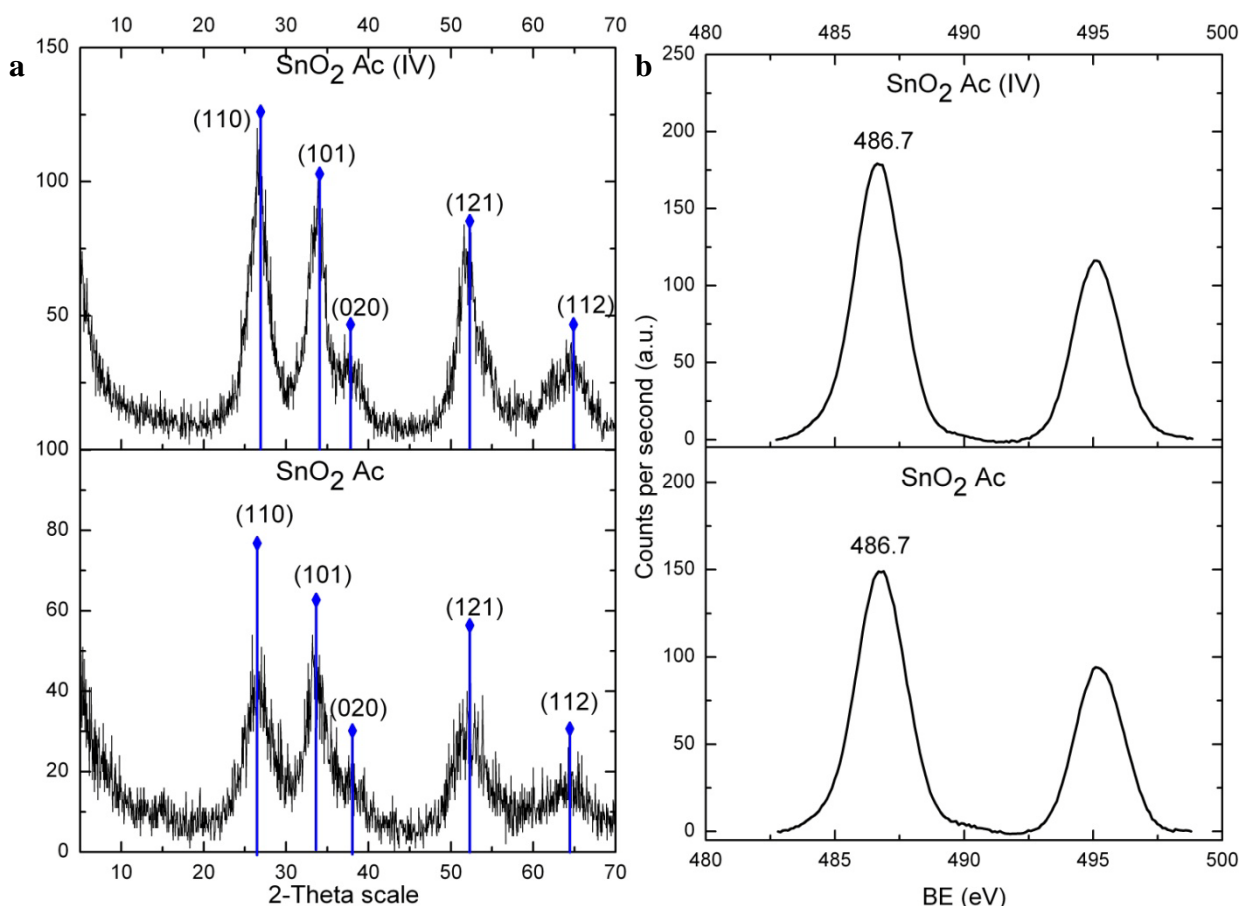


**Figure 20.** XRD diffractograms (a) and XPS spectra (b) of SnO<sub>2</sub> synthesized from tin hydroxide acetate and tin tetraacetate (Aldrich).

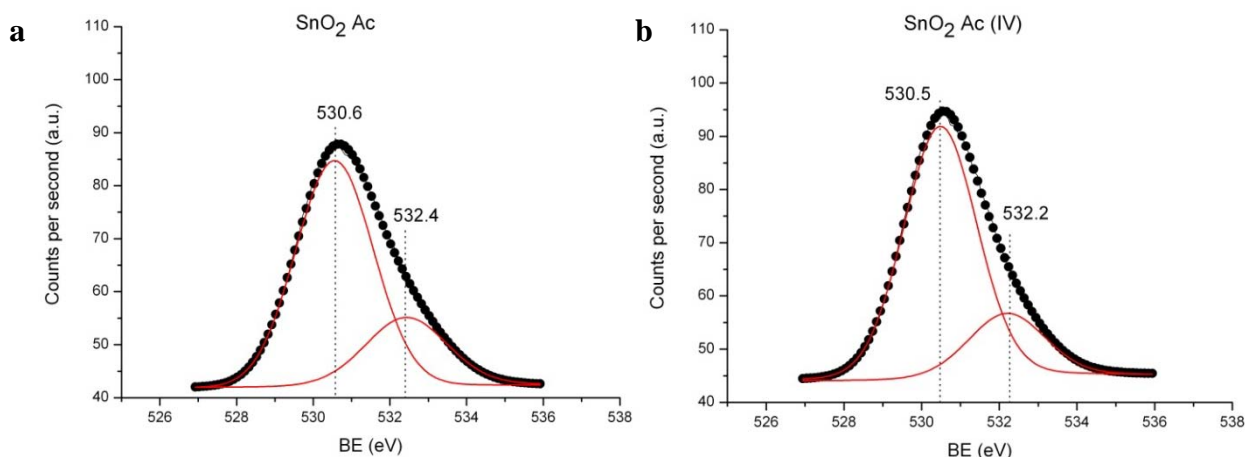


**Figure 21.** XPS spectra of SnO<sub>2</sub> synthesized from tin hydroxide acetate and tin tetraacetate (Aldrich).

FTIR spectra of the materials demonstrate vibrations of hydroxyl groups, Sn-O vibrations and molecular water, which deformation mode is usually observed between 1500 and 1650 cm<sup>-1</sup> (**Figure 22a**). The main difference between two spectra is related with hydroxyl groups. The

band positions and their maxima indicate that both materials contain bridging OH groups with slightly different nature. Among the OH groups of SnO<sub>2</sub> Ac (IV) one can distinguish two fractions with slightly different acidity at 3378 and 3434 cm<sup>-1</sup> [106]. Spectrum of SnO<sub>2</sub> Ac does not demonstrate such heterogeneity in the acidity of the bridging hydroxyls. In the rest the positions of the characteristic bands for two materials are quite similar.

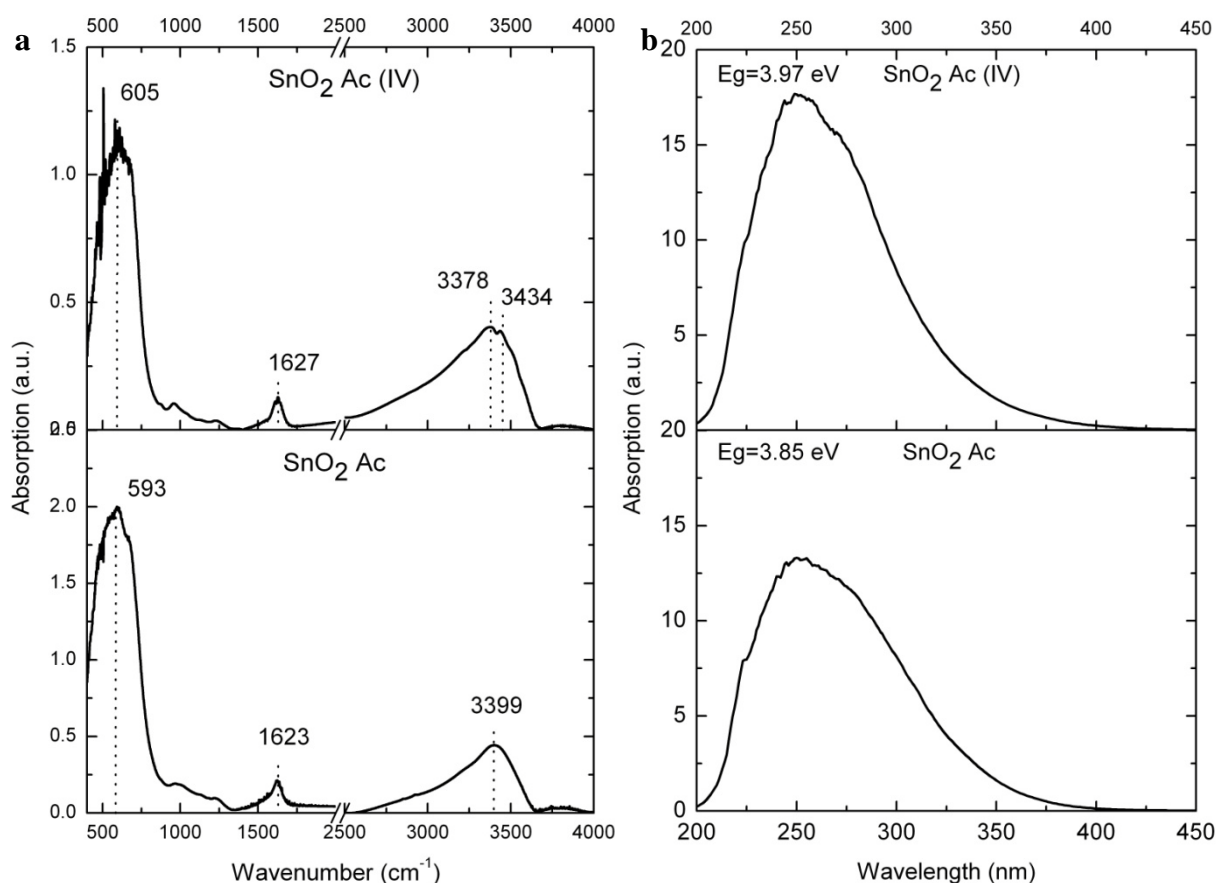


**Figure 22.** FTIR (a) and UV-VIS (b) spectra of SnO<sub>2</sub> synthesized from tin hydroxide acetate and tin tetraacetate (Aldrich)

The normalized intensities of the  $\nu_{OH}$  and  $\nu_{SnO}$  bands differ to higher degree than their positions. From the comparison of intensity ratio  $I_{OH}/I_{SnO}$  it becomes clear that SnO<sub>2</sub> Ac contains hydroxyl groups almost two times as much as SnO<sub>2</sub> Ac (IV): 0.36 against 0.21. This remarkably exceeds the results obtained by XPS analysis, where  $O_{OH}/O_{lat}$  ratio was found higher for SnO<sub>2</sub> Ac only by a factor of 1.2.

DR UV-VIS spectra of both materials represent broad absorption with maximum at the same wavelength: around 250 nm (**Figure 22b**). The absorption in this region corresponds to the charge-transfer process between valence band formed by oxygen ligands (2p orbitals) and conduction band formed by Sn<sup>4+</sup> (5s orbitals) [161]. The major contribution to this process is

believed to originate from surface ions [145]. The intensity of the band is higher for SnO<sub>2</sub> Ac (IV) suggesting that concentration of chromophore groups related with this specific charge transfer-process is higher in respect to SnO<sub>2</sub> Ac. Both materials demonstrate remarkable absorbance in the low-energy region 280-400 nm which indicates availability of donor levels located within forbidden band. This becomes more evident after comparison of the spectra with that of SnO<sub>2</sub> Aldrich (not shown). The later shows symmetric absorption band with low-energy shoulder extended to *ca.* 350 nm.

The optic band gap width calculated from the spectra (edge energy) was found 3.85 and 3.97 eV for SnO<sub>2</sub> Ac and SnO<sub>2</sub> Ac(IV), resp. The values are clearly higher than that for bulk SnO<sub>2</sub> (3.6 eV), which is probably due to the effect of the quantum confinement in nanocrystalline semiconductors: the band gap increases with the decreasing crystallite size [162]. On the other hand these values are lower than that of commercial material - 4.1 eV. The mean crystallite size of the latter was found 33 (1) nm, however, the quantum behaviour of charge carriers in semiconductor materials predominates for particles of less than 10 nm in diameter [163].

Furthermore, after comparing edge energies of synthesized oxides and their mean crystallite sizes, it becomes clear that the effect of the quantum confinement influences the electronic structure of the materials to the minor degree. As long as crystallite size of SnO<sub>2</sub> Ac is lower than that of SnO<sub>2</sub> Ac (IV), the former should have higher bandgap width than the latter. However, in our case material with lower crystallite size has lower optical band gap. The possible partial reduction of Sn<sup>4+</sup> to Sn<sup>2+</sup> and therefore additional donor levels in SnO<sub>2</sub> Ac should be discarded since both materials contain tin in the highest oxidation state according to the XPS analysis. Moreover as it was found by XPS analysis SnO<sub>2</sub> Ac (IV) contains slightly higher concentration of oxygen vacancies, which should act as electron donors. So what could be the reason of the different optic band gap of the materials?

Probably the effect is due to the surface hydroxylation. It is known from literature that optic band gap for more hydroxylated TiO<sub>2</sub> materials is more shallow [164]. And as it was found by XPS and FTIR analysis, SnO<sub>2</sub> Ac contains more bridging hydroxyls than SnO<sub>2</sub> Ac (IV)

### 4.1.3. Summary

The obtained results as well as available information in the literature suggest that interaction of metallic tin with hot acetic acid in ambient air results in tin(IV) hydroxide acetate with general formula  $[\text{Sn}(\text{OH})_n(\text{Ac})_m]$ . Probably the complex has second coordination sphere with molecular water. The hydroxide groups in the complex demonstrate bridging character. Acetate ligands are bonded to the central atom through highly unsymmetrical bidentate chelating. The complex is rather unstable and upon temperature the weakest bond breaks and is substituted by hydroxyl group probably from molecular water. This explains low temperature formation of tin(IV) oxide (*ca.* 100 °C). At 300 °C the IR spectrum of the compound represents tin dioxide with acetate fragments and apparently molecular water.

Both synthesized oxides are SnO<sub>2</sub> with cassiterite structure. Employment of tin(IV) hydroxide acetate as precursor results in more dispersed material with mean crystallite size 1.69 nm, which is lower than that of SnO<sub>2</sub> Ac (IV). As was established by XPS, SnO<sub>2</sub> Ac contains higher amount of chemisorbed oxygen species and lower content of oxygen vacancies in comparison with SnO<sub>2</sub> Ac (IV). The origin of the superstoichiometric oxygen is related with hydroxyl groups, which content was found much higher for SnO<sub>2</sub> Ac by means of FTIR results. Higher hydroxylation degree probably explains lower edge energy of SnO<sub>2</sub> Ac compared with SnO<sub>2</sub> Ac (IV).

Taking into account the above results the assumption of hydroxyl incorporation into the coordination sphere of the complex appears very probable. Low crystallite size together with high content of hydroxyl groups suggests that upon addition of ammonia solution hydrolysis of  $[\text{Sn}(\text{OH})_n(\text{Ac})_m]$  occurs much faster than polycondensation reaction. The fact of high hydroxylation degree for both materials suggests that among various polycondensation processes (see part 2.1.2) the fastest one isolation.

## 4.2. *Material science: ex situ characterization*

This chapter consists of three parts dedicated to SnO<sub>2</sub> materials synthesized through co-precipitation technique (with IIIB and IVB metal oxides), the ones with deposited noble metals and the last part summarizes the obtained results. Analysis of all materials is given in comparison with blank tin dioxide (SnO<sub>2</sub> Ac), using laser-spark element analysis, TEM, XRD, FTIR, TGA and UV-Vis techniques.

Before we start the comparison of the synthesized SnO<sub>2</sub> systems, it is worthwhile to compare results of element analysis for blank SnO<sub>2</sub>, synthesized through original method, and commercial tin dioxide nanopowder, supplied by Sigma-Aldrich (p/n 549657), since one of the key ideas of the method is to decrease impurity content in the final product.

As it was expected, employment of metalorganic complexes as starting materials remarkable decreases the content of the main impurities usually found in conventional tin dioxide materials. Results of the element analysis performed for commercial and synthesized SnO<sub>2</sub> are given in **Table 11**.

**Table 11.** Weight content of the main impurities found by laser spark element analysis in synthesized and commercial SnO<sub>2</sub>.

Element	Weight content, ppm	
	Commercial	Synthesized <sup>5</sup>
C	32	61
F	4	2
Na	3049	179
Mg	33	13
Al	30	74
Si	80	208
P	61	14
S	22	22
Cl	4120	222
K	47	69
Ca	97	185

<sup>5</sup> The values presented here are the lowest found for synthesized tin dioxide after threefold washing with hot dionized water.



The main impurities in commercial tin dioxide are Na and Cl, which is the result of employing tin chloride and sodium hydroxide as precursor and precipitation agent respectively. These impurities are roughly 20 times lower for tin dioxide synthesized through original method starting from tin(IV) hydroxide acetate complex. Content of some of impurities in synthesized SnO<sub>2</sub> is higher though, *e.g.* Si, Al, Ca and C. The purity can be increased to the same level as was found in commercial material after additional washing procedures. However, these elements and their respective oxides are not known to provoke recrystallization phenomena or catalytic poisoning.

The impurity level was fairly the same for all synthesized oxide systems. Accordingly, in the following chapters the results of element analysis will be given only to estimate the content of the introduced elements

#### 4.2.1. Oxide system SnO<sub>2</sub>-MetO<sub>x</sub>

The following two parts give results of *ex situ* characterization for SnO<sub>2</sub>-MetO<sub>x</sub>, where Met is one of the metals from group IIIB and IVB of periodic system. The results are given separately for each group of elements and start with metals from IVB group. As we have shown earlier the IIIB oxides are known to form mixed oxides with tin dioxide phase, while IVB oxide form solid solutions with isostructural cassiterite phase. Bearing this in mind let us pass to the discussion of the obtained results.

##### 4.2.1.1. SnO<sub>2</sub>-MetO<sub>2</sub>, Met=Ti, Zr, Hf

As it was mentioned in the experimental section the MetO<sub>x</sub> content in SnO<sub>2</sub>-MetO<sub>x</sub> system was set to 10 w.%. Using laser-spark mass spectrometry the content of the introduced element was estimated and the corresponding values are given in **Table 12**. Under the assumption of solid solution formation the following formulae correspond to the synthesized compounds: Sn<sub>0.94</sub>Ti<sub>0.06</sub>O<sub>2</sub>, Sn<sub>0.97</sub>Zr<sub>0.03</sub>O<sub>2</sub>, and Sn<sub>0.98</sub>Hf<sub>0.02</sub>O<sub>2</sub>.

**Table 12.** Atomic content of Ti, Zr and Hf elements in the corresponding oxide systems.

Material	SnO <sub>2</sub> -TiO <sub>2</sub>	SnO <sub>2</sub> -ZrO <sub>2</sub>	SnO <sub>2</sub> -HfO <sub>2</sub>
Tin atomic content, %	31.1	32.0	32.6
Target element atomic content, %	2.13	1.18	0.61

As it was established by TEM analysis the synthesized materials consist of particles roughly of the same size 4-6 nm which is slightly higher than it was found for blank SnO<sub>2</sub>: 2-5 nm (**Figure 23**). Particles tend to form agglomerates and for two-component systems seem to be more closely packed than SnO<sub>2</sub> Ac.

**Figure 24** shows XRD diffractograms for the materials in question. The synthesized compounds apparently consist of one phase which corresponds to cassiterite structure (peaks at 40, 46 and 67 2 $\theta$  in SnO<sub>2</sub>-TiO<sub>2</sub> diffractogram are assigned to the Pt sample holder, corresponding to crystalline planes: 111, 002 and 220, resp.).

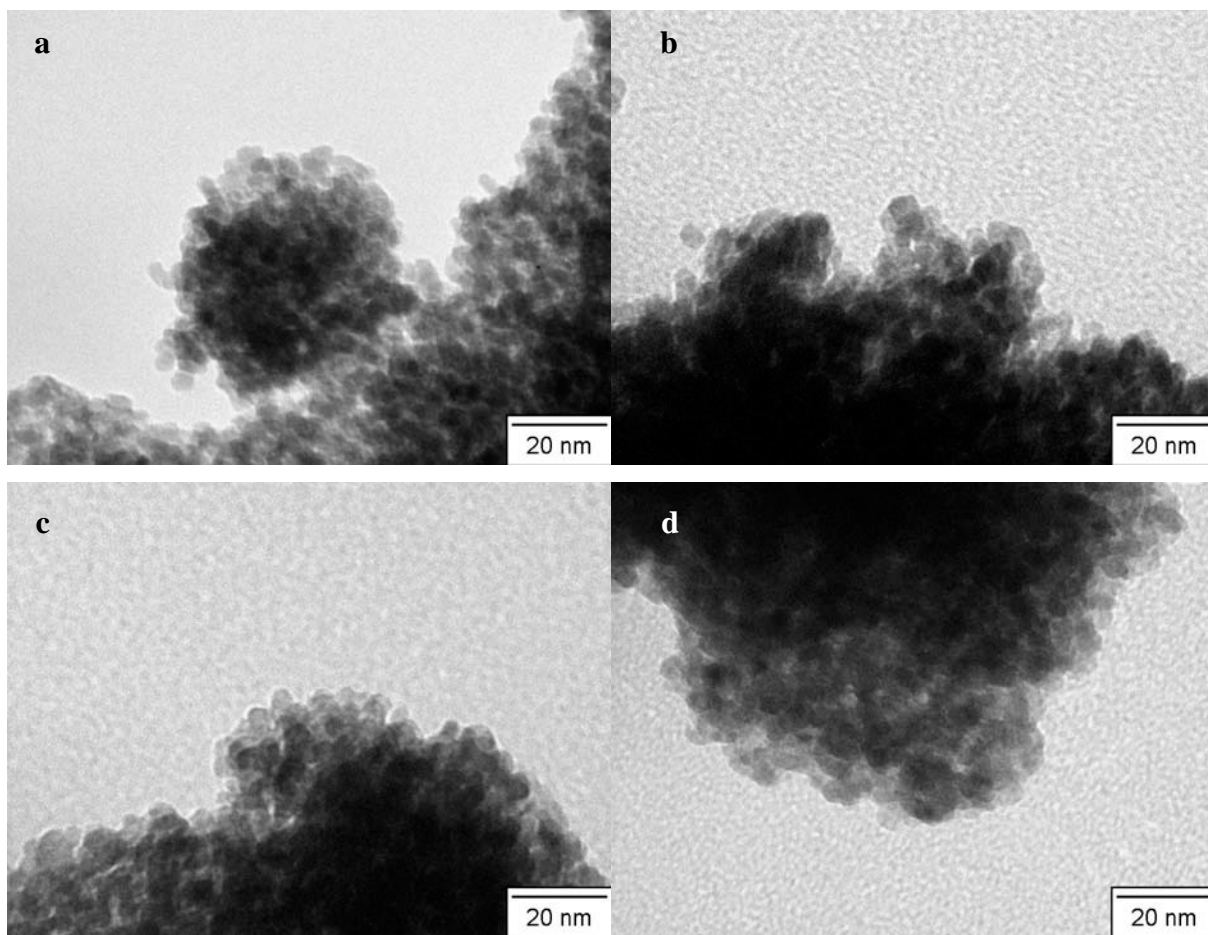


**Figure 23.** TEM pictures of blank SnO<sub>2</sub> (a), SnO<sub>2</sub>-TiO<sub>2</sub> (b), SnO<sub>2</sub>-ZrO<sub>2</sub> (c), and SnO<sub>2</sub>-HfO<sub>2</sub> (d).

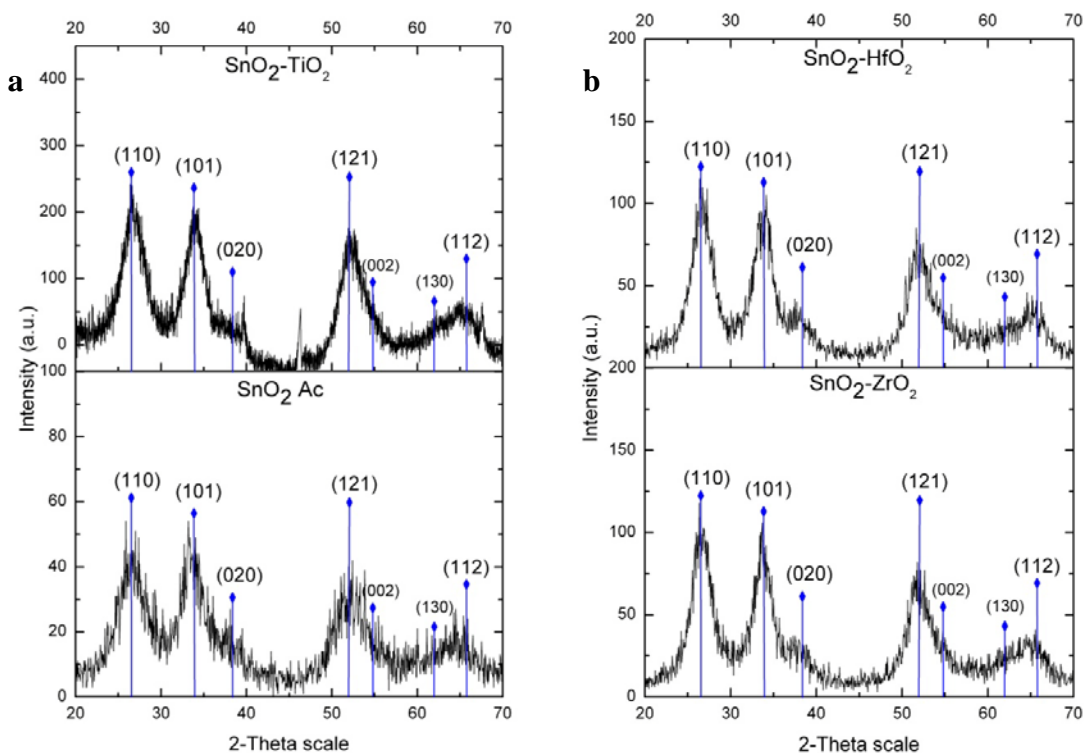


**Figure 24.** XRD diffractograms of SnO<sub>2</sub> Ac and SnO<sub>2</sub>-TiO<sub>2</sub> (a), and SnO<sub>2</sub>-ZrO<sub>2</sub> and SnO<sub>2</sub>-HfO<sub>2</sub> (b).

The cell parameters ( $a$  and  $c$  in the tetragonal cell) as well as mean crystallite size are given in **Table 13**. Parameters  $a$ ,  $c$  and  $D$  were calculated using fitting procedure for the diffractograms recorded three times separately for the same material. In the table the given values are average with the experimental error given in parenthesis.

**Table 13.** Cell parameters ( $a$  and  $c$ ) and crystallite size ( $D$ ) for synthesized compounds in comparison with standardized crystallographic data of pure oxides in tetragonal modification.

Compound	$a=b$ , Å	$c$ , Å	$a/c$	$D$ , nm	Ref.
SnO <sub>2</sub> standard	4.737	3.186	1.487	-	[89, 117]
TiO <sub>2</sub> standard	4.593	2.960	1.552	-	[117]
ZrO <sub>2</sub> standard	3.638	5.281	0.689	-	[165]
HfO <sub>2</sub> standard	5.176	5.298	0.977	-	[166]
SnO <sub>2</sub> Ac	4.67(1)	3.17(2)	1.48(2)	1.69(6)	
SnO <sub>2</sub> -TiO <sub>2</sub>	4.68(3)	3.16(3)	1.48(3)	1.84(8)	
SnO <sub>2</sub> -ZrO <sub>2</sub>	4.71(3)	3.18(3)	1.48(3)	2.28(10)	

SnO <sub>2</sub> -HfO <sub>2</sub>	4.74(3)	3.19(3)	1.49(3)	2.10(9)	
------------------------------------	---------	---------	---------	---------	--

It was found that cell parameters of synthesized materials are lower than that of well ordered standard cassiterite structure. Let us compare the values found for solid solutions with the ones for blank SnO<sub>2</sub>. Tin substitution with elements of different ionic radii (in the quantities of 1-2 at.%) brings about only slight change of cell parameters in comparison with blank SnO<sub>2</sub>. For example in the case of SnO<sub>2</sub>-TiO<sub>2</sub> the experimental error of 3 pm corresponds to *ca.* 20 % of the theoretical difference between cell parameters of pure TiO<sub>2</sub> and pure SnO<sub>2</sub> (the highest possible change) [117]. Therefore the change of the cell parameters probably is below experimental error. For Zr and Hf doped SnO<sub>2</sub> the crystalline lattice is slightly expanded, which suggests incorporation of the metal ions with bigger radius into the crystalline structure of SnO<sub>2</sub>. Within the experimental error the lattice expands almost isotropically.

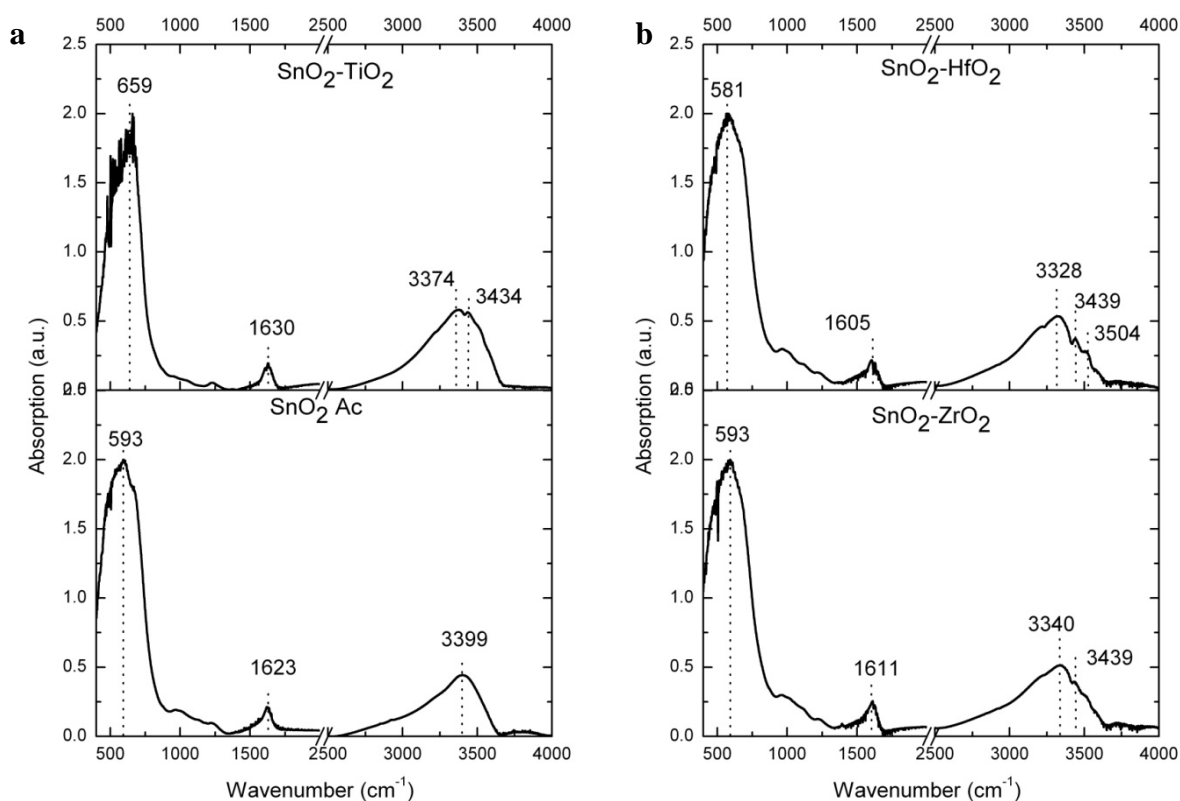


**Figure 25.** FTIR spectra of SnO<sub>2</sub> Ac and SnO<sub>2</sub>-TiO<sub>2</sub> (a), and SnO<sub>2</sub>-ZrO<sub>2</sub> and SnO<sub>2</sub>-HfO<sub>2</sub> (b).

**Figure 25** shows results of FTIR characterization. The spectra of the materials are quite similar. All compounds contain molecular water, which deformation vibration can be observed

between 1500 and 1650 cm<sup>-1</sup> [107]. Sn-O vibrations for the materials occur in the region 580-660 cm<sup>-1</sup> and represent broad adsorption bands, suggesting heterogeneous particle shape [167].

OH stretching vibrations occur in the region 2700-3650 cm<sup>-1</sup>. Their maximum positions correspond to the bridging OH groups where hydrogen interacts with neighbouring oxygen atoms. For given materials the corresponding peak position gradually shifts from higher towards lower frequencies in the following way: SnO<sub>2</sub> Ac > SnO<sub>2</sub>-TiO<sub>2</sub> > SnO<sub>2</sub>-ZrO<sub>2</sub> > SnO<sub>2</sub>-HfO<sub>2</sub>. Probably this phenomenon is related to the change in the acidic/basic character of the corresponding oxides. Accordingly, the observed shift can be assigned to the acidity change of bridging hydroxyl groups, since it is known that SnO<sub>2</sub> and TiO<sub>2</sub> are amphoteric oxides, while ZrO<sub>2</sub> and HfO<sub>2</sub> are basic ones. The same trend (however for terminal OH groups in the case of SnO<sub>2</sub>) was observed by N. Sergent *et al.* The authors found that vibrations at 3740 cm<sup>-1</sup> correspond to the less acidic hydroxyls than those at 3640 cm<sup>-1</sup> [106].

In general, all two-component materials manifest remarkable heterogeneity of the bridging hydroxyls. The additional shoulders can be observed in the high-frequency region. The most prominent case of the OH heterogeneity is presented by SnO<sub>2</sub>-HfO<sub>2</sub>.

**Table 14.** Comparative analysis of normalized intensities I<sub>OH</sub>, I<sub>SnO</sub>, their ratio I<sub>OH</sub>/I<sub>SnO</sub> and integral of the band ν<sub>OH</sub> between 2500-3700 cm<sup>-1</sup>.

Compound	I <sub>OH</sub> , a.u.	I <sub>SnO</sub> , a.u.	I <sub>OH</sub> /I <sub>SnO</sub>	Integral (ν <sub>OH</sub> )
SnO <sub>2</sub> Ac	0.44	1.97	0.22	193
SnO <sub>2</sub> -TiO <sub>2</sub>	0.58	1.88	0.31	261
SnO <sub>2</sub> -ZrO <sub>2</sub>	0.5	1.97	0.25	208
SnO <sub>2</sub> -HfO <sub>2</sub>	0.53	1.97	0.27	223

To analyse the hydroxylation degree of the materials let us compare intensity ratio I<sub>OH</sub>/I<sub>SnO</sub> and normalized integrals calculated as peak area between 2500 and 3700 cm<sup>-1</sup> (**Table 14**). Both parameters reach their highest values for SnO<sub>2</sub>-TiO<sub>2</sub>, suggesting that this material contains the highest amount of OH groups. The lowest hydroxylation degree was found for blank oxide.

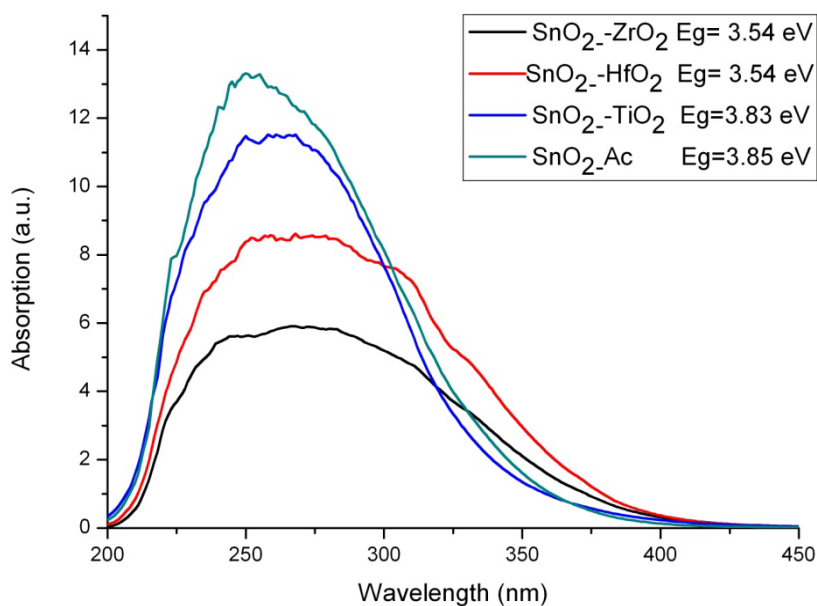


**Figure 26.** UV-VIS spectra of SnO<sub>2</sub> Ac, SnO<sub>2</sub>-TiO<sub>2</sub>, SnO<sub>2</sub>-ZrO<sub>2</sub> and SnO<sub>2</sub>-HfO<sub>2</sub>.

UV-VIS spectra of the materials in question are shown in **Figure 26**. The absorption intensity as well as peak shape and its position differ from the blank material. Doping with Ti results in decrease of the peak at 250 nm. In the case of Zr and Hf the absorption bands demonstrate shoulders around 305 and 330 nm, and remarkable broadening in the low-energy region extending up to 430 nm. The observed changes in the spectra indicate that following phenomena occur upon doping: decrease of the electron transfer between tin and oxygen ligands and appearance of the new low-energy transitions in the region 270-340 nm and higher. The former is probably due to the tin substitution in the crystalline lattice. Absorption in the region 270-340 nm can be caused by new  $\pi \rightarrow d$  transitions between oxygen and d element or/and intershell  $d \rightarrow d$  transitions in the dopants [161, 168, 169]. The surface vacancies are believed to contribute to the vibration in the region 350-400 nm [145].

The edge energies of the solid solutions found from the spectra are lower in comparison with blank oxide. The values decrease gradually in a following way: SnO<sub>2</sub> Ac > SnO<sub>2</sub>-TiO<sub>2</sub> > SnO<sub>2</sub>-ZrO<sub>2</sub> = SnO<sub>2</sub>-HfO<sub>2</sub>. According to the literature following factors can contribute to the decrease of the energy band gap: substitution of tin atoms with metals of lower electronegativity, increase of crystallite size being accompanied by the loss of quantum confinement dimensions [162, 163], and generation of the donor levels within forbidden band due to high hydroxylation of the surface [145, 164].

**Figure 27** illustrates the comparison of the mentioned factors with the energy bandgap of the materials. The change of the energy optic band gap is seemed to have a hybrid phenomenon,

since all the factors evolve complementary with element atomic numbers. However, hydroxylation degree together with quantum confinement factor has the minor contribution to the phenomenon.

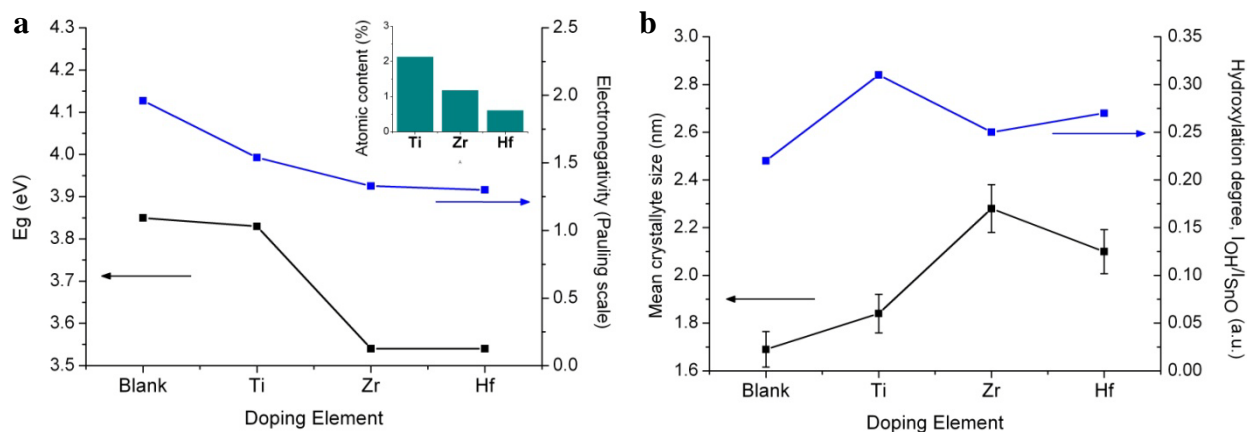


**Figure 27.** Comparison of the  $E_g$  with electronegativity of the introduced metals (a), mean crystallite size and hydroxylation degree of the materials (b). Inset – atomic content of the given elements.

#### 4.2.1.2. SnO<sub>2</sub>-Met<sub>2</sub>O<sub>3</sub>, Met=Sc, Y, La

Results of laser-spark element analysis for the material in question are given in **Table 15**. As it was shown earlier the elements do not form solid solution with tin dioxide, however, formation of stannates with pyrochlore structure should not be discarded. Accordingly, the compounds represent a mixture of different oxide phases: SnO<sub>2</sub> and Met<sub>2</sub>O<sub>3</sub>, SnO<sub>2</sub> and Sn<sub>2</sub>Met<sub>2</sub>O<sub>7</sub>, or three phases can form simultaneously.

**Table 15.** Atomic content of Sc, Y and La elements in corresponding mixed oxides.

Material	SnO <sub>2</sub> -Sc <sub>2</sub> O <sub>3</sub>	SnO <sub>2</sub> -Y <sub>2</sub> O <sub>3</sub>	SnO <sub>2</sub> -La <sub>2</sub> O <sub>3</sub>
Tin atomic content, %	32.3	32.7	33.2
Target element atomic content, %	1.62	1.21	0.74

TEM analysis did not reveal the pronounced two-phase character of the particles. Particle size of SnO<sub>2</sub>-Sc<sub>2</sub>O<sub>3</sub> is in the range of 4-8 nm, which is slightly higher than it was found for SnO<sub>2</sub>-Y<sub>2</sub>O<sub>3</sub> and SnO<sub>2</sub>-La<sub>2</sub>O<sub>3</sub>: 4-6 and 3-6 nm (**Figure 28**). The particles seem to be more aggregated and closely packed than that of blank tin dioxide.



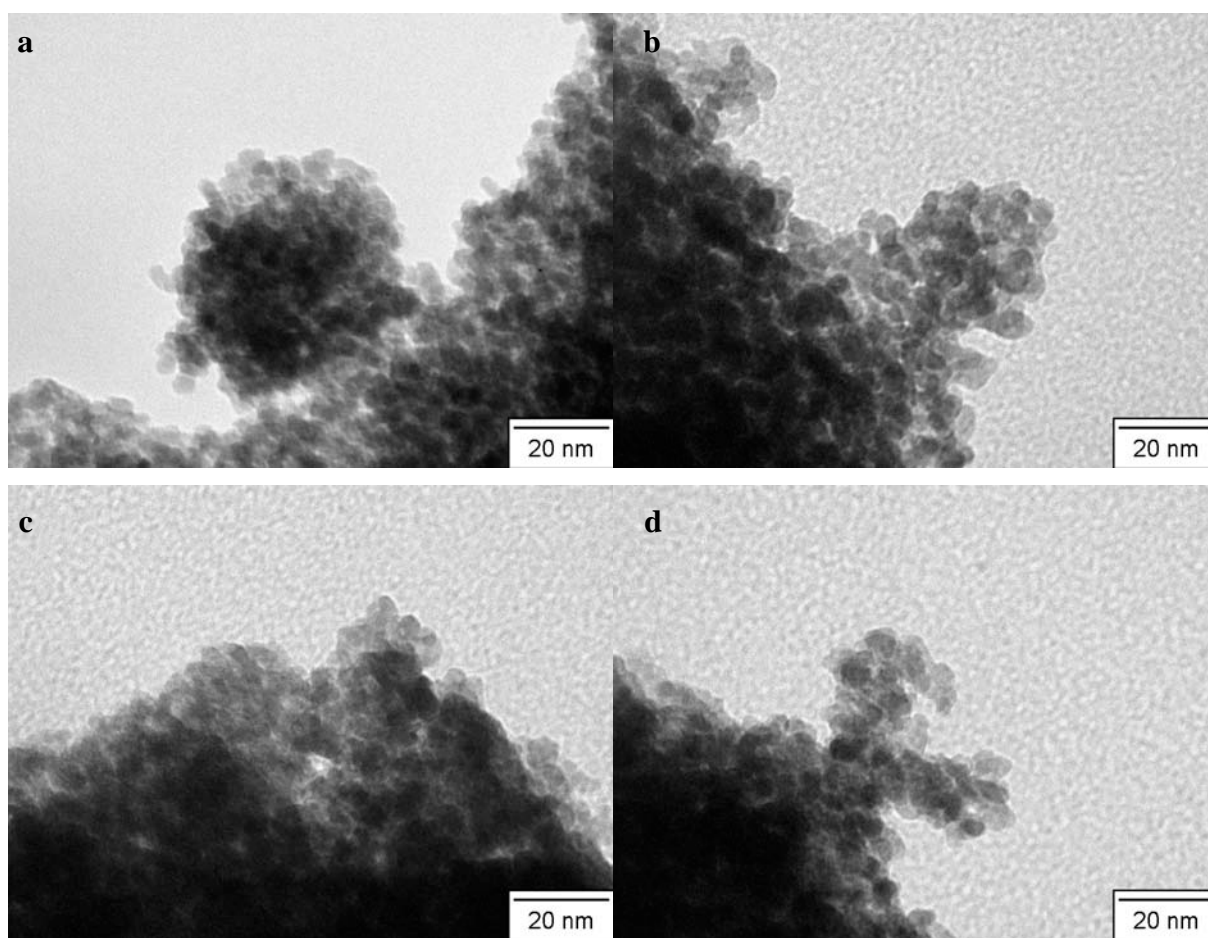


**Figure 28.** TEM pictures of blank SnO<sub>2</sub> (a), SnO<sub>2</sub>-Sc<sub>2</sub>O<sub>3</sub> (b), SnO<sub>2</sub>-Y<sub>2</sub>O<sub>3</sub> (c), and SnO<sub>2</sub>-La<sub>2</sub>O<sub>3</sub> (d).

XRD diffractograms show only one phase for all synthesized materials (**Figure 29b**, again peaks at 40, 46 and 67  $2\theta$  in SnO<sub>2</sub>-Y<sub>2</sub>O<sub>3</sub> diffractogram correspond to the Pt sample holder). This suggests that either this technique is insensitive to the amount of introduced oxides (*ca.* 4-6 at %), or the oxides are amorphous and this hardly can be seen against the background of poor crystallized main phase of SnO<sub>2</sub>.

The cell parameters and crystallite size of the synthesized materials are given in **Table 16**. The fact that cell parameters expand upon doping with Sc, Y, and La, suggests that there is phase interaction between SnO<sub>2</sub> and Met<sub>2</sub>O<sub>3</sub>, which consists probably of partial incorporation of the metal ions with much bigger ionic radii (**Table 5**) into the near-surface region of SnO<sub>2</sub> crystallites. While *a* and *c* increase slightly anisotropically for SnO<sub>2</sub>-Sc<sub>2</sub>O<sub>3</sub> and SnO<sub>2</sub>-La<sub>2</sub>O<sub>3</sub>, the yttrium doping results in more even expansion of the cell parameters. The mean crystallite size of the mixed oxides is higher comparing with blank SnO<sub>2</sub>. The highest increase is observed for SnO<sub>2</sub>-Sc<sub>2</sub>O<sub>3</sub> and SnO<sub>2</sub>-La<sub>2</sub>O<sub>3</sub>.

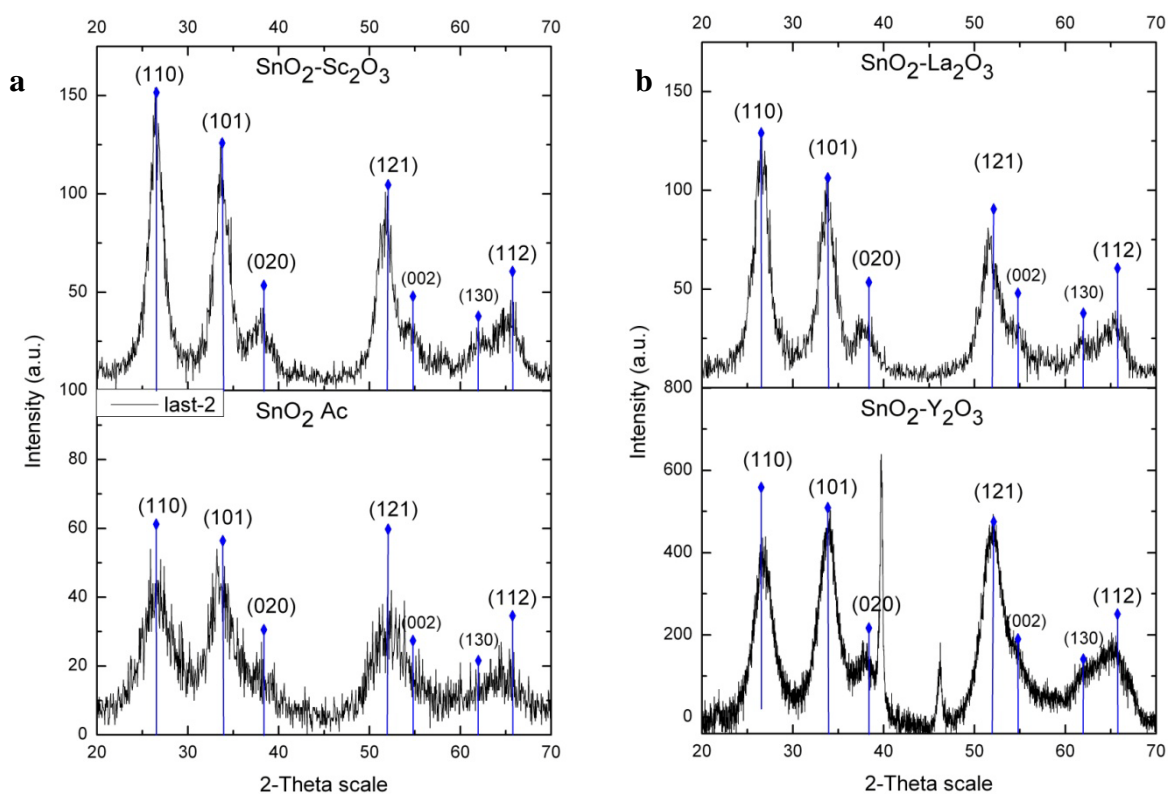


**Figure 29.** XRD diffractograms of SnO<sub>2</sub> Ac, SnO<sub>2</sub>-Sc<sub>2</sub>O<sub>3</sub> (a), and SnO<sub>2</sub>- Y<sub>2</sub>O<sub>3</sub>, SnO<sub>2</sub>- La<sub>2</sub>O<sub>3</sub> (b).

**Table 16.** Cell parameters (*a* and *c*) and crystallite size (*D*) for synthesized compounds in comparison with standardized crystallographic data of pure SnO<sub>2</sub>.

Compound	<i>a</i> = <i>b</i> , Å	<i>c</i> , Å	<i>a</i> / <i>c</i>	<i>D</i> , nm	Ref.
SnO <sub>2</sub> standard	4.737	3.186	1.487	-	[89, 117]
SnO <sub>2</sub> Ac	4.67(1)	3.17(2)	1.48(2)	1.69(6)	
SnO <sub>2</sub> -Sc <sub>2</sub> O <sub>3</sub>	4.74(3)	3.19(3)	1.49(3)	2.9(1)	
SnO <sub>2</sub> - Y <sub>2</sub> O <sub>3</sub>	4.73(3)	3.19(3)	1.48(3)	2.3(1)	
SnO <sub>2</sub> - La <sub>2</sub> O <sub>3</sub>	4.74(3)	3.19(3)	1.49(3)	2.6(1)	

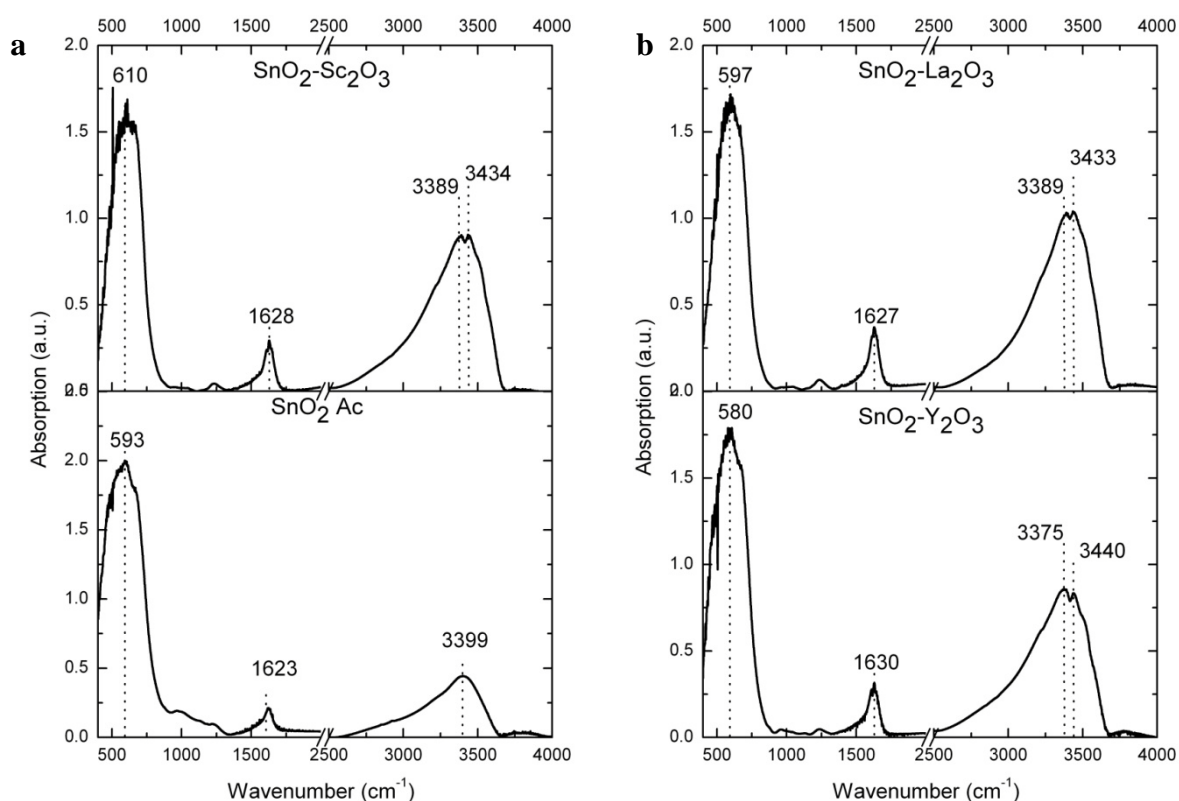


**Figure 30.** FTIR spectra of SnO<sub>2</sub> Ac, SnO<sub>2</sub>-Sc<sub>2</sub>O<sub>3</sub> (a), and SnO<sub>2</sub>- Y<sub>2</sub>O<sub>3</sub>, SnO<sub>2</sub>- La<sub>2</sub>O<sub>3</sub> (b).

FTIR spectra of synthesized compounds are given in **Figure 30**. The mixed oxides seem to contain more molecular water (vibrations at 1630 cm<sup>-1</sup>). However again, the most pronounced difference is related with hydroxyl stretching vibrations in the region 2500-3700 cm<sup>-1</sup>. The band in this region is more intense for mixed oxides and contains additional peak around 3433-3440 cm<sup>-1</sup>. The appearance of the peak in the high frequency region suggests that together with acidic bridging hydroxyls the material contains a fraction of slightly more neutral OH groups. On the other hand, the band, observed in SnO<sub>2</sub> Ac at 3399 cm<sup>-1</sup>, undergoes a shift towards lower frequencies in mixed oxides (so called red shift). In other words some of the bridging hydroxyls become more acidic. The highest shift of the band is observed for SnO<sub>2</sub>-Y<sub>2</sub>O<sub>3</sub>. However, we should note that peak positions are quite similar for the mixed oxides and no trend regarding this parameter can be derived for IIIB metal oxides. Comparison of the normalized ratios  $I_{OH}/I_{SnO}$  and  $\nu_{OH}$  integrals clearly evidences that mixed oxides contain OH groups more than 2 times as much as blank SnO<sub>2</sub> (**Table 17**).

**Table 17.** Comparative analysis of normalized intensities  $I_{OH}$ ,  $I_{SnO}$ , their ratio  $I_{OH}/I_{SnO}$  and integral of the band  $\nu_{OH}$  between 2500-3700 cm<sup>-1</sup>.

Compound	I <sub>OH</sub> , a.u.	I <sub>SnO</sub> , a.u.	I <sub>OH</sub> /I <sub>SnO</sub>	Integral (v <sub>OH</sub> )
SnO <sub>2</sub> Ac	0.44	1.97	0.22	193
SnO <sub>2</sub> -Sc <sub>2</sub> O <sub>3</sub>	0.90	1.65	0.54	431
SnO <sub>2</sub> - Y <sub>2</sub> O <sub>3</sub>	0.85	1.79	0.47	407
SnO <sub>2</sub> - La <sub>2</sub> O <sub>3</sub>	1.03	1.70	0.61	460

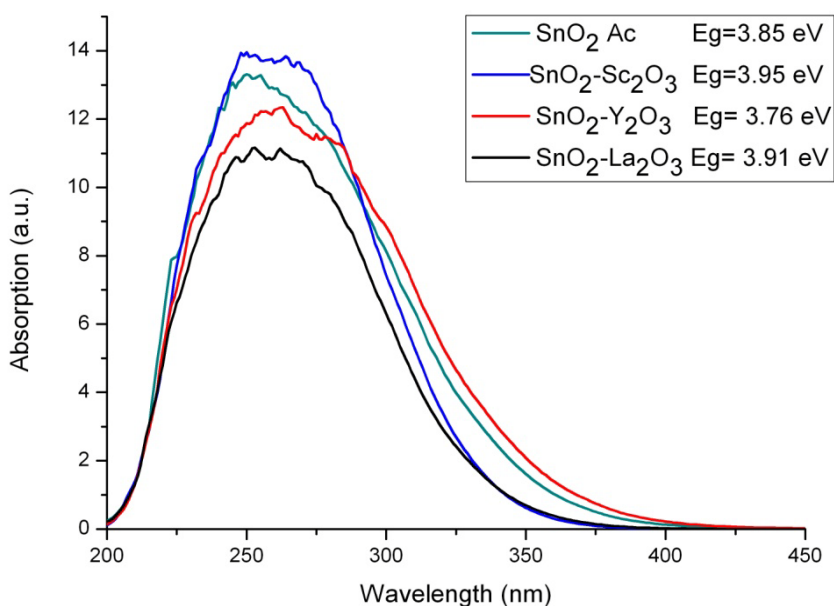


**Figure 31.** UV-VIS spectra of SnO<sub>2</sub> Ac, SnO<sub>2</sub>-Sc<sub>2</sub>O<sub>3</sub>, SnO<sub>2</sub>- Y<sub>2</sub>O<sub>3</sub> and SnO<sub>2</sub>- La<sub>2</sub>O<sub>3</sub>.

The UV-Vis absorbance spectra of the mixed oxides are illustrated in **Figure 31**. The common trend for the mixed oxides is that the doping slightly change intensity and width of the absorption band. Doping with Sc to a little degree increases absorption in the region of electron transfer between valence and conduction band, however, in the same time a decrease of low-energy transitions occur in the region 300-400 nm, assigned to the oxygen vacancy effect [145]. In the case of SnO<sub>2</sub>-Y<sub>2</sub>O<sub>3</sub> the absorption band becomes slightly red-shifted with pronounced shoulder in the region 270-285 nm. A slight increase of low-energy electron transitions is observed for this material as well. Doping with La more decreases vibrations corresponded to the charge transfer and low-energy region 300-400 nm.

The edge energies found from UV-VIS spectra of the mixed oxides do not differ from the blank materials in such pronounced way as it was found for elements from IVB group (**Figure 31**). Comparing the values it was found that  $E_g$  is slightly higher for SnO<sub>2</sub>-Sc<sub>2</sub>O<sub>3</sub> and SnO<sub>2</sub>-La<sub>2</sub>O<sub>3</sub>, while that of SnO<sub>2</sub>-Y<sub>2</sub>O<sub>3</sub> is lower in respect to blank oxide.

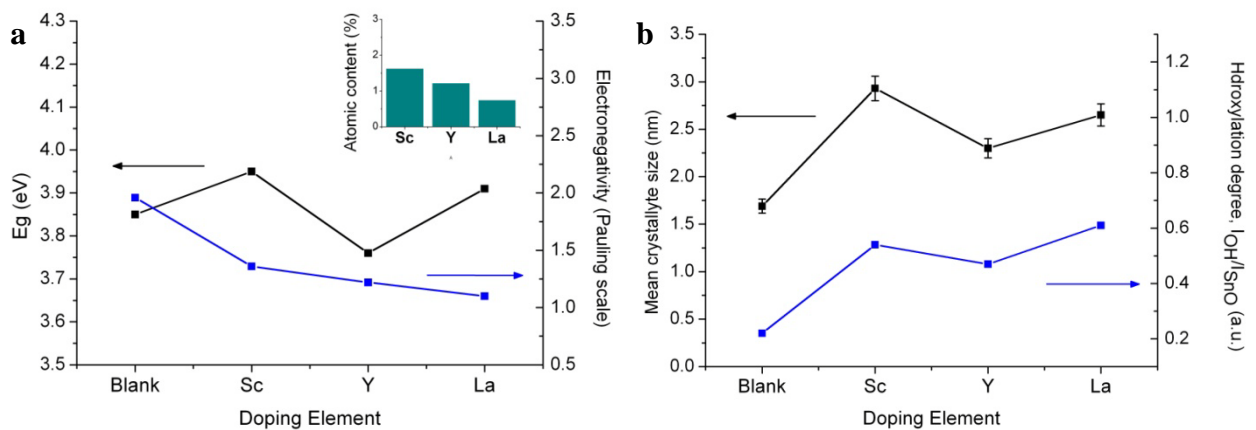


**Figure 32.** Qualitative comparison of the  $E_g$  with electronegativity of the metals (a), mean crystallite size and hydroxylation degree of the materials (b). Inset – atomic content of the given elements.

The fact that edge energy for the mixed oxides, evolving with element atomic number, remains relatively closely to the value of the blank oxide, suggests that the electronic structure of tin dioxide is modified to a little degree by the second phase oxide (**Figure 32 a**). Hydroxylation degree of the materials is believed to be related predominantly with the second phase oxides, rather than with SnO<sub>2</sub> (**Figure 32 b**).

#### 4.2.2. SnO<sub>2</sub> with deposited noble metals: Pd, Pt, Rh

As it was found by element analysis the weight content of the deposited noble metals is in good agreement with calculated metal-to-SnO<sub>2</sub> ratio, set to 1 w. % for all materials (**Table 18**).

**Table 18.** Atomic content of Pd, Pt and Rh in the corresponding materials.

Material	SnO <sub>2</sub> -Pd	SnO <sub>2</sub> -Pt	SnO <sub>2</sub> - Rh
Target element atomic content, %	0.52	0.30	0.55
Target element weight content, %	1.1	1.2	1.1

The surface doped materials consist of closely packed particles of 4-6 nm in diameter (**Figure 33**). By means of conventional TEM the metal clusters were not visible on highly textured surface of the carrier. However, using HRTEM it was possible to overcome this obstacle.

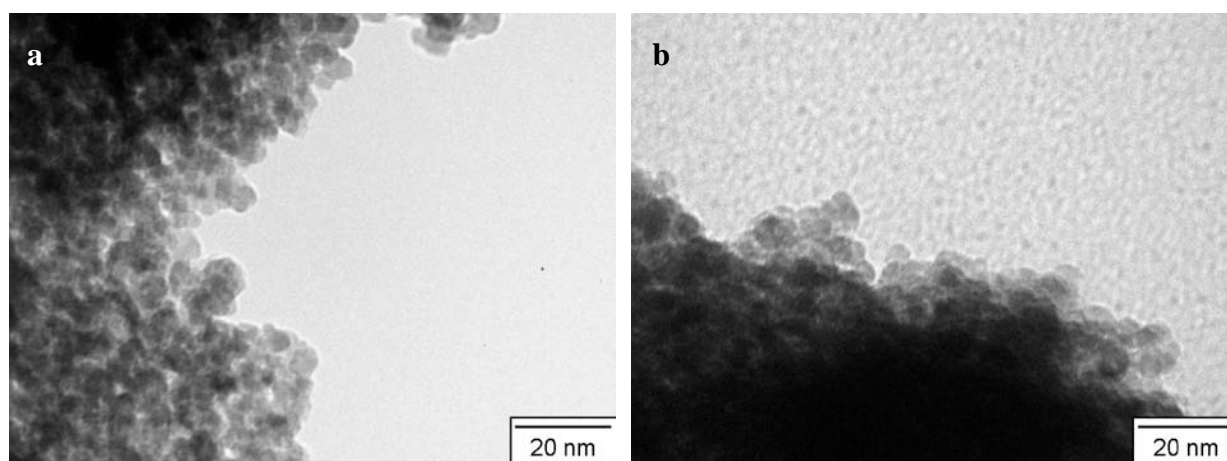


**Figure 33.** TEM images of SnO<sub>2</sub> Ac-Pd (a) and SnO<sub>2</sub> Ac-Pt (b).

**Figure 34** shows HRTEM picture and its Fourier Transform (FT) image obtained for Pd doped SnO<sub>2</sub>. The area labelled “1” contains lattice fringes with the spacing 3.35 Å corresponding to the (110) plane of SnO<sub>2</sub>, while that labelled “2” with 3.05 Å between the planes corresponds to the crystallite structure of PdO in the direction of (100). The size of PdO particles was found to be 1-3 nm.

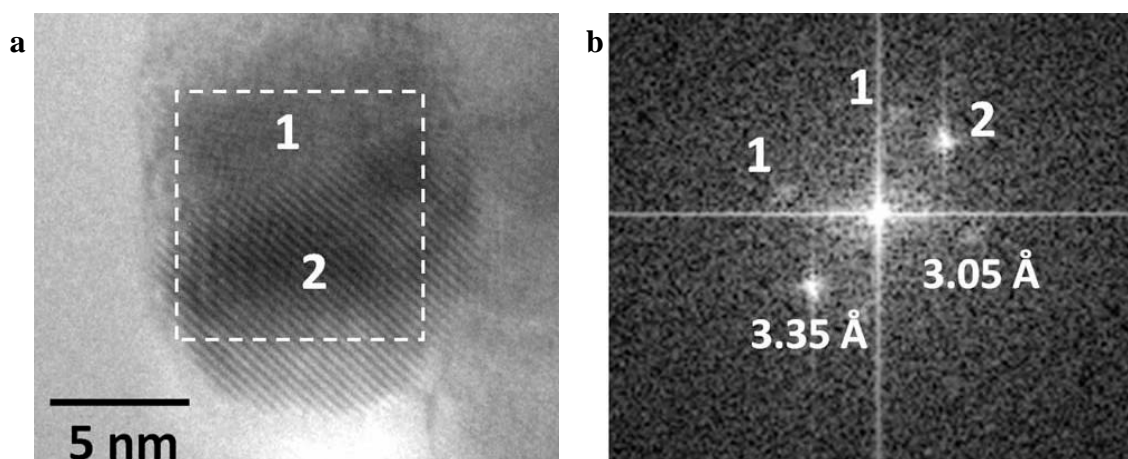


**Figure 34.** HRTEM (a) and FT (b) images of SnO<sub>2</sub> Ac-Pd. Areas 1 and 2 correspond to SnO<sub>2</sub> and PdO (resp.).

According to XRD analysis the sample contains one main phase – SnO<sub>2</sub> with cassiterite structure. The mean crystallite sizes of the doped materials are higher as well as in the previous materials. In addition, deposition of noble metals increases cell parameter *a* in the cassiterite structure to the same degree as it was found for mixed oxides and some solid solutions. This means that apart from being a separate phase noble metals are partially incorporated into SnO<sub>2</sub> crystallite structure.

**Table 19.** Cell parameters (*a* and *c*) and crystallite size (*D*) for synthesized compounds in comparison with standardized crystallographic data of pure SnO<sub>2</sub>.

Compound	a=b, Å	c, Å	a/c	D, nm	Ref.
SnO <sub>2</sub> standard	4.737	3.186	1.487	-	[89, 117]
SnO <sub>2</sub> Ac	4.67(1)	3.17(2)	1.48(2)	1.69(6)	
SnO <sub>2</sub> -Pd	4.72(1)	3.18(1)	1.48(1)	2.50(3)	
SnO <sub>2</sub> - Pt	4.71(2)	3.18(1)	1.48(2)	2.14(9)	

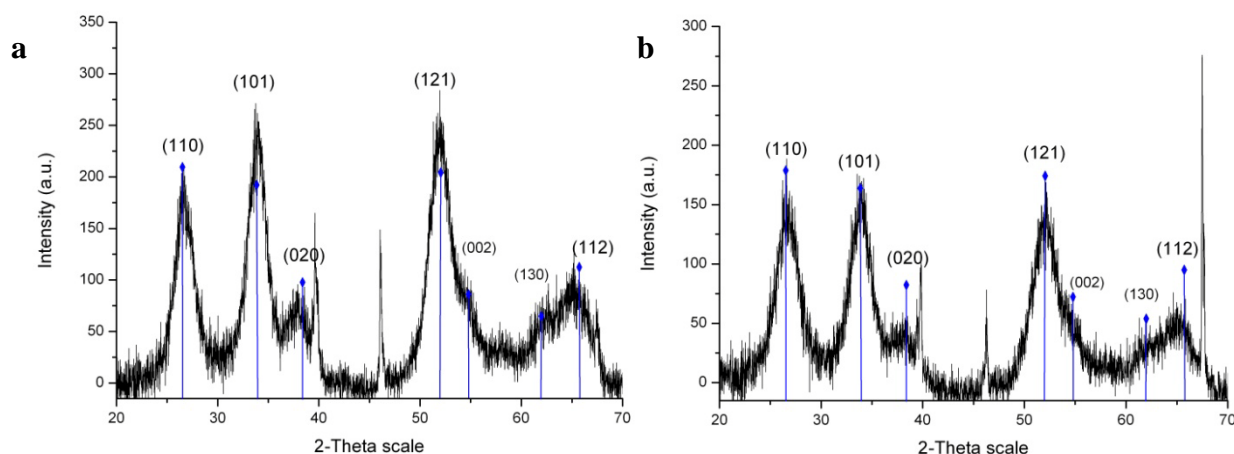


**Figure 35.** XRD diffractograms of SnO<sub>2</sub> Ac-Pd (a) and SnO<sub>2</sub> Ac-Pt (b).

XPS analysis was performed for SnO<sub>2</sub>-Pd and revealed that surface tin atoms of this material are in the highest oxidation state with a binding energy 486.7 eV (**Figure 36 a**). Signal of oxygen also manifest two components. As mentioned above, one corresponds to the lattice oxygen signal and another one originates from hydroxyl groups (**Figure 36 b**).

**Table 20.** Comparison of XPS results

Material	(O <sub>OH</sub> +O <sub>lat</sub> )/Sn	O <sub>OH</sub> /O <sub>lat</sub>
SnO <sub>2</sub> Ac	2.52	0.33
SnO <sub>2</sub> Ac-Pd	2.13	0.37

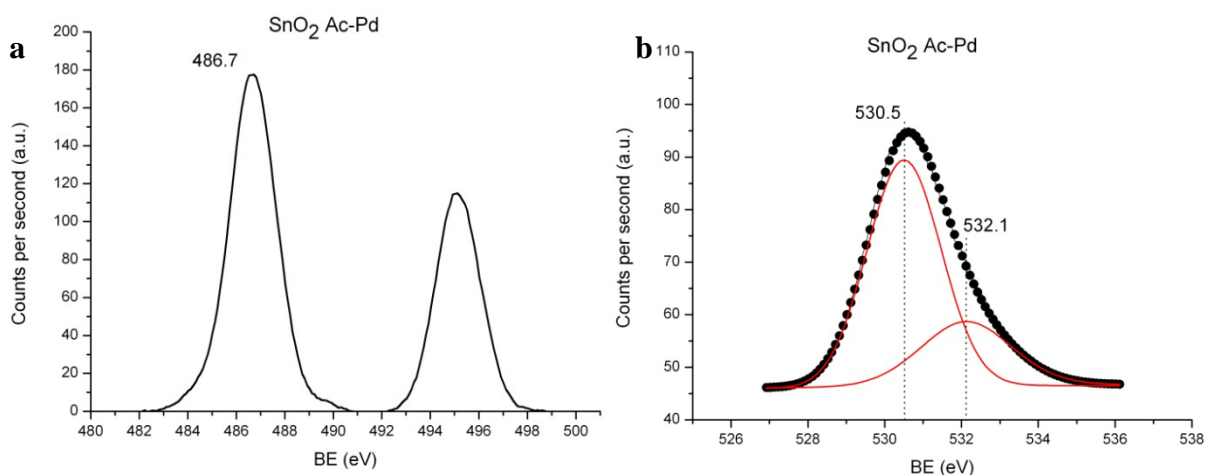


**Figure 36.** XPS spectra of SnO<sub>2</sub> Ac-Pd: bands corresponded to Sn3d<sub>5/2</sub> (a) and O1s (b).

The found overall oxygen-to-tin and hydroxyl-to-lattice oxygen ratios are given in **Table 20**. Using the obtained results we can compare the formation of oxygen vacancies in the case of



two materials, as it has been performed earlier for SnO<sub>2</sub> Ac and SnO<sub>2</sub> Ac (IV). The overall oxygen-to-tin ratio for both materials can be represented as follows:

$$\left( \frac{O_{OH} + O_{lat}}{Sn} \right)_{Blank} = 2.52 \quad (4-5)$$

$$\left( \frac{O_{OH} + O_{lat}}{Sn} \right)_{Pd} = 2.13 \quad (4-6)$$

where,  $O_{OH}$  – the surface hydroxyl concentration,  $O_{lat}$  – the one of lattice oxygen,  $Sn$  – concentration of surface tin atoms. If we divide the both parts of equations by concentration of lattice oxygen  $O_{lat}$ , and substitute the resulting ratio ( $O_{OH}/O_{lat}$ ) by the corresponding values from **Table 20**, we obtain the following ratios:

$$\left( \frac{Sn}{O_{lat}} \right)_{Blank} = 0.53 \quad (4-7)$$

$$\left( \frac{Sn}{O_{lat}} \right)_{Pd} = 0.64 \quad (4-8)$$

The results definitely show that content of lattice oxygen is lower by a factor of 1.2 in the case of Pd-doped material. This means that Pd doping provokes in addition to the slight hydroxylation of the material remarkable formation of oxygen vacancies on the surface.

Binding energy of Pd3d<sub>5/2</sub> core was found to be 337.8 eV, which corresponds to PdO<sub>2</sub> (not shown). This result contradicts to the one obtained by HRTEM, the latter suggested that deposited particles corresponds to PdO phase. The explanation to this could be different penetration depth of the radiation in the given methods. While HRTEM has very high penetration capacity, the signal obtained by XPS is originated from atoms that are within 2-5 nm of surface layer.

FTIR spectra of the surface doped materials differ from SnO<sub>2</sub> Ac by narrow and blue shifted band of Sn-O stretching vibrations and increased hydroxyl vibrations (**Figure 37**). The former band is less broad for all doped oxides. Together with the shift of the band this indicates that the material consists of the particles with more homogeneous distribution of shapes [170]. In other words the crystalline structure is more ordered and the amorphous component became less intense. In addition to the narrowing there is a pronounced decrease of the  $\nu_{SnO}$  intensity for all doped materials. The lowest intensity was found for Rh doped oxide.

Increase of hydroxyl vibration intensity together with shoulder formation around 3433 cm<sup>-1</sup> is observed for all catalyst systems, suggesting that surface hydroxylation becomes more intense and hydroxyl nature is more heterogeneous.

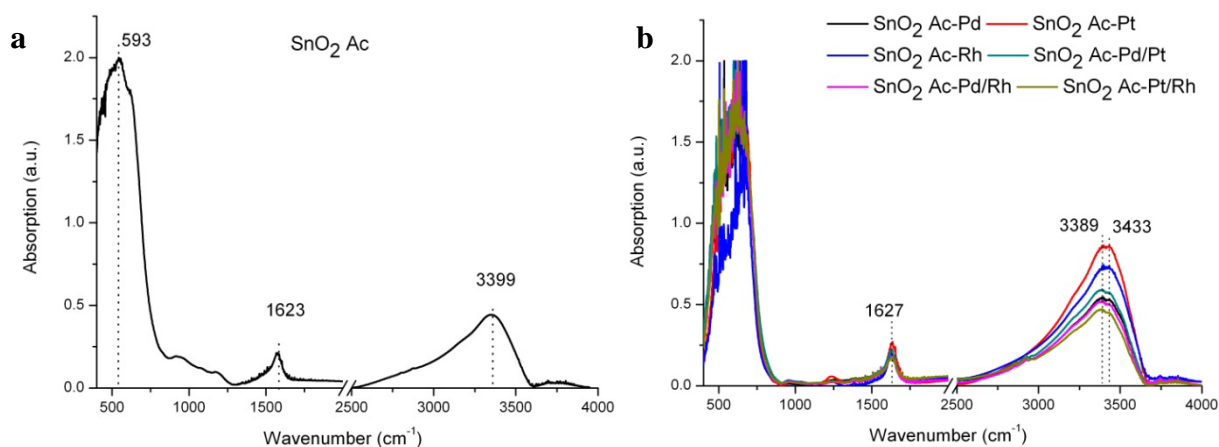


**Figure 37.** FTIR spectra of SnO<sub>2</sub> Ac (a) and SnO<sub>2</sub> Ac with deposited noble metals (b).

As it was found by XPS analysis, doping with noble metals brings about formation of the oxygen vacancies on SnO<sub>2</sub> surface. Spiking nature of the bands at 630 cm<sup>-1</sup> together with band narrowing and intensity decrease (especially in the case of Rh-doped SnO<sub>2</sub>) indirectly supports this assumption, since the band corresponds to metal-oxygen fundamental vibrations. Therefore the  $I_{OH}/I_{SnO}$  ratio probably could not be used to compare hydroxylation degree of the materials. Let us suppose that comparison of the  $\nu_{OH}$  integrals reflects better difference between blank and doped SnO<sub>2</sub>.

According to integral calculations, the highest hydroxylation degree was found in the case of Pt and Rh catalysts (**Table 21**). It is remarkable, that bimetallic catalyst systems manifest rather low hydroxylation degree in respect with monometallic ones.

**Table 21.** Comparative analysis of normalized intensities  $I_{OH}$ ,  $I_{SnO}$ , their ratio  $I_{OH}/I_{SnO}$  and integral of the band  $\nu_{OH}$  between 2500-3700 cm<sup>-1</sup>.

Compound	$I_{OH}$ , a.u.	$I_{SnO}$ , a.u.	$I_{OH}/I_{SnO}$	Integral ( $\nu_{OH}$ )
SnO <sub>2</sub> Ac	0.44	2.00	0.22	193
SnO <sub>2</sub> Ac-Pd	0.54	1.5	0.36	244
SnO <sub>2</sub> Ac-Pt	0.86	1.75	0.49	396
SnO <sub>2</sub> Ac-Rh	0.73	1.45	0.50	321
SnO <sub>2</sub> Ac-Pd/Pt	0.58	1.72	0.34	268
SnO <sub>2</sub> Ac-Pd/Rh	0.51	1.72	0.30	241
SnO <sub>2</sub> Ac-Pt/Rh	0.47	1.68	0.28	213

Deposition of noble metals causes remarkable changes in electronic structure of the blank material. As one can see from UV-VIS spectra (**Figure 38**) the materials doped with only one noble metal remarkably differ from that doped with bimetallic catalyst. Let us consider first the case of one noble metal (**Figure 38 a**).

The absorbance intensity between 230 and 300 nm is remarkably higher for these materials. All spectra are slightly red-shifted exhibiting their maxima in the region 250-260 nm. Doping with Rh and Pt brings about significant broadening of the band in the low-energy as well as in the high-energy region of vibrations. Deposition of Pd, in contrary, makes the adsorption band narrower in respect with blank SnO<sub>2</sub>, however, the band expands up to 500 nm.

For bimetallic catalysts absorption in the region 230-300 nm occurs in a lower degree comparing with monometallic catalytic systems. Instead, the absorption in low-energy region remarkably higher: the bands similarly expand up to 630 nm.

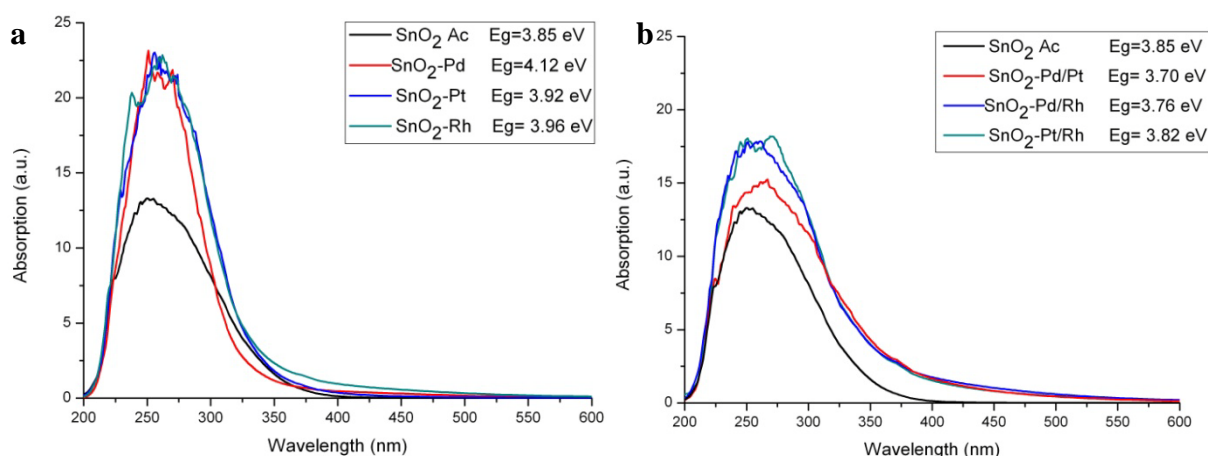


**Figure 38.** UV-VIS spectra of SnO<sub>2</sub> Ac-Pd, Pt, Rh (a) and SnO<sub>2</sub> Ac-Pt/Rh, Pd/Rh, Pd/Pt (b).

The difference between two catalytic systems (mono and bimetallic) can be either due to the effect of the second noble metal or because of different metal concentration in the material, since total content of the noble metals for the bimetallic system was set to 2 w.% (1% for each metal), whereas for monometallic catalysts – 1 w.%. Additional experiments are needed to assign the difference more accurately. However, it is known from the literature that increase of Pd content on TiO<sub>2</sub> results in gradual growth of the background absorption at wavelength larger than 400 nm due to absorption of metallic phase [169]. The latter (by example of Pd) is also characterized by adsorption in all UV-Vis range without definite structure [171]. Therefore we can assume that the effect of higher catalyst concentration should be expected mainly in the low-energy region and should not bring additional bands to the spectra.

From literature is also known, that highly dispersed forms of PdO exhibit signals at 250-260 nm and 410-420 nm [171]. Accordingly, the observed remarkable increase in this region for monometallic catalysts should be probably assigned to the dispersed particles of Pd, Pt and Rh oxides. The oxygen vacancies, formed upon catalyst doping (proved by XPS), should be considered as a possible source of contribution to the absorption in the range 400-600 nm. Among monometallic catalysts the highest absorption in this region demonstrated SnO<sub>2</sub>-Rh. The latter fact is in line with FTIR results.

Interesting tendency is observed for edge energies of the given materials. Again, the case of monometallic catalytic system is different from the bimetallic one. Deposition of one noble metal brings about increase of the optic band gap, while opposite phenomenon is observed upon doping with two metals. Apparently, the oxide formation in the case of monometallic materials, which increases electron acceptor states on the surface, dominates the generation of oxygen vacancies. In the case of bimetallic catalysts it is clear that metallic phase (formed either because of higher catalyst concentration or due to the mixed catalyst nature) plays principal role in the formation of new surface donor states.

### 4.2.3. Summary

All synthesized compounds represent polycrystalline material on the basis of SnO<sub>2</sub> cassiterite structure with particle sizes 4-8 nm and mean crystallite sizes 2-3 nm. In the case of surface doped SnO<sub>2</sub>, by example of Pd, it was found that noble metals are in the oxidized form and particle size is about 1-3 nm, which is comparable with crystallite size of the carrier.

The obtained results suggest that co-precipitation of SnO<sub>2</sub> with IVB metal oxides most probably results in formation of solid solutions, since cell parameters of the synthesized materials evolve in the same manner as it was expected from the comparison of Ti, Zr and Hf ionic radii. On the other hand, SnO<sub>2</sub> co-precipitation with IIIB oxides also results in lattice expansion. However, all compounds have roughly the same cell parameters, in spite of the fact that their ionic radii differ greatly from each other. The same effect was observed for SnO<sub>2</sub> surface doped with noble metals. This indicates that the synthesized compounds are mixed oxides (or in general – two-phase compounds), rather than solid solutions, with remarkable interphase interaction.

Hydroxylation degree was found to be slightly increased in the case of solid solutions, while mixed oxides demonstrated two and threefold rise of this parameter. FTIR results also evidenced that tin substitution with Ti, Zr and Hf results in gradual increase of OH basicity with increase of element atomic number, whereas mixed oxide did not exhibit any remarkable trend. As for catalyst doped oxides, the hydroxylation degree of Pt and Rh-doped SnO<sub>2</sub> is remarkably higher in respect with blank oxide. It seems that Rh deposition brings about intensive formation of oxygen vacancies on SnO<sub>2</sub> surface, since this phenomenon was found by example of SnO<sub>2</sub> Ac-Pd using XPS analysis.

UV-Vis absorption spectra of the solid solutions demonstrate remarkable decrease around 250 nm which was assigned to the decrease of charge transfer between tin ions and oxygen ligands due to tin substitution. This phenomenon was observed neither for mixed oxides, nor for tin dioxide with deposited noble catalysts. Edge energies of solid solutions gradually decrease with atomic number of elements, while this was not observed for mixed oxides. Deposition of one noble metal remarkably increases optic band gap of the materials, which is in line with fact that catalysts on the surface are in the form of oxides. The fact of oxygen vacancy formation (from XPS and FTIR) together with the latter finding suggests that oxygen from SnO<sub>2</sub> surface partially diffuse towards deposited phase to form noble metal oxides. In contrary bimetallic systems decrease  $E_g$ , suggesting that catalyst system demonstrate more metallic character.

Finally, we should point out that among mixed oxides SnO<sub>2</sub>-Y<sub>2</sub>O<sub>3</sub> demonstrates the most different case regarding all measured parameters: crystallite size (the lowest in the group), hydroxylation degree (also the lowest one) and optic band gap (again the lowest one). Analyzing and comparing all these features with the ones found for solid solutions it seems that in this system yttrium interacts with tin dioxide more than other IIIB elements, probably due to formation of yttrium stannate Y<sub>2</sub>Sn<sub>2</sub>O<sub>7</sub> with pyrochlore structure (see section 2.4.2, p. 47).

### **4.3. Material science: *in situ* characterization**

For the majority of the synthesized oxides *in situ* characterization was performed using TGA/DSC and TXRD techniques. The rest of the experiments were realized only for blank and Pd-doped materials. In the following parts the experiments are listed according to the following order: TGA, MS-study, TPR, DRIFT and TXRD

### 4.3.1. TGA analysis

The analysis was performed for all synthesized materials. Accordingly, the chapter consists of three parts dealing with solid solutions, mixed oxides and SnO<sub>2</sub> with deposited noble metals. The final part summarizes the results.

In this study TGA profiles are given as weight derivative against temperature and are used as main source of information. The features of the obtained TGA profiles were assigned with the help of additional MS experiment realized under the same conditions by example of SnO<sub>2</sub> Ac. In general two bands were observed for all materials: low-temperature band, assigned to molecular water desorption, and high-temperature one, corresponded to the recombinative desorption of bridging OH groups [107]. The mathematical analysis was performed only for the last band. Two parameters were used to compare:  $S$  – is the linear slope of the low-temperature side of the peak, and  $NA$  – is the normalized by weight area of the same peak, found as  $A_{OH}/w_{samp}$ , where  $A_{OH}$  – is the peak area and  $w_{samp}$  – is the sample weight. The parameter  $S$  allows one to estimate kinetics of water desorption which depends on the strength of the OH bonding to the surface. In other words, activity of hydroxyl groups can be estimated through OH desorption kinetics. The parameter  $NA$  can be used to evaluate water desorption quantity and therefore quantity of surface OH groups without contribution from the occluded hydroxyls, if compared with overall hydroxylation degree found by FTIR analysis.

#### 4.3.1.1. Blank materials

Blank materials synthesized from two different precursors manifest rather different desorption profiles (**Figure 39**). The main difference is related with quantity of desorbed water, estimated from the parameter  $NA$ : the value is lower by a factor of *ca.* 2 in the case of SnO<sub>2</sub> Ac (IV). Taking into account that hydroxylation degree was found also lower for this compound by a factor of two (from FTIR results), it becomes evident that content of inert or occluded hydroxyls is similar for both materials and seems rather low in comparison with chemically active OH groups. The desorption rate of the surface hydroxyl groups is slightly higher in the case of SnO<sub>2</sub> Ac, suggesting that chemical reactivity of the species should be expected slightly higher.



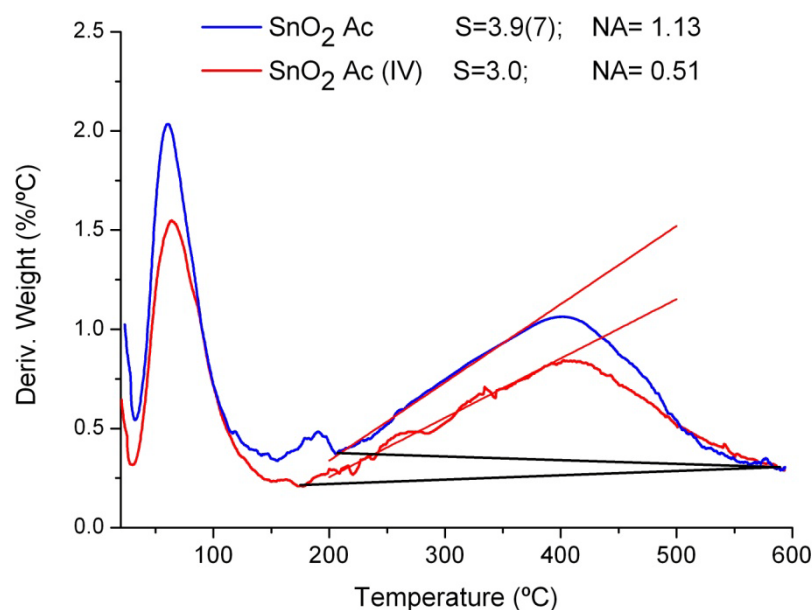


**Figure 39.** TGA profiles for SnO<sub>2</sub> Ac (a) and SnO<sub>2</sub> Ac (IV). *S* – slope of the fitted line, *NA* – normalized area of the desorption band.

Molecular water content is also higher in case SnO<sub>2</sub> Ac. However, this can be partially due to the storage conditions, in spite of the fact that all materials were stored similarly in the closed containers and underwent stabilization at RT before the experiment. In general, SnO<sub>2</sub> Ac seems much more hydrolyzed than SnO<sub>2</sub> Ac (IV) with more reactive hydroxyls.

#### 4.3.1.2. SnO<sub>2</sub>-MetO<sub>2</sub>, Met=Ti, Zr, Hf

**Figure 40** illustrates TGA profiles for the materials in question in comparison with blank SnO<sub>2</sub>. In general, solid solutions manifest increased affinity to water chemisorption in respect with blank material, which can be deduced from lower values of *S* and *NA*. This phenomenon is probably due to slightly higher surface polarity, induced by the admixtures. On the other hand hydroxylation degree, found by FTIR analysis, is remarkably higher than that of blank oxide, which suggests, in the light of the TGA experiment, that two-component compounds contain more occluded or very strongly bonded hydroxyl groups.

Analysis of TGA profile for SnO<sub>2</sub>-TiO<sub>2</sub> suggests that this material has the most chemically active hydroxyls in the group, which was estimated from the comparison of the chemisorbed water desorption rate. In the same time the material has remarkably less molecular water. As we have already mentioned, though, this parameter should be considered carefully, since its origin can be artificial.

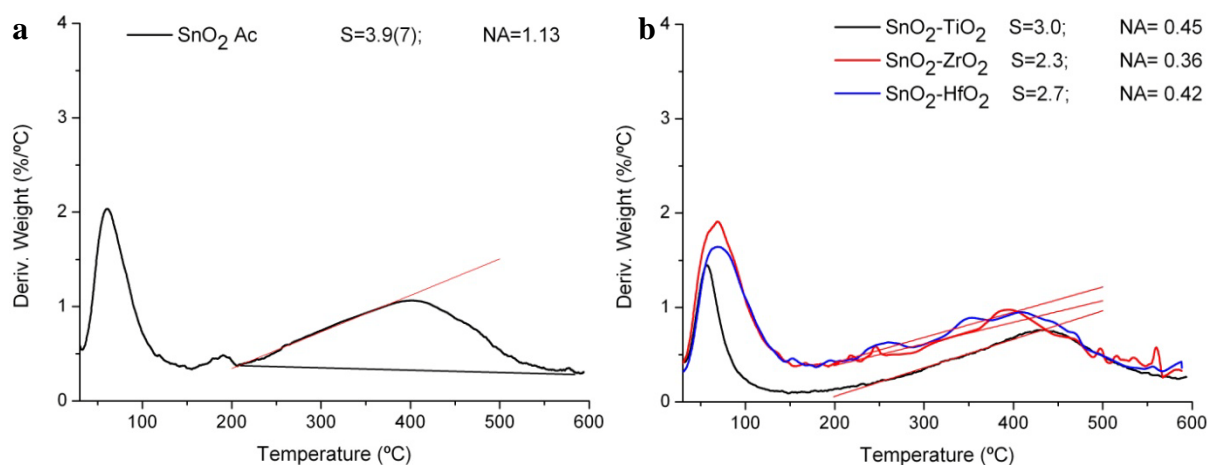


**Figure 40.** TGA profiles for SnO<sub>2</sub> Ac (a) and SnO<sub>2</sub> doped with IVB elements (b).  $S$  – slope of the fitted line,  $NA$  – normalized area of the desorption band.

Hafnia doped oxide demonstrates slightly lower chemical activity of OH groups, comparing with titania doped one. Among the materials SnO<sub>2</sub>-ZrO<sub>2</sub> manifests the lowest hydroxyl activity, and the lowest quantity of the desorbed water. These facts remarkably correspond to the hydroxylation degree of the solid solutions. The value, found by FTIR analysis, was the lowest for SnO<sub>2</sub>-ZrO<sub>2</sub> as well.

#### 4.3.1.3. SnO<sub>2</sub>-Met<sub>2</sub>O<sub>3</sub>, Met=Sc, Y, La

TGA profiles for SnO<sub>2</sub> doped with IIIB elements are shown in **Figure 41**. Again the case of SnO<sub>2</sub>-Y<sub>2</sub>O<sub>3</sub> differs from the rest of the materials: it has the lowest desorption rate and weight loss among two-phase compounds. In general, these systems manifest lower quantity of the desorbed water in respect with blank oxide. On the other hand, SnO<sub>2</sub>-Sc<sub>2</sub>O<sub>3</sub> and SnO<sub>2</sub>-La<sub>2</sub>O<sub>3</sub> show the highest desorption rate, which suggests that these oxide has the most chemically active OH groups.

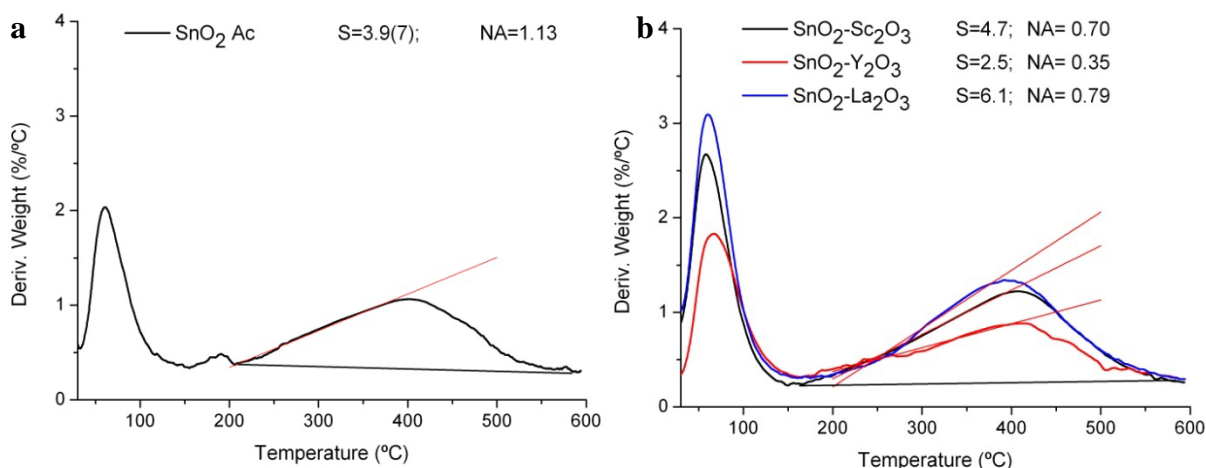


**Figure 41.** TGA profiles for SnO<sub>2</sub> Ac (a) and SnO<sub>2</sub> doped with IIIB elements (b). *S* – slope of the fitted line, *NA* – normalized area of the desorption band.

These facts together with hydroxylation degree of the materials which was found 2-3 times higher compared to blank oxide, suggest that hydroxyls are very heterogeneous in their nature and therefore consist of very reactive ones and occluded or chemically inert (strongly bonded to the surface) OH groups. SnO<sub>2</sub>-Sc<sub>2</sub>O<sub>3</sub> and SnO<sub>2</sub>-La<sub>2</sub>O<sub>3</sub> also manifest quite increased quantity of molecular water, which can contribute to the IR  $\nu_{OH}$  fundamental vibrations and therefore slightly change the ratio between reactive and inert surface hydroxyls.

#### 4.3.1.4. SnO<sub>2</sub> with deposited catalysts: Pd, Pt, Rh

Deposition of noble metals brings about remarkably higher rates of hydroxyl desorption in respect with blank material (**Figure 42**). In the case of monometallic catalysts the increase in desorption rate is accompanied with decrease of the desorbed water quantity. The lowest corresponding value was found for Pt and Rh-doped SnO<sub>2</sub>. Since for these very materials the hydroxylation degree was found the highest, we conclude that majority of surface hydroxyls is inert.

Bimetallic catalyst systems manifest outstanding reactivity of the hydroxyl groups, which are readily desorbed from the surface at a rate *ca.* 10 times higher than that observed for blank oxide. Another distinctive feature of these materials is related with the quantity of molecular and chemisorbed water. It seems that simultaneous deposition of two catalysts increases to a great extent dissociation of molecular water, which content is the lowest among all the synthesized materials. On the other hand the chemisorption water quantity is the highest in respect with monometallic systems as well as blank oxide.

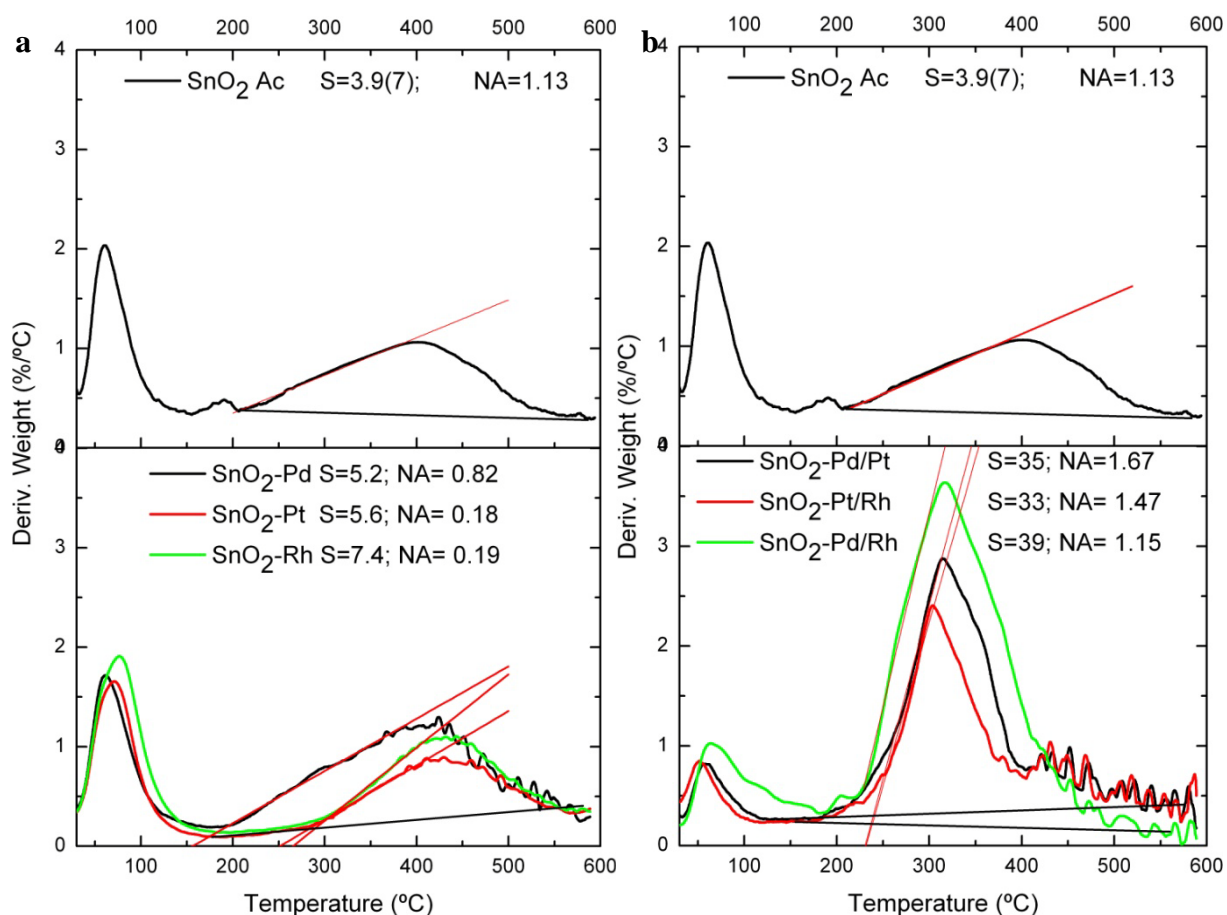


**Figure 42.** TGA profiles for monocatalytic (a) and bicatalytic (b) systems deposited on SnO<sub>2</sub> Ac in comparison with blank oxide. *S* – slope of the fitted line, *NA* – normalized area of the desorption band.

#### 4.3.1.5. Summary

With the help of TGA analysis, namely on the basis of desorption rate comparison, chemical activity of the hydroxyl groups was estimated. Among the materials doped with IVB elements, SnO<sub>2</sub>-TiO<sub>2</sub> demonstrates the most reactive OH groups. In contrary Zr and Hf doped oxides seem to firmly bond hydroxyls, which are therefore believed to be less active.

Among the materials doped with IIIB elements yttria doped SnO<sub>2</sub> again represents separate case, consisted in rather low activity of the hydroxyl groups. Doping with La and Sc in contrary has positive effect on OH chemical activity which can be compared with Pd-doped material.

Deposition of noble metal remarkably increases reactivity of the OH groups. It was found that majority of hydroxyl groups in the case of Pt and Rh-doped oxides are either occluded or inert. The most pronounced positive effect on OH group chemical activity was observed for bimetallic catalyst systems.

### 4.3.2. MS-study of the catalytic activity: H<sub>2</sub> oxidation in air

This investigation was performed for two materials: SnO<sub>2</sub> Ac and SnO<sub>2</sub>-Pd, and therefore permit us reveal the effect of deposited noble metal on hydrogen oxidation (0.3% in air). The results are given in the form of MS signals to hydrogen ( $MS_{H_2}$ , mass 2) and water ( $MS_{water}$ , mass 18) together with signal derivatives in **Figure 43** and **Figure 44**. Let us start first with hydrogen signals.

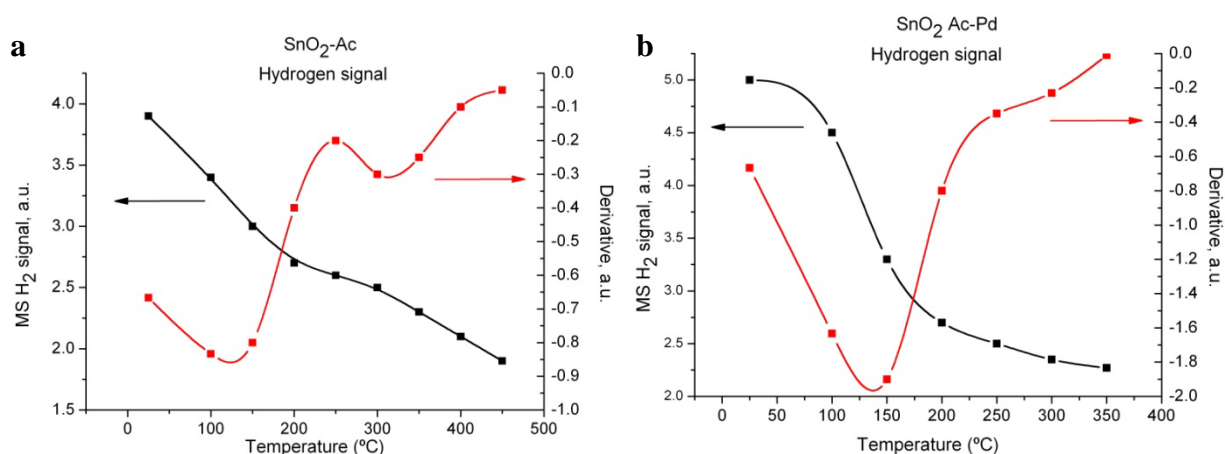


**Figure 43.** MS signals of hydrogen (black line) and signal derivative (red line) vs temperature of isothermal heating of SnO<sub>2</sub> Ac (a) and SnO<sub>2</sub>-Pd (b) in 3100 ppm of H<sub>2</sub> in air (black line MS)

Both materials manifest hydrogen consumption in the low-temperature region. For blank SnO<sub>2</sub> the maximum of the consumption occurs between 120 and 130 °C, while that for Pd-doped material at 130-140 °C. In the latter case the drop of H<sub>2</sub> concentration is more profound than was found for SnO<sub>2</sub> Ac (appr. by 2 times). However, this remarkable feature is the only one for SnO<sub>2</sub>-Pd, since another feature at *ca.* 300 °C is very faint. In contrary, blank material demonstrates another peak at higher temperatures: between 300 and 320 °C. The band expands up to 400 °C and represents reliable evidence of H<sub>2</sub> consumption in this region.

**Figure 44** illustrates evolution of MS signal to water in the same experiment. Again low-temperature peaks can be observed for both materials, with their maxima of water release between 125-135 °C and 145-155 °C in the case of SnO<sub>2</sub>-Ac and SnO<sub>2</sub>-Pd, resp. The bands are slightly shifted in respect with the ones found for H<sub>2</sub> consumption, and clearly correspond to the catalytic oxidation of hydrogen. If we compare normalized areas of the water peaks, it turns out that catalytic activity of Pd-doped material just in 2.0 times higher than that of blank SnO<sub>2</sub>.

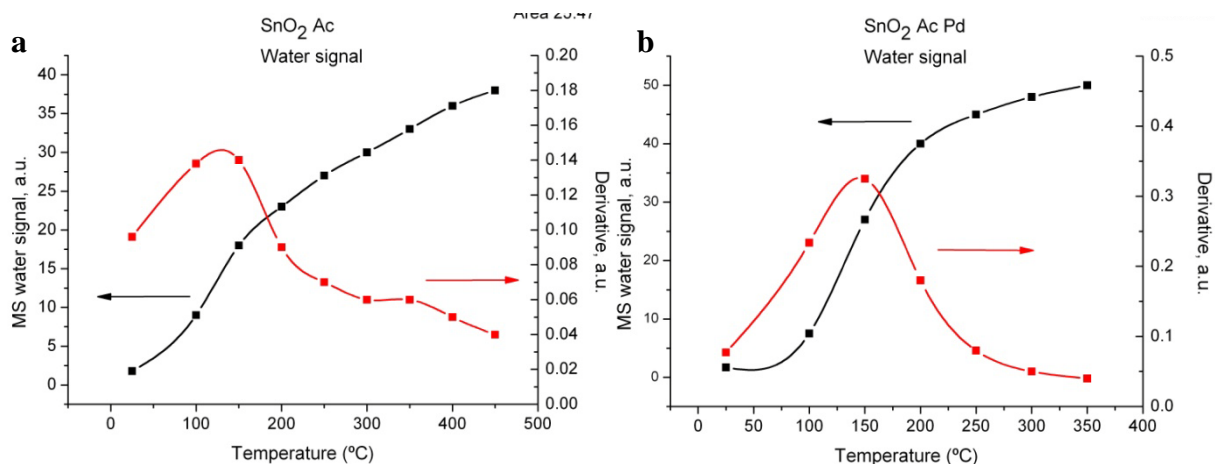


**Figure 44.** MS signals of water (black line) and signal derivative (red line) vs temperature of isothermal heating of SnO<sub>2</sub> Ac (a) and SnO<sub>2</sub>-Pd (b) in 3100 ppm of H<sub>2</sub> in air (black line MS)

Another striking feature is related with high temperature region of SnO<sub>2</sub> Ac. In spite of the fact that remarkable adsorption of H<sub>2</sub> was observed between 300-320 °C for this material, only a faint increase of water production can be seen around 350 °C. In other words increase in hydrogen consumption does not result in additional production of water.

To better estimate what kind of surface species can be involved in the oxidation process let us confront the obtained results with that of TGA. For both materials first pronounced peak of H<sub>2</sub> consumption and water formation occurs between 120 and 150 °C which corresponds to the region of TGA profile just after molecular water desorption, but before the onset of the chemical water desorption. This means that neither surface molecular water, nor OH groups are responsible for hydrogen oxidation under these conditions. On the other hand high-temperature peak of H<sub>2</sub> consumption in the case of blank material (300-320 °C) suggests that this process occurs through interaction with surface OH groups. Note that water production growth is scarce in this case. Bearing this in mind let us estimate stoichiometry of the observed reactions.

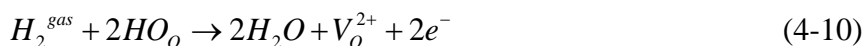
The water-to-hydrogen mole ratio was calculated using following formula:

$\frac{MS_{water} \cdot Mr(H_2)}{MS_{H_2} \cdot Mr(H_2O)}$ , the resulting value was plotted against temperature in **Figure 45**. Before

considering the results it is worthwhile to estimate possible reactions hydrogen oxidation. The classic reaction is based on hydrogen oxidation *via* surface oxygen species [172]:



In this case the water-to-hydrogen molar ratio will be close to the value of 1. On the other hand, hydrogen can also interact with surface hydroxyls in the case of hydroxylated surfaces:



For this scenario the ratio will be close to the value of 2.

From **Figure 45** one can easily see that for both materials hydrogen oxidation in the region 120-150 °C occurs according to equation (4-9) with water-to hydrogen ratio close to 1. Note that for blank material the ratio is lower, suggesting that consumed hydrogen partially remains on the surface.

At higher temperatures the ratio for both materials converges to the values higher than 2. This suggests that oxidation occurs predominantly through hydroxyl species. The ratio exceeds the theoretical one probably due to desorption of hydroxyl species formed at lower temperatures.

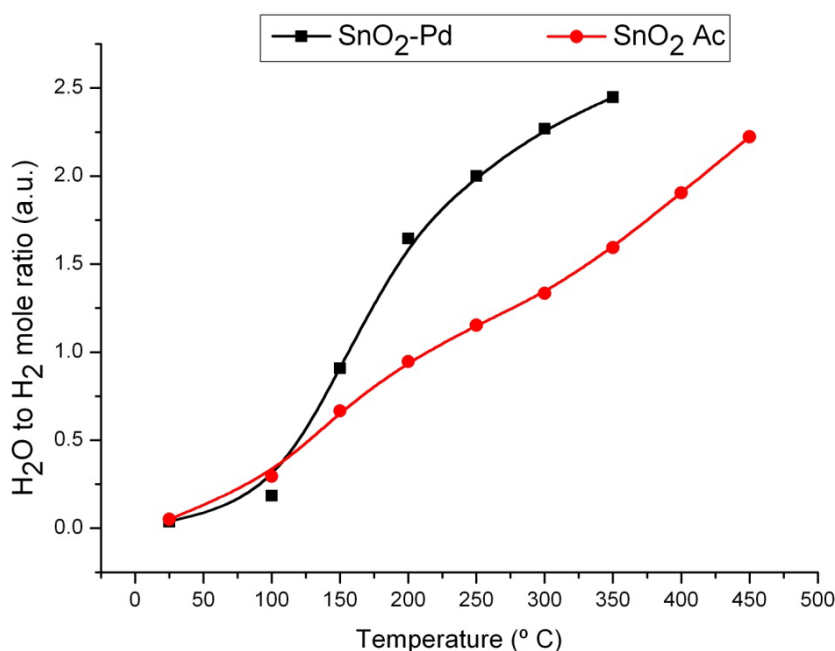


**Figure 45.** Stoichiometry of hydrogen oxidation represented as water to hydrogen mole ratio vs temperature.

Thus, from the obtained results it seems that both materials in the low-temperature region (120-150 °C) interact with H<sub>2</sub> through surface oxygen species according to Eq. (4-9). In the high temperature region (300-400 °C) both materials more likely interact with hydrogen through surface hydroxyls according to Eq. (4-10).

The found stoichiometry in the low-temperature region is in line with TGA results, since the temperature of the most intense H<sub>2</sub> consumption and water production for both materials lies before desorption of surface OH groups and high temperature hydrogen oxidation corresponds to the intense desorption of chemisorbed water.

High values of water-to-hydrogen ratio at high temperatures indicate that in addition to the direct water formation from the consumed hydrogen there is another source of water in the



system. The latter can be related with intrinsic hydroxyl groups or/and the hydroxyls formed upon hydrogen irreversible adsorption at lower temperatures. The latter can significantly decrease the water production, which was observed in the case of blank material.

Note that found stoichiometry is not a real, but apparent one, since processes like H<sub>2</sub> irreversible chemisorption at low temperatures and desorption of the resulting hydroxyls at higher temperatures can change remarkably the water-to-hydrogen ratio.



### 4.3.3. TPR

This study was performed for synthesized and commercial oxides (both blank and Pd-doped) under two different conditions: true reduction, comprised sample heating in the gas mixture of 5% H<sub>2</sub> in argon, and pseudo-reduction – sample was heated in 0.1% H<sub>2</sub> in air. Accordingly this chapter is divided into two parts, dealing with the specified regimes. The final part summarizes the obtained results.

Before considering the results, it is worthwhile to dedicate some attention to the thermal conductivity detector (TCD) used in this study to estimate hydrogen consumption during heating. This detector is known to be not very selective, since thermal conductivity of different gases can be similar. Thermal conductivity of hydrogen is approximately 8 times as high as that of water: 230 against 27 mW/KT (at 400 K) [173]. However, the latter should be expected to be not only the main product of the hydrogen oxidation, but the product of thermal desorption from oxide surface at temperatures higher than 120 °C (pre-treatment temperature). Unfortunately the corresponding experiments to reveal the impact of water desorption on TCD signal has not been performed. Thus, considering the following results, especially TPR in the presence of oxygen and low hydrogen concentration, we should not forget that the observed features can be partially due to water desorption. Accordingly it is difficult to compare the results with that of MS-study.

#### 4.3.3.1. 5% H<sub>2</sub> in argon

TPR profile of SnO<sub>2</sub> Ac displays one broad intense peak at 360 °C, followed by the onset of bulk reduction starting from 550 °C (**Figure 46, a**). Commercial SnO<sub>2</sub> shows a different profile with small peak around 200 °C and bulk reduction starting from 450 °C. The low-temperature reduction peak can be attributed to the reduction of surface and subsurface of SnO<sub>2</sub>, while the bulk reduction of SnO<sub>2</sub> is observed at higher temperature (>500 °C).

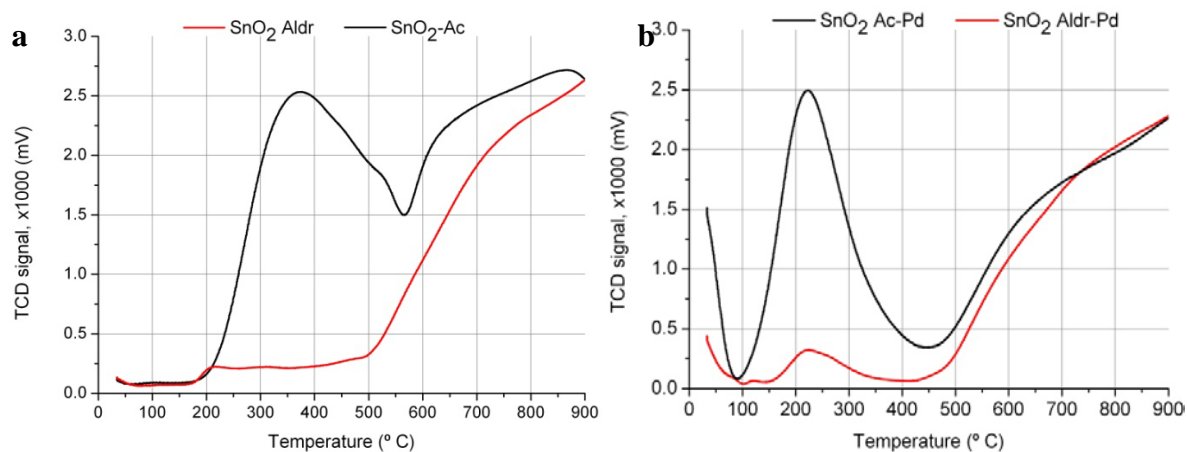


**Figure 46.** TPR profiles of SnO<sub>2</sub> Aldr, SnO<sub>2</sub> Ac (a) and SnO<sub>2</sub>-Pd, SnO<sub>2</sub> Ac (b) in 5% H<sub>2</sub> in Ar.

Deposition of 1 % of Pd changes remarkably the TPR profile of the synthesized SnO<sub>2</sub> (**Figure 46**, b). Namely, the band corresponded to the surface reduction shifts from 360 °C to 220 °C and becomes more detached from that assigned to the bulk reduction. The H<sub>2</sub> oxidation already starts at 100 °C and goes on up to 400 °C, demonstrating significant decrease in activation energy of the oxidation processes.

In the case of SnO<sub>2</sub> Aldr-Pd the changes are less pronounced. The peak corresponded to the surface reduction has appeared in the same region as for SnO<sub>2</sub> Ac-Pd. Peak maximum positions are same for both materials (*ca.* 220 °C), which indicates that nature of the active species is pretty similar. However, judging by peak intensity it seems that their surface concentration is very different.

#### 4.3.3.2. 0.1% H<sub>2</sub> in air

Presence of oxygen in the gas phase drastically changes the TPR profiles. The band corresponded to the irreversible surface reduction in the oxygen absence should be assigned now to the hydrogen oxidation by surface active species. In the case of synthesized blank material this process starts at *ca.* 100 °C and reaches its maximum between 240 and 270 °C (**Figure 47**, a). The band is broad and extends up to 470 °C. Commercial material manifests lower catalytic activity with one faint and broad band with maximum between 340 and 360 °C.

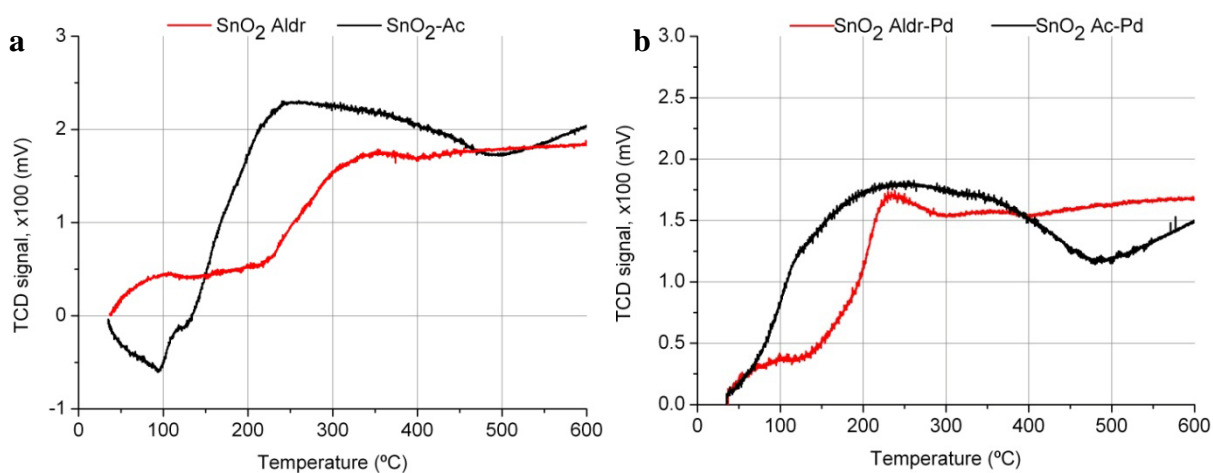


**Figure 47.** TPR profiles of SnO<sub>2</sub> Aldr, SnO<sub>2</sub> Ac (a) and SnO<sub>2</sub>-Pd, SnO<sub>2</sub> Ac (b) in 0.1% H<sub>2</sub> in air.

Doping with the catalyst again brings about low-temperature features: hydrogen consumption for synthesized SnO<sub>2</sub> starts already at 50 °C, and in the case of commercial material – at *ca.* 140 °C. The broad band of SnO<sub>2</sub> Ac-Pd suggests that either active species are different in

nature or that we face the interference from water. Note, that band intensities for SnO<sub>2</sub> Ac and SnO<sub>2</sub> Ac-Pd are very similar as well as in the absence of oxygen.

#### **4.3.3.3. Summary**

From the results one can easily see that materials on the basis of SnO<sub>2</sub> Ac demonstrate higher catalytic activity in respect with commercial SnO<sub>2</sub>. Doping with palladium brings about formation of very active surface species which are manifest catalytic activity in the low-temperature region. Considering the case of SnO<sub>2</sub> Ac-Pd, these active sites seem to be the only ones responsible for hydrogen consumption in the absence of oxygen.

When oxygen is available in the gas phase the band corresponded to H<sub>2</sub> consumption becomes very broad, suggesting either heterogeneous nature of surface active species, or interference from the water production.

### 4.3.4. DRIFT spectroscopy

This chapter is dedicated to the DRIFT experiment performed to study interaction of water, hydrogen and their mixtures with blank and Pd-doped SnO<sub>2</sub> Ac. The chapter is divided into four parts dedicated to analysis of the spectra recorded in dry air, 0.01% H<sub>2</sub> in dry air and 2.1% H<sub>2</sub>O in air. The final part summarizes the results.

#### 4.3.4.1. Dry air

**Figure 48** shows the IR absorbance spectra at various temperatures for blank and Pd doped SnO<sub>2</sub> in dry air. The spectra were obtained using following equation:  $A = -\lg\left(\frac{S_T}{S_{RT}}\right)$ , where  $A$  is the absorbance intensity,  $S_{RT}$  is the single channel spectra obtained at RT, and  $S_T$  is the single channel spectra obtained at higher temperatures. Thus, the observed features represent the effect of temperature on SnO<sub>2</sub> materials.

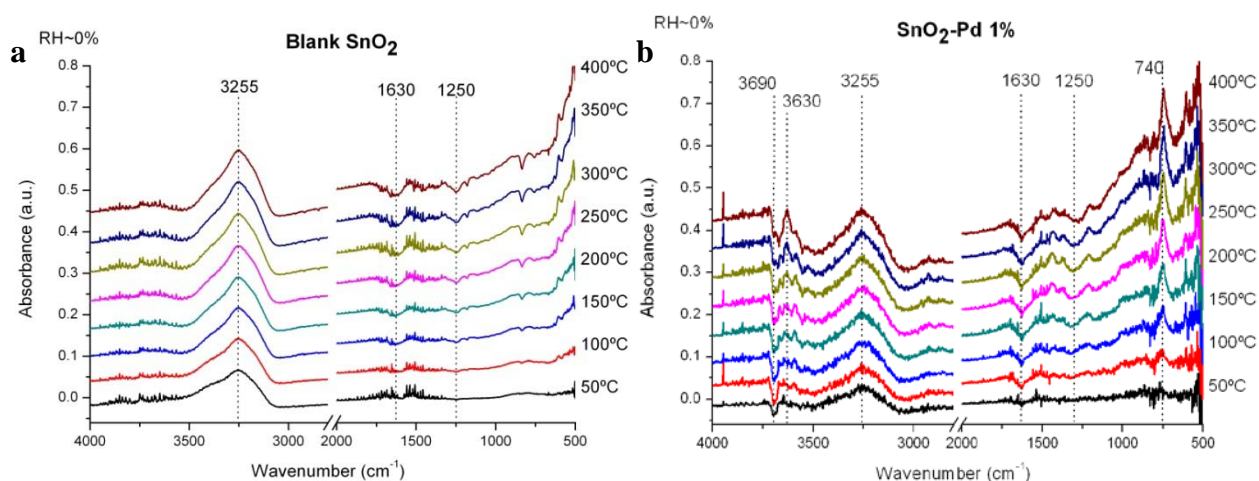


**Figure 48.** Variation in the absorbance spectra of blank (a) and Pd doped (b) SnO<sub>2</sub> in dry air as a function of temperature.

Both samples have common features including an increase of an intense, broad band between 3500-3070 cm<sup>-1</sup> with a peak at 3255 cm<sup>-1</sup> and negative absorption bands at 1630 and 1250 cm<sup>-1</sup>. The band at 3255 cm<sup>-1</sup> can be assigned to the family of bridged OH groups, which interact with neighbouring oxygen atoms *via* hydrogen bonds, rather than to the physisorbed water [103, 174, 175]. This assignment is consistent with the fact that the band at 3255 cm<sup>-1</sup> evolves with temperature, reaching intensity maximum at 350-400 °C (for both materials). In contrast, in the region corresponded to the water deformation mode (~1630 cm<sup>-1</sup>), a negative adsorption is observed which becomes more pronounced at higher temperatures.

These hydroxyls are believed to be partially occluded in the bulk or near-surface region, which make them inaccessible to chemisorbed species [106]. The band intensity was much higher for blank SnO<sub>2</sub> and increased remarkably upon temperature increase for both materials. The negative absorption around 1630 cm<sup>-1</sup> is attributed to OH deformation vibrations in molecular water [103, 176], whilst the loss of absorption at 1250 cm<sup>-1</sup> corresponds to the consumption of terminal OH groups upon water thermodesorption.

Unlike the blank material, the Pd doped sample demonstrates a wide-range of negative absorptions between 3500 and 3700 cm<sup>-1</sup> starting from 50 °C. However, by 300 °C the absorption band at 3630 cm<sup>-1</sup> was observed to increase. Vibrations in this region are usually assigned to the stretching vibrations of terminal OH groups [103, 112, 177].

Another distinctive feature of the doped material was a sharp and intense peak at 740 cm<sup>-1</sup>, which has been attributed to the asymmetric stretching vibrations of surface bridging oxygen between Sn cations, (Sn-O-Sn) [103]. These are believed to be formed by condensation of adjacent surface hydroxyls upon heating [178].

#### 4.3.4.2. 0.01% H<sub>2</sub> in dry air

**Figure 49** shows the DRIFTS spectra at 100 ppm of H<sub>2</sub> in dry air as a function of temperatures where the absorbance was calculated by:  $A = -\lg\left(\frac{S_{HYD}}{S_{AIR}}\right)$ , where  $A$  is the absorbance intensity,  $S_{HYD}$  is the single channel spectrum obtained in 100 ppm of H<sub>2</sub> in dry air at a certain temperature, and  $S_{AIR}$  – the single channel spectrum obtained in dry air at the same temperature.

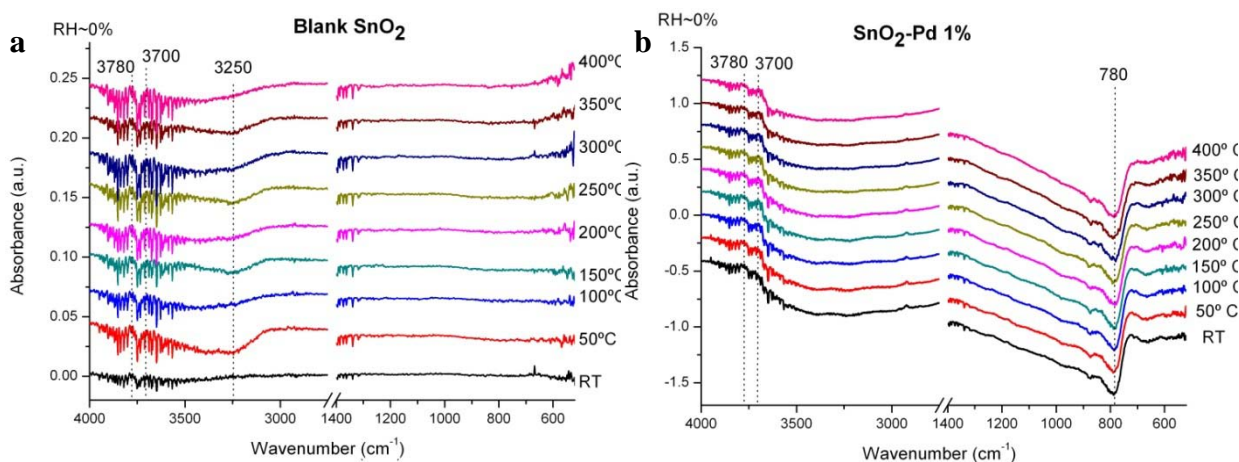


**Figure 49.** Variation of the absorbance spectra of blank (a) and Pd doped (b) SnO<sub>2</sub> in the presence of 100 ppm of H<sub>2</sub> in dry air as a function of temperature.

Again, the spectra of the blank SnO<sub>2</sub> demonstrate features related only with hydroxyls: broad consumption of bridging groups at ~3250 cm<sup>-1</sup> and the formation of terminal hydroxyls at 3700 and 3780 cm<sup>-1</sup>. The blank SnO<sub>2</sub> shows significantly different spectra with hydrogen compared with water. No intense formation of terminal hydroxyls (especially in the region 1160-1330 cm<sup>-1</sup>) and no formation of bridging hydroxyls was observed. In contrast, the Pd doped sample showed almost the same behaviour for both gases with only a slight increase in terminal hydroxyls (at 3700 and 3780 cm<sup>-1</sup>) upon exposure to hydrogen.

#### 4.3.4.3. 2.1% H<sub>2</sub>O in air

**Figure 50** shows the effect of a humid atmosphere on the absorption spectra of the materials as a function of temperature. The spectra were obtained using following equation:

$$A = -\lg\left(\frac{S_{RH}}{S_{DRY}}\right),$$

where  $S_{RH}$  is the single channel spectrum obtained in humid air at a given temperature and  $S_{DRY}$  is the single channel spectrum obtained in dry air at the same temperature.

temperature and  $S_{DRY}$  is the single channel spectrum obtained in dry air at the same temperature.

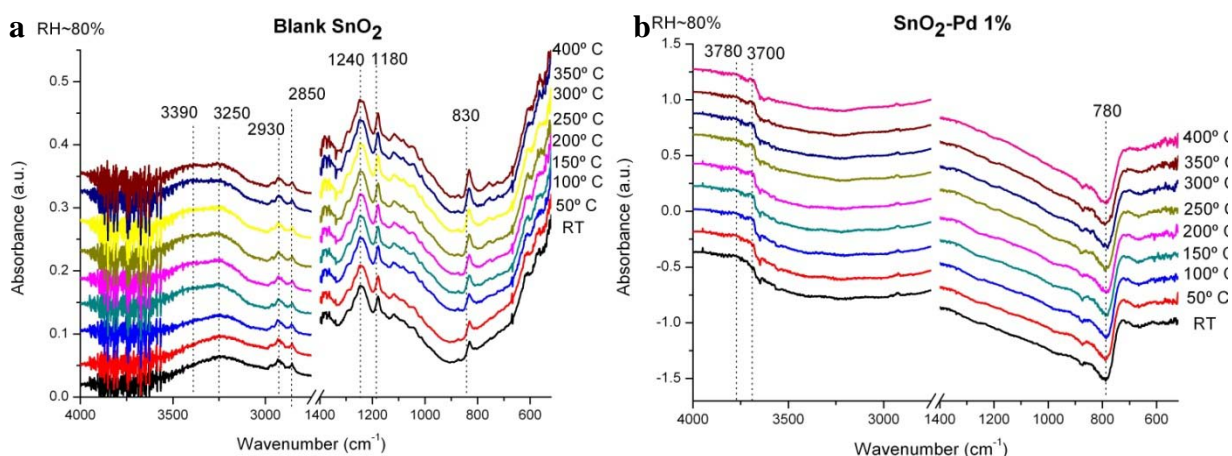


**Figure 50.** Variation of the absorbance spectra of blank (a) and Pd doped (b) SnO<sub>2</sub> at 80% RH as a function of temperature.

In the case of blank SnO<sub>2</sub> it is clear that surface interaction with water vapor results in the formation of terminal hydroxyls associated with the intense peaks in the region 1160-1330 cm<sup>-1</sup> due to deformation vibrations of terminal hydroxyls and an increase in the bridging OH groups at 2900-3500 cm<sup>-1</sup> [103]. The spectra of the Pd doped samples are much simpler. The features at 3630 and 740 cm<sup>-1</sup>, observed in dry air, disappear in the presence of water vapour and only broad and intense absorption losses at these wavenumbers were observed. On the basis of previously



reported data, the weak features at 3700 and 3780 cm<sup>-1</sup> are thought to be due to terminal hydroxyls [103, 106, 174, 179].

#### 4.3.4.4. Summary

Thus, the obtained results evidence that highly hydroxylated surface of the blank SnO<sub>2</sub> reacts with hydrogen predominantly through bridging hydroxyls independently of the water content in the gas phase even in the low-temperature region. Prima facie this result contradicts with that of MS-study, where we found out that in the region 120-150 °C the water-to-hydrogen ratio amounts *ca.* 0.7 and this suggested the surface oxygen was involved in the oxidation process. However, low stoichiometry ratio could be the result of hydrogen chemisorption without formation of water, and therefore real stoichiometry could be considerably higher.

In contrast to the blank oxide, the hydrogen interaction with the Pd doped material depends on the water concentration: while at low RH (up to 20%) the hydrogen oxidation seems to realize through bridging oxygen in the whole temperature range (which is again slightly differs with the results of MS-study), at high RH (*e.g.* 50 and 80%) the oxidation occurs through surface hydroxyls.

For Pd-doped material intense consumption of bridging oxygen together with formation of terminal OH groups occurs upon exposure to water vapour as well as to hydrogen. All the corresponding bands are observed starting from RT (**Figure 50** **Figure 49**). To better resolve the features, which overlap with the intense bands at 780 and 3700 cm<sup>-1</sup>, a normalization procedure using the RT spectra as a background was performed (Figure 51).

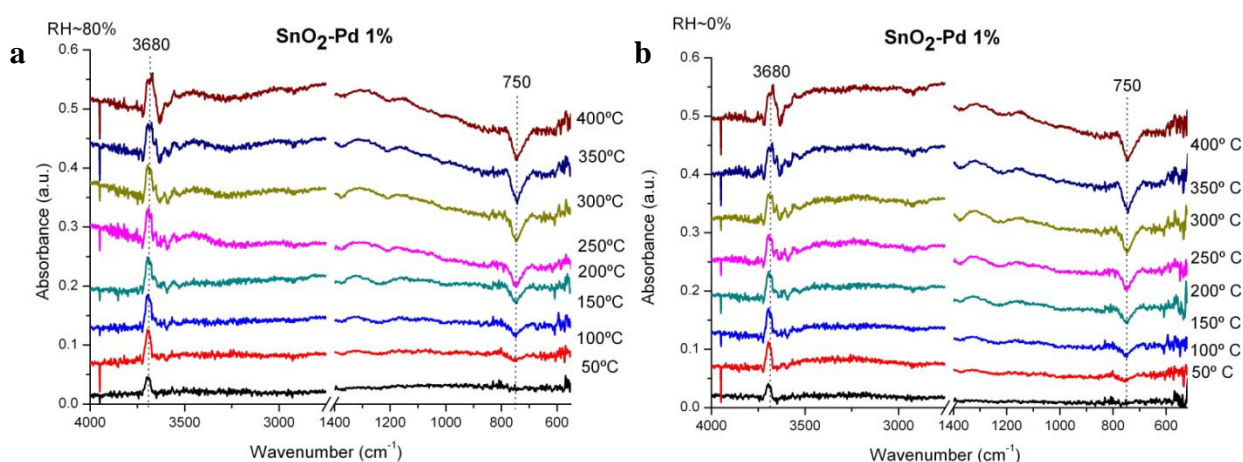


**Figure 51.** Normalized DRIFT spectra of SnO<sub>2</sub>-Pd in air with 25800 ppm of H<sub>2</sub>O (a) and 100 ppm of H<sub>2</sub> (b).

From these spectra in the low temperature region (up to 200 °C), both gases interact identically with the surface, producing new terminal OH groups (stretching vibrations at 3680 cm<sup>-1</sup> and weak deformation vibrations between 1350 and 1250 cm<sup>-1</sup>) and consuming the bridging oxygen (absorption loss at 750 cm<sup>-1</sup>). The formation of the bridging hydroxyls shown by the broad band at ~3450 cm<sup>-1</sup> in both cases only becomes noticeable at temperatures above 200 °C, suggesting a minor role in the processes related with increasing conduction at around 140 °C.



### 4.3.5. TXRD study of crystallite growth kinetics

Earlier we have found, that the proposed method allows one to synthesize tin dioxide based materials with particle size 4-8 nm. The latter consist of crystallites with mean diameter 2-3 nm. However, as it was already mentioned, structures with the size of several nanometers are non-equilibrium formations due to coordinatively unsaturated surface, and therefore demonstrate poor thermal stability.

Several methods allow us to evaluate thermal stability of the nanodispersed materials, among them *in situ* X-ray diffraction, which provides a reliable characterization of the growth processes during powder annealing [154]. On the basis of the diffraction line broadening analysis, which comprises reflection fitting in the whole range of the diffraction pattern, one calculates mean crystallite size as a function of time and temperature of the annealing.

This chapter is dedicated to discussion of the results of TXRD study applied to reveal factors causing poor thermal stability of synthesized materials, comparing their kinetics of crystallite growth. The latter can be estimated from the crystallite size evolution applying various models. Comparative analysis of two models is given by example of blank SnO<sub>2</sub> in the first part of this chapter. The second part is dedicated to the impurity effect on crystallite growth kinetics. Here we compare Cl, S, Pd and NaCl doped SnO<sub>2</sub>. Once the role of impurities has been established, we compare thermal stability of solid solutions, mixed oxides and some catalyst doped materials in the following parts. Summary of the study is given in the last part.

#### 4.3.5.1. Comparison of kinetics models by example of SnO<sub>2</sub> Ac

Early considerations of isothermal crystallite growth kinetics assumed asymptotic power-law dependency of the crystallite size change on annealing time (*generalized parabolic model*):

$$D^n - D_0^n = kt, \quad (4-11)$$

where  $D_0$  is the initial crystallite size at annealing time  $t = 0$ ,  $D$  – crystallite size at time  $t \neq 0$ ,  $k$  – rate constant, which is a function of the activation energy of isothermal growth,  $n$  – crystallite size exponent and  $t$  – annealing time. The empiric parameter  $n$  depends on diffusion mechanism: in the case of  $n = 3$  volume diffusion mechanism is believed to be predominant, when  $n = 4$  surface diffusion governs crystallite growth [22].

Later, the model was modified by including a drag term, which took into account the solute drag effect and limiting crystallite size [180]. Finally, Michels et al. [181] demonstrated that retardation effect caused by pores or impurities with low mobility should depend on crystallite size (*grain growth model with size-dependent impediment*):

$$D(t) = \sqrt{D_{lim}^2 - (D_{lim}^2 - D_0^2) \exp(-2At / D_{lim}^2)} \quad (4-12)$$

where  $D_{lim}$  – limiting crystallite size and  $A$  – constant, which is the product of specific interface energy and crystallite boundary mobility.

Two models we used to fit the experimental values of mean crystallite size evolution under isothermal conditions at 600, 700 and 800 °C. **Figure 52** illustrates of the fitting procedure. To compare the fit results we used the residual sum of square ( $\chi^2$ ), known as reliable parameter to estimate the goodness-of-fit. For good fitting model this parameter should be minimized. The closer the fit is to the experimental points, the closer  $\chi^2$  will be to 0. This parameter was used as a built-in function in Origin 8 software.

In spite of the fact that *generalized parabolic model* fits experimental data slightly better, the difference between two models is lower than experimental error and therefore both models can be used for analysis. The obtained parameters are listed in **Table 22**. In *generalized parabolic model* the obtained values of size exponent exceed remarkably the acceptable range, which is normal for nanomaterials, but can hardly be explained from the physical point of view [180-183].

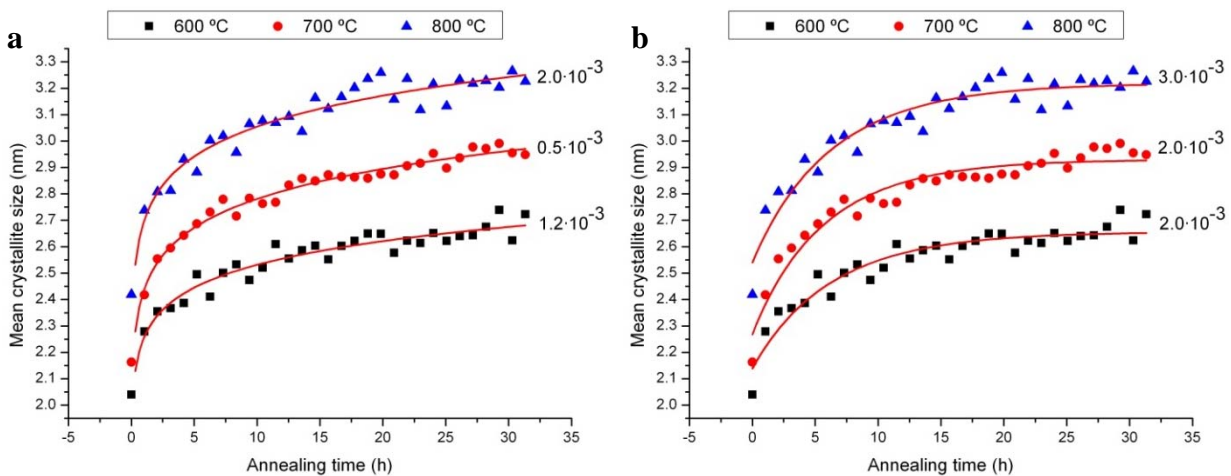


**Figure 52.** Time evolution of mean crystallite size of blank SnO<sub>2</sub> at 600, 700 and 800 °C: experimental data are fitted with generalized parabolic model (a), and with size-dependent impediment model (b). The values of  $\chi^2$  are shown close to the fit curves.

On the other hand using *size-dependent impediment model* we obtain fitting parameters which is of the same order of magnitude reported in literature. Accordingly, we have two values with clear physical meaning: constant  $A$  – related with specific interface energy and crystallite boundary mobility, and  $b$  is the drag parameter (defined as  $A/D_{lim}^2$ ), which allows one to estimate the extent of the growth impediment by increasing size of the crystallite. Since key idea of the

model is based on assumption that increased crystallite size decreases grain-boundary volume and therefore results in concentration of impurities in the grain boundaries, we can deduce that  $b$  indirectly reflects the impediment by the segregated second phase [180, 181].

**Table 22.** Fitting parameters of the models in question.

Model	T, °C	$k$	$n$	$A$	$D_{lim}$ , nm	$b$ , s <sup>-1</sup>
<i>Generalized parabolic</i>	600	2.25(2)	20(1)	-	-	
	700	2.43(1)	17(1)	-	-	
	800	2.69(2)	18(1)	-	-	
<i>Size-dependent impediment</i>	600	-	-	0.52(7)	2.65(2)	0.074(3)
	700	-	-	0.69(7)	2.93(1)	0.080(3)
	800	-	-	0.76(9)	3.22(2)	0.073(5)

Taking into account the obtained results we deem that model with size-dependent impediment should be the most appropriate and handy way to describe and analyze the crystallite growth kinetics of nanomaterials. Accordingly, we decided to use *size-dependent impediment model* in all our following analysis.

Constant  $A$  from equation (2) can be used to estimate apparent activation energy of the crystallite growth [180, 181]:

$$TA \propto \exp(-Q/RT) \quad (4-13)$$

where  $T$  – temperature,  $R$  – gas constant and  $Q$  – activation energy.

The obtained value of apparent activation energy for blank SnO<sub>2</sub> amounts to 23(2) kJ/mol, which is lower comparing with that found in literature for nanocrystalline SnO<sub>2</sub>: 31 kJ/mol (calculated using relaxation model) [183].

Since  $A$  is the product of specific interface energy (which is supposed to be more dependent on material nature, rather than temperature) and crystallite boundary mobility, it is reasonable to deduce that low activation energy of crystallite growth should be mainly due to boundary mobility. The latter is closely related with diffusion of mobile species in the crystalline lattice [22]. Taking this into account let us consider activation energies for oxygen and tin self-diffusion in SnO<sub>2</sub>.

Activation energies for oxygen self-diffusion in single-crystalline SnO<sub>2</sub> are higher in comparison with our results. For example, Kamp *et al.* reported values *ca.* 100 kJ/mol [184]. Even though data on tin self-diffusion in SnO<sub>2</sub> are scarce in the literature, it is known that diffusion of interstitial metal ions is lower than that of oxygen in the case of TiO<sub>2</sub> [185] (including nonstoichiometric TiO<sub>2-x</sub> [186]) and ZnO [187]. Therefore we can assume that diffusion of tin ions is more probable in the oxide, especially if we take into account that upon heating SnO<sub>2</sub> surface loses oxygen and becomes more metallic. Apparent activation energy, obtained for crystallite growth of blank SnO<sub>2</sub>, was found to be very close to that of self-diffusion in the metallic tin: 24.7 kJ/mol [188]. Thus, it is possible to assume that growth of the highly defective crystallites occurs through diffusion of tin atoms, rather than through oxygen ones. Therefore, tin self-diffusion on the Sn-rich surface can be an explanation to the low activation energy. Other explanations can be related with relaxation phenomenon in highly defective nanostructures, as was proposed in [183].

#### 4.3.5.2. Impurity effect

Impurity effect was studied by example of tin dioxide precipitated in the presence of HCl, H<sub>2</sub>SO<sub>4</sub> and NaCl. Results of element analysis for the synthesized materials are shown in **Table 23**. The XRD patterns were recorded at 700 °C and were used to calculate mean crystallite size.

**Table 23.** Weight content of the target admixtures in synthesized materials.

Sample name	Cl, ppm	S, ppm	Na, ppm
SnO <sub>2</sub> Ac	222	22	179
SnO <sub>2</sub> -Cl	<b>380</b>	20	110
SnO <sub>2</sub> -S	110	<b>360</b>	180
SnO <sub>2</sub> -NaCl	<b>466</b>	20	<b>322</b>

Fitting of the experimental model was performed with *size-dependent impediment model*; the results are shown in **Figure 53**. As it can be seen from the fitting results the model fits worse the experimental data for doped materials, however can be still applied (**Figure 54**). The reason for this can be the concept of limiting crystallite size ( $D_{lim}$ ) used in the model. For SnO<sub>2</sub>-NaCl the standard error of this parameter is the highest among the rest of materials: 0.6%. Of course this is acceptable, but this fact indicates that SnO<sub>2</sub>-NaCl crystallites do not reach their limiting size as fast as blank material, and still gradually grow after 30 h of annealing.

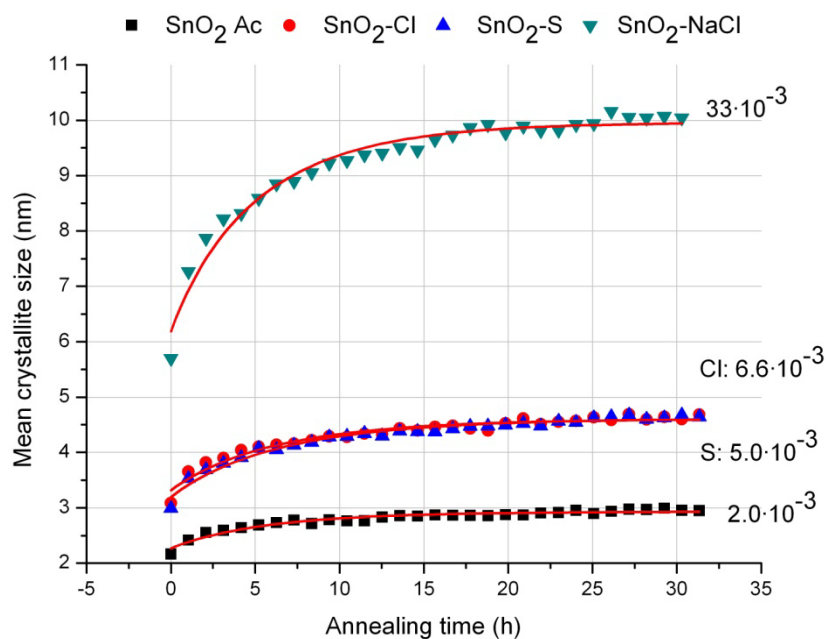


**Figure 53.** Time evolution of mean crystallite size of blank SnO<sub>2</sub>, SnO<sub>2</sub>-Cl, SnO<sub>2</sub>-S and SnO<sub>2</sub>-NaCl at 700 °C. The values of  $\chi^2$  are shown close to the fit curves.

It was found that doping with chlorine and sulphur ions increases growth rate almost identically in respect with SnO<sub>2</sub> Ac. Comparing fitting parameters from **Table 24** one can see that impurities drastically increase constant  $A$  (specific interface energy and crystallite boundary mobility), rather than play drag role in the growth processes.

**Table 24.** Fitting parameters of the model.

Sample name	$A$	$D_{lim}$ , nm	$b$ , s <sup>-1</sup>
SnO <sub>2</sub> Ac	0.69(7)	2.93(1)	0.080(3)
SnO <sub>2</sub> -Cl	1.5(1)	4.60(3)	0.072(1)
SnO <sub>2</sub> -S	1.4(1)	4.61(3)	0.068(1)
SnO <sub>2</sub> -NaCl	8.3(6)	9.96(6)	0.084(1)

The highest decrease of SnO<sub>2</sub> thermal stability was observed in the case of SnO<sub>2</sub>-NaCl. Parameter  $A$  for this material was found 8.3(6), which is more than by 12 times higher than that of blank material. This indicates that poor thermal stability is caused not only by increased concentration of some impurities, but rather by combination of some impurities like Na and Cl. Note, that while Cl and S decrease drag parameter, doping with NaCl slightly increase it,

comparing with blank SnO<sub>2</sub>, suggesting that phase of NaCl act as drag component once it has segregated on crystallite surface [180].

### 4.3.5.3. Comparison of synthesized compounds SnO<sub>2</sub>-MetO<sub>x</sub>

Doping with IIIB and IVB elements increase remarkably crystallite growth rate. The general tendency is that the lightest elements in the groups – Sc and Ti – exert growth rate in a higher degree than other elements.

Again, the model fits the experimental results with different goodness, mainly due to deviation of the calculated value of  $D_{lim}$  from the experimental one. In the case of SnO<sub>2</sub>-Sc<sub>2</sub>O<sub>3</sub> and SnO<sub>2</sub>-La<sub>2</sub>O<sub>3</sub> crystallites reach their limiting size after *ca.* 20 h, while for SnO<sub>2</sub>-Y<sub>2</sub>O<sub>3</sub> (note, that this compound again differ from other materials doped with IIIB elements) and solid solutions the growth rate increases almost linearly after *ca.* 20 h, without reaching limiting size. Nevertheless,  $\chi^2$  is still low and indicates that the probability of the model confidence is very high (Figure 54).

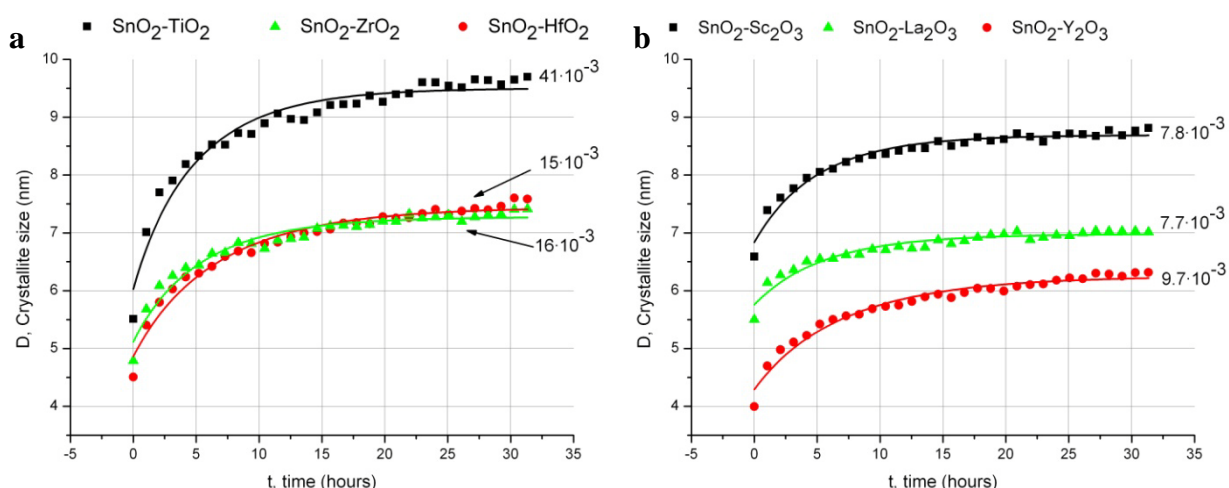


**Figure 54.** Time evolution of mean crystallite size of SnO<sub>2</sub>-TiO<sub>2</sub>, SnO<sub>2</sub>-ZrO<sub>2</sub>, SnO<sub>2</sub>-HfO<sub>2</sub>(a) and SnO<sub>2</sub>-Sc<sub>2</sub>O<sub>3</sub>, SnO<sub>2</sub>-Y<sub>2</sub>O<sub>3</sub>, SnO<sub>2</sub>-La<sub>2</sub>O<sub>3</sub> (b) at 700 °C. The values of  $\chi^2$  are shown close to the fit curves.

Let us consider first the case of solid solutions. From **Table 25** it can be seen that both *A* and *b* parameters decrease gradually with increase of ionic radius of IVB element. The results suggest that crystallite growth occur mainly due to migration of admixtures, which rate is supposed to be a function of ion size. A combination of the lowest growth rate and the lowest drag term in the case of doping with Hf (the largest ionic radius in the group) supports this assumption. On the other hand high value of drag parameter for SnO<sub>2</sub>-TiO<sub>2</sub> is probably due to

segregation of TiO<sub>2</sub> in the grain boundaries at 700 °C, since its diffusion rate is supposed to be the highest in the group.

As it was already mentioned, limiting size of crystallites for these materials does not seem to be reached even after 30 h of annealing, which suggests that source of migrating species is not exhausted still. The latter can be achieved only in the case of even distribution of dopants or in other words in the case of solid solutions.

**Table 25.** Fitting parameters of the model.

Sample name	<i>A</i>	<i>D<sub>lim</sub></i> , nm	<i>b</i> , s <sup>-1</sup>
SnO <sub>2</sub> Ac	0.69(7)	2.93(1)	0.080(3)
SnO <sub>2</sub> -TiO <sub>2</sub>	7.9(7)	9.50(6)	0.087(2)
SnO <sub>2</sub> -ZrO <sub>2</sub>	4.4(4)	7.27(4)	0.083(2)
SnO <sub>2</sub> -HfO <sub>2</sub>	3.6(3)	7.44(5)	0.064(1)
SnO <sub>2</sub> -Sc <sub>2</sub> O <sub>3</sub>	6.9(5)	8.69(3)	0.092(7)
SnO <sub>2</sub> -Y <sub>2</sub> O <sub>3</sub>	2.4(2)	6.25(4)	0.062(1)
SnO <sub>2</sub> -La <sub>2</sub> O <sub>3</sub>	4.1(4)	6.98(3)	0.084(5)

In the case of IIIB elements the highest growth rate together with the highest impediment was observed again for the material doped with element of the lowest ionic radius in the group: SnO<sub>2</sub>-Sc<sub>2</sub>O<sub>3</sub>. Another interesting feature is related with parameter *D<sub>lim</sub>*. From **Figure 54** it can be easily seen that SnO<sub>2</sub>-Sc<sub>2</sub>O<sub>3</sub> and especially SnO<sub>2</sub>-La<sub>2</sub>O<sub>3</sub> reach their limiting crystallite size faster than SnO<sub>2</sub>-Y<sub>2</sub>O<sub>3</sub>. Thus, we can suppose that while SnO<sub>2</sub>-Sc<sub>2</sub>O<sub>3</sub> and SnO<sub>2</sub>-La<sub>2</sub>O<sub>3</sub> evidence prominent two-phase character, SnO<sub>2</sub>-Y<sub>2</sub>O<sub>3</sub> is closer to solid solutions, which can be explained by yttrium incorporation into the SnO<sub>2</sub> lattice.

#### 4.3.5.4. Effect of noble metal

Crystallite growth kinetics was studied for one bulk doped and two surface doped materials: SnO<sub>2</sub>-PdO, SnO<sub>2</sub>-Pd and SnO<sub>2</sub>-Pt, resp. In general, doping with noble metals results in decrease of drag parameter and remarkable increase of constant *A* (**Figure 55**). Again, the model fits experimental data with less credibility in respect with blank material. The highest deviation was observed for bulk doped SnO<sub>2</sub>. Note that limiting crystallite size in this case has not been reached after 32 h as well as in the case of solid solutions. To a lesser degree this can be

observed for surface doped materials. This characteristic feature suggests that bulk doped material indeed has noble metal incorporated into the crystalline structure, while noble metals, deposited on surface, only partially penetrate into the lattice.

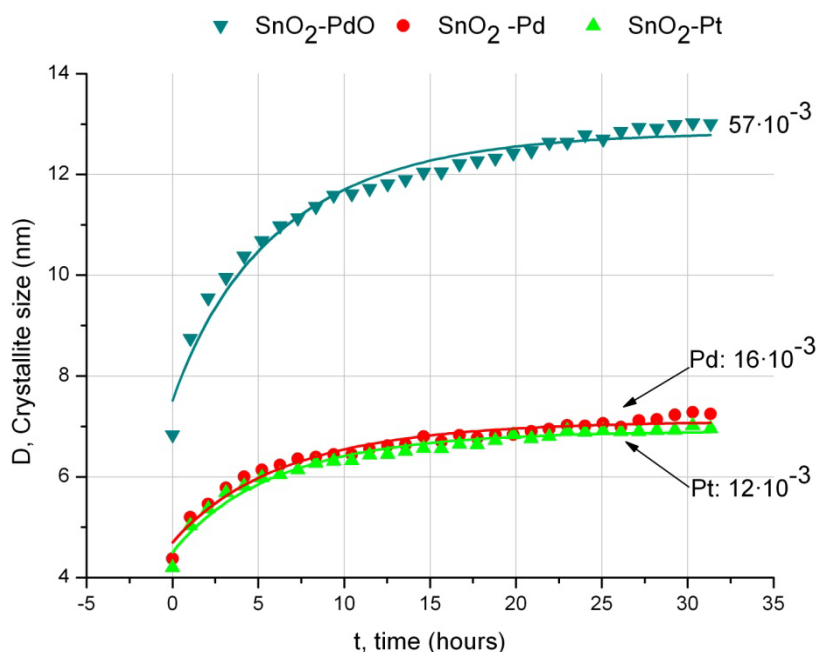


**Figure 55.** Time evolution of mean crystallite size of SnO<sub>2</sub>-PdO, SnO<sub>2</sub>-Pd and SnO<sub>2</sub>-Pt at 700 °C. The values of  $\chi^2$  are shown close to the fit curves.

As it was revealed by element analysis the content of the noble metal in SnO<sub>2</sub>-PdO amounts only to 200 ppm, however, its impact on thermal stability has dramatic character. Normalized by dopant weight the observed growth rate is the highest among all materials studied in TXRD experiment.

**Table 26.** Fitting parameters of the model.

Sample name	<i>A</i>	<i>D<sub>lim</sub></i> , nm	<i>b</i> , s <sup>-1</sup>
SnO <sub>2</sub> Ac	0.69(7)	2.93(1)	0.080(3)
SnO <sub>2</sub> Ac-Pd	3.3(3)	7.10(5)	0.066(1)
SnO <sub>2</sub> Ac-Pt	3.4(2)	6.91(4)	0.071(1)
SnO <sub>2</sub> Ac-PdO	11.1(8)	12.84(9)	0.068(1)

Drag parameter found for SnO<sub>2</sub>-PdO is lower in respect with SnO<sub>2</sub> Ac. Taking into account that crystallite limiting size is more than four times higher for Pd doped material and the dopant content is comparable with impurity level of the blank oxide, we conclude that in this case drag effect does not related with the size of the crystallite but rather with segregated impurities in the



grain boundaries, which concentration is high for blank oxide and low for all catalyst doped specimens. Generally speaking, deposition of catalysts remarkably increases diffusion rate and specific interphase energy in the blank oxide and what is also important decreases intrinsic impediment ability of the blank oxide.

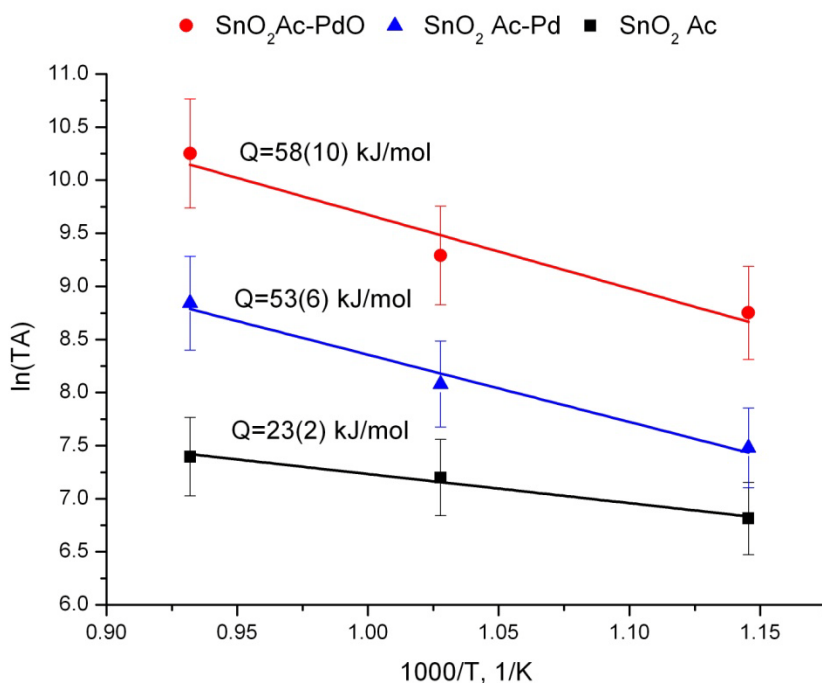


**Figure 56.** Arrhenius plot of  $\ln(TA)$  vs  $1000/T$ , where  $A$  – growth rate constant and  $T$  – temperature (in  $K$ ).

For two Pd-doped compounds as well as for blank oxide we performed TXRD measurements at 600 and 800 °C and therefore were able to estimate apparent activation energy of the crystallite growth. As it can be seen from Figure 56 bulk and surface doping of tin dioxide results in remarkable increase of activation energy and crystallite growth rate.

It is known from literature that activation energy for self-diffusion is considered to be the sum of the defect formation energy and the energy required to move the defect (migration energy barrier) [187]. Simultaneous rise of activation energy and growth rate for doped materials suggests that migration energy barrier is notably lower for SnO<sub>2</sub> Ac-PdO system (resulting in high growth rate) and energy required for defect formation is much higher than for blank SnO<sub>2</sub>.

#### 4.3.5.5. Summary

Analyzing the obtained results it seems reasonable to suppose that synthesized blank SnO<sub>2</sub> is highly equilibrium composition, since any additives either in the bulk or on the surface result in remarkable rise of crystallite growth rate. This equilibrium structure manifests properties of two-phase composition. The role of second phase is played more likely by the partially reduced SnO<sub>2</sub> surface, which impedes crystal growth rate under isothermal conditions and in the same time reduces activation energy of the growth rate, apparently due to low energy of defect formation.

Impurities as well as the majority of the solid solutions and mixed oxides remarkably increase growth rate and in the same time demonstrate slight increase of drag parameter which suggests that segregation of the second phase takes place in the grain boundaries of these oxide systems. The case of SnO<sub>2</sub>-HfO<sub>2</sub> and SnO<sub>2</sub>-Y<sub>2</sub>O<sub>3</sub> is different. These compounds do not increase drag parameter and demonstrate the lowest growth rates. Comparing ionic radii of the elements it becomes evident that for solid solutions (what is most likely the case of SnO<sub>2</sub>-Y<sub>2</sub>O<sub>3</sub> as well) the following empiric rule can be derived: the bigger ion is the slower crystallite growth is, which leads to decrease of phase segregation.

Doping with noble metals results in decrease of the drag term, suggesting that impediment effect of the reduced SnO<sub>2</sub> surface is brought down. Thermal stability of the material is drastically deteriorated in the case of SnO<sub>2</sub> Ac-PdO. In spite of the worse thermal stability doped materials manifest higher activation energies of crystallite growth. The latter indicates that migration energy barrier is notably lower and energy required for defect formation is higher for these systems in respect with blank oxide.

#### **4.4. Sensing properties**

This chapter deals with sensing properties of the materials in question, studied with the help of the “Temperature” experiment. The experiment was performed for all synthesized materials. The results are given as plots of sensor signal (resistance ratio  $R_0(T)/R_g(T)$ ) as a function of temperature:  $S(T)$ .

Three main parameters were used to compare materials:  $S_{max}$  – is the signal maximum,  $T_{Smax}$  – is the temperature of signal maximum, and  $E_{act}$  – is the activation energy of the conductivity change (or gas-sensor effect). Since the latter was estimated from the plots of  $\ln(S)$  vs.  $1/kT$  (see experimental part), the value reflects only gas adsorption component without contribution from the thermal activation of the charge carriers, connected with the Schottky barrier height. This assumption is based on the well known concept of adsorption-caused change in electrophysical characteristics of a semiconductor adsorbent and will be explain in more detail. For the sake of brevity the Arrhenius plots are not shown, however an example of the plot and  $E_{act}$  calculations can be seen in the experimental part 1.1.1.

The chapter is built up from several parts according to the type of the material: blank oxides are given in the first part, oxides doped with IVB and IIIB elements are given in the second and third parts, tin oxides doped with noble metals are described in the fourth part, the final part summarizes the results and conclusions.

#### 4.4.1. Blank materials

Let us start first with the signal comparison of the synthesized blank oxides and commercial SnO<sub>2</sub> at 0% RH (**Figure 57**). The signals of the synthesized materials manifest one broad band between 300 and 400 °C, whilst signal of commercial nanopowder contains three consecutive peaks at *ca.* 190, 310 and 450 °C. Appearance of several peaks suggests that surface of the material is not homogeneous from the chemical point of view and contains species with different reactivity. From this standpoint the most homogeneous surface is observed in the case of SnO<sub>2</sub> Ac. In general synthesized materials are quite similar, however, signal band of SnO<sub>2</sub> Ac(IV) consist of two components, where high-temperature one is more pronounced.

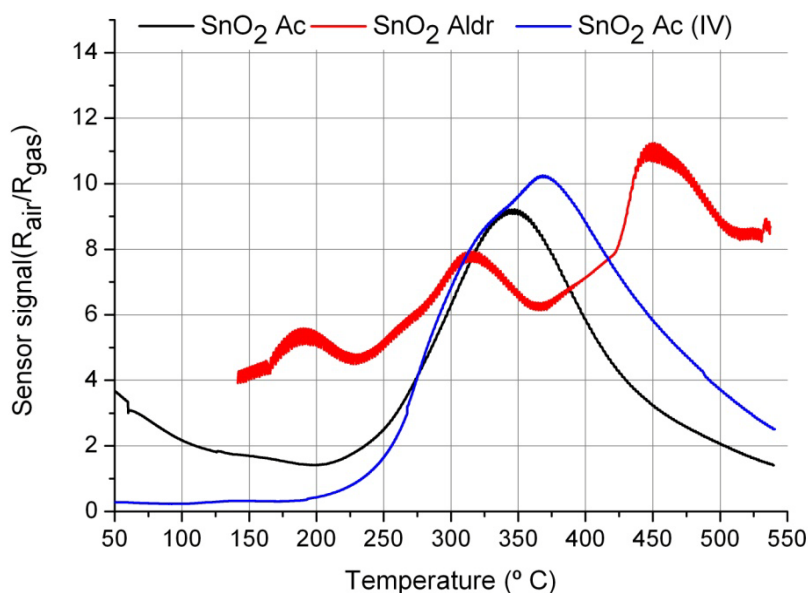
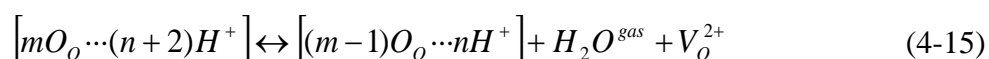
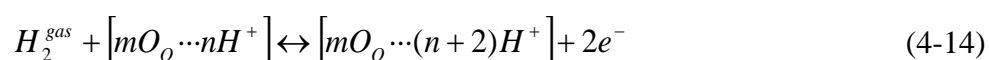


**Figure 57.** Signals to H<sub>2</sub> as a function of  $T$  at 0% RH for blank materials in question.

The parameter  $T_{Smax}$  in the case of SnO<sub>2</sub> Ac is observed at 345 °C which is slightly shifted towards higher temperatures in respect with the temperature of the highest rate of H<sub>2</sub> consumption found in MS-study (between 300 and 320 °C) and corresponds to the stage of active desorption of chemisorbed water according to TGA results. Let us discuss the case of MS-study in more detail.

As it was found, hydrogen consumption was much more intense than the water production for this material, but even in this case the water-to-hydrogen ratio amounts to *ca.* 1.8 at 350 °C, *i.e.* higher than 1, the latter corresponds to hydrogen oxidation through oxygen. This means that hydrogen tends to be chemisorbed under these conditions and water release occurs mainly in the form of hydroxyl desorption.

All these facts together with the observation of bridging hydroxyl consumption in the presence of H<sub>2</sub>, found by DRIFTS study, allow one to assume that *conductance change in the material is mainly due to hydrogen chemisorption on bridging hydroxyls and not due to the classic hydrogen oxidation on oxygen species producing water*. The bridging hydroxyls are known to contain hydrogen atoms mobile along the rows of bridging oxygen sites, which implies that neighbouring oxygen atoms statistically share hydrogen and therefore can act as strong adsorption centres [107]. From the broad and intense nature of the absorption band corresponded to these species, it is likely that they form an interconnected family of paired OH groups of different coordination number. Hydrogen interaction with such species can be represented as follows:



where,  $[mO_o \cdots nH^+]$  is the paired bridging OH groups with mobile hydrogen atoms, “*m*” denotes surface concentration of bridging oxygen ions, “*n*” – variable content of the mobile hydrogen ions, and  $V_o^{2+}$  is an oxygen vacancy.

Catalytic activity of surface hydroxyl groups is getting more attention nowadays. Their role has been recognized in water gas shift reaction, where different types of OH groups are responsible for CO chemisorption in the form of formate, and decomposition of the latter to give CO<sub>2</sub> and H<sub>2</sub> [109]. Also they are known as active species in hydrocarbon oxidation, methanol formation from synthesis gas and other catalytic and photo-catalytic processes [110, 189-191]. Therefore the idea of sensing mechanism realized through hydroxyl groups is based on the reliable experimental evidence.

Uneven shape of the signal in the case of SnO<sub>2</sub> Ac (IV) seems to be then due to the heterogeneous character of the bridging hydroxyl groups. Indeed, FTIR study revealed that SnO<sub>2</sub> Ac (IV) contains hydroxyls which are more acidic (peak at 3378 cm<sup>-1</sup>) in respect with SnO<sub>2</sub> Ac. In addition, the former material contains hydroxyls with slightly higher basicity (shoulder at 3434 cm<sup>-1</sup>). In general, basic hydroxyls are known to be more chemically active than acidic ones, which can explain complex nature of SnO<sub>2</sub> Ac(IV) signal band [106].

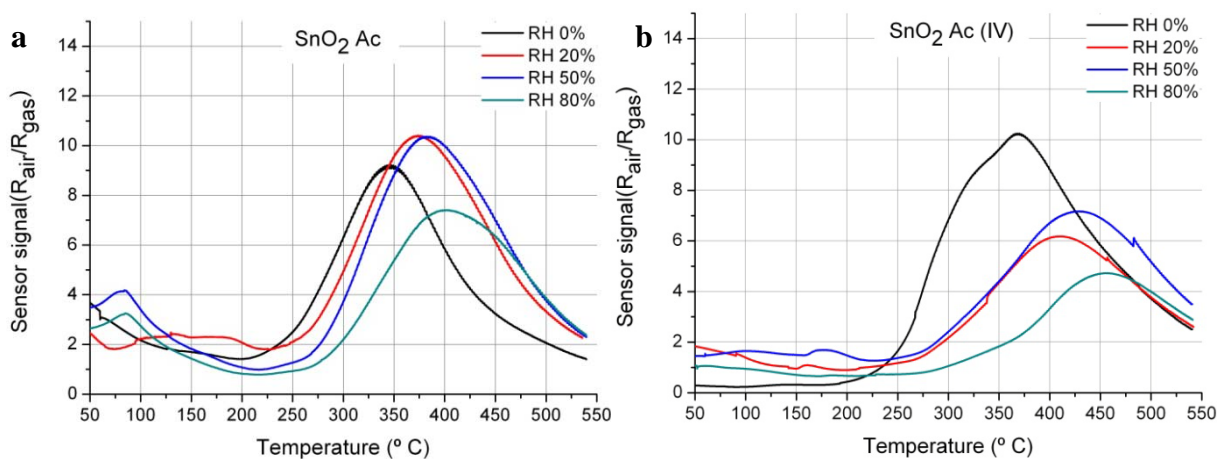


**Figure 58.** Signals to  $H_2$  as a function of  $T$  at 0, 20, 50, 80% RH for synthesized blank materials.

**Figure 58** shows signal evolution upon temperature at various RH for synthesized compounds. The common trend for both materials is that water vapours bring about shift of  $T_{S_{max}}$  towards higher temperatures and signal bands become broader. The difference between two materials is mainly related with  $S_{max}$ . The latter was found to be slightly increased at 20 and 50% RH in the case of  $SnO_2$  Ac and remarkably brought down with increased water content in the case of  $SnO_2$  Ac (IV), which is normal and is quite known in the literature.

The strange behaviour of the former oxide suggests that water at certain concentration favours hydrogen chemisorption. Decrease of the signal with increase of water content can be related with competitive adsorption of water and hydrogen molecules for the same surface sites. The same idea was proposed by several groups in the field of heterogeneous catalysis in order to explain inhibiting character of water vapours in methane oxidation [192].

Thus, it seems that water interacts with the same adsorption centres as hydrogen. However, nowadays the existing three models of water interaction with semiconductor surfaces, resulting in an increase of surface conductivity, are based on dissociative water adsorption on either surface tin or oxygen ions [111, 139]. In the case of highly hydroxylated surfaces of blank  $SnO_2$ , with no evidence of bridging oxygen (mainly from DRIFT results), it is reasonable to suppose that water interacts either with surface hydroxyl groups as well as hydrogen, or with surface tin ions. To resolve this problem let us consider sensor signals to water vapours only (**Figure 59**).

It was found that signals to water vapours occur at lower temperatures than that of hydrogen for both materials. However, the most pronounced difference between water and hydrogen signals is observed for  $SnO_2$  Ac, while  $SnO_2$  Ac (IV) manifests a certain overlap of the signals to water and hydrogen. This is perfectly constituent with the results of humidity effect on hydrogen signals, which was found higher in the case of  $SnO_2$  Ac (IV).

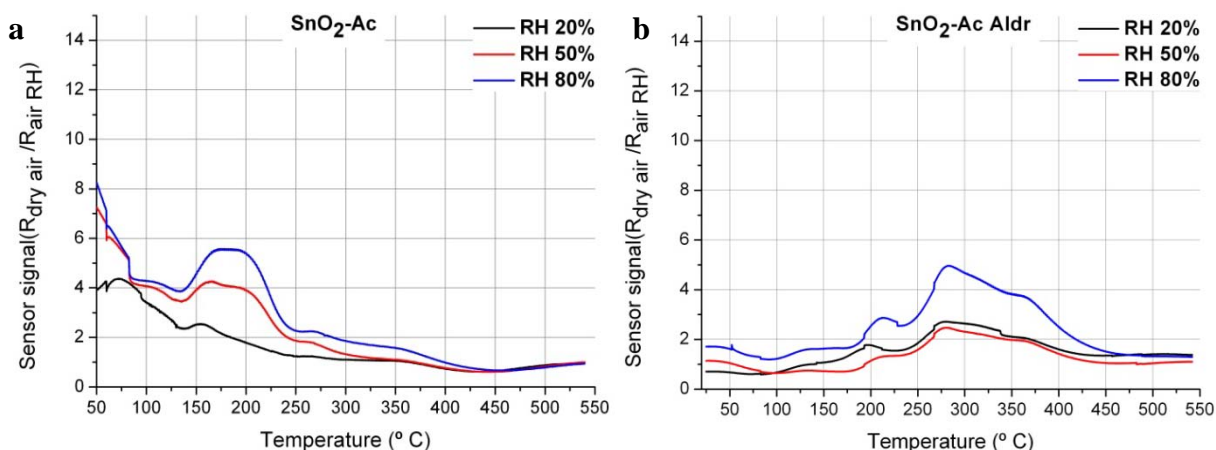
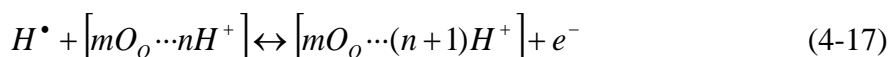
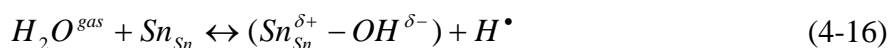


**Figure 59.** Sensor signal of SnO<sub>2</sub> Ac (a) and SnO<sub>2</sub> Ac Aldrich (b) to water vapour against temperature.

Thus, in the case of SnO<sub>2</sub> Ac water clearly interacts with other species than surface hydroxyls. An increase in the signal was observed between 150 and 210 °C for 50 and 80% RH, which corresponds to the early stage of chemisorbed water desorption (from TGA results).

From DRIFTS results the interaction with water vapour from RT up to 400 °C results in an increase in bridging hydroxyls and the formation of terminal OH groups. Taking into account that no surface oxygen was observed, it is thought that first dissociative adsorption of water takes place on surface metal atoms giving rise to terminal OH groups and hydrogen atoms which can join the “family” of bridging hydroxyls. The two-step interaction can be represented as follows:



where,  $Sn_{Sn}$  is lattice tin atom,  $(Sn_{Sn}^{\delta+} - OH^{\delta-})$  is the terminal OH group,  $[mO_o \cdots nH^+]$  is the paired bridging OH groups with mobile hydrogen atoms, “ $m$ ” denotes surface concentration of bridging oxygen ions and “ $n$ ” – variable content of the mobile hydrogen ions.

In the case of SnO<sub>2</sub> Ac (IV) water seems to interact either with surface tin ions of different nature (coordination number, ion surrounding etc) or with other species, which should be studied with DRIFTS technique in the future. In any case the fact that water electronically interacts with SnO<sub>2</sub> surface in the temperature region close to the one of H<sub>2</sub> interaction results in higher humidity effect on the signal parameters, which can be seen in **Figure 60a**.

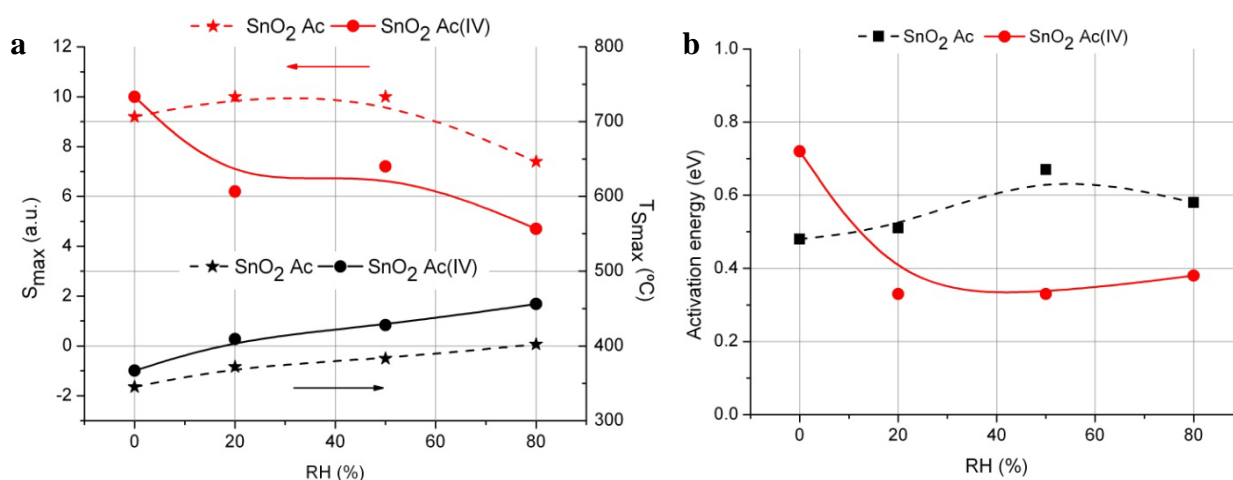


**Figure 60.** Variation of  $S_{max}$ ,  $T_{Smax}$  (a) and  $E_{act}$  (b) with relative humidity.

It is widely accepted that sensor signal is a function of the surface coverage by gaseous species, described as a difference between adsorption and desorption processes [130]. In our experiment we observe a combination of two processes: the first one corresponds to the low-temperature region when the signal rises with temperature and is characterized by H<sub>2</sub> adsorption rate higher compared with that of water desorption (according to Eq. 4-2 and 4-3), the second one occurs in the high-temperature region when the signal decreases which corresponds to the domination of the water desorption process.

This combination of the two processes leads to the well known volcano shape of the signal evolution upon temperature. Accordingly, fitting with linear function of the volcano-shaped curve plotted in the Arrhenius coordinates ( $\ln(S)$  vs.  $1/kT$ ) from the low-temperature side allows one to estimate the apparent activation energy of hydrogen chemisorption or its dissociation on SnO<sub>2</sub> surface (see an example of the fitting in the Experimental part). The results of the fitting are shown in **Figure 60b**.

The found values of activation energy are rather low in respect with the ones experimentally found for hydrogen dissociation on ZnO and MgO surfaces: 1.2 eV [130, 193]. However, low activation energies for hydrogen chemisorption found from electrical measurements were quite often reported in the literature [130]. The phenomenon supposed to be due to partial ionization of the molecule, which chemisorption is facilitated. In the case of SnO<sub>2</sub> Ac water vapours slightly increase the energetic barrier for hydrogen chemisorption, while for SnO<sub>2</sub> Ac (IV) the effect is opposite. The change of the value in this case indicates that adsorption centres transform in the presence of water which increases H<sub>2</sub> ionization. The most pronounced increase of  $E_{act}$  for SnO<sub>2</sub> Ac is observed between 20 and 50% RH.



The obtained results indicate that materials compared have rather different surface chemistry of hydrogen and water chemisorption, which is first of all due to different hydroxylation degree and different nature of surface hydroxyls. The firmer reason can be deduced from the fact that material with higher hydroxylation degree – SnO<sub>2</sub> Ac –, which was found by FTIR, XPS and TGA, manifests the lowest humidity effect caused on signal parameters  $S_{max}$  and  $T_{Smax}$ . The latter one becomes evident from the temperature of water signals, which is very different for two materials.

#### 4.4.2. SnO<sub>2</sub>-MetO<sub>2</sub>, Met=Ti, Zr, Hf

**Figure 61** illustrates sensor signal evolution as a function of temperature at various values of RH for given materials. In general, doping with IVB metal oxides brings about more complex behaviour of the sensing materials. However, the suggested mechanism of hydrogen interaction with the surface seems to be applicable here as well. Since almost all the changes are related with the high-temperature main signal band.

The latter upon doping with IVB elements becomes unsymmetrical and broader. This fact together with low-temperature features remarkably differs the doped materials from the blank oxide. The complex signal profile again well corresponds with the heterogeneous nature of bridging hydroxyl groups found from FTIR analysis.

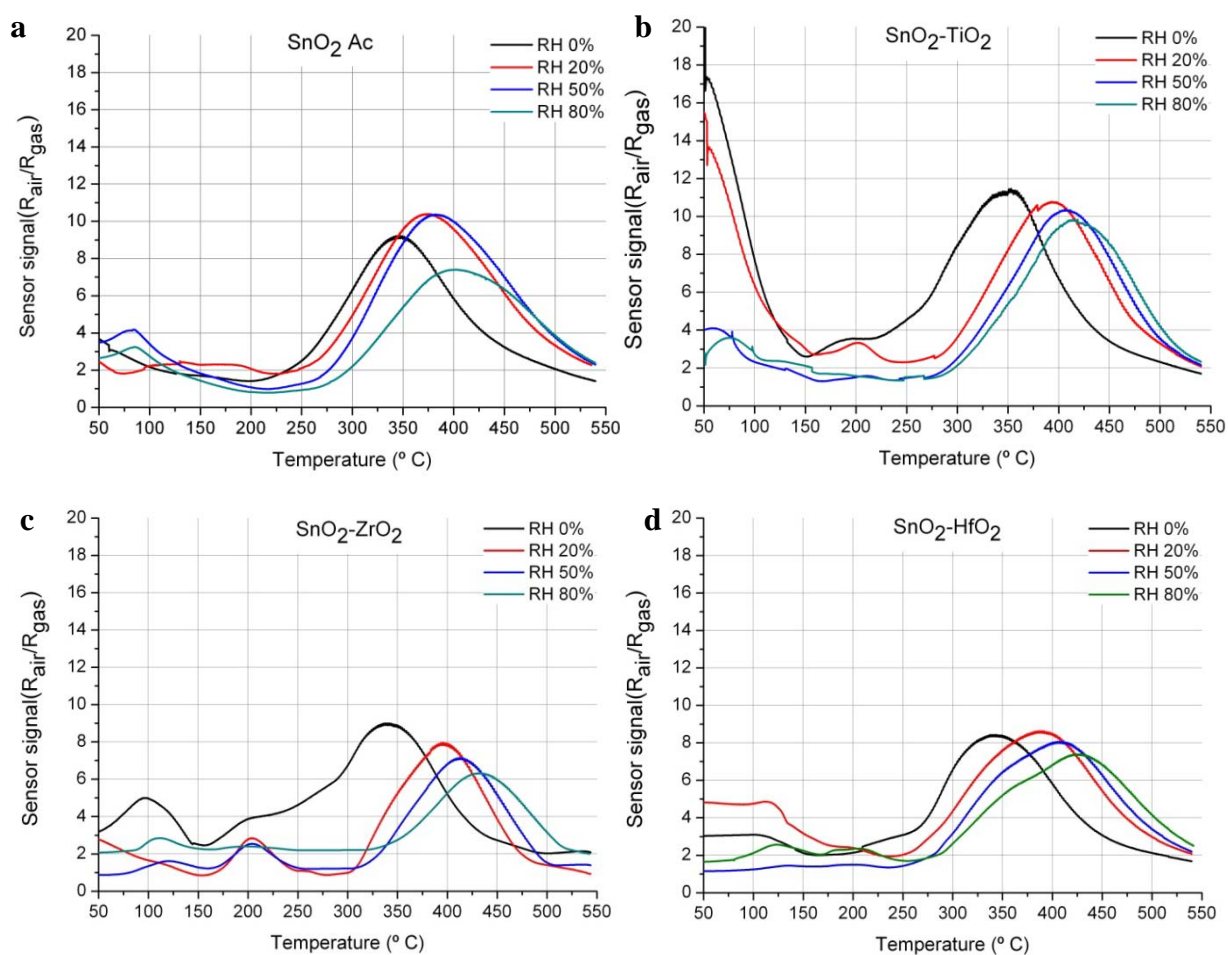


**Figure 61.** Signals to H<sub>2</sub> as a function of  $T$  at 0, 20, 50, 80% RH for blank and doped SnO<sub>2</sub>.

In dry air the signal is the highest in the case of SnO<sub>2</sub>-TiO<sub>2</sub> and the lowest for SnO<sub>2</sub>-ZrO<sub>2</sub> and SnO<sub>2</sub>-HfO<sub>2</sub>.  $T_{Smax}$  for all materials lies between 340 and 350 °C, however the lowest value in

dry air is observed for Zr and Hf doped SnO<sub>2</sub>. Zr and especially Ti-doped materials demonstrate remarkable signals in low-temperature region, which becomes negligible at high RH.

The fact that sensor signals are higher for Ti-doped material indicates that hydrogen chemisorption in this case is more intense. Note that hydroxylation degree as well as hydroxyl desorption rate (or activity as we assume) for the same compound, estimated from FTIR and TGA results (resp.), was found the highest among the given materials, which indicates that hydroxyl groups indeed take part in sensing phenomenon.

The evidence of intense low-temperature signals in the case of SnO<sub>2</sub>-TiO<sub>2</sub> suggests that H<sub>2</sub> chemisorption takes place either through very reactive oxygen species or loosely bonded OH groups, both probably formed upon molecular water desorption. However, the temperature of the observed features is not reliable since no comparison of the signals with the ones obtained under isothermal conditions in this temperature region was performed. We can just assume that the bands observed at 50 °C would be shifted towards higher temperatures by 20-40 °C. It is remarkable that upon increase of RH the signals disappear, indicating that chemisorption takes place more probably through non-hydroxyl species.

To compare the effect of RH on sensor parameters and apparent activation energy of H<sub>2</sub> chemisorption let us consider results shown in **Figure 62**. The highest value of  $S_{max}$  in the whole range of RH was found in the case of SnO<sub>2</sub>-TiO<sub>2</sub>. However, the lowest change of this parameter upon increasing RH was observed for hafnia-doped material. All materials demonstrate rather similar  $T_{Smax}$  and its change with humidity. Doped materials manifest slightly lower activation energy of H<sub>2</sub> chemisorption in comparison with blank oxide. Increase of water content changes insignificantly the values of SnO<sub>2</sub>-ZrO<sub>2</sub> and SnO<sub>2</sub>-HfO<sub>2</sub>, suggesting that nature of adsorption centres does not change upon water content increase in the gas phase. In the case of titania doped material the most pronounced change is observed between 0 and 20% RH.

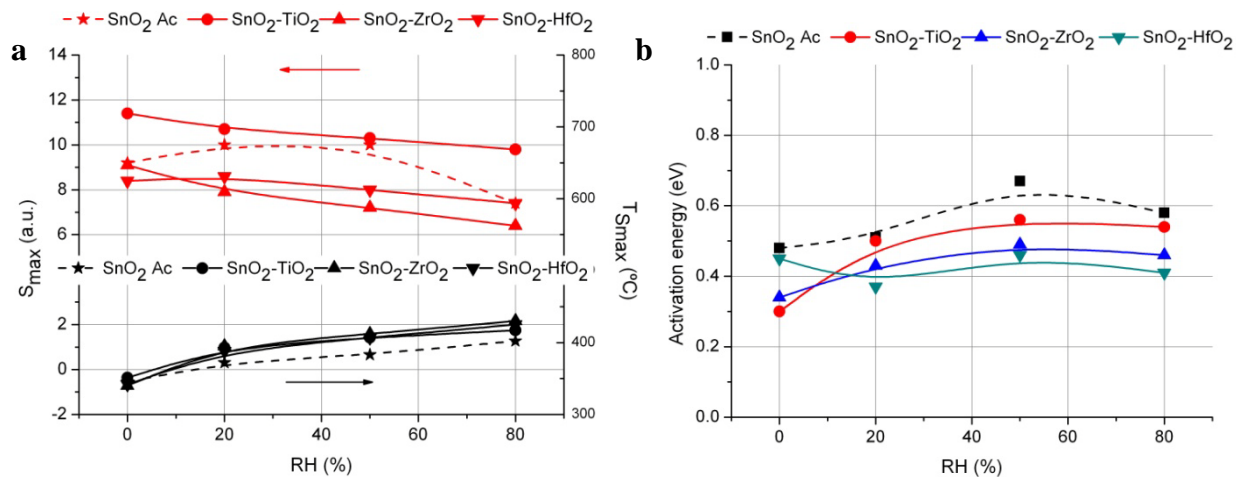


**Figure 62.** Variation of  $S_{max}$ ,  $T_{Smax}$  (a) and  $E_{act}$  (b) with relative humidity.

In general, doping SnO<sub>2</sub> with IVB oxides does not enhance significantly selectivity of H<sub>2</sub> chemisorption in the presence of water vapours. On the other hand, activation energy of H<sub>2</sub> chemisorption for these materials is fairly constant in the range 20-80% RH as well as  $T_{Smax}$  and  $S_{max}$  seem to reach the constant value in the range  $\geq$  50% RH. These facts indicate that sensing mechanisms do not change abruptly upon water increased concentration. The case of titania doped material seems the most interesting one since the material manifests the highest sensor signal together with rather low change of signal parameters in the region 20-80% RH.

### 4.4.3. SnO<sub>2</sub>-Met<sub>2</sub>O<sub>3</sub>, Met=Y, La

As it was already mentioned in the experimental part, in this study sensing properties of SnO<sub>2</sub>-Sc<sub>2</sub>O<sub>3</sub> will not be discussed since the material manifested an outstanding high electric resistance in the whole range of temperatures and gas mixtures.

**Figure 63** illustrates sensor signals to 20 ppm H<sub>2</sub> for the materials in question. Both materials represent complex signal evolution upon temperature increase. The high temperature bands are broad and unsymmetrical which can be explained by the presence of various types of surface OH groups. In dry air the materials represent the highest  $S_{max}$  and the lowest  $T_{Smax}$  in respect with blank oxide. However, water brings these advantages down.

The signal evolution of the compared materials differs greatly. While yttria-doped material manifest similar signal evolution in respect with previous materials, SnO<sub>2</sub>-La<sub>2</sub>O<sub>3</sub> represents very complex behaviour. The most striking feature of the SnO<sub>2</sub>-La<sub>2</sub>O<sub>3</sub> is very intense signals in the low-temperature region. In dry air the material manifests several bands. The one occurred at the lowest temperature resembles the low temperature features of SnO<sub>2</sub>-TiO<sub>2</sub> which were assigned to the H<sub>2</sub> chemisorption on non-hydroxyl surface species. The latter assumption is consistent with the fact that the band is not observed in the presence of water. It is interesting that these two materials have the highest amount of molecular water on their surface according to TGA, which indicates that surface contains rather weak polar adsorption centres which can be strongly affected by hydrogen adsorption in the absence of water.

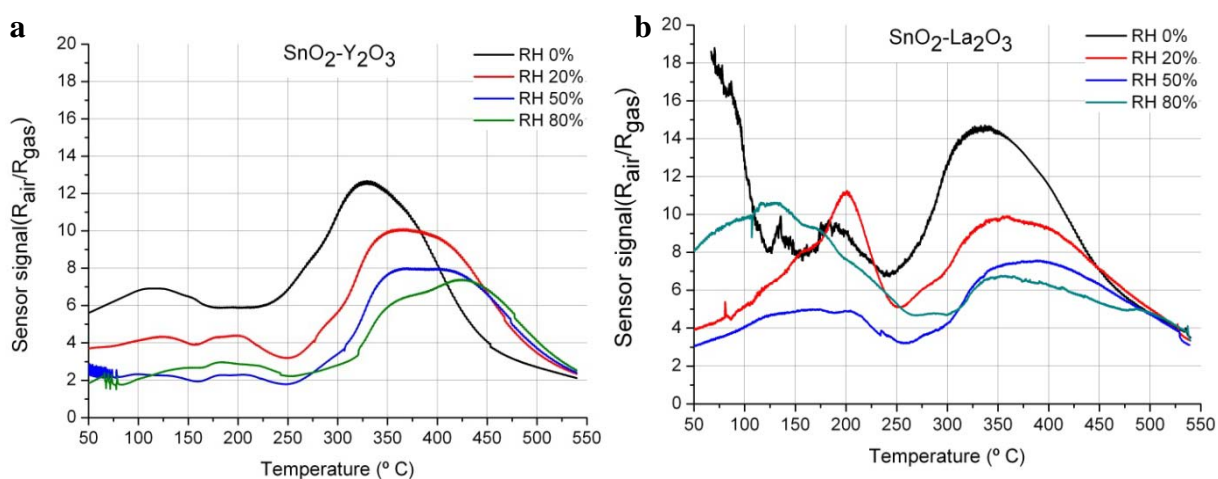


**Figure 63.** Signals to H<sub>2</sub> as a function of  $T$  at 0, 20, 50, 80% RH for doped SnO<sub>2</sub>.

Other low-temperature signals in the case of SnO<sub>2</sub>-La<sub>2</sub>O<sub>3</sub> can be observed at higher water content in the gas phase, which intensity and position vary as a function of humidity. On the basis of TGA and FTIR results we can conclude that this complex behaviour is due to very

heterogeneous surface: the material demonstrates the highest hydroxylation degree among the synthesized compounds (found by FTIR) and in the same time the desorbed water quantity is rather modest (TGA) despite of very high desorption rate (TGA). This means that either material has a considerable part of OH groups occluded in the bulk, or several types of very different hydroxyl groups are presented on the surface (*e.g.* with high chemical activity and almost inert). Another interesting feature of this material is that the low temperature signal at 80% RH becomes higher than the high-temperature component, which is unusual for these conditions.

Yttria-doped oxide has the second highest value of  $S_{max}$  among the oxides. However, according to TGA, hydroxyl activity for this material was found rather low in respect with blank oxide as well as the total quantity of the desorbed water. On the other hand, FTIR results indicate that overall hydroxylation degree of the material is higher than that of blank oxide by a factor of 2. This means that either other than hydroxyl species contributed to the sensor signal, which is doubtful due to high  $T_{Smax}$ , or that occluded or inaccessible OH groups somehow participate into the detection process.

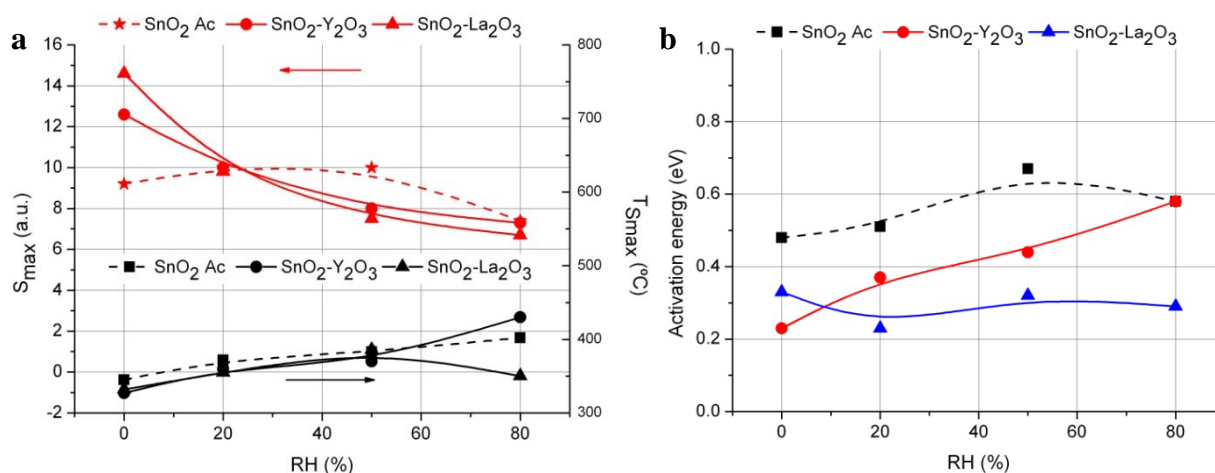


**Figure 64.** Variation of  $S_{max}$ ,  $T_{Smax}$  (a) and  $E_{act}$  (b) with relative humidity.

**Figure 64** summarizes the obtained results. The common trend of the doped materials is rather high humidity effect on sensor signal parameters. In the case of SnO<sub>2</sub>-La<sub>2</sub>O<sub>3</sub> one can observe the highest drop of the  $S_{max}$ , while  $E_{act}$  of H<sub>2</sub> chemisorption is roughly the same in dry and humid air. This suggests that the signal drop is mostly due to competitive adsorption. For yttria-doped material the activation energy remarkably rises upon increase of water content suggesting that adsorption centres change their nature in humid air.

#### 4.4.4. SnO<sub>2</sub> with deposited noble metals: Pd, Pt, Rh

Figure 65 shows sensor signal evolution for catalyst-doped materials as a function of temperature at various values of RH. Let us consider first the measurements performed in dry air.

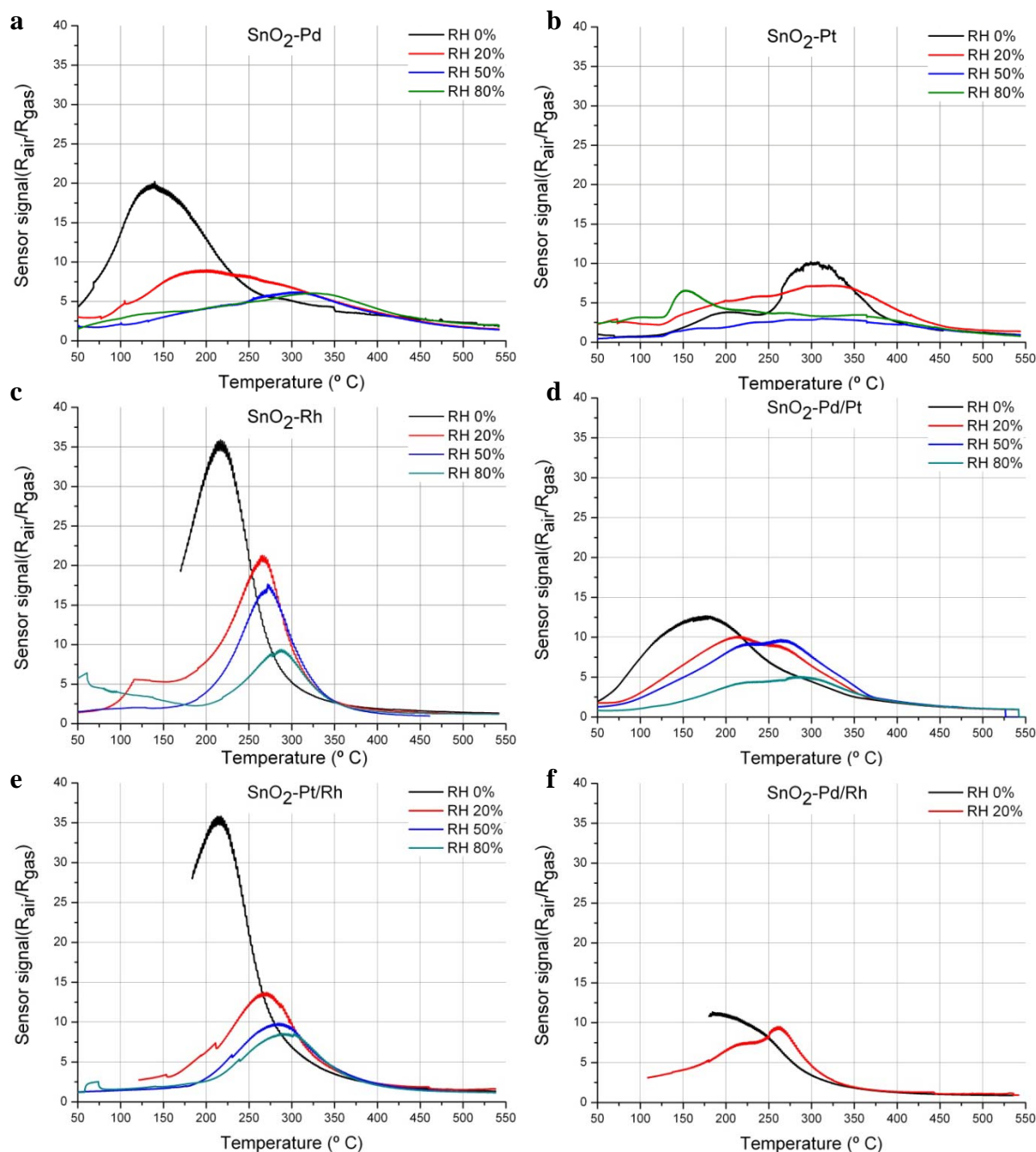


Figure 65. Signals to H<sub>2</sub> as a function of  $T$  at 0, 20, 50, 80% RH for catalysts-doped SnO<sub>2</sub>.

$T_{Smax}$  of the majority of materials was found between 100 and 250 °C which is rather low compared with blank oxide and corresponds to the TGA region of low hydroxyl activity. The obtained results for Pd-doped oxide at 0% RH corresponds well with the temperature of the

highest catalytic activity of the material found in MS experiment. The doped oxide, unlike the blank one, manifested the pronounced signals both for hydrogen consumption and water production, which indicates that in this case the classic hydrogen oxidation occurs on the surface. And therefore due to similarity of the  $T_{Smax}$  and the temperature of the highest catalytic activity for Pd-doped material, it seems reasonable to assume that *charge transfer occurs as a result of hydrogen oxidation on the surface and not only due to hydrogen chemisorption*.

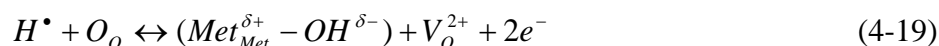
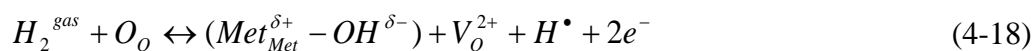
Judging from signal profiles of the materials, the sensing mechanism is very different compared with blank oxides. The following observations suggest that in the case of catalyst-doped materials surface OH groups do not play the principal role in the sensing mechanism. In other words we assume that they do not act as the adsorption centres in the hydrogen interaction with the surface.

If hydroxyls had played the principal role in the sensing mechanism, we would have observed sensor signal in the range 300-400 °C, especially in the case of bimetallic catalyst systems, for which we have found an outstanding chemical activity of OH groups (from TGA). However, signals for these materials were found mainly in the low-temperature range. Moreover, for the materials which had manifested the highest OH group chemical activity (doped with Pd/Pt and Pd/Rh) we do not observe any remarkable signals values at all. In general, for all catalyst doped materials activity of surface OH groups does not correspond with sensor signals, which suggests that surface species other than hydroxyls are involved in the sensing process.

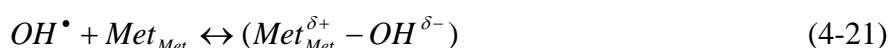
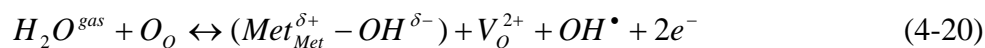
As we have already shown, XPS analysis together with HRTEM indicates that clusters of noble metals (by example of Pd) are in the oxidized form, which is in full agreement with the literature [21]. This fact allows us to suppose that low-temperature signals are due to hydrogen interaction with oxygen species. The latter are known to be much more reactive than hydroxyls and this explains the decrease of the signal temperature [194].

However, the most reliable evidence of hydrogen interaction through surface oxygen can be provided by DRIFT results. As we have shown earlier by example of Pd-doped oxide, hydrogen as well as water interacts similarly with oxide surface, consuming bridging oxygen and producing new terminal OH groups (**Figure 51**). Bridging OH groups also form upon interaction with the gases, however, at temperatures above 200 °C, suggesting a minor role in the processes related with increasing conduction at around 140 °C. Thus, taking into account results of DRIFTS and DC measurements, the low temperature hydrogen interaction with the surface can be represented as follows:





and that of water:



where,  $Met_{Met}$  is lattice tin or palladium atom.

The fact that both gases interact with the same surface species, was derived from the evidence of the similar sensor signals and DRIFT spectra for hydrogen and water. If this assumption is correct it is understandable that simultaneous interaction of hydrogen and water with the surface will be competitive.

Indeed, sensor signals to H<sub>2</sub> in humid air are less intense and their maxima significantly shifted towards higher temperatures, which implies that the sensing mechanism changes upon increased water content in the gas phase. Again, the most prominent change is observed when the volumetric concentration of water in the gas phase is higher than that of H<sub>2</sub> by a factor of 1000 (Figure 7, b).

Due to the fact that electrical measurements were performed separately for each gas mixture, it was possible to separate and compare signals towards hydrogen in the presence of water and water signal in the presence of hydrogen. Such cross-sensitivity of the materials enables the dominant effect to be determined, *i.e.* whether the effect of hydrogen on the water signal or that of water on the hydrogen signal is larger.

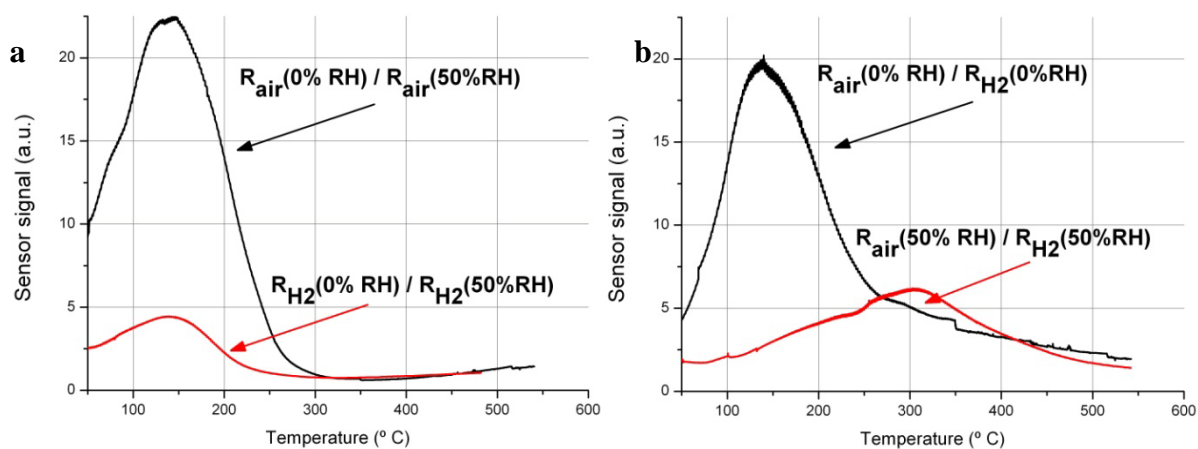


**Figure 66.** Signals of SnO<sub>2</sub>-Pd to H<sub>2</sub>O in dry air and in the presence of H<sub>2</sub> (a), and signals to H<sub>2</sub> in dry air and in the presence of H<sub>2</sub>O (b).

From Figure 66, in the presence of hydrogen, the water signal drops, but does not shift with temperature. In the presence of water, a similar decrease occurs as well as a shift of the  $T_{Smax}$  towards higher temperatures was observed. Thus, highly hydroxylated surfaces react with hydrogen only at high temperatures, which suggests that, at high water content, the H<sub>2</sub> detection mechanism switches from oxygen to hydroxyl-based interaction which was observed for blank SnO<sub>2</sub> (*i.e.* through bridging hydroxyls, Eqs. 4-14 and 4-15).

The case of Pt-doped material is amazingly supports the idea of oxygen mediated mechanism, since it is known from literature that more oxidized Pt surface manifest lower catalytic activity compared to the reduced one [21]. This means that Pt-doped materials should be better under reducing conditions. Indeed, in our previous works the highest signal in hydrogen-rich atmosphere (1000 ppm in air, which is obviously closer to the reducing conditions than 20 ppm H<sub>2</sub> in air) has been observed in the case of Pt-doped SnO<sub>2</sub> [195].

Doping with Rh results in the highest signal to 20 ppm H<sub>2</sub> in dry air. However,  $T_{Smax}$  for this material is higher as well compared with SnO<sub>2</sub>-Pd: 216 against 139 °C, resp. These facts suggest that in the case of SnO<sub>2</sub>-Rh oxygen species (if we accept the idea that oxygen is responsible for low-temperature signals) are less reactive, however, much more numerous on catalyst surface. In addition their nature seems more homogeneous compared with Pd-doped oxide. The latter assumption can be derived from the narrow form of the signal peak in the case of Rh-doped oxide.

Another quite interesting behaviour was observed for bimetallic systems. The highest signal manifests only one Rh-contained system: Pt/Rh. While  $S_{max}$  is slightly higher for this catalyst, parameter  $T_{Smax}$  is the same compared with SnO<sub>2</sub>-Rh material. This means that against the background of very low sensing (and apparently catalytic) performance of platinum, the material's properties almost entirely determined by Rh-catalyst. In contrary, Pd seems to interact with the phase of Rh and brings down its reactivity. As a result, the signal profile of SnO<sub>2</sub>-Pd/Rh at 0% RH resembles more Pd-doped oxide than Rh-doped one. The same phenomenon occurs with Pd/Pt system which signal evolution in dry air is close to Pd-doped oxide, with 2 times lower  $S_{max}$  and slightly higher  $T_{Smax}$ . Thus, it turns out that the presence of Pd catalyst inhibits chemical reactivity of other catalysts.

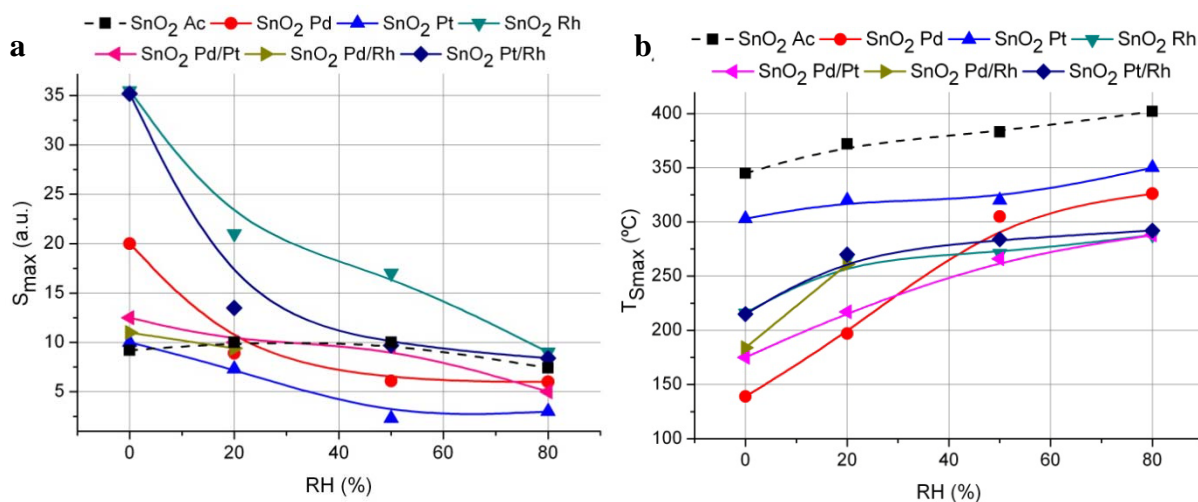


**Figure 67.** Variation of  $S_{max}$  (a) and  $T_{Smax}$  (b) with relative humidity for catalyst-doped SnO<sub>2</sub>.

Now let us consider the effect of water vapours on signal evolution. All materials demonstrate remarkable change of both parameters ( $S_{max}$  and  $T_{Smax}$ ) upon increase of humidity. The results are summarized in **Figure 67**. The general trend for the catalyst-doped oxides can be stated as follows: the higher catalytic activity of the noble metal (*i.e.* activity of surface oxygen species), the more dramatic decrease it undergoes in the presence of water vapours. Indeed,  $S_{max}$  of two Rh-doped oxides at 0% RH amounts to 35 and then drops down to *ca.* 9 at 80% RH. The change of  $T_{Smax}$  for the same materials is also remarkable – more than 70 °C. However, the highest change of  $T_{Smax}$  is observed for Pd-doped material, which sensing properties should be apparently the most affected by water vapours. Note that in humid air, especially at high RH, blank SnO<sub>2</sub> demonstrates the signal which is compared and even higher than that of catalysts doped materials.

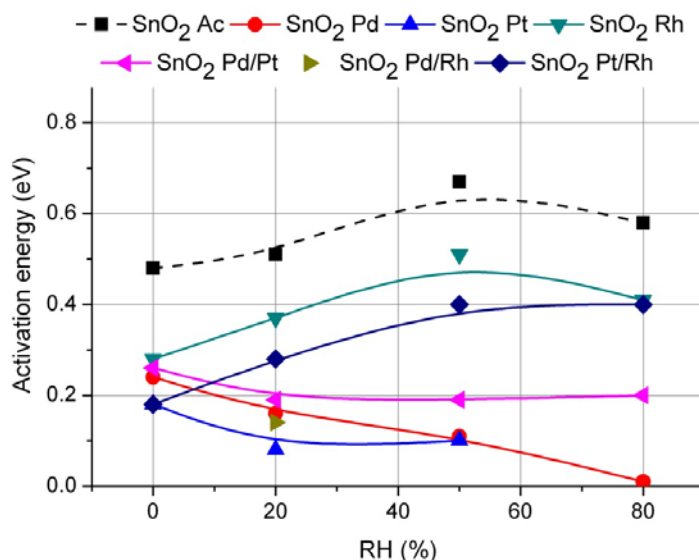


**Figure 68.** Variation of  $E_{act}$  with relative humidity for catalyst-doped SnO<sub>2</sub>.

Apparent activation energy estimated for catalyst doped materials should be related mainly with the process 4-6, since interaction of hydrogen radical with oxygen species is supposed to be without activation energy at all [130]. The found values are lower for the catalyst doped oxides compared with blank material. Rh and Pt/Rh catalysts manifest similar behaviour upon increase of humidity: the parameter increases as well.  $E_{act}$  for the rest of the materials, in contrary decreases with the rise of RH. As we have already mentioned low values (*e.g.* 0.1 eV) of the activation energy do not contradict with that reported in the literature, *e.g.* for the H<sub>2</sub> interaction with ZnO [130], and similarly can be explained by the assumption that hydrogen arrive at the surface of the semiconductor in the ionized form which is highly reactive towards oxygen species. Therefore increase of water vapours for some catalysts favours hydrogen ionization, resulting in the drop of  $E_{act}$ .

#### 4.4.5. Summary

Measuring electrical parameters of the synthesized materials as a function of temperature and gas composition we found out that SnO<sub>2</sub> surface doped with noble metals manifest very different surface chemistry upon hydrogen interaction compared with blank SnO<sub>2</sub> or oxides bulk doped with metals IIIB and IVB groups. The latter react with hydrogen predominantly through bridging hydroxyls independently of the water content in the gas phase. In contrast, hydrogen interaction with the materials doped with noble metals depends on the water concentration: while at low RH (up to 20%) the mechanism is based on oxidation through bridging oxygen, at high RH (*e.g.* 50 and 80%) the oxidation occurs through surface hydroxyls. The reason for these changes is that the oxygen species interact similarly both with hydrogen and water, leading to the low sensor selectivity, while a hydroxylated surface demonstrates different reactivity towards these compounds. As a result all catalyst doped materials manifest pronounced change of signal parameters  $S_{max}$  and  $T_{Smax}$  with increase of water content in the gas phase.

Blank oxides, solid solutions and mixed oxides clearly demonstrate that sensor signal parameters depend on hydroxylation degree and homogeneity of the nature of surface hydroxyls. As a general trend it was found that the higher hydroxylation degree is the lower change of  $S_{max}$  and  $T_{Smax}$  is observed. It is difficult to figure out which material has demonstrated the best performance in the whole range of RH. However, between 20 and 80% RH the lowest change of the signal together with its rather high signal (*ca.* 10) was found for SnO<sub>2</sub>-TiO<sub>2</sub> at *ca.* 400 °C. Among catalyst doped materials rather acceptable properties in the same range of RH were found for Pt/Rh system at *ca.* 320 °C (with signal *ca.* 8).

Activation energy of hydrogen chemisorption was found to be quite low compared with hydrogen dissociation on ordered oxide surfaces but it is in good agreement with the literature, where the low values are explained by hydrogen ionization. The lowest  $E_{act}$  were observed for catalyst doped oxides.

## 4.5. Conclusion

This thesis is dedicated to the synthesis, material science and sensing properties of SnO<sub>2</sub>-based oxide systems. The comprehensive analysis of highly dispersed oxides was systematically performed for SnO<sub>2</sub> based oxide systems, starting from precursor nature, synthesis conditions, and then going through various *ex-situ* and *in-situ* techniques to better understand the surface chemistry of sensing phenomenon. Special accent was made to study the role of surface hydroxyl groups, which was very helpful to explain sensor selectivity in the presence of hydrogen and water vapours. As a result the mechanism of hydrogen and water chemisorption on the surface of semiconductor adsorbents has been proposed for various oxide systems.

The main results and achievements are listed in the following chapters, according to the field of investigation: synthesis, material science and sensing properties.

### 4.5.1. Synthesis

For the first time we propose the method of synthesis very pure and dispersed SnO<sub>2</sub> starting from metallic tin and comprising synthesis of the final product from metalorganic complex, without separation of the latter, by precipitation from organic polar solvents. The advantage of this method comprises not only low impurity level of the oxide and narrow distribution of the particle size in the range 2-5 nm, but also low cost of the process, since all the starting reagents are well available and cheap.

The chemical formula of the metalorganic compound is supposed to correspond to tin(IV) hydroxide acetate with general formula [Sn(OH)<sub>n</sub>(Ac)<sub>m</sub>]. The presence of OH groups in the inner (assumed) coordination sphere is essential regarding the final properties of the oxide. It was found that the very complex leads to formation of numerous hydroxyl groups on SnO<sub>2</sub> surface, which nature was found more homogeneous, their chemical activity enhanced and their surface content higher compared to the materials synthesized from tin(IV) acetate. In addition tin hydroxyl acetate complex leads to the formation of more dispersed particles with very low crystallite size. This together with high content of bridging hydroxyl groups suggests that hydrolysis of [Sn(OH)<sub>n</sub>(Ac)<sub>m</sub>] occurs much faster than polycondensation reaction and the latter seems to be dominated by olation.

The proposed method is very flexible from the experimental point of view and therefore was modified to synthesize SnO<sub>2</sub> doped with IVB and IIIB elements. The latter were introduced into the system of the precursor as metalorganic complexes as well.

Low impurity level of the synthesized oxides allowed us to synthesize materials doped with Cl, S, Pd and NaCl to investigate effect of the impurities on thermal stability of the nanodispersed oxides.

## 4.5.2. Material science

### 4.5.2.1. *Ex-situ* methods

The method used herein allows one to decrease the impurity level down to *ca.* 200 ppm of NaCl without continuous washing which is impossible to achieve using SnCl<sub>4</sub> and NaOH as starting reagents. Mean crystallite size for all oxide systems were found in the range 1.7-2.9 nm. In general, doping of the oxide brings about increase of this parameter. The highest value was found for SnO<sub>2</sub> doped with IIIB elements, and the lowest one for blank oxide.

In addition to the increased crystallite size, doped materials manifest higher hydroxylation degree. The highest value was found again for IIIB elements. Optic band gap was observed decreased for SnO<sub>2</sub> doped with IVB elements, while doping with IIIB elements do not have the common trend of the band gap evolution. Deposition of one noble metal remarkably increases optic band gap of the materials, which is in line with fact, found by HRTEM and XPS, that noble metals on the surface are in the form of oxides. In contrary, bimetallic systems decrease  $E_g$ , suggesting that catalyst system demonstrate more metallic character.

FTIR analysis permitted us to estimate the overall hydroxylation degree of the synthesized materials and compare homogeneity of the OH groups regarding their acidity. Accordingly, it was found that doping with either IVB or IIIB elements brings about heterogeneity of surface hydroxyls and increased hydroxylation degree. In addition, hydroxyls were found to become gradually more basic upon doping with Ti, Zr and Hf. The highest hydroxylation degree was found for IIIB elements.

### 4.5.2.2. *In-situ* methods

TGA analysis allowed us to estimate chemical activity of surface hydroxyls of synthesized materials. The comparative analysis of TGA and FTIR results allow us to estimate the extent of the chemical inertness of the OH groups. Doping with IVB elements brings about formation of occluded or inert OH groups. The hydroxyl activity within the group was found the lowest for Zr and the highest for Ti. Oxide doped with IIIB elements manifest very heterogeneous nature of the surface hydroxyl which consists of very reactive species and inert ones. The content of the later seems to be the highest among all the synthesized compounds. The highest hydroxyl reactivity in the group was observed for SnO<sub>2</sub>-La<sub>2</sub>O<sub>3</sub>. Doping with noble metals increases

dramatically the chemical activity of the surface hydroxyls, especially in the case of bimetallic catalyst systems.

MS-study of the catalytic activity of blank and Pd-doped materials reveals that hydrogen predominantly remain chemisorbed on blank oxide surface, while Pd deposition brings about water desorption. The hydrogen oxidation stoichiometry between 100-200 °C corresponds to the process mediated through surface oxygen, while at higher temperatures the stoichiometry suggests hydroxyl mediated reaction.

DRIFT spectroscopy at various temperatures and gas compositions (water and hydrogen in air) revealed that hydrogen interacts with the blank SnO<sub>2</sub> surface predominantly through bridging hydroxyls independently of the water content in the gas phase even in the low-temperature region. In contrast to the blank oxide, the hydrogen interaction with the Pd doped material depends on the water concentration: while at low RH (up to 20%) the hydrogen oxidation seems to realize through bridging oxygen in the whole temperature range (which is again slightly differs with the results of MS-study), at high RH (*e.g.* 50 and 80%) the oxidation occurs through surface hydroxyls.

On the basis of TXRD study it was pointed out that blank oxide is highly equilibrium two-phase composition. The role of the second phase is played more likely by the partially reduced SnO<sub>2</sub> surface, which impedes crystal growth rate under isothermal conditions and in the same time decreases activation energy of the growth rate, apparently due to low energy of defect formation. Impurities as well as the majority of the solid solutions and mixed oxides remarkably increase crystallite growth rate.

### 4.5.3. Sensing properties

The main achievement of this study is the experimental evidence of two very different sensing mechanisms in the presence of hydrogen, water and their mixtures. While blank oxide systems on the basis of SnO<sub>2</sub> all manifest high-temperature interaction with hydrogen, oxides doped with noble metals demonstrates their sensing activity in the low-temperature region. The whole battery of the performed *in-situ* and *ex-situ* analysis suggests that SnO<sub>2</sub> Ac and SnO<sub>2</sub>-MetO<sub>x</sub> from one side, and SnO<sub>2</sub> doped with noble metals from another, interact with hydrogen and/or water through very different adsorption centres: bridging hydroxyls and oxygen species, resp.

It seems that oxide systems react with hydrogen predominantly through bridging hydroxyls independently of the water content in the gas phase. However, for catalyst doped materials at low RH (up to 20%) the mechanism is based on oxidation through bridging oxygen, and at high RH



(e.g. 50 and 80%) the oxidation occurs through surface hydroxyls. It was found that surface oxygen species interact similarly both with hydrogen and water, leading to the low sensor selectivity, while a hydroxylated surface demonstrates different reactivity towards these compounds. As a result all catalyst doped materials manifest pronounced change of signal parameters  $S_{max}$  and  $T_{Smax}$  with increase of water content in the gas phase.

## 5. Bibliography

1. Yamazoe, N., *Toward innovations of gas sensor technology*. Sensors and Actuators B-Chemical, 2005. **108**(1-2): p. 2-14.
2. Volkenshtein, F.F., *POLUPROVODNIKI KAK KATALIZATORY KHIMICHESKIKH REAKTSII*. Uspekhi Fizicheskikh Nauk, 1956. **60**(2): p. 249-293.
3. Volkenshtein, F.F., *SOVREMENNOE SOSTOYANIE ELEKTRONNOI TEORII KATALIZA NA POLUPROVODNIKAKH*. Uspekhi Khimii, 1958. **27**(11): p. 1304-1320.
4. Volkenshtein, F.F. and S.M. Kogan, *THE CONCEPT OF QUASI-ISOLATED SURFACE IN THE THEORY OF CHEMISORPTION*. Zhurnal Fizicheskoi Khimii, 1960. **34**(9): p. 1996-2004.
5. Myasnikov, I.A., *A STUDY OF THE RELATIONSHIP BETWEEN THE ELECTROCONDUCTIVITY AND THE ADSORPTION AND SENSIBILIZING PROPERTIES OF ZINC OXIDE .1. ELECTRONIC PHENOMENA IN ZNO DURING OXYGEN ADSORPTION*. Zhurnal Fizicheskoi Khimii, 1957. **31**(8): p. 1714-1731.
6. Myasnikov, I.A., *SURFACE PROCESSES ON ZNO AND ITS ELECTRICAL CONDUCTIVITY IN A HYDROGEN ATMOSPHERE*. Zhurnal Fizicheskoi Khimii, 1958. **32**(4): p. 841-847.
7. Myasnikov, I.A., *ELECTROCONDUCTIVITY OF SEMI-CONDUCTORS IN THE CHEMISORPTION OF MOLECULES, ATOMS AND RADICALS*. Zhurnal Fizicheskoi Khimii, 1960. **34**(2): p. 395-404.
8. Seiyama, T., et al., *A NEW DETECTOR FOR GASEOUS COMPONENTS USING SEMICONDUCTIVE THIN FILMS*. Analytical Chemistry, 1962. **34**(11): p. 1502-&.
9. Gopel, W. and K.D. Schierbaum, *SNO<sub>2</sub> SENSORS - CURRENT STATUS AND FUTURE-PROSPECTS*. Sensors and Actuators B-Chemical, 1995. **26**(1-3): p. 1-12.
10. Kupriyanov, L.Y., ed. *Semiconductor Sensors in Physico-Chemical Studies*. Handbook of Sensors and Actuators, ed. S. Middelhoek. Vol. 4. 1996, Elsevier: Amsterdam.
11. Heilig, A., et al., *Gas identification by modulating temperatures of SnO<sub>2</sub>-based thick film sensors*. Sensors and Actuators B-Chemical, 1997. **43**(1-3): p. 45-51.
12. Lee, A.P. and B.J. Reedy, *Temperature modulation in semiconductor gas sensing*. Sensors and Actuators B-Chemical, 1999. **60**(1): p. 35-42.
13. Samotaev, N.N., et al., *The mechanism of the formation of selective response of semiconductor gas sensor in mixture of CH<sub>4</sub>/H<sub>2</sub>/CO with air*. Sensors and Actuators B-Chemical, 2007. **127**(1): p. 242-247.
14. Cabot, A., et al., *Mesoporous catalytic filters for semiconductor gas sensors*. Thin Solid Films, 2003. **436**(1): p. 64-69.
15. Fleischer, M., et al., *Selective gas detection with high-temperature operated metal oxides using catalytic filters*. Sensors and Actuators B-Chemical, 2000. **69**(1-2): p. 205-210.

16. Cabot, A., et al., *Analysis of the noble metal catalytic additives introduced by impregnation of as obtained SnO<sub>2</sub> sol-gel nanocrystals for gas sensors*. Sensors and Actuators B-Chemical, 2000. **70**(1-3): p. 87-100.
17. Dieguez, A., et al., *Influence on the gas sensor performances of the metal chemical states introduced by impregnation of calcinated SnO<sub>2</sub> sol-gel nanocrystals*. Sensors and Actuators B-Chemical, 2000. **68**(1-3): p. 94-99.
18. Tournier, G., et al., *SELECTIVE DETECTION OF CO AND CH<sub>4</sub> WITH GAS SENSORS USING SNO<sub>2</sub> DOPED WITH PALLADIUM*. Sensors and Actuators B-Chemical, 1995. **26**(1-3): p. 24-28.
19. Chane-Ching, J.-Y., et al., *Nanostructured materials with highly dispersed Au-Ce<sub>0.5</sub>Zr<sub>0.5</sub>O<sub>2</sub> nanodomains: A route to temperature stable Au catalysts?* Journal of Materials Chemistry, 2008. **18**(39): p. 4712-4717.
20. Gopel, W., J. Hesse, and J.N. Zemel, eds. *Sensors. A Comprehensive survey*. . Chemical and Biochemical Sensors, Part I., ed. W. Gopel, T.A. Jones, M. Kleitz, J. Lundstrom, T. Seiyama. Vol. 2. 1991, VCH Verlagsgesellschaft mbh, Weinheim (Federal Rep. of Germany), VCH Publishers Inc., New York. 31-32.
21. Gelin, P. and M. Primet, *Complete oxidation of methane at low temperature over noble metal based catalysts: a review*. Applied Catalysis B-Environmental, 2002. **39**(1): p. 1-37.
22. Fang, Z.Z. and H. Wang, *Densification and grain growth during sintering of nanosized particles*. International Materials Reviews, 2008. **53**(6): p. 326-352.
23. Huxter, V.M., et al., *CdSe Nanoparticle Elasticity and Surface Energy*. Nano Letters, 2009. **9**(1): p. 405-409.
24. Qi, W.H., *Size effect on melting temperature of nanosolids*. Physica B-Condensed Matter, 2005. **368**(1-4): p. 46-50.
25. Xu, C.N., et al., *GRAIN-SIZE EFFECTS ON GAS SENSITIVITY OF POROUS SNO<sub>2</sub>-BASED ELEMENTS*. Sensors and Actuators B-Chemical, 1991. **3**(2): p. 147-155.
26. Harrison, P.G., C. Bailey, and W. Azelee, *Modified Tin(IV) Oxide (M/SnO<sub>2</sub>M=Cr, La, Pr, Nd, Sm, Gd) Catalysts for the Oxidation of Carbon Monoxide and Propane*. Journal of Catalysis, 1999. **186**(1): p. 147-159.
27. Fokema, M.D. and J.Y. Ying, *THE SELECTIVE CATALYTIC REDUCTION OF NITRIC OXIDE WITH METHANE OVER NONZEOLITIC CATALYSTS*. Catalysis Reviews: Science and Engineering, 2001. **43**(1): p. 1 - 29.
28. Zhang, H.J., G.H. Chen, and D.W. Bahnemann, *Photoelectrocatalytic materials for environmental applications*. Journal of Materials Chemistry, 2009. **19**(29): p. 5089-5121.
29. Aiken, J.D. and R.G. Finke, *A review of modern transition-metal nanoclusters: their synthesis, characterization, and applications in catalysis*. Journal of Molecular Catalysis a-Chemical, 1999. **145**(1-2): p. 1-44.
30. Yamazoe, N., G. Sakai, and K. Shimano, *Oxide semiconductor gas sensors*. Catalysis Surveys from Asia, 2003. **7**(1): p. 63-75.
31. Riley, D.J., J.P. Waggett, and K.G.U. Wijayantha, *Colloidal bismuth sulfide nanoparticles: a photoelectrochemical study of the relationship between bandgap and particle size*. Journal of Materials Chemistry, 2004. **14**(4): p. 704-708.
32. Themlin, J.M., et al., *RESONANT-PHOTOEMISSION STUDY OF SNO<sub>2</sub> - CATIONIC ORIGIN OF THE DEFECT BAND-GAP STATES*. Physical Review B, 1990. **42**(18): p. 11914-11925.
33. Korotcenkov, G., *Gas response control through structural and chemical modification of metal oxide films: state of the art and approaches*. Sensors and Actuators B-Chemical, 2005. **107**: p. 209-232.

34. Choy, K.L., *Chemical vapour deposition of coatings*. Progress in Materials Science, 2003. **48**(2): p. PII S0079-6425(01)00009-3.
35. Fendler, J.H., *Self-assembled nanostructured materials*. Chemistry of Materials, 1996. **8**(8): p. 1616-1624.
36. Ocana, M., R. Rodriguezclemente, and C.J. Serna, *UNIFORM COLLOIDAL PARTICLES IN SOLUTION - FORMATION MECHANISMS*. Advanced Materials, 1995. **7**(2): p. 212-216.
37. Lewis, J.A., *Colloidal processing of ceramics*. Journal of the American Ceramic Society, 2000. **83**(10): p. 2341-2359.
38. *Handbook of preparative and inorganic chemistry*. second ed, ed. G. Brauer. Vol. 1. 1963, London: Academic Press Inc.
39. Simone, D.O., et al., *REVERSIBLE POISONING OF PALLADIUM CATALYSTS FOR METHANE OXIDATION*. Applied Catalysis, 1991. **70**(1): p. 87-100.
40. Zhang, J.R. and L. Gao, *Synthesis and characterization of nanocrystalline tin oxide by sol-gel method*. Journal of Solid State Chemistry, 2004. **177**(4-5): p. 1425-1430.
41. Gamard, A., et al., *New fluorinated stannic compounds as precursors of F-doped SnO<sub>2</sub> materials prepared by the sol-gel route*. Inorganic Chemistry, 1999. **38**(21): p. 4671-4679.
42. Humphreys, F.J. and M. Haterly, *Recrystallization and Related Annealing Phenomena*. 2004: Elsevier. 146.
43. Manjanna, J., T. Kozaki, and S. Sato, *Fe(III)-montmorillonite: Basic properties and diffusion of tracers relevant to alteration of bentonite in deep geological disposal*. Applied Clay Science, 2009. **43**(2): p. 208-217.
44. Dieguez, A., et al., *Parameter optimisation in SnO<sub>2</sub> gas sensors for NO<sub>2</sub> detection with low cross-sensitivity to CO: sol-gel preparation, film preparation, powder calcination, doping and grinding*. Sensors and Actuators B-Chemical, 2000. **65**(1-3): p. 166-168.
45. Mishra, S., et al., *Alcohol sensing of tin oxide thin film prepared by sol-gel process*. Bulletin of Materials Science, 2002. **25**(3): p. 231-234.
46. Rumyantseva, M.N., et al., *Nanocomposites SnO<sub>2</sub>/Fe<sub>2</sub>O<sub>3</sub>: Wet chemical synthesis and nanostructure characterization*. Sensors and Actuators B-Chemical, 2005. **109**(1): p. 64-74.
47. Epifani, M., et al., *Sol-gel processing and characterization of pure and metal-doped SnO<sub>2</sub> thin films*. Journal of the American Ceramic Society, 2001. **84**(1): p. 48-54.
48. Maire, J.C., *PREPARATION ET PROPRIETES DES ALCOXYDES DE LETAIN IV*. Annales De Chimie France, 1961. **6**(9-1): p. 969-&.
49. *ISI Web of Knowledge*. Copyright © 2008 Thomson Reuters [cited].
50. Shukla, S., et al., *Synthesis and characterization of sol-gel derived nanocrystalline tin oxide thin film as hydrogen sensor*. Sensors and Actuators B-Chemical, 2003. **96**(1-2): p. 343-353.
51. Mihaiu, S., L. Marta, and M. Zaharescu, *SnO<sub>2</sub> and CeO<sub>2</sub>-doped SnO<sub>2</sub> materials obtained by sol-gel alkoxide route*. Journal of the European Ceramic Society, 2007. **27**(2-3): p. 551-555.
52. Canevali, C., et al., *Surface reactivity of SnO<sub>2</sub> obtained by sol-gel type condensation: Interaction with inert, combustible gases, vapour-phase H<sub>2</sub>O and air, as revealed by electron paramagnetic resonance spectroscopy*. Journal of Materials Chemistry, 1997. **7**(6): p. 997-1002.
53. Huang, R., et al., *Formation and characterization of tin oxide aerogel derived from sol-gel process based on tetra(n-butoxy)tin(IV)*. Journal of Non-Crystalline Solids, 2005. **351**(1): p. 23-28.

54. Ardizzone, S., et al., *Low-temperature sol-gel nanocrystalline tin oxide integrated characterization of electrodes and particles obtained by a common path*. *Electrochimica Acta*, 2005. **50**(22): p. 4419-4425.
55. de Monredon, S., et al., *Synthesis and characterization of crystalline tin oxide nanoparticles*. *Journal of Materials Chemistry*, 2002. **12**(8): p. 2396-2400.
56. Verdenelli, M., et al., *Tin dioxide thin films from Sn(IV) modified alkoxides - synthesis and structural characterization of Sn(OEt)(2)(eta(2)-acac)(2) and Sn-4(mu(3)-O)(2)(mu(2)-OEt)(4)(OEt)(6)(eta(2)-acac)(2)*. *Polyhedron*, 2000. **19**(18-19): p. 2069-2075.
57. Bitterer, H., ed. *Gmelin Handbuch der Anorganischen Chemie*. Zinn, Verbindungen mit Wasserstoff, Sauerstoff, Stickstoff und Halogenen, ed. H. Bergman, H. Bitterer, and A.B.-N.e. al. Vol. C 1. 1972, Springer-Verlag: Berlin-Heidelberg.
58. Wilkinson, G., ed. *Comprehensive coordination chemistry*. Ligands. Vol. 2. 1987, Pergamon Press: Oxford.
59. Mizukami, F., *Design of Solid Catalysts by Sol-gel Method Using Organic Polydentate Ligands and Their Catalytic Performance*. *Journal of the Japan Petroleum Institute*, 2008. **51**(6): p. 332-347.
60. Bitterer, H., ed. *Gmelin Handbuch der Anorganischen Chemie*. Zinn, Verbindungen mit Schwefel, Selen, Tellur, Polonium, Bor, Kohlenstoff, Silicium, Phosphor, Arsen, Antimon und Wismut, ed. H. Bitterer and e.a. H. Katscher. Vol. C 2. 1975, Springer-Verlag: Berlin-Heidelberg.
61. Christie, A.D., R.A. Howie, and W. Moser, *TIN(II) OXALATE STRUCTURES*. *Inorganica Chimica Acta*, 1979. **36**(2): p. L447-L448.
62. Alcantara, R., et al., *Tin oxalate as a precursor of tin dioxide and electrode materials for lithium-ion batteries*. *Journal of Solid State Electrochemistry*, 2001. **6**(1): p. 55-62.
63. Dean, J.A., ed. *Lange's handbook of chemistry*. Fifteenth Edition ed. 1999, McGraw-Hill, Inc.: New York.
64. Stafeeva, V.S., et al., *Crystal structure and chemical bonding in tin(II) acetate*. *Polyhedron*, 2007. **26**(18): p. 5365-5369.
65. Schleitzer-Rust, E., ed. *Gmelin Handbuch der Anorganischen Chemie*. Zinn, Komplexverbindungen des Zinns, ed. H. Demmer and E. Schleitzer-Rust. Vol. C 5. 1977, Springer-Verlag: Berlin-Heidelberg.
66. Harrison, P.G. and E.W. Thornton, *DERIVATIVES OF BIVALENT GERMANIUM, TIN, AND LEAD .21. TIN(II) FORMATE - REINVESTIGATION*. *Journal of the Chemical Society-Dalton Transactions*, 1978(10): p. 1274-1278.
67. Hampden-Smith, M.J., T.A. Wark, and C.J. Brinker, *The solid state and solution structures of tin(IV) alkoxide compounds and their use as precursors to form tin oxide ceramics via sol-gel-type hydrolysis and condensation*. *Coordination chemistry reviews*, 1992. **112**: p. 81-116.
68. Chandler, C.D., et al., *THE STRUCTURES OF MONO AND BIS BETA-DIKETONATE TIN(IV) ALKOXIDE COMPLEXES*. *Australian Journal of Chemistry*, 1987. **40**(8): p. 1427-1439.
69. Hampdensmith, M.J., et al., *SOLID-STATE AND SOLUTION STRUCTURAL INVESTIGATION OF HOMOLEPTIC TIN(IV) ALKOXIDE COMPOUNDS .1. SN(O-TERT-BU)4 AND [SN(O-ISO-PR)4.HO-ISO-PR]2*. *Canadian Journal of Chemistry- Revue Canadienne De Chimie*, 1991. **69**(1): p. 121-129.
70. Alcock, N.W. and V.L. Tracy, *ACETATES AND ACETATO COMPLEXES .4. CRYSTAL AND MOLECULAR-STRUCTURE OF TIN TETRAACETATE*. *Acta Crystallographica Section B-Structural Science*, 1979. **35**(JAN): p. 80-83.

71. Alcock, N.W., V.M. Tracy, and T.C. Waddington, *ACETATES AND ACETATO-COMPLEXES .1. PREPARATION OF ACETATO-COMPLEXES AND CONDUCTIMETRIC STUDIES IN ACETIC-ANHYDRIDE SOLVENT SYSTEM*. Journal of the Chemical Society-Dalton Transactions, 1976(21): p. 2238-2242.
72. Hagemeyer, A., et al., *High surface area tin oxide*. Applied Catalysis a-General, 2007. **317**(2): p. 139-148.
73. Toupance, T., et al., *Nanocrystalline mesoporous tin dioxide prepared by the sol-gel route from a dialkoxydi(beta-diketonato)tin complex*. Chemistry of Materials, 2003. **15**(24): p. 4691-4697.
74. Briois, V., et al., *Solid-state and solution structural study of acetylacetonate-modified tin(IV) chloride used as a precursor of SnO<sub>2</sub> nanoparticles prepared by a sol-gel route*. Chemistry of Materials, 2004. **16**(20): p. 3885-3894.
75. Gonzalez, R.D., T. Lopez, and R. Gomez, *Sol-Gel preparation of supported metal catalysts*. Catalysis Today 1997. **35**: p. 293-317.
76. Brinker, C.J. and G.W. Scherer, *Sol-gel science. The physics and chemistry of sol-gel processing*. 1990, San Diego, California: Academic Press. 908.
77. Parks, G.A., *The Isoelectric Points of Solid Oxides, Solid Hydroxides, and Aqueous Hydroxo Complex Systems*. Chemical Reviews, 1965. **65**(2): p. 177-198.
78. Belin, S., et al., *Preparation of ceramic membranes from surface modified tin oxide nanoparticles*. Colloids and Surfaces a-Physicochemical and Engineering Aspects, 2003. **216**(1-3): p. PII S0927-7757(02)00548-4.
79. Song, K.C. and J.H. Kim, *Preparation of nanosize tin oxide particles from water-in-oil microemulsions*. Journal of Colloid and Interface Science, 1999. **212**(1): p. 193-196.
80. Chen, L.Y., et al., *Synthesis of ZnO-SnO<sub>2</sub> nanocomposites by microemulsion and sensing properties for NO<sub>2</sub>*. Sensors and Actuators B-Chemical, 2008. **134**(2): p. 360-366.
81. Zhou, J.X., et al., *Structural and spectral properties of SnO<sub>2</sub> nanocrystal prepared by microemulsion technique*. Applied Physics a-Materials Science & Processing, 2005. **81**(1): p. 177-182.
82. Pileni, M.P., *Nanosized particles made in colloidal assemblies*. Langmuir, 1997. **13**(13): p. 3266-3276.
83. Ahmed, J., et al., *Tin dioxide nanoparticles: Reverse micellar synthesis and gas sensing properties*. Materials Research Bulletin, 2008. **43**(2): p. 264-271.
84. Hench, L.L. and J.K. West, *THE SOL-GEL PROCESS*. Chemical Reviews, 1990. **90**(1): p. 33-72.
85. Jitianu, A., et al., *New SnO<sub>2</sub> nano-clusters obtained by sol-gel route, structural characterization and their gas sensing applications*. Journal of Sol-Gel Science and Technology, 2003. **26**(1-3): p. 483-488.
86. Zhang, R., J.Y. Lee, and Z.L. Liu, *Pechini process-derived tin oxide and tin oxide-graphite composites for lithium-ion batteries*. Journal of Power Sources, 2002. **112**(2): p. 596-605.
87. Sergent, N., et al., *Preparation and characterisation of high surface area stannic oxides: structural, textural and semiconducting properties*. Sensors and Actuators B: Chemical, 2002. **84**(2-3): p. 176-188.
88. Ristic, M., et al., *Dependence of nanocrystalline SnO<sub>2</sub> particle size on synthesis route*. Journal of Non-Crystalline Solids, 2002. **303**(2): p. 270-280.
89. Chichagov, A.V. and e. al., *Information-Calculating System on Crystal Structure Data of Minerals (MINCRYST)*. Kristallografiya, 1990. **35**: p. p.610-616 (in Russian).
90. Godinho, K.G., A. Walsh, and G.W. Watson, *Energetic and Electronic Structure Analysis of Intrinsic Defects in SnO<sub>2</sub>*. The Journal of Physical Chemistry C, 2009. **113**: p. 439-448.

91. Smith, P.J., ed. *Chemistry of Tin*. 1998, Blackie Academic & Professional: London.
92. Batzill, M. and U. Diebold, *The surface and materials science of tin oxide*. Progress in Surface Science, 2005. **79**(2-4): p. 47-154.
93. Cox, D.F., T.B. Fryberger, and S. Semancik, *Oxygen vacancies and defect electronic states on the SnO<sub>2</sub>(110)-1 X 1 surface*. Physical Review B, 1988. **38**(3): p. 2072.
94. Barsan, N. and U. Weimar, *Conduction model of metal oxide gas sensors*. Journal of Electroceramics, 2001. **7**(3): p. 143-167.
95. Nekrasov, B.V., *Fundamentals of General Chemistry*. Vol. 1. 1973, Moscow: Khimiya (in Russian).
96. Lidin, R.A., V.A. Molochko, and L.L. Andreeva, *Reactivity of Inorganic Substances*, ed. R.A.Lidin. 2000, Moscow: Khimiya (in Russian).
97. Brauer, G., ed. *Handbook of Preparative Inorganic Chemistry*. 2 ed. Vol. 1. 1963, Academic Press: New York.
98. Harrison, P.G. and E.W.Thornton, *Tin Oxide Surfaces:IV. Infrared Study of the Adsorption of Oxygen and Carbon Monoxide + Oxygen Mixtures on Tin(IV) Oxide, and the Adsorption of Carbon Dioxide on Ammoniapretreated Tin(IV) Oxide*. J. Chem. Soc., Faraday Trans. 1, 1978. **74**: p. 2597 - 2603.
99. Rantala, T.T., T.S. Rantala, and V. Lantto, *Surface relaxation of the (110) face of rutile SnO<sub>2</sub>*. Surface Science 1999. **420** p. 103-109.
100. Barsan, N. and U. Weimar, *Conduction Model of Metal Oxide Gas Sensors*. Journal of Electroceramics 2001. **7**: p. 143-167.
101. Gurlo, A., *Interplay between O<sub>2</sub> and SnO<sub>2</sub> : Oxygen Ionosorption and Spectroscopic Evidence for Adsorbed Oxygen*. ChemPhysChem, 2006. **7**: p. 2041 – 2052.
102. Slater, B., et al., *Dissociation of O<sub>2</sub> on the reduced SnO<sub>2</sub> (110) surface*. Chem. Commun. , 2000: p. 1235-1236.
103. Amalric-Popescu, D. and F. Bozon-Verduraz, *Infrared studies on SnO<sub>2</sub> and Pd/SnO<sub>2</sub>*. Catalysis Today, 2001. **70**.
104. Sergeant, N., et al., *Interactions of nanocrystalline tin oxide powder with NO<sub>2</sub>: A Raman spectroscopic study*. Sensors and Actuators B: Chemical, 2007. **126**(1): p. 1-5.
105. Gercher, V.A. and D.F. Cox, *Water adsorption on stoichiometric and defective SnO<sub>2</sub>(110) surfaces*. Surface Science, 1995. **322**(1-3): p. 177-184.
106. Sergeant, N., et al., *FTIR study of low-temperature CO adsorption on high surface area tin(IV) oxide: Probing Lewis and Brønsted acidity*. Phys. Chem. Chem. Phys., 2002. **4**: p. 4802-4808.
107. Henderson, M.A., *The interaction of water with solid surfaces: fundamental aspects revisited*. Surface Science Reports, 2002. **46**(1-8): p. 5-308.
108. Gercher, V.A. and D.F. Cox, *Water adsorption on stoichiometric and defective SnO<sub>2</sub> (110) surfaces*. Surface Science, 1995. **322**: p. 177-184.
109. Graf, P.O., et al., *New insights in reactivity of hydroxyl groups in water gas shift reaction on Pt/ZrO<sub>2</sub>*. Journal of Catalysis, 2009. **262**(2): p. 181-187.
110. Noei, H., et al., *The identification of hydroxyl groups on ZnO nanoparticles by infrared spectroscopy*. Physical Chemistry Chemical Physics, 2008. **10**: p. 7092-7097.
111. Barsan, N. and U. Weimar, *Understanding the fundamental principles of metal oxide based gas sensors; the example of CO sensing with SnO<sub>2</sub> sensors in the presence of humidity*. Journal of Physics-Condensed Matter, 2003. **15**(20): p. R813-R839.
112. Harbeck, S., et al., *DRIFT studies of thick film un-doped and Pd-doped SnO<sub>2</sub> sensors: temperature changes effect and CO detection mechanism in the presence of water vapour*. Thin Solid Films, 2003. **436**(1): p. 76-83.
113. Sahm, T., et al., *Fundamental studies on SnO<sub>2</sub> by means of simultaneous work function change and conduction measurements*. Thin Solid Films, 2005. **490**(1): p. 43-47.

114. Kanofsky, J.R., et al., *DIRECT IDENTIFICATION OF REACTIVE CHANNELS IN REACTIONS OF OXYGEN-ATOMS AND HYDROXYL RADICALS WITH ACETYLENE AND METHYLACETYLENE*. Journal of Physical Chemistry, 1974. **78**(4): p. 311-316.
115. Zakrzewska, K., *Mixed oxides as gas sensors*. Thin Solid Films, 2001. **391**(2): p. 229-238.
116. Kikoin, I.K., ed. *Tablitsy Fizicheskikh Velichin (Tables of Physical Quantities)*. 1976, Atomizdat: Moscow. 1008.
117. Sun, B.J., et al., *Subsolidus phase relations in the ternary system SnO<sub>2</sub>-TiO<sub>2</sub>-Y<sub>2</sub>O<sub>3</sub>*. Journal of Alloys and Compounds, 2008. **455**(1-2): p. 265-268.
118. Gaillard-Allemand, B., et al., *Experimental study of the SnO<sub>2</sub>-ZrO<sub>2</sub> phase diagram*. Journal of the European Ceramic Society, 2002. **22**(13): p. 2297-2303.
119. Brauer, G., ed. *Handbook Of Preparative Inorganic Chemistry Brauer 2nd Ed.* Vol. 1. 1963, Academic Press: London.
120. Shi, Z.M. and L. Yan, *Phase transformation and crystal growth behaviors of La<sup>3+</sup>/Ce<sup>3+</sup>-doped TiO<sub>2</sub>-20 wt% SnO<sub>2</sub> gels*. Journal of Non-Crystalline Solids, 2008. **354**(40-41): p. 4654-4660.
121. Biju, K.P. and M.K. Jain, *Sol-gel derived TiO<sub>2</sub>:ZrO<sub>2</sub> multilayer thin films for humidity sensing application*. Sensors and Actuators B: Chemical, 2008. **128**(2): p. 407-413.
122. Radecka, M., K. Zakrzewska, and M. Rekas, *SnO<sub>2</sub>-TiO<sub>2</sub> solid solutions for gas sensors*. Sensors and Actuators B-Chemical, 1998. **47**(1-3): p. 194-204.
123. Janghorban, K. and et al., *The Hume-Rothery size rule and double-well microstructures in gold-nickel*. Journal of Physics: Condensed Matter, 2001. **13**(38): p. 8661.
124. Alemi, A. and R.E. Kalan, *Preparation and characterization of neodymium tin oxide pyrochlore nanocrystals by the hydrothermal method*. Radiation Effects and Defects in Solids, 2008. **163**(3): p. 229-236.
125. Fokema, M.D. and J.Y. Ying, *The selective catalytic reduction of nitric oxide with methane over nonzeolitic catalysts*. Catalysis Reviews-Science and Engineering, 2001. **43**(1-2): p. 1-29.
126. Hanada, N., et al., *Development of carbon dioxide sensor using semiconductive oxide*. Nippon Kagaku Kaishi, 2000(11): p. 763-772.
127. Marsal, A., A. Cornet, and J.R. Morante, *Study of the CO and humidity interference in La doped tin oxide CO<sub>2</sub> gas sensor*. Sensors and Actuators B: Chemical, 2003. **94**(3): p. 324-329.
128. Gurlo, A. and R. Riedel, *In situ and operando spectroscopy for assessing mechanisms of gas sensing*. Angewandte Chemie-International Edition, 2007. **46**: p. 3826-3848.
129. Seiyama, T., et al., *A New Detector for Gaseous Components Using Semiconductive Thin Films*. Analytical Chemistry, 1962. **34**(11): p. 1502-1503.
130. Kupriyanov, L.Y., ed. *Handbook of sensors and actuators*. Semiconductor sensors in physico-chemical study, ed. S. Middelhoek. Vol. 4. 1996, Elsevier: Amsterdam.
131. Taguchi, N., *Japanese Patent 45-38200*.
132. Dieguez, A., et al., *The complete Raman spectrum of nanometric SnO<sub>2</sub> particles*. Journal of Applied Physics, 2001. **90**(3): p. 1550-1557.
133. Oprea, A., et al., *Conduction model of SnO<sub>2</sub> thin films based on conductance and Hall effect measurements*. Journal of Applied Physics, 2006. **100**(3): p. 033716.
134. Ionescu, R., C. Moise, and A. Vancu, *ARE MODULATIONS OF THE SCHOTTKY SURFACE-BARRIER THE ONLY EXPLANATION FOR THE GAS-SENSING EFFECTS IN SINTERED SNO<sub>2</sub>*. Applied Surface Science, 1995. **84**(3): p. 291-297.
135. Hahn, S.H., et al., *CO sensing with SnO<sub>2</sub> thick film sensors: role of oxygen and water vapour*. Thin Solid Films, 2003. **436**(1): p. 17-24.



136. Neri, G., et al., *A study of water influence on CO response on gold-doped iron oxide sensors*. Sensors and Actuators B-Chemical, 2004. **101**(1-2): p. 90-96.
137. Morimitsu, M., et al., *Effects of surface modification with platinum and ruthenium on temperature and humidity dependence of SnO<sub>2</sub>-based CO gas sensors*. Sensors and Actuators B-Chemical, 2000. **67**(1-2): p. 184-188.
138. Ionescu, R., et al., *Role of water vapour in the interaction of SnO<sub>2</sub> gas sensors with CO and CH<sub>4</sub>*. Sensors and Actuators B-Chemical, 1999. **61**(1-3): p. 39-42.
139. Robert, S., *Book Review: The Surface Science of Metal Oxides*. By V. E. Henrich and P. A. Cox. Angewandte Chemie International Edition in English, 1996. **35**(3): p. 347.
140. *FOCT 12.1.005-88*.
141. *Gmelins Handbuch der Anorganischen Chemie, Zinn, Teil C2, Verlag Chemie GmbH, Weinheim, 1975*.
142. Parks, G.A., *ISOELECTRIC POINTS OF SOLID OXIDES SOLID HYDROXIDES AND AQUEOUS HYDROXO COMPLEX SYSTEMS*. Chemical Reviews, 1965. **65**(2): p. 177-&.
143. *TOPAS, General Profile and Structure Analysis Software for Powder Diffraction Data, V3.1, Bruker AXS GmbH, Karlsruhe, Germany*.
144. Stokes, A.R. and A.J.C. Wilson, *A method of calculating the integral breadths of Debye-Scherrer lines*. Mathematical Proceedings of the Cambridge Philosophical Society, 1942. **38**(03): p. 313-322.
145. Popescu, D.A., et al., *Nanosized tin dioxide: Spectroscopic (UV-VIS, NIR, EPR) and electrical conductivity studies*. Physical Chemistry Chemical Physics, 2001. **3**(12): p. 2522-2530.
146. Weber, R.S., *Effect of Local Structure on the UV-Visible Absorption Edges of Molybdenum Oxide Clusters and Supported Molybdenum Oxides*. Journal of Catalysis, 1995. **151**(2): p. 470-474.
147. Wagner, C.D., et al., *Empirical atomic sensitivity factors for quantitative analysis by electron spectroscopy for chemical analysis*. Surface and Interface Analysis, 1981. **3**(5): p. 211-225.
148. Topsoe, H., *Developments in operando studies and in situ characterization of heterogeneous catalysts*. Journal of Catalysis, 2003. **216**(1-2): p. 155-164.
149. Tinnemans, S.J., et al., *Combining operando techniques in one spectroscopic-reaction cell: New opportunities for elucidating the active site and related reaction mechanism in catalysis*. Catalysis Today, 2006. **113**(1-2): p. 3-15.
150. Koziej, D., et al., *Complementary phenomenological and spectroscopic studies of propane sensing with tin dioxide based sensors*. Sensors and Actuators B: Chemical, 2005. **108**(1-2): p. 75-83.
151. Koziej, D., et al., *Influence of annealing temperature on the CO sensing mechanism for tin dioxide based sensors-Operando studies*. Catalysis Today, 2007. **126**(1-2): p. 211-218.
152. Koziej, D., et al., *Spectroscopic insights into CO sensing of undoped and palladium doped tin dioxide sensors derived from hydrothermally treated tin oxide sol*. Sensors and Actuators B-Chemical, 2006. **118**(1-2): p. 98-104.
153. Meunier, F.C., et al., *A modified commercial DRIFTS cell for kinetically relevant operando studies of heterogeneous catalytic reactions*. Applied Catalysis A: General, 2008. **340** p. 196-202.
154. Audebrand, N., J.P. Auffredic, and D. Louer, *X-ray diffraction study of the early stages of the growth of nanoscale zinc oxide crystallites obtained from thermal decomposition of four precursors. General concepts on precursor-dependent microstructural properties*. Chemistry of Materials, 1998. **10**(9): p. 2450-2461.

155. Malyshev, V.V. and A.V. Pislyakov, *Investigation of gas-sensitivity of sensor structures to carbon monoxide in a wide range of temperature, concentration and humidity of gas medium*. Sensors and Actuators B-Chemical, 2007. **123**(1): p. 71-81.
156. Ionescu, R., C. Moise, and A. Vancu, *Are the modulations of the Schottky surface-barrier the only explanation for the gas-sensing effectes in sintered SnO<sub>2</sub>*. Applied Surface Science, 1995. **84**(3): p. 291-297.
157. Alcock, N.W., V.M. Tracy, and T.C. Waddington, *Acetates and acetate-complexes. Part 1. Preparation of acetato-complexes and conductimetric studies in the acetic anhydride solvent system*. Journal of the Chemical Society-Dalton Transactions, 1976. **21**: p. 2238-2242.
158. Donaldson, J.D., W. Moser, and W.B. Simpson, *Tin(II) acetates*. Journal of the Chemical Society, 1964: p. 5942 - 5947.
159. Alcock, N.W. and V.L. Tracy, *Acetates and acetate-complexes. Part 4. Crystal and molecular structure of tin tetraacetate*. Acta Crystallographica Section B-Structural Science, 1979. **35**(JAN): p. 80-83.
160. Alcock, N.W., V.M. Tracy, and T.C. Waddington, *Acetates and acetato-complexes. Part 2. Spectroscopic studies* Journal of the Chemical Society-Dalton Transactions, 1976. **21**: p. 2243-2246.
161. Sakthivel, S., et al., *Enhancement of photocatalytic activity by metal deposition: characterisation and photonic efficiency of Pt, Au and Pd deposited on TiO<sub>2</sub> catalyst*. Water Research, 2004. **38**(13): p. 3001-3008.
162. Li, M. and J.C. Li, *Size effects on the band-gap of semiconductor compounds*. Materials Letters, 2006. **60**(20): p. 2526-2529.
163. Hoffmann, M.R., et al., *Environmental Applications of Semiconductor Photocatalysis*. Chemical Reviews, 2002. **95**(1): p. 69-96.
164. Sanchez, E. and T. Lopez, *Effect of the preparation method on the band gap of titania and platinum-titania sol-gel materials*. Materials Letters, 1995. **25**(5-6): p. 271-275.
165. Pierre, A. and T. Jean-Pierre, *Structure and Ionic Mobility of Zirconia at High Temperature*. Journal of the American Ceramic Society, 1985. **68**(1): p. 34-40.
166. Achour, M., P. Delamoye, and A. Pialoux, *Revue Internationale des Hautes Temperatures et des Refractaires* 1975. **12**: p. 273-279.
167. Ocana, M. and C.J. Serna, *Variations of the infrared powder spectra of TiO<sub>2</sub> and SnO<sub>2</sub> (rutile) with polarization*. Spectrochimica Acta., 1991. **47A**(6): p. 765-774.
168. Jackson, S.D. and S.J. Hargreaves, eds. *Metal oxide catalysis. The application of UV-Visible-NIR spectroscopy to oxides*. Vol. 1. 2009, Wiley-VCH: Weinheim.
169. Belver, C., et al., *Palladium enhanced resistance to deactivation of titanium dioxide during the photocatalytic oxidation of toluene vapors*. Applied Catalysis B: Environmental, 2003. **46**(3): p. 497-509.
170. Jimenez, V.M., et al., *Structural characterization of partially amorphous SnO<sub>2</sub> nanoparticles by factor analysis of XAS and FT-IR spectra*. Solid State Ionics, 1999. **116** p. 117-127.
171. Pestryakov, A.N., et al., *Influence of modifying additives on the electronic state of supported palladium*. Chemical Physics Letters, 2003. **367**(1-2): p. 102-108.
172. Gellings, P.J. and H.J.M. Bouwmeester, *Solid state aspects of oxidation catalysis*. Catalysis Today, 2000. **58**(1): p. 1-53.
173. [www.engineersedge.com](http://www.engineersedge.com).
174. Sergent, N., et al., *Preparation and characterisation of high surface area stannic oxides: structural, textural and semiconducting properties*. Sensors and Actuators B-Chemical, 2002. **84**(2-3): p. 176-188.

175. Zholobenko, V.L., et al., *A new type of acidic hydroxyl groups in ZSM-5 zeolite and in mordenite according to diffuse reflectance i.r. spectroscopy*. Zeolites, 1988. **8**(3): p. 175-178.
176. Thornton, E.W. and P.G. Harrison, *Tin oxide surfaces. Part 1. —Surface hydroxyl groups and the chemisorption of carbon dioxide and carbon monoxide on tin(IV) oxide*. J. Chem. Soc., Faraday Trans. 1, 1975. **71**: p. 461 - 472.
177. Popescu, D.A., et al., *Nanosized tin dioxide : Spectroscopic (UV-VIS, NIR, EPR) and electrical conductivity studies*. Phys. Chem. Chem. Phys., 2001. **3**: p. 2522-2530.
178. Harrison, P.G. and A. Guest, *Tin oxide surfaces. Part 17. —An Infrared and Thermogravimetric Analysis of the Thermal Dehydration of Tin(Iv) Oxide Gel*. J. Chem. Soc., Faraday Trans. 1, 1987. **83**(11): p. 3383-3397.
179. Wakabayashi, F., et al., *FT-IR studies of the interaction between zeolitic hydroxyl groups and small molecules. I. Adsorption of nitrogen on H-mordenite at low temperature*. The Journal of Physical Chemistry, 2002. **97**(41): p. 10761-10768.
180. Natter, H., et al., *Grain-growth kinetics of nanocrystalline iron studied in situ by synchrotron real-time X-ray diffraction*. Journal of Physical Chemistry B, 2000. **104**(11): p. 2467-2476.
181. Michels, A., et al., *Modelling the influence of grain-size-dependent solute drag on the kinetics of grain growth in nanocrystalline materials*. Acta Materialia, 1999. **47**(7): p. 2143-2152.
182. Rock, C. and K. Okazaki, *Grain growth kinetics and thermal stability in a nanocrystalline multiphase mixture prepared by low-energy ball milling*. NanoStructured Materials, 1995. **5**(6): p. 657-671.
183. Shek, C.H., J.K.L. Lai, and G.M. Lin, *Grain growth in nanocrystalline SnO<sub>2</sub> prepared by sol-gel route* NanoStructured Materials, 1999. **11**(7): p. 887-893.
184. Kamp, B., et al., *Chemical diffusion of oxygen in tin dioxide: Effects of dopants and oxygen partial pressure*. Journal of Solid State Chemistry, 2005. **178**(10): p. 3027-3039.
185. Henderson, M.A., *Surface perspective on self-diffusion in rutile TiO<sub>2</sub>*. Surface Science, 1999. **419**(2-3): p. 174-187.
186. Iddir, H., et al., *Diffusion mechanisms of native point defects in rutile TiO<sub>2</sub>: Ab initio total-energy calculations*. Physical Review B, 2007. **75**(7).
187. Janotti, A. and C.G.V. de Walle, *Native point defects in ZnO*. Physical Review B, 2007. **76**(16).
188. Fensham, P.J., *Self diffusion in tin crystals*. Australian Journal of Scientific Research, Series A: Physical Sciences, 1950. **3**: p. 91.
189. Marsh, A.L. and J.L. Gland, *Effect of coadsorbed water on deep oxidation mechanisms: temperature programmed reactions of benzene and hydroxyl on the pt(111) surface*. Catalysis Letters, 2004. **93**(3-4): p. 165-170.
190. Korhonen, S.T., M. Calatayud, and A.O.I. Krause, *Stability of Hydroxylated (1h11) and (1h01) Surfaces of Monoclinic Zirconia: A Combined Study by DFT and Infrared Spectroscopy*. J. Phys. Chem. C, 2008. **112**: p. 6469-6476
191. Ignatchenko, A., et al., *Interaction of water with titania and zirconia surfaces*. Journal of Molecular Catalysis A: Chemical, 2006. **256**: p. 57–74.
192. Gélin, P., et al., *Complete oxidation of methane at low temperature over Pt and Pd catalysts for the abatement of lean-burn natural gas fuelled vehicles emissions: influence of water and sulphur containing compounds*. Catalysis Today, 2003. **83**: p. 45–57.
193. Wu, G., et al., *Adsorption and dissociation of hydrogen on MgO surface: a first-principles study*. Journal of Alloys and Compounds, 2009. **480** p. 788-793.

194. Kanofsky, J.R., et al., *Direct identification of reactive channels in reactions of oxygen- atoms and hydroxyl radicals with acetylene and methylacetylene*. *Journal of Physical Chemistry*, 1974. **78**(4): p. 311-316.
195. Pavelko, R.G., et al., *The Influence of Wide Range Humidity on Hydrogen Detection with Sensors Based on Nano-SnO<sub>2</sub> Materials*. *Proceedings of the 13th International Symposium on Olfaction and Electronic Nose*, M. Pardo and G. Sberveglieri, Eds., American Institute of Physics, 2009. **1137**: p. 29-33.

## 6. List of Tables

<b>TABLE 1.</b> PHYSICAL PROPERTIES OF HOMOLEPTIC TIN (IV) COMPLEXES. ....	22
<b>TABLE 2.</b> DEGREE OF HYDROLYSIS ( <i>H</i> ) FOR DIFFERENT PRECURSORS AND EXPERIMENTAL CONDITIONS. ....	28
<b>TABLE 3</b> BET SURFACE AREA OF SnO <sub>2</sub> SYNTHESIZED VIA DIFFERENT METHODS AS REPORTED IN [72] .....	30
<b>TABLE 4.</b> IONIC RADII, IONIZATION ENERGIES AND ELECTRONEGATIVITIES OF THE SELECTED ELEMENTS .....	46
<b>TABLE 5.</b> IONIC RADII, IONIZATION ENERGIES AND ELECTRONEGATIVITY OF THE SELECTED ELEMENTS .....	47
<b>TABLE 6.</b> LIST OF THE SYNTHESIZED MATERIALS. ....	67
<b>TABLE 7.</b> DETAILS OF TXRD EXPERIMENT. ....	76
<b>TABLE 8.</b> THE GAS MIXTURES USED IN THE EXPERIMENT. ....	82
<b>TABLE 9.</b> COMPARISON OF PEAK POSITIONS (IN CM <sup>-1</sup> ) IN THE IR SPECTRA OF Sn(AC) <sub>2</sub> , Sn(AC) <sub>4</sub> REPORTED IN THE LITERATURE, AND Sn(AC) <sub>4</sub> , [SnAC <sub>N</sub> ] <sub>M</sub> ·H <sub>2</sub> O RT FOUND IN THIS WORK.....	89
<b>TABLE 10.</b> COMPARISON OF XPS RESULTS .....	93
<b>TABLE 11.</b> WEIGHT CONTENT OF THE MAIN IMPURITIES FOUND BY LASER SPARK ELEMENT ANALYSIS IN SYNTHESIZED AND COMMERCIAL SnO <sub>2</sub> . ....	98
<b>TABLE 12.</b> ATOMIC CONTENT OF TI, ZR AND HF ELEMENTS IN THE CORRESPONDING OXIDE SYSTEMS.....	100
<b>TABLE 13.</b> CELL PARAMETERS ( <i>A</i> AND <i>C</i> ) AND CRYSTALLITE SIZE ( <i>D</i> ) FOR SYNTHESIZED COMPOUNDS IN COMPARISON WITH STANDARDIZED CRYSTALLOGRAPHIC DATA OF PURE OXIDES IN TETRAGONAL MODIFICATION. ....	102
<b>TABLE 14.</b> COMPARATIVE ANALYSIS OF NORMALIZED INTENSITIES <i>I</i> <sub>OH</sub> , <i>I</i> <sub>SNO</sub> , THEIR RATIO <i>I</i> <sub>OH</sub> / <i>I</i> <sub>SNO</sub> AND INTEGRAL OF THE BAND <i>N</i> <sub>OH</sub> BETWEEN 2500-3700 CM <sup>-1</sup> . ....	104
<b>TABLE 15.</b> ATOMIC CONTENT OF SC, Y AND LA ELEMENTS IN CORRESPONDING MIXED OXIDES. .	106
<b>TABLE 16.</b> CELL PARAMETERS ( <i>A</i> AND <i>C</i> ) AND CRYSTALLITE SIZE ( <i>D</i> ) FOR SYNTHESIZED COMPOUNDS IN COMPARISON WITH STANDARDIZED CRYSTALLOGRAPHIC DATA OF PURE SnO <sub>2</sub> . ....	108
<b>TABLE 17.</b> COMPARATIVE ANALYSIS OF NORMALIZED INTENSITIES <i>I</i> <sub>OH</sub> , <i>I</i> <sub>SNO</sub> , THEIR RATIO <i>I</i> <sub>OH</sub> / <i>I</i> <sub>SNO</sub> AND INTEGRAL OF THE BAND <i>N</i> <sub>OH</sub> BETWEEN 2500-3700 CM <sup>-1</sup> . ....	109

<b>TABLE 18.</b> ATOMIC CONTENT OF Pd, Pt AND Rh IN THE CORRESPONDING MATERIALS. ....	112
<b>TABLE 19.</b> CELL PARAMETERS ( <i>a</i> AND <i>c</i> ) AND CRYSTALLITE SIZE ( <i>D</i> ) FOR SYNTHESIZED COMPOUNDS IN COMPARISON WITH STANDARDIZED CRYSTALLOGRAPHIC DATA OF PURE SnO <sub>2</sub> . .....	113
<b>TABLE 20.</b> COMPARISON OF XPS RESULTS .....	114
<b>TABLE 21.</b> COMPARATIVE ANALYSIS OF NORMALIZED INTENSITIES $I_{OH}$ , $I_{SnO}$ , THEIR RATIO $I_{OH}/I_{SnO}$ AND INTEGRAL OF THE BAND $N_{OH}$ BETWEEN 2500-3700 $cm^{-1}$ .....	116
<b>TABLE 22.</b> FITTING PARAMETERS OF THE MODELS IN QUESTION. ....	141
<b>TABLE 23.</b> WEIGHT CONTENT OF THE TARGET ADMIXTURES IN SYNTHESIZED MATERIALS. ....	142
<b>TABLE 24.</b> FITTING PARAMETERS OF THE MODEL. ....	143
<b>TABLE 25.</b> FITTING PARAMETERS OF THE MODEL. ....	145
<b>TABLE 26.</b> FITTING PARAMETERS OF THE MODEL. ....	146

## 7. List of Figures

- FIGURE 1.** THE EVOLUTION OF WET CHEMICAL PROCESS: 1 – PRECURSOR DISSOLUTION, 2 – PRECURSOR HYDROLYSIS AND CONDENSATION, 3 – GELATION AS A RESULT OF COLLOID CONDENSATION AND POLYMERIZATION, 3-1 – SOLVENT EXTRACTION UNDER SUPERCRITICAL DRYING, 3-2 – CONVENTIONAL SOLVENT EVAPORATION, 3-3 – SOLVENT EVAPORATION FROM THE THIN LAYER, 4 – SEDIMENTATION..... 19
- FIGURE 2.** SnO<sub>2</sub> UNIT CELL WITH TIN ATOMS IN OCTAHEDRAL COORDINATION ..... 33
- FIGURE 3.** BAND MODEL (A), CALCULATED BAND STRUCTURE (B, FROM [92]) AND ILLUSTRATION OF THE CONTRIBUTION OF THE HYBRIDIZATION OF Sn AND O MOLECULAR ORBITALS FOR THE VALENCE AND CONDUCTION BANDS (C, FROM [92]).  $\Phi$  DENOTES THE WORK FUNCTION,  $M$  IS THE ELECTROCHEMICAL POTENTIAL,  $E_{VAC}$ ,  $E_C$ ,  $E_V$ ,  $E_F$  ARE THE VACUUM ENERGY LEVEL, BOTTOM OF THE CONDUCTION BAND, TOP OF THE VALENCE BAND AND FERMI LEVEL ENERGIES, RESPECTIVELY..... 34
- FIGURE 4.** ELECTRON MOBILITY (A) AND RESISTANCE (B) AS A FUNCTION OF TEMPERATURE IN MC-SnO<sub>2</sub>. CURVES IN FIGURE B ARE: 1 – INITIAL SAMPLE, 2 AND 3 – PRE-ANNEALED IN AIR, 2A AND 3A – PRE-ANNEALED IN DRY AR, 4 – PRE-ANNEALED AT 0.06 ATM OF O<sub>2</sub> AND STABILIZED FOR 282 H, 5-10 PRE-ANNEALED AT 1 ATM OF OXYGEN FOR VARIOUS PERIODS OF TIME (FROM 71 TO 161 H), 11-12 – SnO<sub>2</sub> DOPED WITH Sb [91]. ..... 35
- FIGURE 5.** BALL MODEL REPRESENTATION OF STOICHIOMETRIC (A), REDUCED (B) AND DEFECTIVE (C) (110) SnO<sub>2</sub> SURFACE, BASED ON IONIC RADII OF Sn<sup>4+</sup> AND O<sup>2-</sup> (ADAPTED FROM [93]). .... 39
- FIGURE 6.** BAND MODEL OF AN SEMICONDUCTOR: THE CASE OF REDUCED AND DEFECTIVE SURFACE (A) AND FULLY OXIDIZED SURFACE (B) (ADAPTED FROM [100]).  $E_{VAC}$ ,  $E_C$ ,  $E_F$ ,  $E_V$ , – VACUUM, CONDUCTION BAND, FERMI, AND VALENCE BAND ENERGY LEVELS;  $E_{C,s}$ ,  $E_{V,s}$  – CONDUCTION AND VALENCE BAND ENERGY LEVELS ON THE SURFACE;  $E_A$ ,  $E_D$  – ACCEPTOR AND DONOR ENERGY LEVELS;  $X$ ,  $M$ ,  $qV_s$  – ELECTRON AFFINITY, ELECTROCHEMICAL POTENTIAL AND BAND BENDING VALUE, RESP..... 40
- FIGURE 7.** THE BALL MODEL REPRESENTATION OF WATER CHEMISORPTION ON DEFECTIVE SnO<sub>2</sub> SURFACE (A) AND THE MODEL OF HYDROXYLATED DEFECTIVE SnO<sub>2</sub> SURFACE (B), ADAPTED FROM [108]. ..... 43
- FIGURE 8.** REPRESENTATION OF THE ELECTRON DEPLETED REGIONS IN A POLYCRYSTALLINE MATERIAL (A) AND REPRESENTATION OF THE BAND BENDING AS A FUNCTION OF THE PARTICLE CROSS SECTION (B), ADAPTED FROM [130]. ..... 52
- FIGURE 9.** UV-VIS ABSORBANCE SPECTRA OF COMMERCIAL SnO<sub>2</sub> (ALDRICH) AFTER KUBELKA-MUNK CONVERSION (A) AND LEAST SQUARES FIT OF A LINE THROUGH THE LOW ENERGY EDGE OF THE TRANSFORMED SPECTRUM (B). ..... 71

<b>FIGURE 10.</b> TOP (A) AND LATERAL (B) VIEW OF THE MICROSUBSTRATE MOUNTED ON TO-8 PACKAGE; THE MICROSUBSTRATE WITH DEPOSITED SENSING MATERIAL (C). .....	78
<b>FIGURE 11.</b> AN EXAMPLE OF CALIBRATION PLOTS OBTAINED FOR A MICROSUBSTRATE. ....	79
<b>FIGURE 12.</b> EXPERIMENTAL SET-UP FOR SENSING PROPERTIES CHARACTERIZATION. 1-4 – GAS CYLINDERS, 5 – GAS MIXING SYSTEM (ENVIRONICS), 6 – STAINLESS STEEL CHAMBER WITH SENSORS, 7 – TEFLON™ CHAMBER WITH HUMIDITY AND TEMPERATURE SENSOR (PRACTIC NC), 8 – PORTABLE UNITE FOR HUMIDITY AND TEMPERATURE MEASUREMENTS (PRACTIC NC), 9 – DIGITAL MULTIMETER (AGILENT), 10 – POWER SUPPLY (AGILENT), 11 – COMPUTER. ....	80
<b>FIGURE 13.</b> PLOTS OF RESISTANCE VS HEATER TEMPERATURE FOR BLANK SnO <sub>2</sub> IN DRY AIR (A) AND IN HUMID AIR (B). THE LEGENDS DENOTE THE NUMBER OF THE SUCCESSIVE MEASUREMENTS. ....	81
<b>FIGURE 14.</b> ARRHENIUS PLOT: SENSOR SIGNAL AGAINST $1/kT$ . ....	83
<b>FIGURE 15.</b> FTIR SPECTRA OF THE SYNTHESIZED TIN ACETATE COMPLEX AND COMMERCIAL TIN TETRAACETATE IN THE RANGE OF 400-4000 $\text{cm}^{-1}$ (A) AND 400-2000 $\text{cm}^{-1}$ (B). ....	88
<b>FIGURE 16.</b> FTIR SPECTRA OF THE SYNTHESIZED COMPLEX AFTER HEAT TREATMENT AT 50, 100 AND 300 °C FOR 20 H AT EACH TEMPERATURE. ....	90
<b>FIGURE 17.</b> XRD DIFFRACTOGRAMS OF THE COMPLEX AFTER HEAT TREATMENT AT 100 °C FOR 20 H. ....	90
<b>FIGURE 18.</b> MOLECULAR STRUCTURE OF TIN TETRAACETATE (A) AND SUPPOSED STRUCTURE OF THE SYNTHESIZED COMPLEX (B).....	91
<b>FIGURE 19.</b> TEM IMAGES OF SnO <sub>2</sub> AC (A) AND SnO <sub>2</sub> AC (IV) (B).....	92
<b>FIGURE 20.</b> XRD DIFFRACTOGRAMS (A) AND XPS SPECTRA (B) OF SnO <sub>2</sub> SYNTHESIZED FROM TIN HYDROXIDE ACETATE AND TIN TETRAACETATE (ALDRICH). ....	94
<b>FIGURE 21.</b> XPS SPECTRA OF SnO <sub>2</sub> SYNTHESIZED FROM TIN HYDROXIDE ACETATE AND TIN TETRAACETATE (ALDRICH).....	94
<b>FIGURE 22.</b> FTIR (A) AND UV-VIS (B) SPECTRA OF SnO <sub>2</sub> SYNTHESIZED FROM TIN HYDROXIDE ACETATE AND TIN TETRAACETATE (ALDRICH).....	95
<b>FIGURE 23.</b> TEM PICTURES OF BLANK SnO <sub>2</sub> (A), SnO <sub>2</sub> -TiO <sub>2</sub> (B), SnO <sub>2</sub> -ZrO <sub>2</sub> (C), AND SnO <sub>2</sub> -HfO <sub>2</sub> (D).....	101
<b>FIGURE 24.</b> XRD DIFFRACTOGRAMS OF SnO <sub>2</sub> AC AND SnO <sub>2</sub> -TiO <sub>2</sub> (A), AND SnO <sub>2</sub> -ZrO <sub>2</sub> AND SnO <sub>2</sub> -HfO <sub>2</sub> (B). ....	102
<b>FIGURE 25.</b> FTIR SPECTRA OF SnO <sub>2</sub> AC AND SnO <sub>2</sub> -TiO <sub>2</sub> (A), AND SnO <sub>2</sub> -ZrO <sub>2</sub> AND SnO <sub>2</sub> -HfO <sub>2</sub> (B).....	103
<b>FIGURE 26.</b> UV-VIS SPECTRA OF SnO <sub>2</sub> AC, SnO <sub>2</sub> -TiO <sub>2</sub> , SnO <sub>2</sub> -ZrO <sub>2</sub> AND SnO <sub>2</sub> -HfO <sub>2</sub> . ....	105
<b>FIGURE 27.</b> COMPARISON OF THE $E_G$ WITH ELECTRONEGATIVITY OF THE INTRODUCED METALS (A), MEAN CRYSTALLITE SIZE AND HYDROXYLATION DEGREE OF THE MATERIALS (B). INSET – ATOMIC CONTENT OF THE GIVEN ELEMENTS.....	106
<b>FIGURE 28.</b> TEM PICTURES OF BLANK SnO <sub>2</sub> (A), SnO <sub>2</sub> -Sc <sub>2</sub> O <sub>3</sub> (B), SnO <sub>2</sub> -Y <sub>2</sub> O <sub>3</sub> (C), AND SnO <sub>2</sub> -La <sub>2</sub> O <sub>3</sub> (D).....	107
<b>FIGURE 29.</b> XRD DIFFRACTOGRAMS OF SnO <sub>2</sub> AC, SnO <sub>2</sub> -Sc <sub>2</sub> O <sub>3</sub> (A), AND SnO <sub>2</sub> - Y <sub>2</sub> O <sub>3</sub> , SnO <sub>2</sub> -La <sub>2</sub> O <sub>3</sub> (B).....	108



<b>FIGURE 30.</b> FTIR SPECTRA OF SnO <sub>2</sub> AC, SnO <sub>2</sub> -Sc <sub>2</sub> O <sub>3</sub> (A), AND SnO <sub>2</sub> - Y <sub>2</sub> O <sub>3</sub> , SnO <sub>2</sub> - La <sub>2</sub> O <sub>3</sub> (B).	109
<b>FIGURE 31.</b> UV-VIS SPECTRA OF SnO <sub>2</sub> AC, SnO <sub>2</sub> -Sc <sub>2</sub> O <sub>3</sub> , SnO <sub>2</sub> - Y <sub>2</sub> O <sub>3</sub> AND SnO <sub>2</sub> - La <sub>2</sub> O <sub>3</sub> .....	110
<b>FIGURE 32.</b> QUALITATIVE COMPARISON OF THE <i>EG</i> WITH ELECTRONEGATIVITY OF THE METALS (A), MEAN CRYSTALLITE SIZE AND HYDROXYLATION DEGREE OF THE MATERIALS (B). INSET – ATOMIC CONTENT OF THE GIVEN ELEMENTS. ....	111
<b>FIGURE 33.</b> TEM IMAGES OF SnO <sub>2</sub> AC-Pd (A) AND SnO <sub>2</sub> AC-Pt (B).....	112
<b>FIGURE 34.</b> HRTEM (A) AND FT (B) IMAGES OF SnO <sub>2</sub> AC-Pd. AREAS 1 AND 2 CORRESPOND TO SnO <sub>2</sub> AND PDO (RESP.). ....	113
<b>FIGURE 35.</b> XRD DIFFRACTOGRAMS OF SnO <sub>2</sub> AC-Pd (A) AND SnO <sub>2</sub> AC-Pt (B).....	114
<b>FIGURE 36.</b> XPS SPECTRA OF SnO <sub>2</sub> AC-Pd: BANDS CORRESPONDED TO Sn3D <sub>5/2</sub> (A) AND O1s (B). ....	114
<b>FIGURE 37.</b> FTIR SPECTRA OF SnO <sub>2</sub> AC (A) AND SnO <sub>2</sub> AC WITH DEPOSITED NOBLE METALS (B). ....	116
<b>FIGURE 38.</b> UV-VIS SPECTRA OF SnO <sub>2</sub> AC-Pd, Pt, Rh (A) AND SnO <sub>2</sub> AC-Pt/Rh, Pd/Rh, Pd/Pt (B). ....	117
<b>FIGURE 39.</b> TGA PROFILES FOR SnO <sub>2</sub> AC (A) AND SnO <sub>2</sub> AC (IV). <i>S</i> – SLOPE OF THE FITTED LINE, <i>NA</i> – NORMALIZED AREA OF THE DESORPTION BAND. ....	123
<b>FIGURE 40.</b> TGA PROFILES FOR SnO <sub>2</sub> AC (A) AND SnO <sub>2</sub> DOPED WITH IVB ELEMENTS (B). <i>S</i> – SLOPE OF THE FITTED LINE, <i>NA</i> – NORMALIZED AREA OF THE DESORPTION BAND. ....	124
<b>FIGURE 41.</b> TGA PROFILES FOR SnO <sub>2</sub> AC (A) AND SnO <sub>2</sub> DOPED WITH IIIB ELEMENTS (B). <i>S</i> – SLOPE OF THE FITTED LINE, <i>NA</i> – NORMALIZED AREA OF THE DESORPTION BAND. ....	125
<b>FIGURE 42.</b> TGA PROFILES FOR MONOCATALYTIC (A) AND BICATALYTIC (B) SYSTEMS DEPOSITED ON SnO <sub>2</sub> AC IN COMPARISON WITH BLANK OXIDE. <i>S</i> – SLOPE OF THE FITTED LINE, <i>NA</i> – NORMALIZED AREA OF THE DESORPTION BAND. ....	126
<b>FIGURE 43.</b> MS SIGNALS OF HYDROGEN (BLACK LINE) AND SIGNAL DERIVATIVE (RED LINE) VS TEMPERATURE OF ISOTHERMAL HEATING OF SnO <sub>2</sub> AC (A) AND SnO <sub>2</sub> -Pd (B) IN 3100 PPM OF H <sub>2</sub> IN AIR (BLACK LINE MS).....	127
<b>FIGURE 44.</b> MS SIGNALS OF WATER (BLACK LINE) AND SIGNAL DERIVATIVE (RED LINE) VS TEMPERATURE OF ISOTHERMAL HEATING OF SnO <sub>2</sub> AC (A) AND SnO <sub>2</sub> -Pd (B) IN 3100 PPM OF H <sub>2</sub> IN AIR (BLACK LINE MS).....	128
<b>FIGURE 45.</b> STOICHIOMETRY OF HYDROGEN OXIDATION REPRESENTED AS WATER TO HYDROGEN MOLE RATIO VS TEMPERATURE. ....	129
<b>FIGURE 46.</b> TPR PROFILES OF SnO <sub>2</sub> ALDR, SnO <sub>2</sub> AC (A) AND SnO <sub>2</sub> -Pd, SnO <sub>2</sub> AC (B) IN 5% H <sub>2</sub> IN AR.....	131
<b>FIGURE 47.</b> TPR PROFILES OF SnO <sub>2</sub> ALDR, SnO <sub>2</sub> AC (A) AND SnO <sub>2</sub> -Pd, SnO <sub>2</sub> AC (B) IN 0.1% H <sub>2</sub> IN AIR. ....	132
<b>FIGURE 48.</b> VARIATION IN THE ABSORBANCE SPECTRA OF BLANK (A) AND Pd DOPED (B) SnO <sub>2</sub> IN DRY AIR AS A FUNCTION OF TEMPERATURE.....	134
<b>FIGURE 49.</b> VARIATION OF THE ABSORBANCE SPECTRA OF BLANK (A) AND Pd DOPED (B) SnO <sub>2</sub> IN THE PRESENCE OF 100 PPM OF H <sub>2</sub> IN DRY AIR AS A FUNCTION OF TEMPERATURE. ....	135

<b>FIGURE 50.</b> VARIATION OF THE ABSORBANCE SPECTRA OF BLANK (A) AND Pd DOPED (B) SnO <sub>2</sub> AT 80% RH AS A FUNCTION OF TEMPERATURE. ....	136
<b>FIGURE 51.</b> NORMALIZED DRIFT SPECTRA OF SnO <sub>2</sub> -Pd IN AIR WITH 25800 PPM OF H <sub>2</sub> O (A) AND 100 PPM OF H <sub>2</sub> (B). ....	137
<b>FIGURE 52.</b> TIME EVOLUTION OF MEAN CRYSTALLITE SIZE OF BLANK SnO <sub>2</sub> AT 600, 700 AND 800 °C: EXPERIMENTAL DATA ARE FITTED WITH GENERALIZED PARABOLIC MODEL (A), AND WITH SIZE-DEPENDENT IMPEDIMENT MODEL (B). THE VALUES OF $X^2$ ARE SHOWN CLOSE TO THE FIT CURVES. ....	140
<b>FIGURE 53.</b> TIME EVOLUTION OF MEAN CRYSTALLITE SIZE OF BLANK SnO <sub>2</sub> , SnO <sub>2</sub> -CL, SnO <sub>2</sub> -S AND SnO <sub>2</sub> -NaCl AT 700 °C. THE VALUES OF $X^2$ ARE SHOWN CLOSE TO THE FIT CURVES. ....	143
<b>FIGURE 54.</b> TIME EVOLUTION OF MEAN CRYSTALLITE SIZE OF SnO <sub>2</sub> -TiO <sub>2</sub> , SnO <sub>2</sub> -ZrO <sub>2</sub> , SnO <sub>2</sub> -HfO <sub>2</sub> (A) AND SnO <sub>2</sub> -Sc <sub>2</sub> O <sub>3</sub> , SnO <sub>2</sub> -Y <sub>2</sub> O <sub>3</sub> , SnO <sub>2</sub> -La <sub>2</sub> O <sub>3</sub> (B) AT 700 °C. THE VALUES OF $X^2$ ARE SHOWN CLOSE TO THE FIT CURVES. ....	144
<b>FIGURE 55.</b> TIME EVOLUTION OF MEAN CRYSTALLITE SIZE OF SnO <sub>2</sub> -Pdo, SnO <sub>2</sub> -Pd AND SnO <sub>2</sub> -Pt AT 700 °C. THE VALUES OF $X^2$ ARE SHOWN CLOSE TO THE FIT CURVES. ....	146
<b>FIGURE 56.</b> ARRHENIUS PLOT OF LN(TA) VS 1000/T, WHERE A – GROWTH RATE CONSTANT AND T – TEMPERATURE (IN K). ....	147
<b>FIGURE 57.</b> SIGNALS TO H <sub>2</sub> AS A FUNCTION OF T AT 0% RH FOR BLANK MATERIALS IN QUESTION. ....	150
<b>FIGURE 58.</b> SIGNALS TO H <sub>2</sub> AS A FUNCTION OF T AT 0, 20, 50, 80% RH FOR SYNTHESIZED BLANK MATERIALS. ....	152
<b>FIGURE 59.</b> SENSOR SIGNAL OF SnO <sub>2</sub> AC (A) AND SnO <sub>2</sub> AC ALDRICH (B) TO WATER VAPOUR AGAINST TEMPERATURE. ....	153
<b>FIGURE 60.</b> VARIATION OF $S_{MAX}$ , $T_{SMAX}$ (A) AND $E_{ACT}$ (B) WITH RELATIVE HUMIDITY. ....	154
<b>FIGURE 61.</b> SIGNALS TO H <sub>2</sub> AS A FUNCTION OF T AT 0, 20, 50, 80% RH FOR BLANK AND DOPED SnO <sub>2</sub> . ....	156
<b>FIGURE 62.</b> VARIATION OF $S_{MAX}$ , $T_{SMAX}$ (A) AND $E_{ACT}$ (B) WITH RELATIVE HUMIDITY. ....	158
<b>FIGURE 63.</b> SIGNALS TO H <sub>2</sub> AS A FUNCTION OF T AT 0, 20, 50, 80% RH FOR DOPED SnO <sub>2</sub> . ....	159
<b>FIGURE 64.</b> VARIATION OF $S_{MAX}$ , $T_{SMAX}$ (A) AND $E_{ACT}$ (B) WITH RELATIVE HUMIDITY. ....	160
<b>FIGURE 65.</b> SIGNALS TO H <sub>2</sub> AS A FUNCTION OF T AT 0, 20, 50, 80% RH FOR CATALYSTS-DOPED SnO <sub>2</sub> . ....	161
<b>FIGURE 66.</b> SIGNALS OF SnO <sub>2</sub> -Pd TO H <sub>2</sub> O IN DRY AIR AND IN THE PRESENCE OF H <sub>2</sub> (A), AND SIGNALS TO H <sub>2</sub> IN DRY AIR AND IN THE PRESENCE OF H <sub>2</sub> O (B). ....	163
<b>FIGURE 67.</b> VARIATION OF $S_{MAX}$ (A) AND $T_{SMAX}$ (B) WITH RELATIVE HUMIDITY FOR CATALYST-DOPED SnO <sub>2</sub> . ....	165
<b>FIGURE 68.</b> VARIATION OF $E_{ACT}$ WITH RELATIVE HUMIDITY FOR CATALYST-DOPED SnO <sub>2</sub> . ....	165

## 8. List of Publications

### 8.1. Chapters in books

1. **R. Pavelko**, A.Vasiliev, V. Sevastyanov, X. Vilanova, X. Correig, Tin Oxide from organo-metallic compounds: material's properties and sensor characteristics, in *Sensors for Environment, Health and Security: Advanced Materials and Technologies*, Baraton, M.-I. (Ed.), 2009, XXIV, 500 p, Springer, ISBN: 978-1-4020-9008-0.
2. A.A.Vasiliev, **R. Pavelko**, S. Gogish-Klushin, D. Kharitonov, O Gogish-Klushina, A.V.Sokolov, N.Samotaev, V. Guarnieri, M. Zen, L. Lorenzelli, Sensors based on technology "nano-on-micro" for wireless instruments preventing ecological and industrial catastrophes, *Sensors for Environment, Health and Security: Advanced Materials and Technologies*, Baraton, M.-I. (Ed.), 2009, XXIV, 500 p, Springer, ISBN: 978-1-4020-9008-0.

### 8.2. Full papers

1. A. A.Vasiliev, R.G. Pavelko, S. Yu. Gogish-Klushin, D. Yu. Kharitonov, O. S. Gogish-Klushina, A. V.Sokolov, N. N. Samotaev, Alumina MEMS platform for impulse semiconductor and IR optic gas sensors, *Sensors and Actuators B: Chemical*, 132 (1), pp. 216-223, **2008**, DOI:10.1016/j.snb.2008.01.043
2. R. G. Pavelko, A. A. Vasil'ev, V. G. Sevast'yanov, F. Gispert-Guirado, X. Vilanova, N. T. Kuznetsov, Studies of thermal stability of nanocrystalline SnO<sub>2</sub>, ZrO<sub>2</sub>, and SiC for semiconductor and thermocatalytic gas sensors. *Russian Journal of Electrochemistry*, 45 (4), pp 470-475, **2009**, DOI: 10.1134/S1023193509040181
3. R.G. Pavelko, A.A. Vasiliev, E. Llobet, X. Vilanova, N. Barrabés, F. Medina, V.G. Sevastyanov, Comparative study of nanocrystalline SnO<sub>2</sub> materials for gas

- sensor application: thermal stability and catalytic activity, *Sensors and Actuators B: Chemical*, 137, pp. 637–643, **2009**, DOI:10.1016/j.snb.2008.12.025.
4. R. Leghrib, R. Pavelko, A. Felten, A. Vasiliev, C. Cané, I. Gràcia, J.-J. Pireaux, E. Llobet, Gas sensors based on multiwall carbon nanotubes decorated with tin oxide nanoclusters, *Sensors and Actuators B: Chemical*, **2010**, DOI: 10.1016/j.snb.2009.12.044.
  5. R.G. Pavelko, A.A. Vasiliev, F. Gispert-Guirado, N. Barrabes, J. Llorca, E. Llobet, V.G. Sevastyanov, Crystallite growth kinetics of highly pure nanocrystalline tin dioxide: the effect of palladium doping, *Materials Chemistry and Physics*, **2010**, Proof corrected, in print.
  6. M. Hübner, R. Pavelko, N. Barsan, Influence of Oxygen Backgrounds on Hydrogen Sensing with SnO<sub>2</sub> Nanomaterials, *Sensors and Actuators B: Chemical*, **2010**, DOI:10.1016/j.snb.2010.01.049.
  7. R. G. Pavelko, H. Daly, C. Hardacre, A. A. Vasiliev, E. Llobet, Interaction of water, hydrogen and their mixtures with SnO<sub>2</sub> based materials: the role of surface hydroxyl groups in detection mechanisms, *Phys. Chem. Chem. Phys.*, **2010**, DOI: 10.1039/b921219a.

### **8.3. Conference proceedings**

1. A. A.Vasiliev, V. I. Filippov, R. Pavelko, V. G.Sevastianov, A. V.Sokolov, V. Guarnieri, Detection of hydrogen traces using microelectronic gas sensors, International Congress on Analytical Sciences (ICAS), pp. 2-P219, **2006**.
2. A. A.Vasiliev, R. G. Pavelko, V. Guarnieri, L. Lorenzelli, V. G. Sevastianov, A.V.Sokolov, N.N.Samotaev, X.Vilanova, Micromachined thermocatalytic gas sensor with improved selectivity based on Pd/Pt doped YSZ material, 11th International Meeting on Chemical Sensors (IMCS 11), pp. 257, **2006**.
3. V. Guarnieri, L. Lorenzelli, A. Vasiliev, R. Pavelko, Sevastianov, V; Vilanova, X, Semiconductor and thermocatalytic gas sensor based on doped nano-particle oxide material and SiO<sub>2</sub>/Si<sub>3</sub>N<sub>4</sub> microhotplate, XX Eurosensors, pp. WA1-P22, **2006**.
4. R.G. Pavelko, A.A. Vasiliev, X. Vilanova, A.V. Sokolov, V.G. Sevastianov, V. Guarnieri, L. Lorenzelli, N.N. Samotaev, B. Podlepetski, Sensing YSZ Nano-Material for Thermocatalytic Micromachined Gas Sensor with Improved Selectivity, Conferencia de Dispositivos Electronicos, pp. 4-16, **2007**.

5. R.G.Pavelko, A.A. Vasiliev, S.Yu Gogish-Klushin, D. Yu Kharitonov, O.S. Gogish-Klushina, Micromachined Alumina Membranes for Gas sensors and IR Radiation Source, Conferencia de Dispositivos Electronicos, pp. 4-16, **2007**.
6. N.N.Samotaev, A.V.Sokolov, A.A.Vasiliev, R.G.Pavelko, A.V.Pisliakov, S.Yu.Gogish-Klushin, O.S.Gogish-Klushina, D.Yu.Kharitonov, A novel approach to the electronic nose concept: the analysis of metal oxide sensor response at fast temperature modulation, International Symposium on Olfaction and Electronic Nose, pp. 29 – 30, **2007**.
7. A.A.Vasiliev, R.G. Pavelko, S.Yu.Gogish-Klushin, D.Yu.Kharitonov, O.S.Gogish-Klushina, A.V.Sokolov, N.N.Samotaev, Alumina MEMS Platform for Impulse Semiconductor and IR Optic Gas Sensors, Transducers 2007/Eurosensors XXI, p. 2035-2038, **2007**.
8. R. Pavelko, A. Vasiliev, V. Sevastyanov, X. Vilanova, New approaches to synthesis of sensing materials for thermocatalytic and semiconducting gas sensors, NATO Advanced Study Institute, pp. 91, **2007**.
9. R. G. Pavelko, V. G. Sevastyanov, A. A. Vasiliev, X. Vilanov and N. T. Kuznetsov, Organo-metal precursors for synthesis of advanced nanodispersed oxides for chemical sensors, International Conference on Organometallic and Coordination Chemistry, pp. O40, **2008**.
10. A.A. Vasiliev, R.G. Pavelko, V.G. Sevastyanov, N.N. Samotaev, A.V. Sokolov, X.Vilanova, Chemical sensors based on nano-particle metal oxide materials: chemical and physical approach, International Conference on Organometallic and Coordination Chemistry, pp. O53, **2008**.
11. N. Samotaev, A. Vasiliev, B. Podlepetsky, A. Sokolov, A. Pisliakov, **R. Pavelko**, Metal oxide sensor with improved selectivity to ammonia, Eurosensors XXII, pp. 1053-1055, **2008**.
12. R.G. Pavelko, A. A. Vasiliev, X. Vilanova, V. G. Sevastyanov, Long-term stability of SnO<sub>2</sub> gas sensors: the role of impurities, IEEE SENSORS, pp. 815-818, **2008**.
13. R. G. Pavelko, A. A. Vasiliev, E. Llobet, X. Vilanova, X. Correig, V. G. Sevastyanov, The Influence of Wide Range Humidity on Hydrogen Detection with Sensors Based on Nano-SnO<sub>2</sub> Materials, 13th International Symposium on Olfaction and Electronic Nose, pp 29-33, **2009**.

14. M. Hübner, R. Pavelko, J. Kemmler, N. Barsan, U. Weimar, Influence of Material Properties on Hydrogen Sensing for SnO<sub>2</sub> Nanomaterials, Eurosenors XXIII, Procedia Chemistry 1, 1423–1426, **2009**.
15. R. Leghrib, E. Llobet, R. Pavelko, A.A. Vasiliev, A. Felten, J.J. Pireaux, Gas sensing properties of MWCNTs decorated with gold or tin oxide nanoparticles, Eurosenors XXIII, Procedia Chemistry 1, 168–171, **2009**.

## 9. Curriculum vitae

### General information

Date and Place of Birth May 6, 1979, Elektrogorsk, Moscow region, Russia

Nationality Russian

### Education

18/06/2001 B.S. in chemistry, Russian Peoples' Friendship  
University, Moscow, Russia.

05/06/2002 Diploma of "consultant-interpreter" from French into  
Russian in natural sciences

19/06/2003 M.S. in chemistry, Russian Peoples' Friendship  
University, Moscow, Russia

19/06/2003 Teaching Diploma in High School Chemistry

24/05/2007 Ph.D. in inorganic chemistry, N. S. Kurnakov Institute  
of General and Inorganic Chemistry, Moscow, Russia.

18/10/2007 M.S. in electronic engineering, University Rovira i  
Virgili, Tarragona, Spain.

### Awards

2008 Patent with my participation (RU(11) 2 339 574) was awarded the  
title of "100 best Russian inventions in 2008" by Russian federal  
service for intellectual property, patents and trademarks.

2009 I was awarded the title of "Best young researcher" at Institute of  
General and Inorganic Chemistry in 2009

2009 FP6 "Structuring the European Research Area" Program  
Scholarship: Centacat centre, Queens University Belfast, UK,  
June-July 2009.

2009 FP6 "Structuring the European Research Area" Program  
Scholarship: Centacat centre, Queens University Belfast, UK,  
Nov-Dec 2009